Extracellular Matrix Hydrogels for Endometrial Regeneration

Maxine Chan

Imperial College London

Department of Materials

Thesis submitted in accordance with the requirements for the degree of Doctor of Philosophy

May 2022

Declaration of originality

I declare that the work included in this thesis is my own, unless otherwise stated or cited. Experimental work or data analysis performed by, in collaboration with, or with the assistance of others has been acknowledged throughout the thesis. The work presented in this thesis was undertaken at Imperial College London, University College London and University of Warwick.

Copyright declaration

The copyright of this thesis rests with the author. Unless otherwise indicated, its contents are licensed under a Creative Commons Attribution-Non Commercial-No Derivatives 4.0 International Licence (CC BY-NC-ND). Under this licence, you may copy and redistribute the material in any medium or format on the condition that; you credit the author, do not use it for commercial purposes and do not distribute modified versions of the work. When reusing or sharing this work, ensure you make the licence terms clear to others by naming the licence and linking to the licence text. Please seek permission from the copyright holder for uses of this work that are not included in this licence or permitted under UK Copyright Law.

Abstract

Intrauterine scarring is an important cause of infertility and other adverse pregnancy outcomes. Current treatments do not specifically address the pathological process of fibrosis and are not highly effective, particularly when it comes to functional endometrial regeneration. This thesis explored a biomaterials approach to preventing intrauterine adhesions and hypothesised that an endometrial ECM hydrogel has favourable bioactive properties to prevent fibrosis and to promote endometrial repair. A new protocol for decellularising porcine endometrial ECM was described and the decellularised ECM was then comprehensively characterised using various biomolecular tools to demonstrate the preservation of important ECM proteins and matrix-bound nanovesicles, with exosome-like properties. An injectable and sprayable, thermo-responsive hydrogel was made from decellularised endometrial ECM, with gelation properties that made it suitable for *in vivo* applications. Using various *in vitro* assays, endometrial ECM hydrogel was demonstrated to be compatible with endometrial cells, improve angiogenesis and possess immunomodulatory properties. It was also capable of mitigating the effect of TGF-β1 in an *in vitro* endometrial fibrosis experiment. A reliable mouse model of intrauterine fibrosis was developed, using ethanol to induce endometrial damage. Applying endometrial ECM hydrogel in this model demonstrated primary prevention of endometrial damage in 60% of the ECM-treated group. ECM hydrogel treatment also significantly reduced the gene expression of Collagen I in the ethanol-injured uterine horns. These results demonstrated the favourable effect of endometrial ECM hydrogel for limiting intrauterine fibrosis and will pave the way for further studies on secondary prevention of scarring and fertility preservation.

Acknowledgements

Completing this PhD has been one of the greatest challenges of my life. I would like to thank all the people who have carried me along this journey, accompanying me through all the highs and the lows, and offering me inspiration, hope, reassurance and compassion when I have needed it the most.

Firstly, I would like to thank my supervisors Professor Molly Stevens, Mr Richard Smith and Mr Srdjan Saso. Thank you for your unwavering support, your positivity and your belief in me. I am grateful to Molly for welcoming me into her group, encouraging and allowing me to pursue every research idea that I approached her with and for telling me it's ok whenever something went wrong. I am grateful to Mr Smith for inspiring me to undertake this PhD, embracing me as part of his research team and for his wonderful anecdotes and pep talks, that never fail to lift my spirits. I would like to say a huge thank you to Srdjan, for his endless optimism, constant moral support and for connecting me to his wide academic network, which has enabled me to form some great research collaborations. Thank you for being a fantastic mentor and my greatest cheerleader.

I would like to express my gratitude to my collaborators, who have believed in my project and been generous with their help. Thank you to Professor Simon Waddington and postdoc, Ashley Boyle, for all their hands-on assistance and guidance with the *in vivo* work at UCL. I really appreciated their wisdom and patience. I would also like to thank Professor Brosens and postdoc, Tom Rawlings, at University of Warwick, for helping me with the organoid work and sharing their expertise.

I have been fortunate to work with, befriend and be guided by many wonderful people in the Stevens Group. I am grateful to my previous post-doc mentor Tim Keane, for inspiring me to work with ECM, teaching me my very first lab skills and helping me to design my project. Thank you to my current post-doc mentor Alice Agliano, for always being ready to lend me her support and for teaching me to become a better scientist. She has been an amazing mentor and someone I could always rely on for good advice. I would also like to thank post-doc extraordinaire, Jono Wojciechowski, for all his help with Rheology and anything chemistry related, and for kindly offering to read my thesis chapter. Also thank you to post-doc Vernon Lalone, who taught me about Raman spectroscopy, helped me with Raman data acquisition for this thesis and worked extensively with me on other projects that were not included in this thesis. I am also grateful to other postdocs and former or current PhD students who have contributed their expertise, help and advice towards this project – Jelle Penders, Tom

Whittaker, James Armstrong, Allie Spiedel, Junyoung Kim, Conor Horgan, Joyce Che, Axel Moore, Lorna Barron, Aida Abdelwahed.

I am extremely thankful for the guidance and friendship of fellow / former PhD students, particularly when I first joined the group with no scientific background or lab experience and terrified of making mistakes with my experiments. Maria Joao (now Dr), in particular, was always so generous with her help and advice, and I'm so happy that she has become a good friend. Other students to whom I am especially grateful for their readiness to help me in the lab are Liliana and Raya.

For their friendship and moral support, I am grateful to fellow newbies 2017 / office buddies and party car 2019 - Raya, Dan, Charlotte and Katya. They helped to make this PhD experience fun and memorable in all the right ways and gave me a reason to look forward to coming into the lab, even on days when I really didn't want to. Thank you for helping me stay sane.

My biggest source of support in this PhD has been my amazing friend and lab buddy, Charlotte Lee-Reeves. We have spent so many days, evenings and weekends in the lab, joined at the hip. I am beyond grateful for her companionship over the last 4.5 years and I feel lucky that we got to work so closely with each other on experiments and coped with so many challenges together as a duo. She has taught me and helped me in more ways than I can count - I certainly owe all my microscopy knowledge and images to her. For so much of this journey, it has felt like we were each other's mentors, and I am really proud of everything that we have overcome and achieved. Thank you for inspiring and encouraging me, and for being my confidante when times were tough. You have been my rock throughout this PhD journey, and I can't imagine how I would have got to the end of it without you. I only hope that I am half as good a friend to you, as you have been to me.

To my fiancé, Alessandro, thank you for being by my side throughout this incredibly stressful and consuming journey. Thank you for putting up with all the late evenings, the weekends in the lab, the grumpy moods and the constant excuse of "my PhD". I know it was not always easy for you and I am so grateful for your patience, your love and for never making me feel bad.

To my mum, who is the most inspiring woman in my life, thank you for your unconditional love and support. Thank you for being such a great example of strength, courage and determination for me, which has motivated me to keep going even when I encounter the toughest obstacles. I would not be where I am today without you. I promise this is the last graduation I will make you attend.

Contents

Abstract 4

Acknowledgements 5

List of figures 14

List of tables 17

List of abbreviations 18

Chapter 1 – Introduction 22

1.1 The Endometrium 22

1.2 Absolute Uterine Factor Infertility 23

1.3 Intrauterine adhesions and Asherman's syndrome 24

1.3.1 Symptoms and clinical consequences of intrauterine adhesions 24

1.3.2 Aetiology and prevalence 26

1.3.3 Molecular mechanisms of intrauterine adhesions 27

1.3.4 Diagnosis and classification 28

1.3.5 Current management 28

1.3.5.1 Preventative strategies 29

1.3.5.2 Treatment and secondary prevention strategies 29

1.3.6 Regenerative medicine approaches for endometrial regeneration 30

1.3.6.1 Stem cell therapy 31

1.3.6.2 Bioengineering approaches to uterine and endometrial regeneration 34

1.3.6.2.1 Decellularised uterine matrices 34

1.3.6.2.2 Cell-loaded scaffolds 35

1.3.6.2.3 Biomaterials scaffolds for growth factor and hormone delivery 35

1.4 Extracellular matrix as a biomaterial for tissue regeneration 36

1.4.1 What is extracellular matrix? 36

1.4.2 Properties and applications of decellularised ECM biomaterials 36

1.4.3 ECM hydrogels 39

1.4.3.1 *In vitro* applications of ECM hydrogels 39

1.4.3.2 *In vivo* applications of ECM hydrogels 40

1.4.3.3 Anti-fibrotic effect of ECM hydrogels 40

1.4.3.4 ECM hydrogels for growth factor delivery 41

1.4.4 Non-tissue-specific ECM for reconstruction of the female reproductive tract 41

Hypothesis 43

Aims and Objectives 43

Chapter 2 – Fabrication and Characterisation of Endometrial ECM 44

2.1 Chapter aims 44
2.2 Introduction to Production of ECM Biomaterials 45
2.2.1 Source of ECM 45
2.2.1.1 Animal species and tissue specificity 45
2.2.1.2 ECM from young versus old animals 45
2.2.2 Production of decellularised ECM biomaterials 46
2.2.2.1 Decellularisation considerations 46
2.2.2.2 Decellularisation methods 47
2.2.2.2.1 Physical methods 47
2.2.2.2.2 Chemical reagents 48
2.2.2.2.3 Enzymatic reagents 49
2.2.2.3 Sterilisation methods 49
2.2.2.4 Evaluation of decellularisation efficiency 50
2.2.3 Uterine tissue decellularisation 50
2.2.4 Preparation and characterisation of ECM hydrogels 54
2.2.5 Matrix-bound nanovesicles 54
2.3 Materials and Methods 57
2.3.1 Preparation and Decellularisation of Porcine ECM 57
2.3.1.1 Morphological comparison of pig and sow endometrium 57
2.3.1.2 Isolation and preparation of porcine endometrium for decellularisation 58
2.3.1.3 Sow endometrial decellularization 59
2.3.1.4 Pig endometrial decellularisation 60
2.3.1.5 Porcine small intestinal submucosa (SIS) decellularisation 61
2.3.1.6 Porcine urinary bladder matrix (UBM) decellularisation 61
2.3.2 Determining efficiency of ECM decellularization 62
2.3.2.1 Qualitative analysis of nuclear content 62
2.3.2.2 DNA isolation from ECM 62
2.3.2.3 DNA quantification 63
2.3.3 Characterisation of decellularised endometrial ECM 64
2.3.3.1 Histology 64
2.3.3.2 Immunofluorescence 64
2.3.3.3 Raman Spectroscopy of endometrial ECM 65
2.3.3.4 Proteomics 66
2.3.3.4.1 Sample preparation for LC/MS 66
2.3.3.4.2 Proteomics data processing and analysis 68
2.3.4 Isolation and characterisation of matrix-bound vesicles (MBV) 69

2.3.4.1 Digestion of ECM and MBV isolation 69
2.3.4.2 Micro-BCA assay 70
2.3.4.3 Nanoparticle Tracking Analysis 71
2.3.4.4 Dot Blotting 71
2.3.4.5 Single particle Raman spectroscopy analysis of MBV 72
2.3.4.5.1 Multivariate analysis 72
2.3.5 Production and characterisation of ECM hydrogels 73
2.3.5.1 Preparation of ECM hydrogels 73
2.3.5.1.1 Preparation of sow endometrial ECM hydrogel for experiments 74
2.3.5.1.2 Preparation of pig endometrial ECM hydrogel for experiments 75
2.3.5.2 Collagen quantification of ECM digests 75
2.3.5.3 Glycosaminoglycan quantification of ECM digests 76
2.3.5.4 Rheology of ECM hydrogels 76
2.3.5.5 Demonstration of sprayable ECM hydrogel 77
2.3.5.6 Demonstration of ECM gel adherence to endometrial tissue 78
2.3.6 Statistical analysis 79
2.4 Results 80
2.4.1 Histology of pig and sow endometrium 80
2.4.2 Evaluating decellularisation efficiency 82
2.4.2.1 Histology and DAPI staining of native and decellularised sow endometrium 82
2.4.2.2 DNA content of sow endometrial ECM 83
2.4.2.3 Histology and DAPI staining of native and decellularised pig endometrium 83
2.4.2.4 DNA content of pig endometrial ECM 84
2.4.3 Characterisation of decellularised endometrial ECM 85
2.4.3.1 Immunofluorescence of ECM proteins 85
2.4.3.2 Raman spectroscopy of endometrial ECM 88
2.4.3.3 Proteomics 90
2.4.4 Matrix-bound vesicles 95
2.4.4.1 Decellularised endometrial ECM contains exosome-like matrix-bound vesicles 95
2.4.4.2 Raman spectroscopic analysis of endometrial MBV 96
2.4.5 Characterisation of endometrial ECM hydrogel 101
2.4.5.1 Collagen and GAG content 101
2.4.5.2 Rheology 102
2.4.5.3 Injectable and sprayable endometrial ECM hydrogel 107
2.4.5.4 ECM hydrogel adherence to endometrial tissue 108
2.5 Discussion and future work 110

2.6 Summary of key findings 117
Chapter 3 – Characterising the *in vitro* effect of endometrial ECM hydrogel 118
3.1 Chapter aims 118
3.2 Introduction to *in vitro* assays 119
3.2.1 Endometrial *in vitro* models 119
3.2.1.1 Traditional endometrial *in vitro* models 119
3.2.1.2 Endometrial organoids 120
3.2.1.3 *In vitro* modelling of endometrial fibrosis 121
3.2.2 TGF-β1 as a fibrosis stimulator 122
3.2.2.1 TGF-β1 in intrauterine fibrosis 124
3.2.3 Macrophage response to ECM biomaterials 124
3.2.4 Angiogenic properties of ECM biomaterials 127
3.3 Materials and Methods 129
3.3.1 Effect of ECM hydrogels on endometrial cells in 2D culture 129
3.3.1.1 Isolation and culture of primary mouse endometrial epithelial and stromal cells 129
3.3.1.2 Immunofluorescence of MEEC and MESC 131
3.3.1.3 Culture of Immortalised Human Endometrial Stromal Cells 132
3.3.1.4 MESC cell viability assay on ECM gel 132
3.3.1.5 BrdU ELISA assay 133
3.3.2 Angiogenesis potential of ECM hydrogels 134
3.3.2.1. Tubule formation assay - cell culture and experimental setup 134
3.3.2.2 Tubule formation assay - image acquisition and analysis 135
3.3.2.3 Human VEGF ELISA assay 136
3.3.3 Endometrial organoid culture in ECM hydrogels 137
3.3.3.1 Endometrial organoid culture 137
3.3.3.2 Immunofluorescence staining and imaging of endometrial organoids 139
3.3.3.3 Organoid formation efficiency assay 139
3.3.4 *In vitro endometrial* fibrosis modelling 140
3.3.4.1 Preparation of TGF-β1 for cell culture experiments 140
3.3.4.2 Stimulation of primary mouse endometrial cells with TGF-β1 140
3.3.4.3 Immunofluorescence and imaging 141
3.3.4.4 RNA isolation 141
3.3.4.5 cDNA synthesis 141
3.3.4.6 RT-qPCR 142
3.3.4.7 Stimulation of endometrial organoids with TGF-β1 143

3.3.4.8 Immunofluorescence and imaging of endometrial organoids 144
3.3.4.9 Fibrosis modelling with cell-derived matrices 144
3.3.4.9.1 General Cell Culture 144
3.3.4.9.2 Production of Cell-Derived Matrices 144
3.3.4.9.3 Decellularising and Staining Cell-Derived Matrices for Imaging 145
3.3.4.9.4 Image acquisition and analysis 146
3.3.5 Immunomodulatory effects of ECM hydrogels 147
3.3.5.1 RAW 264.7 cell culture 147
3.3.5.2 Macrophage polarisation and ECM treatment of unpolarised macrophages 147
3.3.5.3 Macrophage polarisation followed by ECM treatment 147
3.3.5.4 Flow cytometry 148
3.3.5.5 Preparation of samples for RT-qPCR 149
3.3.5.6 RNA isolation and cDNA synthesis 149
3.3.5.7 RT-qPCR 149
3.3.6 Statistical analysis 150
3.4 Results 151
3.4.1 Cytocompatibility of endometrial ECM hydrogels on endometrial cells 151
3.4.1.1 Effect of endometrial ECM hydrogel on cell viability 151
3.4.1.2 Effect of endometrial ECM hydrogel on endometrial cell proliferation 152
3.4.2 Angiogenesis potential of endometrial ECM hydrogels 153
3.4.2.1 Endometrial ECM hydrogel increases tubule formation 153
3.4.2.2 Human VEGF ELISA 156
3.4.3 Endometrial organoid culture in ECM hydrogels 157
3.4.3.1 ECM hydrogels can support endometrial organoid culture 157
3.4.3.2 Organoid formation efficiency in endometrial ECM hydrogel 159
3.4.4 *In vitro* endometrial fibrosis modelling 159
3.4.4.1 Stimulation of primary endometrial cells with TGF-β1 159
3.4.4.2 Stimulation of endometrial organoids with TGF-β1 162
3.4.4.3 *In vitro* fibrosis modelling with cell-derived matrices 164
3.4.4.3.1 Endometrial ECM hydrogel attenuates effect of TGF-β1 on fibroblast CDM . 164
3.4.4.3.2 Endometrial ECM hydrogel attenuates effect of TGF-β1 on endometrial CDM 167
3.4.5 Immunomodulatory effects of endometrial ECM 169
3.4.5.1 Polarisation and ECM treatment of macrophages 169
3.4.5.2 Effect of endometrial ECM on M1-polarised macrophages 171
3.5 Discussion and future work 175

3.6 Summary of key findings 183
Chapter 4 – *In vivo* effect of endometrial ECM hydrogels 184
4.1 Chapter aims 184
4.2 Introduction to *in vivo* modelling of intrauterine fibrosis 185
4.2.1 Mouse models of intrauterine fibrosis 185
4.2.2 Mechanical injury models 186
4.2.3 Ethanol injury model 187
4.2.4 Evaluating endometrial injury and regeneration 189
4.3 Materials and Methods 190
4.3.1 *In vivo* experiments – general process 190
4.3.2 Developing a mechanical injury model for intrauterine fibrosis 191
4.3.3 Developing a chemical injury model for intrauterine fibrosis 193
4.3.4 Evaluating effect of ECM hydrogel on ethanol-induced intrauterine fibrosis 195
4.3.5 Tissue collection and histology 196
4.3.6 Histological analysis of degree of collagen deposition 196
4.3.7 Histological analysis of number of endometrial glands 197
4.3.8 Immunohistochemistry 197
4.3.9 Analysis of immunohistochemistry 198
4.3.10 RNA isolation from uterine tissue and cDNA synthesis 198
4.3.11 RT-qPCR 199
4.3.12 Statistical analysis 200
4.4 Results 201
4.4.1 Mechanical injury does not reliably produce a murine model of intrauterine fibrosis 201
4.4.1.2 Pilot study 2 findings 203
4.4.1.3 Pilot study 3 findings – mechanical injury group 205
4.4.2 Ethanol-induced injury effectively generates intrauterine fibrosis 207
4.4.2.1 Pilot study 3 findings – ethanol injury group 207
4.4.2.2 Pilot study 4 findings 210
4.4.2.3 Final study findings 211
4.4.2.3.1 Histological assessment of injury vs. sham control horns 211
4.4.2.3.2 Immunohistochemical analysis of injury vs. control horns 214
4.4.2.3.3 RT-qPCR analysis of injury vs. control horns 216
4.4.3 Effect of endometrial ECM hydrogel on intrauterine fibrosis 218
4.4.3.1 Histological analysis 218
4.4.3.2 Endometrial gland count 220
4.4.3.3 Immunohistochemistry analysis 221

4.4.3.4 RT-qPCR analysis 223
4.5 Discussion and future work 225
4.6 Summary of key findings 232
Chapter 5 - Conclusion and implications for future research 233
5.1 Summary of findings 233
5.2 Future work 234
5.3 Contextualisation of this research 235
5.4 Implications for other areas of research 236
5.5 Concluding remark 237
Appendix 1 – Supplementary data for chapter 2 238
Appendix 2 – Supplementary data for chapter 3 240
Appendix 3 – Supplementary data for chapter 4 242
Bibliography 244

List of figures

Chapter 1 - Introduction

Figure 1.1 Female reproductive tract and the endometrium
Figure 1.2 Intrauterine adhesions: causes and consequences
Figure 1.3 Trend in regenerative medicine studies for the uterus
Figure 1.4 Overview of regenerative medicine approaches for uterine repair
Figure 1.5 Overview of extracellular matrix biomaterials

Chapter 2 - Fabrication and Characterisation of Endometrial ECM

Figure 2.1 Overview of common decellularisation methods
Figure 2.2 Matrix-bound nanovesicles
Figure 2.3 Photographs of sow, pig and piglet uterus
Figure 2.4 Schematic of sow endometrial decellularisation protocol
Figure 2.5 Decellularised UBM and SIS ECMs
Figure 2.6 Schematic of MBV isolation protocol
Figure 2.7 Steps for ECM hydrogel fabrication
Figure 2.8 Injection and spray of ECM hydrogel
Figure 2.9 Histology of pig and sow endometrium (H&E stained)
Figure 2.10 H&E, Masson's Trichrome and DAPI staining of native and decellularised sow endometrium
Figure 2.11 DNA content and decellularisation efficiency of sow endometrial ECM
Figure 2.12 H&E, Masson's Trichrome and DAPI staining of native and decellularised pig endometrium
Figure 2.13 DNA content and decellularisation efficiency of pig endometrial ECM
Figure 2.14 Immunofluorescence of ECM proteins in native and decellularised sow and pig endometrium
Figure 2.15 Raman spectra of decellularised endometrial sow ECM and other decellularised ECMs
Figure 2.16 Raman spectra of pig endometrial ECM
Figure 2.17 GOBP gene ontology enrichment analysis of full list of endometrial ECM proteins
Figure 2.18 GOMF gene ontology enrichment analysis of full list of endometrial ECM proteins
Figure 2.19 Proteomics analysis - gene list of matrisome proteins
Figure 2.20 GOBP gene ontology enrichment analysis for endometrial ECM matrisome proteins
Figure 2.21 GOMF gene ontology enrichment analysis for endometrial ECM matrisome proteins

Figure 2.22 Endometrial MBV analysis
Figure 2.23 Raman spectra of MBVs acquired by single particle automated Raman trapping analysis
Figure 2.24 Principal component analysis of MBV Raman spectral data
Figure 2.25 Partial least squares discriminant analysis of MBV Raman spectral data
Figure 2.26 Collagen and sGAG content of ECM digests
Figure 2.27 Rheology of sow endometrial ECM hydrogel
Figure 2.38 Rheology of different batches of pig endometrial ECM hydrogel
Figure 2.29 Rheology of ECM hydrogel after injecting and spraying
Figure 2.30 ECM hydrogel adherence to endometrial tissue

Chapter 3 - Characterising the *in vitro* effect of endometrial ECM hydrogel

Figure 3.1 Endometrial *in vitro* models
Figure 3.2 Schematic of TGF-β1/Smad pathway
Figure 3.3 Macrophage polarisation *in vitro*
Figure 3.4 Schematic of primary mouse endometrial cell isolation protocol
Figure 3.5 Schematic of human endometrial organoid culture in ECM hydrogels
Figure 3.6 Schematic of protocol for production, decellularisation and staining of CDM
Figure 3.7 Primary endometrial cell viability and proliferation assays
Figure 3.8 Endometrial stromal cell proliferation assays
Figure 3.9 Tubule formation assays
Figure 3.10 Human VEGF ELISA
Figure 3.11 Human endometrial organoid culture in ECM hydrogels
Figure 3.12 Organoid formation efficiency assay
Figure 3.13 Transdifferentiation of primary endometrial stromal cells when cultured
Figure 3.14 RT-qPCR results for Col1a1 and Acta2 expression in MESC treated with TGF-β1
Figure 3.15 Human endometrial organoids stimulated with TGF-β1
Figure 3.16 Cell-derived matrices stained for collagen I, fibronectin and amine
Figure 3.17 An *in vitro* model of TGF-β1-mediated fibrosis using fibroblast cell-derived matrices
Figure 3.18 An *in vitro* model of endometrial fibrosis using cell-derived matrices
Figure 3.19 RAW 264.7 macrophage polarisation and ECM treatment
Figure 3.20 RT-qPCR of polarised macrophages
Figure 3.21 Brightfield images and RT-qPCR of RAW 264.7 cells polarised and treated with endometrial ECM

Chapter 4: Determining the effect of endometrial ECM hydrogel on an *in vivo* model of intrauterine fibrosis

Figure 4.1 Diagram and histology of the mouse uterus

Figure 4.2 Pilot study 1 overview

Figure 4.3 Pilot study 2 overview

Figure 4.4 Different geometries of 3D-printed endometrial scrapers

Figure 4.5 Intrauterine ethanol perfusion setup

Figure 4.6 Final *in vivo* study overview

Figure 4.6 Pilot study 1 results: Masson's trichrome staining

Figure 4.8 Pilot study 2 findings: Masson's trichrome and Picrosirius red staining

Figure 4.9 Pilot study 3 findings – mechanical injury group: Masson's trichrome staining and immunohistochemistry

Figure 4.10 Pilot study 3 findings – ethanol injury group: Masson's trichrome staining and immunohistochemistry

Figure 4.11 Pilot study 3 RT-qPCR results

Figure 4.12 Pilot study 4 Masson's trichrome stained sections

Figure. 4.13 Final *in vivo* study: injury group - macroscopic observations and Masson's trichrome stained sections

Figure 4.14 Final *in vivo* study: injury group – analysis of Masson's trichrome staining

Figure 4.15 Final *in vivo* study: injury group – immunohistochemistry

Figure. 4.16 Final *in vivo* study: injury group – RT-qPCR results

Figure. 4.17 Final *in vivo* study: injury + ECM treatment group - macroscopic observations and Masson's trichrome stained sections

Figure 4.18 Final *in vivo* study: injury + ECM group – analysis of Masson's trichrome staining

Figure 4.19 Final *in vivo* study: injury + ECM treatment group – immunohistochemistry

Figure. 4.20 Final *in vivo* study: injury + ECM treatment group – RT-qPCR results

Appendix

Figure A: Flow cytometry FSC/SSC plots and gating for blank (unstained) cells

Figure B: Flow cytometry CD86/CD206 dot plots

Figure C: Re-analysis of Masson's trichrome staining, endometrial gland number and immunohistochemistry for final *in vivo* study – with mouse 3 and 5 omitted

List of tables

Chapter 2

Table 2.1: Summary of uterine decellularisation studies involving tissue from large mammals

Table 2.2: Primary and secondary antibodies used for immunofluorescence staining of ECM proteins

Table 2.3: Primary and secondary antibodies used for MBV dot blots

Table 2.4: Pig endometrial ECM digest batches

Table 2.5: Tentative Raman peak assignments relative to biological tissues

Table 2.6: Tentative Raman peak assignments relative to MBVs

Chapter 3

Table 3.1: Primary and secondary antibodies used for immunostaining of MEEC and MESC

Table 3.2: Components of complete endothelial cell growth medium

Table 3.3: Components of human endometrial organoid expansion medium

Table 3.4: Primary and secondary antibodies for immunostaining of endometrial organoids

Table 3.5: TaqMan gene assays used for RT-qPCR analysis of MESC treated with TGF-β1

Table 3.6: Antibodies and amine reactive dye used for staining CDM for fluorescence imaging

Table 3.7: TaqMan gene assays used for RT-qPCR for RAW 264.7 experiments

Table 3.8: Flow cytometry analysis of naïve, cytokine-stimulated and ECM-treated RAW 264.7 macrophages

Chapter 4

Table 4.1: Primary antibodies used for immunohistochemistry

Table 4.2: TaqMan gene assays used for RT-qPCR analysis in this chapter and their relevance

Appendix

Table A1: Sow and pig endometrial decellularisation experiments – protocol optimisation and biological replicates

Table A2: Surgery details for final *in vivo* study

List of abbreviations

a-SMA	Alpha smooth muscle actin
ANOVA	Analysis of variance
AUFI	Absolute uterine factor infertility
BCA	Bicinchoninic acid
BSA	Bovine serum albumin
CDM	Cell-derived matrix
cDNA	Complementary DNA
CHAPS	3-[(3-cholamidopropyl)dimethylammonio]-1-propanesulfonate
CT	Cycle threshold
CTGF	Connective tissue growth factor
DAB	3,3'-Diaminobenzidine
DAPI	4',6-diamidino-2-phenylindole
DMEM	Dulbecco's modified eagle medium
DNA	Deoxyribonucleic acid
DNAse	Deoxyribonuclease
dsDNA	Double stranded deoxyribonucleic acid
ECM	Extracellular matrix
EDTA	Ethylenediaminetetraacetic acid
ELISA	Enzyme-linked immunosorbent assay
EMT	Epithelial-to-mesenchymal transdifferentiation
EV	Extracellular vesicle
FBS	Fetal bovine serum
FSC	Forward scatter
GAG	Glycosaminoglycan
GO	Gene ontology
GO_BP	Gene ontology_biological process
GO_CC	Gene ontology_cellular component
GO_MF	Gene ontology_molecular function
HCl	Hydrochloride / hydrochloric acid
HDF	Human dermal fibroblast
HEPES	4-(2-hydroxyethyl)-1-piperazineethanesulfonic acid
HESC	Human endometrial stromal cell

HPLC	High performance liquid chromatography
HUVEC	Human umbilcal vein epithelial cell
IFNy	Interferon gamma
IHC	Immunohistochemistry
IL-13	Interleukin-13
IL-1β	Interleukin 1-beta
IL4	Interleukin-4
iPSC	Induced pluripotent stem cells
IUA	Intrauterine adhesions
IUD	Intrauterine device
kDa	Kilodaltons
LC-MS	Liquid chromatography-mass spectrometry
LIF	Leukemia inhibitory factor
LPS	Lipopolysaccharide
MBV	Matrix-bound nanovesicles
MEEC	Mouse endometrial epithelial cell
MESC	Mouse endometrial stromal cell
miRNA	micro-RNA
MS	Mass spectrometry
MSC	Mesenchymal stem cells
NaOH	Sodium hydroxide
NTA	Nanoparticle tracking analysis
PAA	Peracetic acid
PBS	Phosphate buffered saline
PCA	Principle component analysis
PFA	Paraformaldehyde
PLSDA	Partial-least squares discriminant analysis
RNA	Ribonucleic acid
RPM	Revolutions per minute
RT-qPCR	Reverse transcription quantitative polymerase chain reaction
SD	Standard deviation
SDS	Sodium dodecyl sulphate
SDS-PAGE	Sodium dodecyl sulphate-polyacrylamide gel electrophoresis
SEC	Size exclusion chromatography

SLRP	Small leucine-rich proteoglycans
SPARTA	Single particle automated Raman trapping analysis
SSC	Side scatter
TBS	Tris-buffered saline
TBS-T	Tris-buffered saline with Tween
TGF-β	Transforming growth factor beta
UBM	Urinary bladder matrix
UV	Ultraviolet
v/v	Volume per volume
VEGF	Vascular endothelial growth factor
w/v	Weight per volume

Chapter 1 – Introduction

1.1 The Endometrium

The endometrium is a dynamic tissue layer that lines the uterine cavity (Figure 1.1). Its main function is to enable embryo implantation and the development of the placenta in order for pregnancy to occur [1]. A functional endometrium is essential for fertility. In humans, the endometrium consists of a columnar epithelium overlying a stroma that contains numerous glands, fibroblast-like stromal cells, spiral arteries and fluctuating populations of immune cells [2]. The endometrium undergoes cyclical, hormone-mediated reorganisation and regeneration, with the stromal layer varying in thickness under the influence of fluctuating oestrogen and progesterone levels during the menstrual cycle [2]. Under normal circumstances the endometrium is highly capable of regenerating itself, doing so about 400 times during a woman's reproductive lifetime. There are two layers of the endometrium; a functional layer which juxtaposes the uterine cavity and a basal layer which lies underneath the functional layer and adjacent to the myometrium [2] (Figure 1.1). It is the functional layer that proliferates, adapts in preparation for embryo attachment and sheds at the end of each menstrual cycle, whilst the basal layer remains relatively consistent [2]. Damage to the basal layer can prevent the endometrium from being able to regenerate [3]. The regenerative capacity of the endometrium is attributable to endometrial stem and progenitor cells, which have been found to reside in the basal layer and in the functional layer and are located perivascularly [3]. Disorders of the endometrium or an inability of the endometrium to regenerate prohibit embryo implantation and development, leading to infertility or pregnancy loss [1].

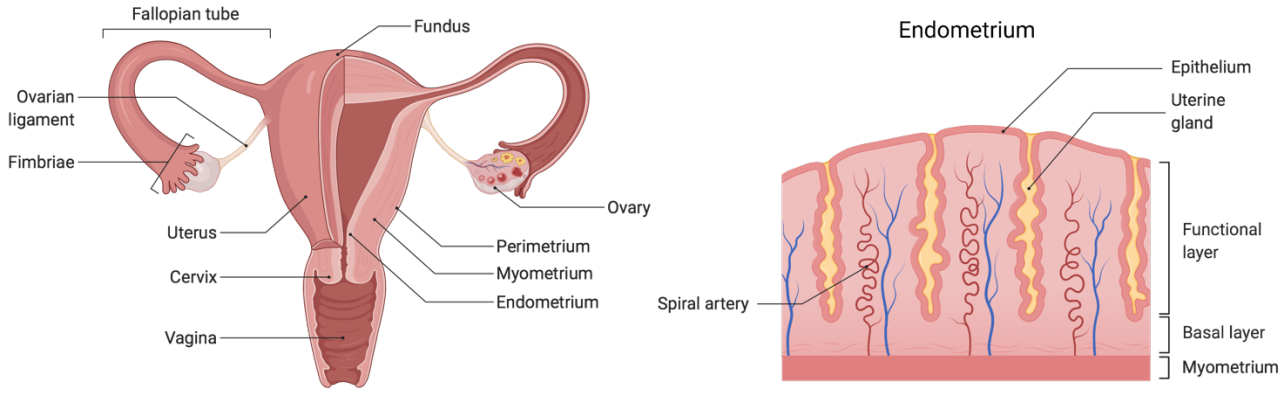


Figure 1.1 Female reproductive tract and endometrium. **Left:** annotated anatomical diagram of female reproductive tract. **Right:** annotated diagram showing cross-section of the human endometrium. Figure created with BioRender.com.

1.2 Absolute Uterine Factor Infertility

Infertility affects 1 in 7 couples in the UK and uterine or peritoneal disorders account for 10% of cases [4]. Absolute uterine factor infertility (AUFI) affects 3-5% of women and refers to the absence of a functional uterus, rendering a woman unable to become pregnant [5]. The aetiology of AUFI can be congenital or acquired. Congenital causes include Mayer-Rokitansky Hauser Syndrome, characterised by uterine agenesis from birth [5]. Acquired causes are typically due to hysterectomy, for benign disease or cancer, or severe endometrial scarring and intrauterine adhesions following uterine cavity trauma [5]. Until recently, a woman affected by AUFI could only become a parent through adoption or surrogacy [5]. Since 2014, uterine transplantation has become a viable option for women with AUFI to become pregnant and give birth [5]. To date, there have been at least 73 reported uterine transplantation cases performed worldwide and 23 livebirths confirmed following the procedure [6]. Although uterine transplantation has been a major breakthrough for AUFI, it is still complicated by the conventional challenges of organ transplantation, which include availability of donors, graft rejection, morbidity associated with major surgery and the risks of immunosuppression [6]. It is also costly and currently not widely available. Whilst women with an absent or severely malformed uterus indefinitely require a new uterus to enable pregnancy, those with a damaged endometrium may only need the restoration of a functional endometrium to become fertile. In 2020, Jones et al. reported a proof-of-concept study on endometrial transplantation and this may become a feasible treatment option in the future [7]. Meanwhile, there is an ongoing need for research and development into endometrial tissue

engineering or therapies that can target intrauterine scarring and promote endometrial regeneration, to treat AUFI secondary to a damaged endometrium.

1.3 Intrauterine adhesions and Asherman's syndrome

Fibrosis represents defective tissue repair in response to trauma and can affect every organ of the body, leading to scar tissue formation, anatomical distortion and organ failure [8]. It is characterised by remodelling of the extracellular matrix with excess deposition of collagen [8]. In gynaecology, fibrosis causes problems with fertility, pregnancy and pelvic pain. In the uterus, fibrosis leads to endometrial scarring and formation of intrauterine adhesions (IUA), bands of fibrous synechiae that form between the walls of the uterine cavity that can distort or obliterate the cavity [9]. (Figure 1.2) When IUA are associated with clinical symptoms, this is a condition known as Asherman's Syndrome[9], first described by Joseph Asherman in 1948 [10]. Consequences of Asherman's syndrome include secondary amenorrhoea, infertility, recurrent pregnancy loss and obstetric complications such as low birthweight [9], [11], retained placenta [11] or a morbidly adherent placenta [12] (Figure 1.2). Intrauterine adhesions have been found in up to 22% of women with infertility [9] and Asherman's syndrome is an important cause of AUFI [5].

1.3.1 Symptoms and clinical consequences of intrauterine adhesions

Most of the information on the prevalence of symptoms and clinical outcomes amongst patients with IUA comes from a study dating back to 1982, which reviewed 2981 cases reported in studies from around the world [13]. The most common symptom in Asherman's syndrome is menstrual disturbance, affecting more than two-thirds of patients. This includes a reduction (hypomenorrhoea) or absence (amenorrhoea) of menstruation [13]. Hypomenorrhoea and amenorrhoea can be due to adhesions that obstruct the cervical canal, inhibiting menstrual flow, or because of endometrial fibrosis destroying the basal layer of the endometrium [9].

Infertility is a significant feature of Asherman's syndrome. Schenker & Margalioth's study reported that 43% of women with IUA were affected by infertility [13]. A more recent study of patients with moderate to severe IUA identified infertility as being the reason for referral in 35.1% of cases [14]. It has been observed that the more severe the adhesions, the lower the fertility rate, even after treatment [15], [16]. Whilst it is widely accepted that moderate to severe IUA can significantly distort

the endometrium and uterine cavity, leading to infertility, a meta-analysis in 2021 found that even mild intrauterine adhesions can negatively impact future reproductive outcomes [17]. The study found that women with mild and treated IUA had significantly lower pregnancy rates compared to the general population (62.3% versus 90% respectively) and significantly decreased live birth rates (86.6% versus 99.5% respectively) [17]. Although this meta-analysis only included 5 studies and 229 women, it suggested the importance of preventing even mild IUA from occurring in women of reproductive age [17]. The exact mechanism for why IUA leads to infertility is unknown but has been hypothesised to be due to the obstruction of the ostia or cervical canal, preventing fertilisation from occurring, or due to the disruption of normal endometrium, preventing implantation and fetal development [18].

IUA have also been associated with recurrent miscarriage, with 14% of patients with IUA reported to be affected by recurrent pregnancy loss [13]. IUA is also be linked to increased incidence of retained placenta or abnormally invasive placenta (including placenta accreta) [12]. In a literature review of 12 studies on pregnancy outcomes after hysteroscopic adhesiolysis of IUA, which included 647 live births, the rate of adherent placenta and placenta accreta were 2.5% and 2.6% respectively [19]. The normal prevalence of placenta accreta ranges from 1 in 300 to 1 in 2000 [20].

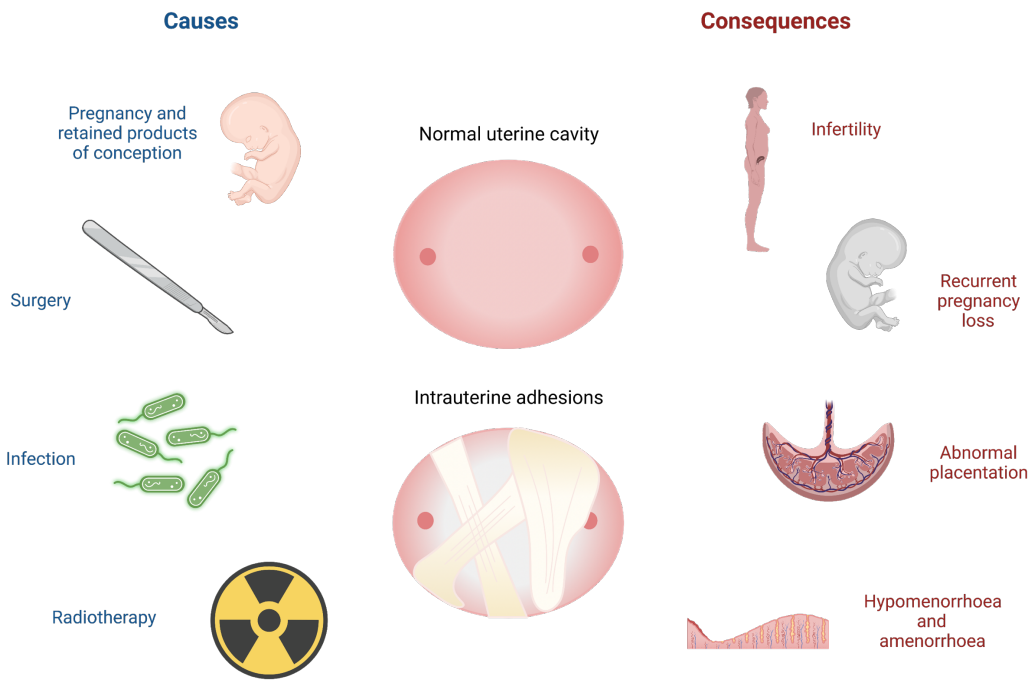


Fig 1.2 Intrauterine adhesions: causes and consequences. The causes of IUA include trauma to a pregnant uterus, uterine surgery, retained products of conception, infection and radiotherapy. The consequences of IUA are hypomenorrhea and amenorrhoea, infertility, recurrent pregnancy loss and abnormal placentation. Figure created with BioRender.com.

1.3.2 Aetiology and prevalence

Endometrial scarring and IUA usually develop iatrogenically and form as a result of common obstetric and gynaecological procedures. Approximately 90% of cases of IUA develop after surgery to the gravid uterus [13](Figure1.2), when injury to the basal layer of the endometrium impedes normal repair and there is extracellular matrix remodelling to form scar tissue [9]. It has been hypothesised that trauma to the endometrial basal layer, and resulting infection or inflammation, damages the stem cell niche [3]. Insufficient endometrial stem or progenitor cells likely contributes to poor endometrial regeneration, predisposing to Asherman's syndrome or endometrial atrophy [3].

The most common cause for Asherman's syndrome is some form of trauma to the pregnant uterus, such as surgical evacuation of products of conception, a procedure performed commonly to manage miscarriage, terminations of pregnancy and removal of retained products of conception after delivery [21]. In a cohort study of 683 patients, it was found that over 50% of patients with intrauterine adhesions had undergone a first trimester uterine curettage for miscarriage or termination of pregnancy and 38% had undergone a postpartum surgical procedure on the uterus, typically to remove retained products of conception [22]. The study also found that postpartum procedures were associated with more severe IUA than an early pregnancy procedure [22]. A meta-analysis by Hooker et al. (2014) reported a prevalence of 19.1% for IUA detected by hysteroscopy after a miscarriage [23]. The majority of IUA occurred in women who had undergone surgical management of miscarriage [23]. Risk factors for developing IUA included recurrent miscarriage (OR 1.99, 95% CI: 1.32–3.00, P = 0.001) and undergoing repeat dilatation and curettage procedures [23]. Of those with IUA that were graded, 58.1% had mild adhesions, 28.2% had moderate adhesions and 13.7% had severe adhesions [23].

Less commonly, IUA can also occur following trauma to a non-pregnant uterus, such as diagnostic curettage, surgical removal of fibroid or endometrial ablation [13]. In the developing world, fibrosis caused by genital tuberculosis can be another important cause of Asherman's syndrome [24]. One Chinese study of 683 patients with moderate to severe IUA found a 5.7% rate of endometrial tuberculosis [14]. Endometrial damage and fibrosis can also be caused by cancer treatment, such as radiotherapy [25]. The importance of this is increasing because cancer survival is improving and there is now more focus on fertility preservation and restoration in young women affected by cancer [25].

It is impossible to determine the exact prevalence of IUA, as not all cases are symptomatic. Of the symptomatic cases, which are Asherman's syndrome by definition, the prevalence is likely to vary

significantly across different regions of the world where clinical practices differ, and different diagnostic and classification criteria are used.

1.3.3 Molecular mechanisms of intrauterine adhesions

There are multiple proposed mechanisms and processes that lead to tissue fibrosis. The precise mechanisms underlying the pathogenesis of intrauterine adhesions are not completely understood though a few studies have highlighted similar molecular processes occurring in intrauterine adhesions that are known to cause fibrosis in other organs. A molecular pathway that has been well recognised as promoting inflammation and fibrosis in different body systems is the TGF-β/Smad pathway [26]. TGF-β1 is a key player in tissue fibrosis by stimulating the influx of pro-inflammatory cells, inducing epithelial-mesenchymal transdifferentiation (EMT), recruiting fibroblasts and stimulating transdifferentiation of mesenchymal cells to myofibroblasts, all of which lead to deposition and remodelling of extracellular matrix (ECM)[27].

Several studies have implicated the TGF-β1/Smad3 pathway in the pathogenesis of intrauterine adhesions. Salma et al. (2016) measured levels of TGF-β1, Smad3 and Smad7 levels in blood and uterine tissue samples from patients with intrauterine adhesions as well as rabbits that had been subjected to an experimental model of intrauterine adhesions [28]. Plasma levels of TGF-β1 were found to be significantly increased in both humans and rabbits with intrauterine adhesions compared to disease-free controls. Additionally, protein and mRNA levels of Smad3 were upregulated in the tissues of patients with intrauterine adhesions, whilst Smad7 was downregulated [28]. When rabbits with intrauterine adhesions were treated with a targeted Smad3 inhibitor (SIS3), TGF-β1 and Smad3 were significantly decreased and Smad7 significantly increased compared to untreated rabbits, further implicating the TGF-β1/Smad signalling pathway in the pathogenesis of intrauterine adhesions [28]. In another study, endometrial biopsies taken from patients with mild, moderate and severe intrauterine adhesions were found to have increased expression of TGF-β1 on immunohistochemistry, western blot and RT-qPCR assays compared to control endometrium. TGF-β1 protein and mRNA levels correlated positively with the severity of adhesions [29]. The same authors also found a positive correlation between TGF-β1 and expression of p65, a protein involved in the NF-κB signalling pathway [29].

1.3.4 Diagnosis and classification

Whilst IUA may be suggested on ultrasound or hysterosalpingogram assessment of the uterus, the gold standard for diagnosis of IUA is by hysteroscopy, an endoscopic procedure to visually assess the uterine cavity [9]. In the uterine cavity, adhesions form between two opposing walls [9]. The appearance of IUA may range from thin, filmy, superficial adhesions that are easily disrupted, to thick and dense fibrous bands that involve the myometrium and are difficult to divide [15]. IUA may be singular and limited to a small region of the uterine cavity or multiple and occupying an extensive portion of the cavity [15]. A diagnosis of Asherman's syndrome is made when IUA are accompanied by one or more clinical symptoms [9].

Histologically, the endometrial stroma of patients with Asherman's syndrome appears fibrosed, with loss of distinction between the basal layer and functional endometrial layer [9]. The endometrial glands appear sparse and are inactive and the defective endometrium is often avascular and does not respond to hormone stimulation [9].

There are multiple different classification systems for IUA and Asherman's syndrome to indicate the severity of the disease [30]. Some classification systems describe IUA as mild, moderate or severe depending on the degree of uterine cavity involvement when assessed hysteroscopically [30]. Other classification systems are more complex and detailed, including scoring for the extent of visualised IUA as well as the severity of symptoms [30]. There have been no studies evaluating the prognostic value of any classification system and there is no consensus on which is the best to use [30]. As such, clinical studies on Asherman's syndrome apply variable classification methods to report their findings, making it a challenge to compare studies and interventions. The description of IUA as mild, moderate and severe appears to be the most commonly reported in the literature.

1.3.5 Current management

The management of IUA can be categorised as preventative measures, to inhibit the development of scarring after trauma, and treatments to abolish adhesions once they have already formed. As surgical procedures are the main cause for IUA, the most effective preventative strategy would be to avoid or limit the performance of surgery or to use less traumatic surgical equipment and techniques [31].

1.3.5.1 Preventative strategies

Preventative strategies include oestrogen therapy, an intrauterine device (IUD), intrauterine insertion of a foley catheter balloon, amnion graft or the use of a barrier anti-adhesive gel [32]. Oestrogen treatment aims to stimulate endometrial regeneration, whilst the other strategies are designed to temporarily mechanically separate the uterine walls and therefore prevent the formation of adhesions between two surfaces [32]. These methods are less commonly used for primary prevention of IUA but are more frequently used as secondary prevention, as an adjunct to surgical treatment of Asherman's syndrome [33]. Aside from barrier anti-adhesive gels, the other preventative strategies have mostly been found to be ineffective in preventing IUA formation or recurrence or in improving reproductive outcomes [32]–[34].

Barrier anti-adhesive gels have been made from biodegradable materials such as hyaluronic acid or carboxymethylcellulose [33]. Hyaluronic acid is often crosslinked to improve its mechanical properties [31]. Several randomised control trials have explored the efficacy of anti-adhesive gels on the primary prevention of IUA post-operatively [33]. The results have been mixed, with some studies suggesting a reduction in IUA formation and improvement in pregnancy rate, whilst others suggest no significant difference between gel treatment and control [33].

1.3.5.2 Treatment and secondary prevention strategies

The current gold standard for treatment of IUA is hysteroscopic adhesiolysis [33] (AAGL 2017). The technique for performing this varies but the aim is to surgically remove or divide adhesions to restore the volume and shape of the uterine cavity, as well as removing any obstructions to the fallopian tubes or cervical canal [33]. The success of the procedure is evaluated by the severity of adhesion reformation at re-look hysteroscopy, the restoration of menstruation and ultimately pregnancy outcomes [15]. The recurrence rate of IUA after hysteroscopic treatment is very high, ranging from 30-66%, therefore an adjunctive treatment, such as oestrogen therapy, intrauterine device or barrier anti-adhesive gel, is frequently used [33]. Guo et al. (2019) conducted a systematic review of 54 studies on reproductive outcomes following hysteroscopic adhesiolysis and found that 53 studies included an adjunctive treatment [12]. Amongst the 4640 women included in the systematic review, there was an overall pregnancy rate of 50.7% [12]. The pregnancy rate was negatively correlated with the severity of IUA after surgical treatment; 69.1% for mild, 61.3% for moderate and 44.3% for severe [12]. Of the pregnancies, the prevalence of livebirth after hysteroscopic adhesiolysis was 64.1% [12].

Interestingly, the pooled prevalence of placenta accreta syndrome was 10.1% amongst 1415 pregnancies following surgical treatment of IUA, suggesting that there was residual underlying endometrial abnormality [12].

Anti-adhesive gels made from hyaluronic acid have been the most extensively studied and have been licensed for clinical use; one example is Hyalobarrier® [35]. Several meta-analyses have been performed on the effect of barrier anti-adhesive gels or hyaluronic acid gels for preventing IUA formation or recurrence after hysteroscopic adhesiolysis [32], [36], [37]. Most of the results indicate that hyaluronic acid gels are likely effective for reducing IUA formation or recurrence [32], [36], [37], particularly in preventing moderate to severe adhesions following adhesiolysis [32] but may not have any significant effect on pregnancy rates [32], [36]. One group recently published the long-term results of the PAPA study, a multi-centre, prospective randomised control trial on the prevalence of IUA after dilatation and curettage with the application of hyaluronic acid gel [38]. At the time of publication, theirs was the largest dataset on reproductive outcomes following hyaluronic acid gel treatment, combined with adhesiolysis, to prevent IUA [38]. The data showed that overall significantly more women conceived in the gel group but there was no significant difference in the ongoing pregnancy rate and live birth rate between the control and gel group [38]. In women who were pursuing a pregnancy, the results were more promising, showing significantly improved rates of ongoing pregnancy and live births in the gel group [38]. However, this study was not adequately powered to assess reproductive outcomes, therefore the findings should be interpreted with caution [38]. A clinical trial is currently underway to specifically clarify the effect of hyaluronic acid gel on fertility after surgical treatment of IUA [35].

1.3.6 Regenerative medicine approaches for endometrial regeneration

Turning to regenerative medicine and tissue engineering approaches for organ replacement or regeneration is a way of overcoming the shortfalls of organ transplantation. Recent years have seen a dramatic increase in the number of studies on regenerative medicine approaches for treatment of IUA and endometrial regeneration (Figure 1.3). These approaches include stem cell therapy and bioengineered scaffolds that can be implanted for uterine repair or used to deliver growth factors or cells to support endometrial healing (Figure1.4). These scaffolds may be made of natural polymers, such as collagen, alginate and cellulose or biodegradable synthetic polymers such as poly(L-glycolic acid). Scaffolds can also be generated from decellularised tissue. Decellularization is a process that

involves removing the cells and nuclear material from tissue and leaving behind ECM that retains its biochemical and structural properties. The scaffold can then be recellularised create an implantable, 3D, tissue-engineered construct.

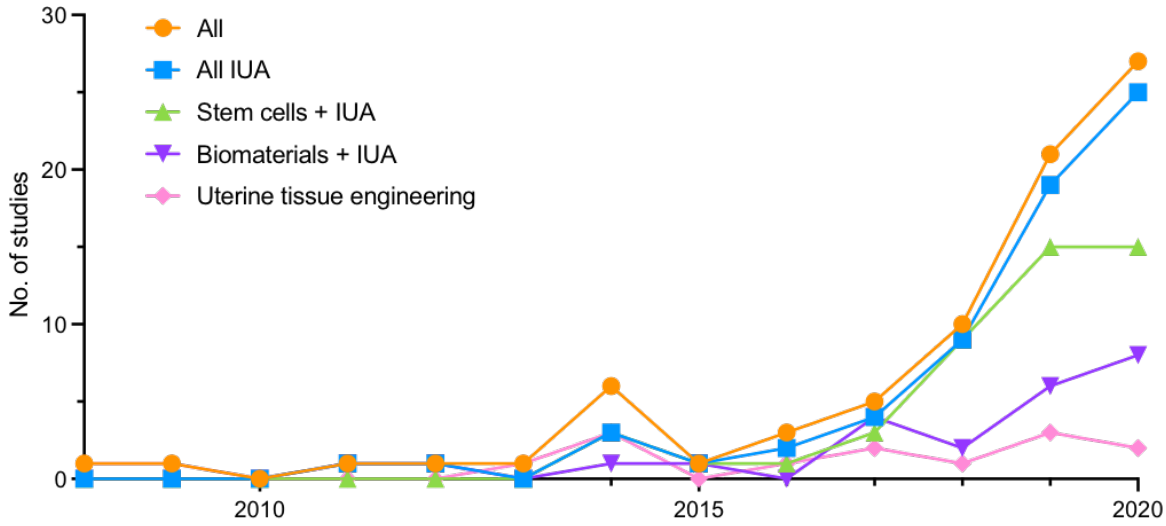


Figure 1.3 Trend in regenerative medicine studies for the uterus. Graph produced from literature review of all identified regenerative medicine studies related to uterine or endometrial regeneration published between 2008 and 2020. Pink is studies related to uterine tissue engineering, purple is studies involving biomaterials for the treatment of intrauterine adhesions, green is studies involving stem cell treatment for intrauterine adhesions, blue is all regenerative medicine studies related to treatment of intrauterine adhesions and orange is all studies related to uterine or endometrial regeneration. Mechanistic and pharmacological studies on intrauterine adhesions or endometrial regeneration were not included.

1.3.6.1 Stem cell therapy

Like most other diseases involving tissue damage and organ failure, stem cell therapy has been explored as a novel strategy for endometrial regeneration. In studies on endometrial repair, adult stem cells have been derived from bone marrow, umbilical cord, adipose tissue, endometrium, and menstrual blood. Stem cells have been delivered either directly to the injured tissue, via a scaffold or systemically via intravenous injection [39]. They have been shown to stimulate the proliferation of endometrial cells and vascularisation in damaged tissue *in vivo* [40]. In numerous animal studies of IUA, stem cell treatment has demonstrated the ability to reduce fibrosis, support healthy endometrial repair and improve fertility [39]. A meta-analysis of 8 clinical studies, involving 84 women with

Asherman's syndrome who received stem cell treatment, reported restoration in menstrual function, increased endometrial thickness and significant improvement in pregnancy outcome, when compared to conventional therapies, such as adhesiolysis [41].

The discovery of multipotent endometrial stem and progenitor cells represents a new source of stem cells for regenerating the endometrium as well as for tissue engineering and regenerative medicine in different organs [42]. Endometrial stem cells were first identified as epithelial and stromal cells which were capable of self-renewal, clonogenicity and multi-lineage differentiation and were able to regenerate the endometrium *in vivo* [42]. Single stromal cells that formed large colony forming units (CFU) were capable of differentiating into adipocytes, chondrocytes and osteoblasts whilst large, single epithelial CFU cultured in Matrigel were found to differentiate into cytokeratin-positive structures resembling glands [42]. Endometrial stromal stem cells can be harvested non-invasively from menstrual [43]. These cells have an important advantage over other sources of stem cells, such as bone marrow, as they are more readily available and have huge expansion capacity [44]. Their multipotency has enabled the use of human endometrial stem cells to regenerate the heart in clinical trials [44] and seed scaffolds for skin tissue engineering [45]. Menstrual-blood derived endometrial stem cells have been shown to improve endometrial repair and pregnancy rates in murine models of IUA [46], [47] as well as in a clinical study of Asherman's syndrome [48].

The tissue regenerating effect of stem cells is most likely related to paracrine mechanisms that lead to immunomodulatory and angiogenic processes which favour tissue healing, particularly because it has been shown that bone marrow-derived stem cells do not transdifferentiate into endometrial cells [49] and actual numbers of engrafted stem cells that survive are very low [50]–[52]. Miguel-Gomez et al. (2020) used gene expression arrays to analyse human endometrial tissues obtained from patients affected by Asherman's syndrome or endometrial atrophy, before and after treatment with CD133+ bone marrow-derived stem cells [52]. They found several genes that were differentially expressed (Ccnd1, Cxcl8, IL-4, Jun, Serpine1), which are related to signalling pathways that mediate downstream cellular proliferation and angiogenesis [52]. In a rat model of IUA, Liu et al. (2019) found that a hyaluronic acid gel loaded with the secretome of mesenchymal stem cells (MSC) improved endometrial thickness and glands and increased the pregnancy rate compared to controls [53]. Although the composition of the secretome was not characterised, this study supported the hypothesis that the regenerative properties of stem cells are linked to paracrine signalling [53].

In further support of the paracrine mechanism, there have been several studies on stem-cell derived exosomes for endometrial regeneration [54]–[56]. Exosomes secreted by stem cells carry protein, lipid and RNA cargoes that are representative of their source cells and have been shown to recapitulate the effect of stem cells [51]. Xin et al. (2020) showed that exosomes isolated from umbilical cord-MSCs supported the polarisation of pro-regenerative, M2 macrophages and in a rat model of IUA, MSC-derived exosomes delivered on a collagen scaffold led to significantly improved endometrial regeneration and superior pregnancy rates [54]. One study directly compared the effect of uterine-derived MSCs and exosomes isolated from uterine-derived MSCs on a rat endometrial injury model [55]. Both treatments increased markers of angiogenesis (VEGF receptor and CD31 expression), whilst significant increase in cellular proliferation and decrease in fibrosis were seen in the exosome treatment group, suggesting that MSC-derived exosomes had a superior therapeutic effect [55]. Xiao et al. (2019) demonstrated that the favourable effect of bone marrow derived stem cells on endometrial fibrosis was related to exosomal transfer of micro-RNA-340 [56]. Bone marrow stem cells (BMSC) with miRNA-340 knockout had significantly inferior effects on endometrial thickness, gland number and fibrosis compared to naïve BMSC, whilst the opposite was true for miRNA-340 overexpressed stem cells [56].

Whilst stem cell therapy is a promising avenue for treatment of IUA, there are still significant challenges to their translation into routine clinical practice. Stem cells need to first be harvested, expanded and prepared for individualised treatment, particularly if the source is autologous. This process is costly and impractical for widespread clinical application and also does not lend itself to primary prevention of IUA. If using allogeneic stem cells, there are issues with immune rejection [50], supply of donors and logistics of cell storage. Problems with stem cell engraftment and survival need to be optimised [50], though combining stem cells with biomaterials delivery platforms would help.

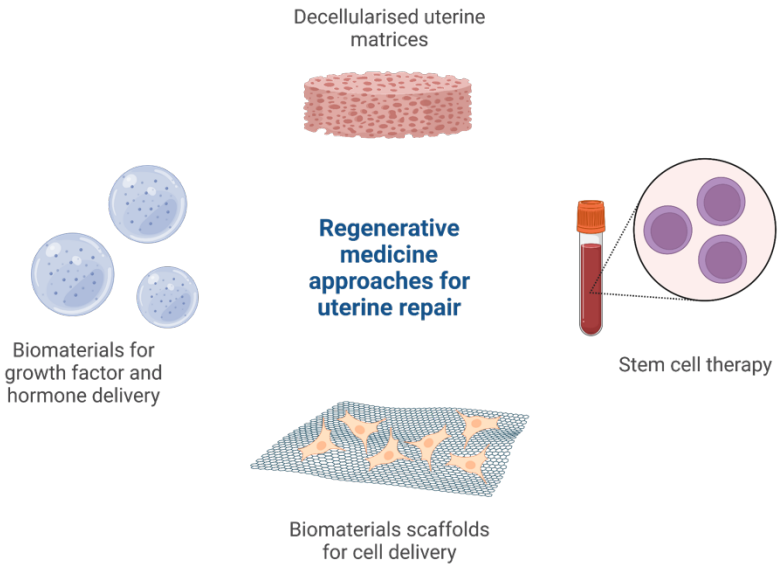


Figure 1.4 Overview of novel regenerative medicine approaches for uterine repair. The main, novel regenerative medicine approaches are stem cell therapy and bioengineering techniques including decellularised uterine matrices, biomaterials scaffolds for cell delivery and biomaterials for growth factor and hormone delivery. These approaches differ to gel barrier methods in that they aim to actively contribute to cell and tissue regeneration. Figure created with BioRender.com.

1.3.6.2 Bioengineering approaches to uterine and endometrial regeneration

1.3.6.2.1 Decellularised uterine matrices

A strategy for bioengineering uterine tissue is the production of scaffolds from decellularised uterine ECM. The properties and applications of decellularised ECM in tissue regeneration is discussed in more detail in section 1.4. Decellularised uterine matrices can be used for tissue regeneration or reconstruction in the context of a uterine defect, and can be recellularised *in vitro* with uterine or stem cells to create a transplantable, tissue-engineered construct [57]. This technique was first reported by Young & Goloman in 2013 [58], who engineered uterine patches from human and rat decellularized myometrial tissue with the aim of developing a way to reinforce uterine defects to prevent uterine rupture during pregnancy. The scaffolds were seeded with human and rat myocytes and the rat scaffolds cultured with human cells demonstrated phasic contractions when placed under tension [58]. Since then, there has been progress from decellularizing full thickness uterine matrices to whole organ decellularization in large mammals such as pig and sheep [59]–[61]. The literature on

uterine tissue decellularisation is discussed in more detail in Chapter 2, section 2.2.3. De- and recellularised uterine scaffolds have been shown to promote regeneration of uterine tissue when transplanted into rats that were given uterine defects, and support pregnancy [62], [63].

1.3.6.2.2 Cell-loaded scaffolds

Another approach to regenerating uterine tissue involves the use of biodegradable scaffolds, seeded with cells, which can be transplanted into the uterus. The scaffold material provides structural and mechanical properties that might facilitate tissue healing as well as helping cell survival and retention in the desired treatment area. Cells may proliferate, differentiate and deposit ECM to generate new tissue and can contribute to other biological processes important for wound healing such as angiogenesis. The majority of cell-scaffold constructs for endometrial regeneration contain stem cells, the properties and effects of which were discussed in section 1.3.6.1. A number of studies have demonstrated improved endometrial regeneration in murine models of IUA with the transplantation of stem cell-loaded scaffolds [40], [64]–[68]. Liu et al. (2020) compared a collagen scaffold loaded with umbilical cord-MSCs with direct injection of MSCs or collagen scaffold alone in a rat model of IUA [68]. Compared to MSCs or collagen alone, the MSC-collagen scaffold reduced fibrosis, improved endometrial gland number, led to significant differential expression of genes related to fibrosis and increased protein levels of factors beneficial for regeneration [68]. Using a 3D-printed hydrogel scaffold, human induced pluripotent stem cell-derived mesenchymal stem cell (hiMSC) survival was improved *in vivo* compared to local administration of hiMSC alone [69]. Following injury, indicators of endometrial recovery, endometrial receptivity and pregnancy outcomes were improved in the hydrogel scaffold combined with hiMSC compared to the scaffold or hiMSC administered independently [69].

1.3.6.2.3 Biomaterials scaffolds for growth factor and hormone delivery

Biomaterials scaffolds functionalised with growth factors or hormones have been used as implantable patches that stimulate the regeneration of uterine tissue *in vivo*. The use of a scaffold enables controlled and sustained release of growth factors or hormones to aid tissue repair. Vascular endothelial growth factor [70] and basic fibroblast growth factor [71] loaded on collagen membranes have demonstrated ability to stimulate endometrial repair and improve pregnancy outcomes in a rat model of iatrogenic uterine damage and scarring. Keratinocyte growth factor encapsulated in a hydrogel made from heparin-poloxamer combined with ε-polylysine enabled controlled release and

enhanced absorption of the growth factor in the endometrium and led to greater gland and epithelial cell proliferation and angiogenesis in the injured tissue compared to control [72]. In a full-thickness uterine injury rat model, Cai et al. (2019) showed that stromal cell-derived factor-1α, incorporated in a silk-fibroin cellulose membrane, promoted regeneration of uterine tissue and enhanced fertility [73].

Oestrogen is a commonly used hormonal therapy for increasing endometrial proliferation. Several studies have described the use of poloxamer-based hydrogels to deliver β-estradiol in murine models of endometrial fibrosis, demonstrated improvement in endometrial regeneration [74]–[76].

1.4 Extracellular matrix as a biomaterial for tissue regeneration

1.4.1 What is extracellular matrix?

Extracellular matrix (ECM) is secreted by cells in every tissue and organ in the body and provides the structural scaffold and mechanical properties of the tissue [77]. It also acts as a reservoir for cell signalling molecules and growth factors and regulates cell attachment, proliferation, organisation and migration [77]. The interactions between cells and the ECM influence embryonic development, the function of organs and tissues, their response to injury and the development and progression of cancer [78]. Mammalian ECM is made up predominantly of collagen, laminin, fibronectin, elastin and glycosaminoglycans [79]. The composition of these substrates and the ultrastructure of ECM vary between tissue sites and reflect the phenotype of the resident cells [80]. ECM gives biochemical and mechanical signals to cells through interactions between ECM substrates and cell surface receptors known as integrins [80]. ECM plays an important role in directing stem cell fate and forms part of the microenvironment that stem cells reside in, known as the stem cell niche [81].

1.4.2 Properties and applications of decellularised ECM biomaterials

Acellular ECM scaffolds have already been used for several decades in surgery and the clinical treatment of wounds [82]. They are good biomaterials for tissue repair because they are biodegradable and have been shown to promote important processes for regeneration, such as cellular infiltration and differentiation and angiogenesis [82]. They have also been demonstrated to modulate the host tissue immune response to favour constructive remodelling instead of scarring [83], a phenomenon which is explored in greater detail in chapter 3. ECM scaffolds are generated through decellularisation (Figure 1.5), to remove cellular and nuclear material, using a variety of

physical, chemical and biological methods [84]. This process effectively removes the immunogenic cellular antigens so that after transplantation, ECM scaffolds are readily incorporated into host tissues without a foreign body immune response and with reduced fibrosis [85]. The methods and implications for decellularisation of ECM are discussed in more detail in chapter 2. Across mammalian species, ECM constituents are highly similar, which has led to the safe use of decellularised ECM bioscaffolds derived from xenogeneic tissues for different tissue reconstruction purposes in surgery, e.g. hernia repair, breast reconstruction, urogenital reconstruction and musculoskeletal repair [82]. The most common sources of xenogenic bioscaffolds are porcine and bovine [82].

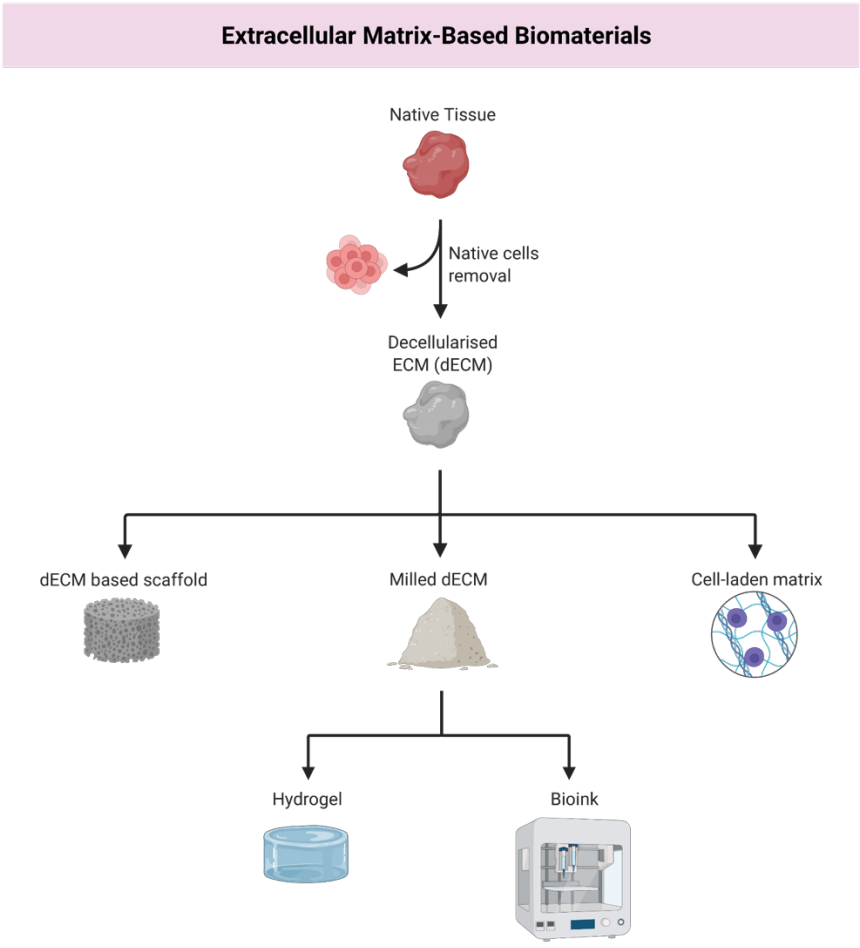


Figure 1.5 Overview of extracellular matrix-based biomaterials. Decellularised ECM is produced by removing cells from native tissue. This can then generate decellularised ECM scaffolds which can be used directly for tissue reconstruction and repair, or which can be milled and turned into hydrogels and bioinks, or they can be recellularised to generate tissue engineered constructs. This figure was adapted from a BioRender.com template.

The use of decellularised ECM as a scaffold for tissue regeneration has several inherent advantages over synthetic materials. Whilst synthetic materials need to be functionalised to provide appropriate conditions for cell attachment, survival and migration, decellularised ECM retains the properties of the native tissue and enables these cellular processes [82]. ECM degradation products have been shown to have favourable properties for tissue healing, such as promoting angiogenesis [86], being antibacterial [87] and recruiting endogenous multipotent stem cells [88], [89]. Decellularised ECM can also be recellularised *in vitro* to generate tissue-engineered constructs for tissue repair [59], [90].

To date, decellularized ECM scaffolds have been made from a variety of different organs and tissues including central nervous system, dermis, oesophagus, oesophageal mucosa, heart, lung, skeletal muscle, trachea, small intestinal submucosa, urinary bladder, liver and uterus [79], [91], [92]. The most commonly used ECM types are small intestinal submucosa (SIS) and urinary bladder matrix (UBM) as these were amongst the earliest decellularised ECMs to be studied [93]. There is evidence that tissue-specific ECM influences cell phenotype and organ specific stem cell differentiation. Keane et al. (2015) showed that oesophageal ECM enhanced *in vitro* migration of oesophageal stem cells and formation of three-dimensional oesophageal organoids when compared to non-oesphageal ECM [94]. Whilst *in vivo* regeneration of oesophageal mucosa was similar for homologous and heterologous ECM scaffolds [94]. Wang et al. (2016) found that induced pluripotent stem cells (iPSCs) were more likely to develop hepatocyte phenotype and function when cultured on cell-free liver ECM scaffold versus a synthetic polymer scaffold [95]. Pluripotent human embryonic stem cells seeded on decellularized kidney scaffolds in the absence of any growth factors or cytokines showed upregulation of renal lineage gene expression markers compared to a synthetic scaffold [96]. Davidov et al. (2021) also demonstrated that tissue-specific ECM drove the differentiation of iPSCs to the phenotype of their corresponding organ [97]. These studies suggest that tissue-specific ECM delivers sufficient cues to govern proliferation of adult stem cells and differentiation of induced pluripotent stem cells or embryonic stem cells to the cellular phenotype of a certain tissue, without the need for co-culture with resident cells or addition of growth factors. However, in animal myocardial infarction models, positive regenerative outcomes have been observed with both cardiac [98], [99] and non-cardiac ECM [100], [101]. The exact importance of tissue-specificity, *in vivo*, is probably application dependent and remains an area that warrants further research.

1.4.3 ECM hydrogels

In recent years ECM has been manipulated into hydrogels, creating greater versatility and enabling more varied clinical applications. The preparation and characterisation of ECM hydrogels is discussed in more detail in chapter 2, sections 2.2.4 and 2.3.5. The gelation of ECM hydrogels is initiated at physiological temperatures therefore pre-gel solutions of ECM, kept at cool temperatures, are easily injectable [102]. It can therefore be applied to fill an organ cavity and spread across a tissue surface, as demonstrated by Keane et al. (2016) in the colon of rats [103].

ECM hydrogels have been produced from a variety of tissues, including SIS, urinary bladder mucosa, brain, spinal cord, heart, liver, adipose tissue, skeletal muscle, tendon, dermis, pancreas, bone, cartilage, kidney, cornea [102]. Recently, another academic group has reported on the production of ECM hydrogels from endometrium [104]–[106]; these studies are examined in more detail in chapters 2 and 4. In a hydrogel state, ECM still retains its biochemical composition, as demonstrated by DeQuach et al. (2010) in their characterisation of solubilised cardiac and skeletal ECM [107]. They have also been shown to retain immunomodulatory properties, demonstrated *in vitro* and *in vivo* [108].

1.4.3.1 *In vitro* applications of ECM hydrogels

In vitro, ECM hydrogels have been used as a coating to enhance cell culture [97], [109]–[111], as a substrate for organoid growth [112]–[114] and as a bio-ink for 3D bioprinting [115]. As a cell culture substrate, tissue derived ECM has compared similarly [111] or favourably [109] to Matrigel or collagen [107], [116]. Unlike standard coatings for cell culture, ECM hydrogels can provide tissue-specific cues to drive cell maturation and differentiation. De Quach et al. (2010) demonstrated that skeletal and cardiac ECM hydrogel coatings were able to enhance, respectively, skeletal myoblast differentiation and the differentiation of cardiomyocytes from human embryonic stem cells [107].

The tissue-specific biochemical properties of ECM hydrogels have been exploited for organoid culture and confer the benefit of a more biomimetic environment for cells [112]–[114]. Organoids are 3D self-assembling cultures of progenitor/stem cells and differentiated cells that resemble tissue [117]. They represent powerful tools for studying tissue development, response to drugs and simulating disease models [117]. Currently, most organoids are cultured in Matrigel, a commercially available basement membrane extract for cell culture [117]. The disadvantages of Matrigel are that its protein components are poorly defined, which can lead to variation in results [118] and it is derived from

mouse sarcoma making it unsuitable for human *in vivo* applications [117]. ECM hydrogels made from decellularized liver ECM have been used to successfully culture organoids from hepatocarcinoma, human umbilical vein endothelial cells and mesenchymal stem cell lines [114]. The liver organoids grown in liver ECM hydrogel showed higher expression of hepatic genes, increased secretion of albumin and urea and increased liver enzyme activity compared to those grown in collagen [114]. Hydrogels made from decellularised ECM of gastrointestinal tissues were able to support the growth of endoderm-derived human organoids, such as gastric, pancreatic and small intestine with comparable efficacy to Matrigel, although transcriptomic analysis of organoids cultured in ECM gels and Matrigel showed differences in how the cells respond to the culture substrate [112].

1.4.3.2 *In vivo* applications of ECM hydrogels

Multiple types of ECM hydrogels have been applied in a variety of *in vivo* models to promote cell infiltration, stem cell differentiation, tissue healing and regeneration in both a tissue specific and non-tissue specific context [102]. Myocardial ECM hydrogels, for regeneration of functional tissue after myocardial infarction (MI), is the most advanced in clinical translation as this has been tested in clinical trials [119]. Although this trial was focused on assessing safety and feasibility of transendocardial injection of a porcine cardiac ECM hydrogel in post-MI patients, the authors also reported improvements in patients' functional outcomes and evidence of more favourable left ventricular remodelling [119].

1.4.3.3 Anti-fibrotic effect of ECM hydrogels

Many organ disorders are a result of tissue fibrosis. ECM hydrogels have demonstrated the ability to prevent fibrosis and support healthy tissue remodelling after injury in a number of different *in vivo* models. In a mouse model of liver fibrosis, Hussein et al. (2020) demonstrated that treatment with decellularised liver ECM hydrogels reduced the histological appearances of fibrotic deposits and collagen deposition and downregulated the expression of fibrosis-related genes, whilst upregulating genes that were associated with normal liver function [120]. Paired *in vitro* studies with hepatic stellate cells suggested that the fibrosis-mitigating effect of ECM hydrogel was associated with inhibition of the TFG-β1/Smad pathway [120] (the relationship between TFG-β1 and fibrosis is discussed in chapter 3, section 3.2.2). Myocardial matrix hydrogel injected in a rat model of chronic myocardial infarction led to a smaller area of fibrosis in the infarct region and improved left ventricular remodelling [121]. Zhou et al. (2020) reported ECM hydrogel-mediated inhibition of epithelial-

mesenchymal transition (EMT) and reduction in hydroxyproline content in rat lungs subjected to radiation injury, suggesting an anti-fibrotic effect [122].

1.4.3.4 ECM hydrogels for growth factor delivery

As well as being therapeutic in themselves, hydrogels can be a vehicle for growth factor or drug delivery. Indeed, ECM hydrogels have been combined with growth factors or bioactive proteins to enhance tissue repair [106], [123], [124]. Sonnenberg et al. (2015) combined hepatocyte growth factor-fragment (HGF-f) with porcine pericardial ECM hydrogel, by utilising the heparin binding capacity of HGF-f59 [123]. HGF is a growth factor that has been shown to improve angiogenesis and repair in the heart after myocardial infarction [123]. Rats with induced myocardial infarction that were injected with ECM hydrogel alone had reduced negative LV remodelling but those injected with ECM hydrogel combined with HGF-f exhibited improved cardiac function [123]. Similarly, a porcine SIS in-situ forming ECM hydrogel loaded with HGF showed sustained release of the growth factor over 21 days and led to functional remodelling in a rabbit model of vocal fold injury, with enhanced mucosal healing, increased hyaluronic acid production, decreased deposition of collagen type I and improved functional outcomes [124]. Recently, a study by Lopez-Martinez et al. (2021) reported the beneficial effect of endometrial ECM hydrogel combined with growth factors (platelet-derived growth factor, basic fibroblast growth factor and insulin-like growth factor-1) on a mouse model of IUA [106]. Collagen deposition in the endometrium was decreased, whilst endometrial area, glands, cell proliferation, neoangiogenesis and pregnancy rates were increased in the mice treated with combined endometrial ECM gel and growth factors, compared to control [106].

1.4.4 Non-tissue-specific ECM for reconstruction of the female reproductive tract

Decellularised uterine matrices, as a potential biomaterial for uterine reconstruction, was discussed in section 1.3.6.2.1 of this chapter and studies on uterine tissue decellularisation are examined in greater detail in chapter 2, section 2.2.3. ECM grafts have also been used to reconstruct other female reproductive organs and anatomy, such as in creating a neovagina [125]–[128] or for reconstructing the cervix [125], [127]. Porcine SIS has been the material most often used because it is well established as a material for tissue repair [125], [127]. There have been two published case series on the use of SIS ECM to rebuild the human uterine cervix in cases of cervical malformations [125] or cervical aplasia [127]. In both these papers, the authors reported good functional outcomes in patients who received SIS grafts as defined by maintained cervical patency.

The use of ECM, in particular non-tissue-specific ECM, for uterine repair or endometrial regeneration is still relatively understudied. However, the few studies published in this field have highlighted not only the potential for non-tissue-specific ECM to reduce endometrial scarring and promote endometrial repair but also its capacity to restore normal endometrial function. In a rat model of IUA, Kong et al. (2017) transplanted SIS ECM into a mechanically and infectiously injured uterine horn and found that the endometrium was thicker, extent of fibrosis significantly lower and pregnancy rate higher compared to the untreated injured horn [129]. PCR analysis showed increased expression of HOXA10, a gene that indicates endometrial receptivity [129]. UBM ECM applied in traumatised rat uterine horn led to improved histological appearances of endometrial repair, a reduction in mRNA of TNF-α and an increase in expression of genes associated with endometrial receptivity compared to the injury only group [130]. Furthermore, the UBM ECM-treated horns showed more embryo development than in the injury group [130].

Hypothesis

An endometrial extracellular matrix hydrogel has bioactive properties that can inhibit intrauterine fibrosis and facilitate endometrial healing after injury.

Aims and Objectives

Aim 1:
Produce and characterise a decellularised porcine endometrial ECM and an endometrial ECM hydrogel.

Objectives:

1. Develop a protocol for decellularisation of porcine endometrium.
2. Characterise the biochemical properties of decellularised endometrial ECM.
3. Produce a hydrogel from decellularised endometrial ECM.
4. Demonstrate the gelation properties of an endometrial ECM hydrogel.

Aim 2:
Determine the *in vitro* effects of an endometrial ECM hydrogel, in the context of tissue regeneration and fibrosis inhibition.

Objectives:

1. Characterise the biocompatibility of endometrial ECM hydrogel for endometrial cells.
2. Determine the angiogenic potential of endometrial ECM hydrogel *in vitro*.
3. Determine the effect of endometrial ECM hydrogel on an *in vitro* model of endometrial fibrosis.
4. Determine the immunomodulatory effect of ECM hydrogel using macrophage cell culture assays.

Aim 3:
Determine the effect of an endometrial ECM hydrogel on an *in vivo* model of intrauterine fibrosis.

Objectives:

1. Establish an *in vivo* mouse model of intrauterine fibrosis.
2. Determine the effect of endometrial ECM hydrogel in an *in vivo* mouse model of intrauterine fibrosis.

Chapter 2 – Fabrication and Characterisation of Endometrial ECM

2.1 Chapter aims

This chapter begins with a literature review on topics that are pertinent to the production and characterisation of decellularised ECM and to the materials and methods subsequently described.

In materials and methods, the steps taken to achieve decellularised porcine endometrial ECM are outlined. Endometrial tissue from older sows and younger pigs were used in this thesis and the rationale for the use of two different ages of animals is discussed. Standard methods for determining decellularisation efficiency are described which included qualitative assessment for nuclear staining and quantitative analysis of DNA content. Histology and immunofluorescence were used to compare decellularised and native endometrium. Raman spectroscopy was used to study the biochemical composition of decellularised sow and pig endometrium, and the Raman spectra of endometrial ECM was compared to other ECM types. Proteomics analysis was employed to characterise decellularised pig endometrial ECM.

Few publications have explored the isolation and characterisation of exosome-like MBVs from decellularised ECM. A size-exclusion chromatography method for MBV extraction is described in 2.3.4 and the outcomes of nanoparticle tracking analysis, BCA protein assay, dot blotting as well as the novel application of single particle automated Raman trapping analysis (SPARTA®) [131] are reported in the results section. The Raman spectra of endometrial MBVs was compared to MBVs derived from an alternative ECM, as well as to cell-line derived extracellular vesicles. This is the first known description of Raman spectroscopy for the analysis of MBVs.

As endometrial ECM is used in hydrogel form in subsequent *in vitro* and *in vivo* experiments, the collagen and GAG content of endometrial ECM digests were compared with other ECMs. The rheological properties of endometrial ECM hydrogel were assessed and discussed. Rheology experiments demonstrated the batch-to-batch variability of ECM gels and helped to identify an optimal batch of ECM digest for *in vivo* studies. A qualitative experiment is also described to demonstrate ECM gel adherence to endometrial tissue.

2.2 Introduction to Production of ECM Biomaterials

2.2.1 Source of ECM

2.2.1.1 Animal species and tissue specificity

Most ECM biomaterials are derived from porcine tissues, although some also come from bovine and human sources [93], [132]. ECM constituents are highly conserved across mammalian species, rendering xenogenic decellularised ECM scaffolds the ability to facilitate constructive tissue healing *in vivo* and clinically [93]. Although the first studies of acellular ECM scaffolds for tissue regeneration were on small intestinal submucosa (SIS) ECM as a material for vascular grafts [133], [134], there has since been more focus and consideration for tissue specificity, meaning the matching of ECM source tissue to the intended organ or tissue for regeneration. It is likely that the interest in tissue specificity is fuelled by the academic desire to describe new decellularisation approaches for novel tissue types and different clinical applications, as there are relatively few studies comparing the biological effect of tissue-specific and non-tissue-specific ECM [94], [135]. However, tissue-specific ECM has been demonstrated to influence lineage-specific stem cell differentiation [110] and to confer more favourable remodelling outcomes *in vivo* compared to non-specific ECM [135].

2.2.1.2 ECM from young versus old animals

It is well known that wound healing in foetal animals is superior to adult animals and that the foetus has a capacity to repair wounds scarlessly [136]. This is partly attributed to the differences in foetal ECM composition, which provides a favourable environment for cell migration and proliferation and has chemotactic properties that reduce inflammation [137]. Some studies have demonstrated differences in the bioactivity of decellularized ECM derived from foetal versus mature animals [138], [139]. Brennan et al. (2008) showed that digests of foetal human skin ECM had much greater chemoattractant properties compared to adult human skin ECM and adult porcine skin ECM [138]. Sood et al. (2016) found that solubilised porcine foetal brain ECM led to enhanced *in vitro* neuronal network formation and activity compared to adult brain ECM [139]. The age of the animal, unsurprisingly, affects the mechanical and biochemical properties of the ECM scaffold. Tottey et al (2011) analysed SIS ECM from pigs aged 3 weeks to 52 weeks and found that tensile stress and elastic modulus were higher for ECM from 12 and 26 week-old animals, compared to 3 weeks and >52 weeks [140]. Similarly, growth factor (bFGF and VEGF) content was higher in ECM from 12 and 26 week-old

pigs compared to 3 weeks and >52 weeks, whist the GAG content of ECM was higher at 3 and 12 weeks compared to older ages [140]. Conversely, the degradation products from ECM led to increased perivascular stem cell proliferation when the source animals were older (26 and >52 weeks) compared to younger [140].

The vast majority of *in vivo* studies on ECM biological scaffolds and hydrogels have used source tissue from adult pigs with satisfactory effects. However, a study performed by Sicari et al. (2012) comparing SIS ECM from pigs aged 3, 12, 26 and >52 weeks showed significant differences in *in vivo* remodelling response and macrophage phenotype based on the age of the source animal [141]. SIS ECM derived from 3-week and 12-week old pigs caused a more prominent M2 macrophage response, which is more favourable for constructive healing, and led to skeletal muscle remodelling that was most similar to native tissue [141]. The remodelled tissue containing ECM from 3-week old pigs was also found to have greater uniaxial tensile strength than other ages [141].

2.2.2 Production of decellularised ECM biomaterials

2.2.2.1 Decellularisation considerations

Efficient and thorough removal of cells and nuclear material is key for the fabrication of biomaterials from decellularized ECM, as the remanence of cellular material can elicit an adverse host immune response to the implanted biomaterial [85], [142]. In preparing decellularized ECM, the aim is to use an optimal balance of methods to thoroughly remove cellular material whilst preserving important ECM proteins and biomolecules. Using methods or chemicals that are too harsh and for too long may remove nearly all cells and DNA but could also damage the ECM architecture, composition and desired bioactivity [143]. The decellularization techniques, reagents and exposure time should be tailored to the type of tissue, taking into account the size, density, lipid content and cellularity of the tissues [132]. Whole organs or dense tissues (e.g. dermis and tendon) require more severe decellularization methods or prolonged decellularisation times, compared to thin tissues (e.g. SIS or UBM) [84]. Whilst fat-rich tissues, such as adipose, pancreas or brain may require extra delipidisation techniques [144]. Most decellularisation protocols combine physical, chemical and enzymatic methods (Figure 2.1), in a series of steps, to achieve satisfactory removal of cells and DNA, whilst retaining key ECM components [84]. Tissue decellularisation can be achieved by whole organ perfusion or by applying decellularisation techniques to isolated tissue fragments or pieces [84]. The former method would be

more suitable for generating a whole organ graft, whilst the latter is more appropriate for producing scaffolds or hydrogels from specific tissue layers.

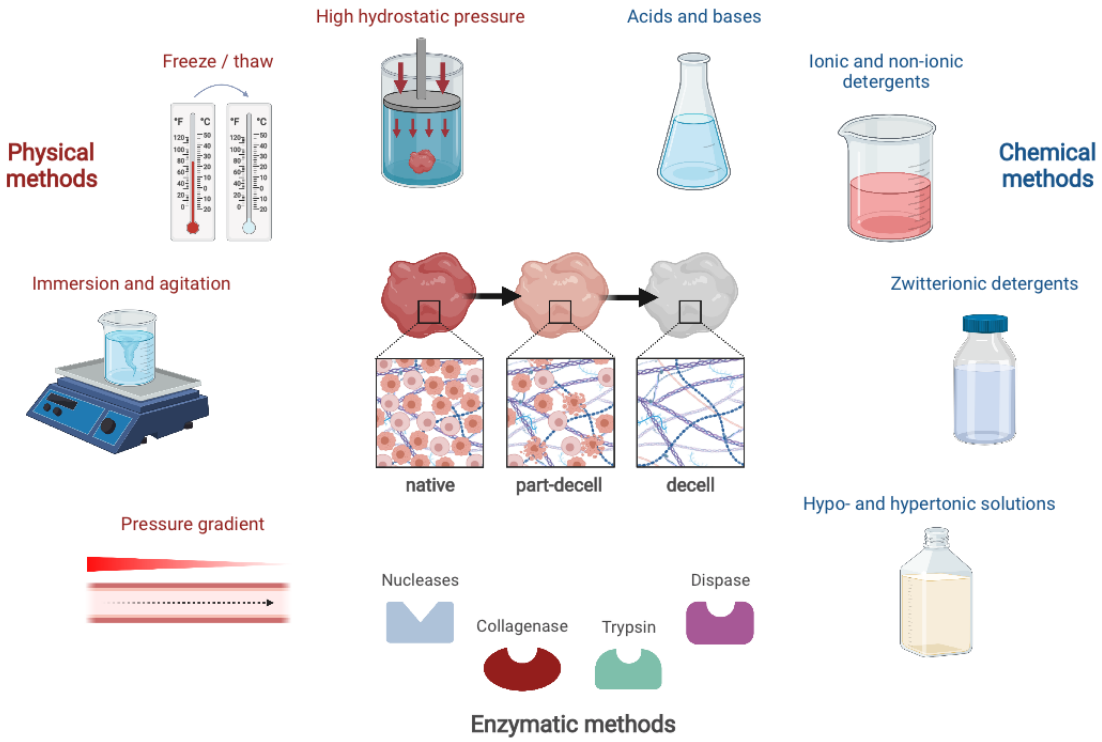


Figure 2.1 Overview of common decellularisation methods. Common physical, chemical and enzymatic methods are represented in this diagram. Use of a single method may help to achieve partial decellularisation and multiple methods are frequently used in combination to achieve adequate decellularisation. Figure created with BioRender.com.

2.2.2.2 Decellularisation methods

2.2.2.2.1 Physical methods

Freeze-thawing of tissue will cause cell lysis, although not necessarily eliminate any cellular material from the ECM [132]. The freeze-thaw step is commonly used as an adjunctive step in decellularization protocols and has been shown to produce minimal disruptions to ECM proteins or architecture [84], [132]. Immersion and agitation of tissues, usually in combination with a chemical reagent or hypertonic solutions, is a method that is frequently used for decellularization [84]. Mechanical

agitation can be achieved using a rotational shaker platform, a rocker platform or a magnetic stir plate. Increased agitation correlates with a higher degree of cell removal [132]. Pressure gradients and high hydrostatic pressure are effective methods of decellularisation, often allowing for shorter exposure times to harsh chemicals [84] or the avoidance of detergents [145].

2.2.2.2.2 Chemical reagents

Ionic, non-ionic and zwitterionic detergents are all commonly employed in decellularisation protocols. Ionic detergents cause cell lysis by disrupting cell membranes, denaturing proteins and solubilizing lipids and DNA [84], [132]. Commonly used ionic detergents in decellularisation protocols are sodium dodecyl sulphate (SDS) and sodium deoxycholate, whilst Triton-X 100 is a popular non-ionic reagent [143], whilst 3-[(3-cholamidopropyl) dimethylammonio]-1-proppane- sulfonate (CHAPS) is an example of zwitterionic detergent [84]. Detergents have been shown to effectively remove major histocompatibility complexes I and II, which mitigates an adverse host immune reaction [146]. Sodium deoxycholate may affect the GAG content and disturb the ultrastructure of ECM [132] but it tends to cause less disruption to ECM proteins and structure compared to SDS [84], [147]. Residual SDS in ECM biomaterials has been reported to cause cytotoxicity [148]–[150], fibroblast activation [151] and an adverse inflammatory response *in vivo* [151]. Decellularisation protocols based on SDS have also been shown to disrupt collagen fibres [148], [152] and reduce GAG content in ECM bioscaffolds [152]. ECMs decellularised with sodium deoxycholate have been shown to result in greater biocompatibility in cell cultures compared to SDS [148], [153]. Sodium deoxycholate can cause agglutination of DNA on the surfaces of ECM so incorporating a DNase step with thorough washing of the ECM has been advised [143]. Due to the potential for significant adverse effects, it is important that ECMs decellularised with chemical reagents are thoroughly washed before processing them further for *in vitro* and *in vivo* use.

The use of hypotonic and hypertonic solutions in decellularization protocols is common. Hypotonic solutions, such as deionised water, cause cell lysis by osmotic shock, without causing disturbance to ECM proteins [132]. Whilst hypertonic solutions are known to dissociate DNA from proteins [84]. The alternation of hypotonic and hypertonic solutions may enhance cell lysis and removal of nuclear material from ECM scaffolds [132].

Peracetic acid (PAA) solubilizes cytoplasmic components and disrupts nucleic acids, to help remove residual DNA [84]. It is also used to disinfect decellularized ECM bioscaffolds, through oxidation [154]. Treatment of ECM with PAA has been shown to preserve fibronectin, GAG and some growth factors,

whilst significantly reducing other growth factors such as VEGF [154]. The exposure time to PAA influences efficiency of DNA elimination, with 2 hours being the standard immersion duration and achieving greater DNA reduction compared to 1 hour [85].

2.2.2.2.3 Enzymatic reagents

Commonly used enzymes in decellularisation protocols include nucleases, collagenase, dispase and trypsin [132]. Nucleases (e.g. DNAse or RNase) hydrolyse nucleotide chains and remove remaining nucleic acids from tissues following cell lysis [132]. They are typically used in combination with detergents to enhance the reduction of DNA content [85]. Trypsin is a serine protease that dissociates cells by cleaving peptides on the carboxyl side of arginine and lysine [132], however, extended exposure time can result in damage to ECM structure [155], [156].

2.2.2.3 Sterilisation methods

In the US, medical devices made from decellularised ECM must adhere to FDA approved methods of sterilisation to achieve certain standards for bacterial load [84]. In the EU, medical devices made of materials from animal origin are subject to EU regulation 2017/745, which specifies that viruses and transmissible agents must be eliminated by validated methods of elimination and viral inactivation [157]. The method of sterilisation can impact on the structure and function of ECM bioscaffolds [158]. Different sterilisation techniques can alter the mechanical properties of ECM hydrogels [159]. Commonly used sterilisation techniques for ECM bioscaffolds include peracetic acid, gamma irradiation, ethylene oxide and supercritical carbon dioxide [84]. Gamma irradiation and ethylene oxide have been shown to affect ECM ultrastructure by weakening collagen fibrils and inhibit cellular adhesion, possibly by damaging RGD peptide motifs [158]. Gamma irradiation has also been shown to reduce the presence of GAGs in ECM scaffolds [160]. High dose irradiation also prevents the formation of hydrogels from lyophilised ECM [159]. Peracetic acid (PAA) is a chemical depyrogenation agent that can inactivate bacteria, viruses and fungi, without causing significant disruption to ECM structure or cell adhesion properties [158]. Whilst not a method of terminal sterilisation, PAA is readily accessible and easy to use in a laboratory setting as no specialist equipment is required. It is important that PAA is handled safely and that ECMs treated with PAA are washed thoroughly before processing for *in vitro* and *in vivo* uses.

2.2.2.4 Evaluation of decellularisation efficiency

Assessment of decellularisation efficacy is highly variable in the ECM biomaterials literature [161]. Typically, decellularisation is evaluated by measuring DNA content and observing for visible nuclei on histological or DAPI staining. However, there is no standardisation in the approach to extracting DNA, measuring DNA or how DNA content is normalised or expressed, such as relative to dry weight or wet weight [161]. Whilst there are numerous FDA approved, "acellular" biological scaffolds commercially available and in clinical use, there are no standardised criteria or legislation to regulate the manufacture of these medical devices and they contain variable amounts of cellular remnants [162]. Crapo et al. (2011) proposed the application of the following criteria for determining satisfactory decellularisation; dsDNA content <50 ng/mg ECM dry weight, DNA fragment length <200 base pairs and lack of visible nuclear material on H&E or DAPI staining [132]. However, these criteria are rather arbitrary and there are no studies that have investigated the threshold of residual DNA that causes adverse host reactions [85]. Indeed, Keane et al. (2012) produced SIS ECM scaffolds using different decellularisation protocols and demonstrated a similar macrophage response, one considered more favourable for re-modelling, in scaffolds containing 62 ± 16.4 ng/mg and 959 ± 9.2 ng/mg of DNA [163]. No obvious adverse effects were observed *in vivo* with either scaffolds, decellularised using peracetic acid, despite both having higher DNA content than the criteria defined by Crapo et al. (2011) [163]. Isolation and quantification of dsDNA from a range of commercially manufactured and experimentally produced SIS and UBM ECM scaffolds show DNA concentrations greater than 1 μg/mg of dry weight [164], at least 20 times higher than the aforementioned acceptable level.

2.2.3 Uterine tissue decellularisation

Since 2014, there have been several studies on decellularisation of uterine tissue from rodents [62], [63], [146], [165]–[168], rabbits [169], [170] and, in the last four years, larger mammals such as pigs [59] and sheep [60], [61]. There have also been two studies published on human endometrial tissue decellularisation [171], [172]. These studies have predominantly investigated the fabrication of a uterine ECM scaffold which could be subsequently recellularised, ultimately supporting the concept of a tissue-engineered endometrial or uterine graft [59]–[61], [171], [172]. ECM hydrogels made from decellularised rabbit proliferating endometrium [169] and rabbit oviduct [170] have also been shown to support the culture of embryos.

Table 2.1 summarises the published studies on human and large animal uterine tissue decellularisation to date (rodent and rabbit studies not included). The protocols for uterine tissue decellularisation have mostly involved SDS and Triton X-100. Tiemann et al. (2020) compares three protocols, one with SDS, one with sodium deoxycholate and one with sodium deoxycholate and Triton X-100 [61]. The authors concluded that the sodium deoxycholate protocol was most optimal for reducing DNA content, preserving collagen and generate scaffolds that were most similar to native tissue [61]. It is worth noting that the method of measuring and reporting the DNA content of decellularised uterine ECM has been variable throughout the literature. DNA extracted from ECM has been measured by spectrophotometry without correlation to DNA standards [59], [60], [172] or using fluorescent quantification of dsDNA relative to a standard curve [104], [171], which is more precise. DNA content has been described relative to the wet tissue mass or lyophilised ECM mass or the normalisation has not been clearly defined. As a result, the reported residual DNA level of decellularised uterine tissue has varied from 0.162 ng/mg to 150 ng/mg and decellularisation efficiencies for uterine tissue range from 75% to over 99% (Table 2.1), although all authors state sufficient removal of cellular material with preservation of ECM proteins. This lack of standardisation of approach to characterising decellularisation efficacy is a common feature of all studies on ECM biomaterials, making it a challenge to compare different protocols [161].

One academic group has recently published three studies on the production and application of porcine endometrial ECM hydrogels [104]–[106]. Endometrial ECM was achieved through perfusion decellularisation of the whole uterus with SDS and Triton X-100, followed by microdissection of the endometrial layer and treatment of endometrial ECM with DNAse I [104]–[106]. Following a standard method for producing ECM digests and hydrogels, the resultant endometrial ECM gels were demonstrated to support the *in vitro* culture of endometrial cells [104], show *in vivo* biocompatibility [104] and enhance organoid growth when used as a culture media supplement [105]. When tested on a mouse model of endometrial damage, Lopez-Martinez et al (2021) reported less collagen deposition and more tissue regeneration was seen when a combination of endometrial ECM hydrogel and growth factors was applied to the traumatised tissue [106]. However, no significant changes were seen with ECM alone [106].

Table 2.1 Summary of uterine decellularisation studies involving tissue from large mammals

Year	Species	Tissue decellularised	ECM biomaterial	Decellularisation method	DNA content - Native	DNA content - ECM	% reduction in DNA	Main study outcome
2017 [171]	Human	Endometrium	Endometrial ECM scaffold	0.25% Triton X-100 and 0.25% sodium deoxycholate at 37 degrees for 48 hours in a shaker. Ribonuclease and DNase I at 37 degrees for 48 hours.	45.4 ng/mg tissue	0.162ng/mg tissue	99.64%	The decellularised endometrial scaffold could be successfully recellularised with endometrial cells, which are hormonally responsive.
2021 [172]	Human	Endometrium	Endometrial ECM scaffold	3 freeze-thaw cycles, 1% Triton X-100 for 15 hours at 50 rpm, 1% SDS for 72 hours	Approximately 900 ng/mg wet tissue	Approximately 100 ng/mg wet tissue	89.89%	Preservation of collagen I and IV, fibronectin and GAGs in decellularised ECM
2021 [104]	Pig	Whole uterus	Endometrial ECM hydrogel	0.1% SDS for 18 hours, distilled H2O 30 mins, 1% Triton X-100 for 30 mins, PBS 5 hours - for 2 cycles. DNase I treatment of endometrial tissue for 1 hour at room temp.	Approximately 1.75 μg/mg lyophilised tissue	Aproximately 0.15 μg/mg lyophilised tissue	92.40%	Endometrial ECM hydrogel supported the culture and co-culture of endometrial cells and demonstrated biocompatibility *in vivo*.
2021 [106]	Pig	Whole uterus	Endometrial ECM hydrogel	0.1% SDS for 18 hrs, 1% Triton X-100 for 30 mins, DNase I	Not reported	Not reported	Not reported	Endometrial ECM hydrogel combined with growth factors supported endometrial regeneration and fertility in a mouse model of endometrial damage.
2021 [105]	Pig	Whole uterus	Endometrial ECM hydrogel	Same method as Campo et al. 2017	Not reported	Not reported	Not reported	Supplementation of organoid culture media with endometrial ECM pre-gel solution enhanced endometrial organoid proliferation.
2017 [59]	Pig	Whole uterus	Uterine ECM scaffold	0.1% SDS for 18hrs, distilled H2O 30 mins, 1% Triton X-100 for 30 mins, PBS 5 hours, for 2 cycles. (Fresh tissue protocol)	Approximately 1500 ng / mg wet tissue	40.792 +/- 16.462 ng / mg wet tissue	97.35%	Decellularised uterine ECM scaffold could support the culture of human side population stem cells
2019 [60]	Sheep	Whole uterus	Uterine ECM scaffold	Optimal protocol: Distilled H2O 24hrs, 0.25% SDS 24 hrs, 0.25% SDS for 48 hrs at 4 degrees at 60 RPM, 0.5% SDS for 24 hrs, distilled water for 24 hours, 10% formalin for 4 hrs, PBS for 96 hrs	180 +/- 64 ng/mg dry tissue	44.7 +/- 10.3 ng/mg dry tissue	75.17%	Decellularised uterine scaffolds implanted into the rat uterus showed evidence of in situ recellularisation and increased Ki67 and CD31 expression compared to control.

2020 [61]	Sheep	Whole uterus	Uterine ECM scaffold	Protocol 1) 0.5% SDS for 8 hours, *26 hour distilled water, PBS overnight, DNAse I at 37°C for 1 hour, distilled water – repeat once from * Protocol 2) 2% sodium deoxycholate for 8 hours, *26 hour distilled water, PBS overnight, DNAse I at 37°C for 1 hour, distilled water – repeat once from * Protocol 3) 2% sodium deoxycholate for 4 hours, **distilled water 6 hours, Triton X-100 12 hours, distilled water 36 hours, repeat one from **, DNAse I at 37°C for 1 hour	398.4 +/- 61.4 ng/mg	1) 4.5 ng/mg 2) 2.3 ng/mg 3) 3.7 ng/mg	1) 98.87% 2) 99.42% 3) 99.07%	Decellularised uterine ECM scaffold could support the growth of fetal stem cells for 2 weeks

2.2.4 Preparation and characterisation of ECM hydrogels

ECM hydrogel formation involves first solubilising ECM, most commonly with Pepsin at low pH, to cleave large protein chains into protein monomers [108]. This is then followed by neutralisation of the pH and salt concentration to physiological levels and raising the temperature, to allow intermolecular bonds to reform between the protein monomers, in a process that relies on self-assembly of collagen and is affected by other ECM proteins, proteoglycans and GAGs [108]. The most common protocol for making ECM gels is that published by Freytes et al. (2008) [173]. Pepsin-prepared ECM digest is brought to a pH of 7.4 using 0.1 N NaOH (1/10 volume of the desired final volume). The neutralised stock solution is then mixed with 10x PBS (1/9 volume of the desired final volume) and diluted with 1x PBS to the final volume and concentration of the pre-gel solution [173]. Heating the pre-gel solution at 37^{o}C leads to the formation of an irreversible gel [173], meaning that injection of the pre-gel solution *in vivo* would enable in situ gelation [102].

ECM hydrogels have been characterised in various different ways to determine their mechanical, biochemical and topological properties, depending on the intended use of the gel. Gelation properties can be determined through rheological testing and turbidimetric assays [108]. The content of ECM hydrogels can be characterised through SDS-PAGE or protein, collagen and sulphated GAG assays or by proteomics [108]. The nanofibrous ultrastructure of ECM hydrogels can also be studied by cryogenic scanning electron microscopy (cryo-SEM) [108].

2.2.5 Matrix-bound nanovesicles

For the last few decades, it has been known that cells secrete extracellular vesicles (EVs), which carry protein, nucleic acid and lipid cargoes, and act as a mechanism for intercellular signalling [174]. EVs play an important role in regulating normal physiological processes, such as cell differentiation and cell fate, adaptive and innate immunity, spermatozoa function, embryonic development, angiogenesis and coagulation, as well as pathological processes like cancer and neurodegenerative disease [174]. EVs have also been demonstrated to have therapeutic purposes in regenerative medicine, such as mediating the paracrine effects of stem cells [51]. In fact, stem-cell derived EVs have been shown, independent of the cells, to have beneficial effects in the treatment of disease [175]. In 2016, Huleihel et al. [164] first reported a new subtype of EVs that are found within decellularised ECM bioscaffolds,

termed matrix-bound nanovesicles (MBV) (Figure 2.2). These bioactive vesicles are thought to be embedded within the scaffolds and closely attached to collagen fibres, which may shield them from the decellularisation processes involved in manufacturing ECM biomaterials [164]. They are released upon enzymatic degradation of the ECM and can then be extracted by EV isolation processes, such as ultracentrifugation [164], [176], [177]. The MBVs isolated by proteinase K digestion were found to range from 10-1000 nm in size, spanning the size range of exosomes, microvesicles and apoptotic bodies, although they were reported to not express any of the typical EV markers (CD63, CD9, CD81 and Hsp70) [164]. Although MBVs were originally secreted by cells into the ECM, they are considered to be a distinct subclass of nanovesicles to liquid-phase cellular EVs. This has been demonstrated in a lipidomics and RNA-sequencing study of EVs isolated from the cell supernatant and nanovesicles extracted from the ECM deposited by the same cells *in vitro*, in which the two different types of nanovesicles exhibit different lipid and miRNA profiles [178].

MBVs have been shown to contain proteins and nucleic acids (Figure 2.2), specifically miRNAs, within their lumen [164], [176], [178], [179]. Like EVs, this cargo is protected from breakdown by nucleases and proteases. Between 33 and 240 different miRNAs have been extracted from SIS-ECM MBVs and UBM-ECM MBVs, and these miRNAs are implicated in various cellular pathways [176]. The miRNAs expressed most highly in SIS and UBM-derived MBVs were found to be miR-145-5p, miR-143-3p, and miR-125b-5p, which are pertinent to macrophage activation and differentiation [176].

The bioactivity of MBVs has been demonstrated by studying their influence on macrophage phenotype [164], [176], neuronal cell growth [164] and in an *in vivo* model retinal ganglion cell degeneration [180]. MBVs alone have been shown to recapitulate the biological effects of their parent ECM [176]. Macrophages treated with SIS ECM-derived MBVs and UBM ECM-derived MBVs had a similar phenotype to macrophages treated with SIS ECM and UBM ECM, with increased expression of the M2 markers Fizz1 and Arg1, compared to an unstimulated macrophage control [164], [176]. The immunomodulatory effect of MBVs has been partly attributed to the finding that these vesicles are enriched with IL-33, an alarmin protein typically secreted by necrotic cells, which influences downstream immune processes by activating the ST2 canonical pathway [179].

Several different techniques can be used to isolate EVs and the use of different methods not only influences the yield and presence of contaminants [181], it can also change the interpretation of EV bioactivity [182]. Size exclusion chromatography (SEC), as an EV isolation method, has been described as being superior to other methods in enhancing EV purity and preserving EV properties [183]. A study

published by Quijano et al. (2020), comparing different MBV isolation methods, demonstrated that a combination of collagenase or liberase ECM digestion with SEC generated MBVs with the highest yield, purity and bioactivity [177].

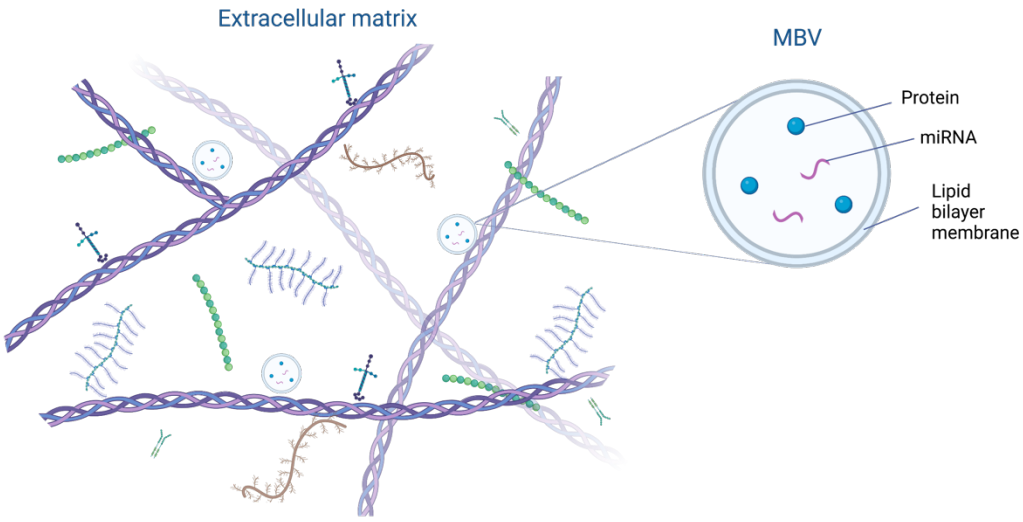


Figure 2.2 Matrix-bound nanovesicles (MBV). MBV are embedded within ECM and appear to withstand decellularisation processes. They are released when the matrix is broken down and can be isolated from decellularised ECM biomaterials with a variety of methods. MBV have been shown to contain proteins, lipids and miRNAs which are bioactive. Figure created with BioRender.com.

2.3 Materials and Methods

2.3.1 Preparation and Decellularisation of Porcine ECM

This protocol for decellularizing the endometrium was designed to combine multiple different physical, chemical and enzymatic methods that are known to disrupt, lyse and remove cells and DNA from endometrial tissue, without causing significant protein destruction.

2.3.1.1 Morphological comparison of pig and sow endometrium

As discussed in section 2.1.1.2, there is a difference between the regenerative potential of ECM obtained from very young animals compared to mature animals. In practice most therapeutic ECM-derived biomaterials come from adult tissues, as it is difficult to obtain large quantities of tissue from new-born animals. In preparing this thesis, uteri were obtained from very young pigs (7 days old and 21 days old) to assess the feasibility of using immature pig tissue for decellularisation. However, pigs of those ages have very small and poorly developed uteri (Figure 2.3a shows a whole uterus isolated from a 21-day old pig). It would not have been feasible to isolate the endometria from these uteri, nor to obtain enough ECM for the current research purposes or future scalability if this research translated to clinical application. The youngest age of adult pig that was readily commercially obtainable was 5 months old (20 weeks). It was also possible to obtain uterine tissue from sows (aged 2-3 years), which are pigs that have born piglets. Theoretically, there could be an advantage to using reproductive tissue obtained from animals with proven fertility. It was therefore decided that for this thesis endometrial ECM would be derived from sows and from 5-month-old pigs, that have never reproduced.

Porcine uteri were obtained from market weight pigs from an abattoir. The porcine uterus is a bicornuate organ and the uterine horns differ from the human uterus in that they are thinner-walled, tubular structures with a thin myometrium (Figure 2.3 b-c). Morphologically, the sow uterus is much larger in size with a thicker, denser and more vascular uterine wall, compared to the pig uterus (Figure 2.3 b-c). The sow uterus has a thicker endometrium that can be clearly distinguished and separated from the underlying myometrium. The pig uterus has thinner endometrium and myometrium which were not as easily separable. The decision was made to first establish and optimise a decellularization process for the sow endometrium as the tissue was more abundantly available.

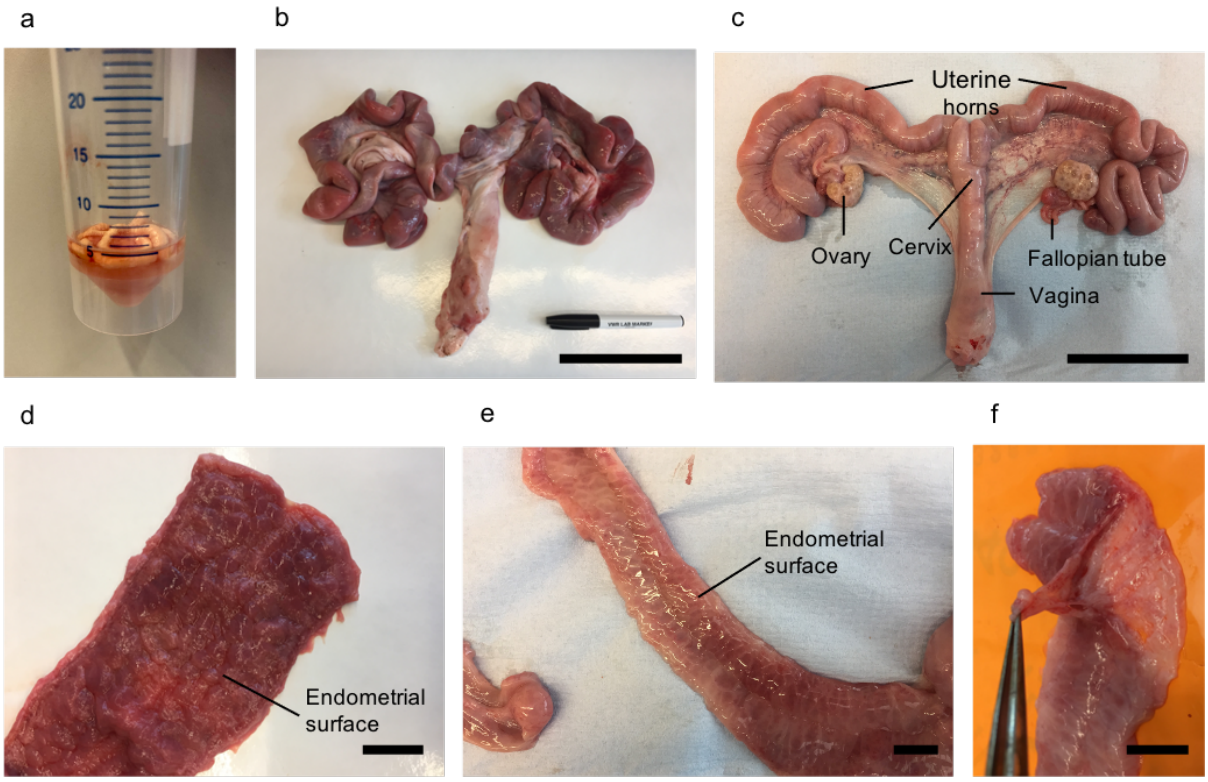


Figure 2.3 Photographs of sow, pig and piglet uterus. **a** Whole piglet (21-day-old) uterus in a 50 ml centrifuge tube, illustrating the small volume of the organ in very young animals. **b** Whole sow uterus. Scale bar = 10cm. **c** Whole pig (20-week-old) uterus, with annotation of anatomy. Scale bar = 10 cm. **d** Sow uterine horn opened up longitudinally with endometrial surface facing up. The sow endometrium appears red and vascular and is thicker than the pig endometrium. Scale bar = 1 cm. **e** Pig uterine horn opened up longitudinally with endometrial surface facing up. Scale bar = 1 cm. **f** Pig endometrium partially dissected off of the underlying myometrium and serosa. Scale bar = 1 cm.

2.3.1.2 Isolation and preparation of porcine endometrium for decellularisation

To isolate and prepare the endometrium, the uterus was first frozen at -80 °C and thawed. The uterine horns were isolated by removing the mesentery, fallopian tubes and the cervix. Each horn was cut open longitudinally along the mesenteric border to expose the endometrial layer and the tissue was rinsed in type 1 ultrapure water (Triple Red, Avidity Science).

With the endometrial surface facing upwards, the endometrial layer was carefully removed from the underlying muscle layer with sharp and blunt dissection. In areas where the tissue was thinner, it was sometimes helpful to lay the uterine tissue with the endometrium face down on a flat, hard surface

and use a scraper to mechanically dissociate the muscle layer away from the endometrium. The dissected endometrium was rinsed in deionized water and stored at -80 ^{o}C if not used immediately. The endometrial tissue was then thawed and cut into 0.5 cm pieces before decellularization.

2.3.1.3 Sow endometrial decellularization

The decellularisation protocol was a multi-step process (Figure 2.4) that involved immersing the tissue pieces in a series of reagents, at 20:1 volume-to-mass ratio and under constant agitation. On protocol days 1-3, the sow endometrium was immersed successively in 4% sodium deoxycholate (4 hours) (Sigma-Aldrich), 1 M sodium chloride (3 hours) and type 1 ultrapure water (Triple Red, Avidity Science) overnight at 4 ^{o}C. The tissue pieces were rinsed briefly with type 1 water in between each reagent step. On day 4 of the decellularisation protocol, DNAse I 100 U/mL (Sigma-Aldrich) was added to the 1 M sodium chloride step (3 hours). On the final day of the protocol, the tissue pieces were immersed in 0.1% peracetic Acid (Merck) in 4% ethanol for 2 hours then washed in 1x PBS (15 minutes), type 1 water (15 minutes), 1x PBS (15 minutes) and type 1 water (15 minutes). For sow endometrial decellularisation all immersion steps were performed at room temperature (apart from the overnight wash step) in a parafilm-sealed beaker on a magnetic stirrer platform (Stuart UC151 magnetic stirrer, dial setting 2.5). All solutions were prepared in type 1 ultrapure water. The decellularised ECM was frozen at -80 ^{o}C, lyophilised in a freeze-dryer (48-72 hours) and stored dry in a sealed container at -20 ^{o}C until use. The sow endometrial decellularisation method is referred to as decellularisation protocol version 1 in this thesis.

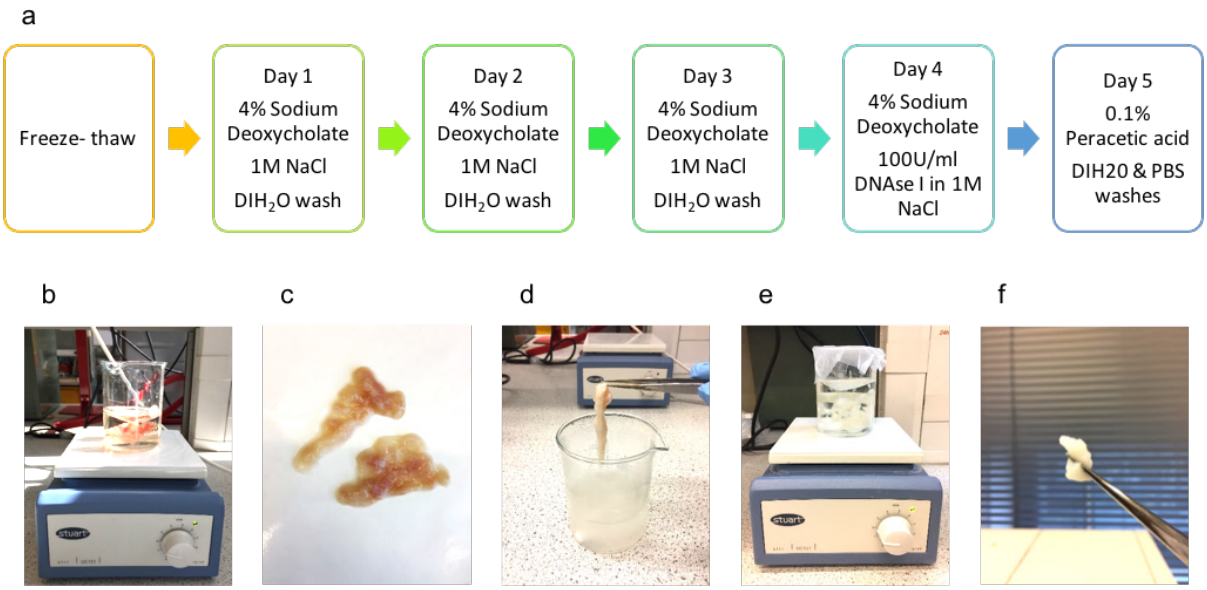


Figure 2.4 Schematic of sow endometrial decellularisation protocol. a Isolated porcine endometrial tissue was first thawed from frozen. The tissue underwent 4 cycles of treatment with each cycle consisting of 4% (w/v) sodium deoxycholate for 4 hours, 1 M sodium chloride for 3 hours and overnight wash in distilled, deionised water at 4 °C. On day 4 of the cycle, 100 U/ml DNAse I was added to the 1 M sodium chloride step. All reagent and wash steps were performed under agitation and at room temperature, apart from the overnight water wash which was performed at 4 °C. On day 5, the tissue is immersed in 0.1% (v/v) peracetic acid for 2 hours then washed for 15 minutes with 1x PBS and 15 minutes with distilled, deionised water twice. This schematic shows the agitation being performed on a magnetic stirrer platform (**b** and **e**). **c** Non-decellularised endometrial tissue appeared pinkish-red. **d** After day 1 of the protocol, the tissue began to appear pale. **e** and **f** The decellularised tissue at the end of day 4 appears white and translucent.

2.3.1.4 Pig endometrial decellularisation

The decellularisation method for pig endometrial tissue was optimised to improve the decellularisation efficiency. The same sequence of steps was used as for sow endometrial decellularisation, but all detergent, chemical and aqueous immersion steps were performed under intense agitation (300 rpm on an orbital shaker) and the DNAse I step was carried out in a 37 °C incubator. Gentle agitation was found to result in suboptimal decellularization efficiency. Table A1 in Appendix 1 summarises all the sow and pig endometrial decellularisation experiments performed, including the parameters that were used and the DNA decellularisation efficiencies achieved. The decellularised and peracetic acid-treated ECM was washed thoroughly alternately with PBS and type

1 water twice before freezing at -80 °C and lyophilisation in a freeze-dryer for 48 hours. The lyophilised ECM was stored at -80 °C until ready to use. The optimised pig endometrial decellularisation method is referred to as decellularisation protocol version 2 in this thesis.

2.3.1.5 Porcine small intestinal submucosa (SIS) decellularisation

Decellularisation of porcine SIS was performed following a published protocol [163]. In brief, the small intestine was prepared by detaching it from the mesentery and washing the lumen with copious tap water. The tissue was then frozen until ready for use. Thawed segments of intestine were opened longitudinally along the mesenteric border and laid flat, mucosal side up. The mucosa was mechanically dissociated from the submucosa by scraping; this process also simultaneously stripped the serosa layer away from underneath the submucosa. The remaining submucosa was then immersed in a large volume of type 1 ultrapure water (Triple Red, Avidity Science) at 4 °C overnight leading to the tissue turning white (Figure2.5). On the following day, the SIS was cut into 2 cm pieces and treated with 0.1% (v/v) peracetic acid in 4% (v/v) ethanol, at 20:1 volume to mass ratio, stirring for 2 hours at room temperature. The ECM was washed in 1x PBS (15 minutes), type 1 water (15 minutes), 1x PBS (15 minutes) and type 1 water (15 minutes), before lyophilisation.

2.3.1.6 Porcine urinary bladder matrix (UBM) decellularisation

Urinary Bladder Matrix was decellularized following a standard protocol [173]. In brief, after freeze-thawing of the bladder, the urothelium was removed by soaking porcine bladders in deionized water. The serosa and muscle layers were mechanically stripped away, leaving behind the basement membrane and the lamina propria layers which collectively form the bladder matrix. This was then decellularized by immersion in deionised water overnight followed by treatment with 0.1% (v/v) peracetic acid and washing with 1x PBS and deionised water. The decellularized ECM was lyophilized before use.

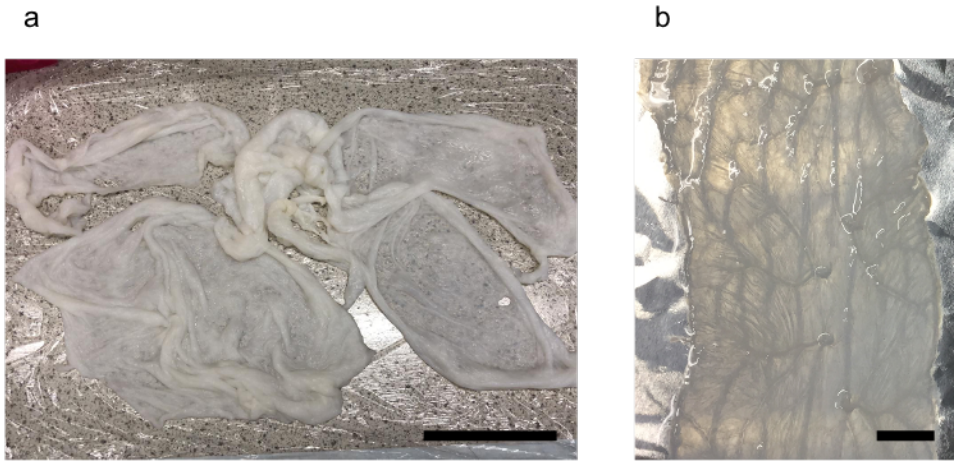


Fig 2.5 Decellularised UBM and SIS ECMs a Photograph of decellularised UBM prior to lyophilisation. Scale bar = 5 cm. **b** Photograph of decellularised SIS ECM prior to lyophilisation. Decellularised ECM appears pale and translucent. Scale bar = 1 cm.

2.3.2 Determining efficiency of ECM decellularization

2.3.2.1 Qualitative analysis of nuclear content

The decellularized ECM was fixed in 10% (v/v) Neutral Buffered Formalin then wax embedded and sectioned at 4 μm per section. The sections were stained with Haematoxylin and Eosin or Masson's Trichrome to examine the presence of intact nuclei and the preservation of the collagen ECM architecture. The ECM sections were compared to stained sections of native tissue. Sections of native tissue and decellularized ECM were stained with 4',6-diamidino-2-phenylindole (DAPI) to assess for nuclear material.

2.3.2.2 DNA isolation from ECM

The lyophilised ECM or native tissue were ground to small fragments and digested in a Proteinase K buffer made of 10 mM Tris-HCL (pH 8.0), 100 mM NaCl, 25 mM EDTA (pH 8.0) and 0.5% (w/v) sodium dodecyl sulphate in type 1 water. An overnight digestion of $\leq$ 100 mg of ground dry ECM or native tissue was performed in 2 mL Proteinase K buffer at 50^{o}C, under gentle agitation (60 rpm), in a 15 ml falcon tube until there were no visible solid pieces. An equal volume of phenol-chloroform-isoamyl alcohol 25:24:1 (v/v/v) mixture (Sigma-Aldrich) was added to the digest and mixed by inverting the

falcon tube. The mixture was centrifuged at 10,000 *g* for 10 minutes to cause phase separation. The aqueous phase was carefully collected above the protein interface and transferred to a new falcon tube and 2 mL of phenol-chloroform-isoamyl alcohol 25:24:1 (v/v/v) mixture was added again. Phase separation was repeated until there was no white residue (protein) left at the interface. The final collected aqueous phase (approximately 2 mL) was transferred to a clean 15 mL falcon tube, followed by addition of 200 μL of 3 M sodium acetate (pH 5.2) and 4 mL of 100% ethanol. The solution was mixed by inverting and then the tube was placed in dry ice until all the liquid was frozen. Whilst still frozen, the tube was centrifuged at 10,000 *g* for 10 minutes to pellet the DNA. The supernatant was carefully removed and the pellet was washed with 7 ml of 70% (v/v) ethanol and centrifuged at 10,000 *g* for 10 minutes. After removing the supernatant, the tube was centrifuged for a further 1 minute and any residual ethanol was carefully pipetted away. The pellet was left to dry in a laminar flow hood for 15 minutes at room temperature before reconstitution with 1 mL of 1x TE buffer (Invitrogen) in preparation for DNA quantification. All centrifugation steps were performed in a fixed rotor centrifuge at 10,000 *g* and 4 °C.

2.3.2.3 DNA quantification

The DNA isolated from decellularized ECM and native tissue were quantified using the Quant-iT™ PicoGreen™ dsDNA Assay Kit (Invitrogen) using a protocol adapted from the manufacturer's instructions. The dsDNA standard curve was prepared by diluting the 100 μg/mL lambda dsDNA stock 1:20 in 1x TE buffer to make a 2 μg/mL stock. The 2 μg/mL DNA stock was then serially diluted 1:1 with 1x TE buffer to create reducing concentrations of DNA until 31.25 ng/mL. The DNA isolated from ECM or tissue were serially diluted 1:10 until 1:10,000 or 1:100,000 with each dilution prepared in a fresh 1.5 mL microcentrifuge tube. The standard curve dilutions and sample dilutions were transferred to a black 96-well microplate with black-bottom wells and plated in triplicates (100 μL per well). Blank wells containing just 1x TE buffer were included in each plate. The Quant-iT™ PicoGreen™ reagent was diluted 1:200 in TE buffer and prepared just before use in a foil-covered falcon tube. The PicoGreen™ solution was added to each well containing the standard curve or sample dilution (100 μL per well) and incubated for 5 minutes in the dark at room temperature. The plate was read on a fluorescence microplate reader (Perkin Elmer) using the following settings; excitation wavelength 480 nm, emission wavelength, 520 nm, cut-off wavelength 515 nm.

To analyse the data, replicates of fluorescence readings were averaged for the standard curve and the sample dilutions. After subtracting the fluorescence readings of the standard curve from the blank, a

standard curve was plotted from 0 ng/mL – 2000 ng/mL and the regression value was checked to ensure the standard curve was linear (R > 0.95). The DNA concentration of the samples was calculated using the standard curve equation and multiplied by the relevant dilution factor. An average of the DNA concentration was taken for multiple dilutions. Results were excluded if they were outside of the linear portion of the standard curve, such as when the fluorescence reading for the sample exceeded the highest reading for the standard curve.

2.3.3 Characterisation of decellularised endometrial ECM

2.3.3.1 Histology

Native porcine endometrial tissue and decellularized endometrial ECM were fixed in 10% (v/v) Neutral Buffered Formalin (Sigma Aldrich) at room temperature for 4-10 hours, depending on the thickness and size of the tissue. The fixed specimens were then dehydrated in 70% (v/v) ethanol prior to paraffin embedding. The tissue or ECM were sectioned at 4 μm thickness and mounted on glass slides. The sections were stained with Haematoxylin and Eosin (H&E) or Masson's Trichrome stain as a standard. All procedures for paraffin embedding, sectioning and staining with H&E and Masson's Trichrome were performed by Miss Lorraine Lawrence, senior histology technician (Sir Alexander Fleming Building, Imperial College London). The stained sections were imaged using 4x and 10x lens objectives on an upright microscope with a colour camera (Olympus IX71). Images were captured via the CellSense software.

2.3.3.2 Immunofluorescence

Sections of fixed and paraffin-embedded native endometrium and EECM (4 μm thickness) were first deparaffinised with Histo-Clear™ (Fisher Scientific) and rehydrated. The slides were immersed successively in Histo-Clear™ (3 minutes), Histo-Clear™ (3 minutes), 100% ethanol (2 minutes), 90% (v/v) ethanol (2 minutes), 70% (v/v) ethanol (2 minutes) and type 1 ultrapure water (2 minutes). Antigen retrieval was performed by placing the slides in hot sodium citrate buffer (sodium citrate 10 mM, 0.05% (v/v) Tween 20, pH 6.0) for 20 minutes. The slides were then rinsed with cold PBS and the sections were blocked in a blocking buffer (2% (v/v) goat serum, 1% (w/v) BSA, 0.1% (v/v) Triton X-100, 0.1% (v/v) Tween) for 1 hour at room temperature, then washed in 1x PBS 3 times for 5 minutes. The sections were incubated with primary antibodies diluted in blocking buffer (see Table 2.2)

overnight at 4 °C in a humidified chamber. After rinsing in PBS (3x 5 minutes), the sections were then incubated with anti-rabbit secondary antibodies diluted in blocking buffer (see Table 2.2) for 30 minutes at room temp then washed again with 1x PBS (3x 5 minutes). The slides were mounted with FluorSave™ (Merck Millipore) and glass coverslips. The slides were imaged on a Zeiss Axio Observer Inverted Widefield Microscope with 10x and 20x lens objectives and images were captured in ZenPro software. The image files were subsequently processed for presentation in ImageJ software.

Table 2.2: Primary and secondary antibodies used for immunofluorescence staining of ECM proteins

Primary antibodies	Secondary antibodies
Anti-Rabbit Collagen Type 1, 1:100 (Abcam ab34710)	Donkey Anti-Rabbit Alexa Fluor 488, 1:1000 (ThermoFisher Scientific A-21206)
Anti-Rabbit Fibronectin, 1:200 (Abcam ab23751)	Donkey Anti-Rabbit Alexa Fluor 594, 1:1000 (ThermoFisher Scientific A-21207)
Anti-Rabbit Laminin, 1:200 (Abcam ab11575)	
Anti-Rabbit Collagen IV, 1:200 (Abcam ab6586)	

2.3.3.3 Raman Spectroscopy of endometrial ECM

Raman spectroscopy is a non-destructive, label-free chemical analysis technique that can be used to obtain information on the biochemical composition of biological samples. Using this technique, the biochemical fingerprint of decellularised sow endometrial ECM was compared to other types of decellularised ECMs used in regenerative medicine (SIS, UBM and cardiac ECM). The Raman data acquisition, pre-processing and analysis were performed by Dr Conor Horgan, an ex-PhD student in the Stevens' group. Raman spectral data for sow endometrial ECM was acquired on a confocal Raman microscope (alpha300R, WITec) with a 785 nm laser, using a 63x water immersion lens objective. To image the endometrial ECM, the sample was immobilised in a petri-dish and immersed in 1x PBS. Raman spectra were captured within a wavelength range of 0 to 3700 cm^{-1} and data was acquired from two different areas of a single sample, with each area measuring 50 x 50 x 50 μm and an average spectrum was generated from the whole image. To prepare the raw Raman data for analysis, pre-processing steps were performed in the WITec Project Four software, including spectra cropping, background subtraction, cosmic ray removal and normalisation of the data to the area under the

curve. The Raman data for endometrial ECM was then compared with Raman spectral data for other decellularised ECM, previously acquired by Dr Horgan using the same data acquisition parameters and pre-processing steps. The spectral data was plotted by Dr Horgan.

In a separate experiment, performed at a later date, Raman spectra were also acquired from decellularised pig endometrial ECM. The same confocal Raman microscope was used as previous (alpha300R, WITec) but this time with a 532 nm laser. Raman data acquisition was undertaken by Dr Vernon Lalone, a postdoctoral researcher in the Stevens' group. Raman spectral data was captured in the range of 0 to 3700 cm^{-1}. For Raman imaging, the endometrial ECM samples were immobilised in 0.5% (w/v) agarose and immersed in 1x PBS imaged with a 63x water immersion lens objective. Data was acquired from 3 different decellularised endometrial ECM samples and the scan area for each sample was 100 x 100 x 100 μm. An average spectrum was then generated from all the spectra acquired across the whole image. Data pre-processing was performed in WITec Project Five software with Dr Lalone and involved, in brief, the following steps; cosmic ray removal, normalisation to water peak (set to a maximum value of 1), background subtractions including shape filter fitting with parameter size of 300. The pre-processed data was then extracted from WITec Project Five software and plotted in GraphPad Prism software (version 9.3.1).

2.3.3.4 Proteomics

The first part of the proteomics protocol was adapted from papers published by Hill et al. 2015 and Barrett et al. 2015, which focused on proteomics of ECM, particularly the extraction of insoluble ECM proteins [184], [185]. Once homogenised and soluble fractions were achieved, the ECM protein extract was then run through and encapsulated in polyacrylamide gels for deglycosylation, reduction, alkylation and downstream LC-MS processing. Sample processing on LC-MS and mass spectrometry data processing were performed by Mr Steve Howell in the Proteomics facility at the Francis Crick Institute, London. All sample preparation prior to trypsin digestion of the polyacrylamide gels was performed by Maxine Chan and Charlotte Lee-Reeves, fellow PhD students in the Stevens' group. All buffers and solutions were made fresh and filtered at the start of the protocol. Two biological replicates of porcine endometrial ECM were processed for proteomics analysis.

2.3.3.4.1 Sample preparation for LC/MS

First, 5 mg of lyophilised and milled decellularised ECM was homogenised by vortexing the sample at room temperature in 1.5 mL of high salt buffer (50 mM Tris-HCl, 0.25% (w/v) CHAPS, 25 mM EDTA, 3 M NaCl (pH 7.4) and 10 µL/mL Halt Protease Inhibitor). The sample was then centrifuged at 18,000 *g* at 4 °C for 20 minutes and the supernatant was collected as fraction 1. The remaining pellet was extracted in 500 µL of high salt buffer (vortexed at 4 °C for 15 minutes and centrifuged for 15 minutes) a further 2 times. After each centrifugation step, the supernatants were collected as fractions 2 and 3. Next the ECM was solubilised by vortexing the pellet at room temperature for 60 minutes in 500 µL of guanidine extraction buffer (6 M guanidine-HCl, adjusted to pH 9 with NaOH). The sample was then centrifuged for 15 minutes and the supernatant was collected as fraction 4. The pellet was then digested in 500 µL of hydroxylamine buffer (1 M hydroxylamine, 4.5 M guanidine-HCl, 0.2 M potassium carbonate, pH adjusted to 9) by vortexing then incubating at 45 °C in a thermomixer under agitation for 17 hours. To collect fraction 5, the sample was centrifuged for 15 minutes at 18,000 *g.* Fractions 4 and 5 were stored at -80 °C and were subsequently carried through for further processing and analysis.

The protein concentrations of fractions 4 and 5 were measured with the Qubit™ protein broad range assay kit (Invitrogen) following the manufacturer's instructions. Denaturing gel electrophoresis was performed to prepare the protein extracts for LC-MS, as advised by Steve Howell. To prepare the protein extracts for gel loading, 10 µg of each sample was diluted with type 1 water to a volume of 29 µL and this was added to 11 µL of 2.5% (v/v) β-mercaptoethanol in 1x NuPAGE™ LDS loading buffer (Invitrogen) to make a total volume of 40 µl. The sample was vortexed to mix then heated at 70 °C for 10 minutes. Precast 10% polyacrylamide bis tris gels (NuPAGE™, Invitrogen) were set up in a mini gel tank and immersed in 1x MOPS buffer (NuPAGE™, Invitrogen). The samples were removed from the heat and 20 µL was immediately loaded into each well of the gel (5 µg of protein per lane). The empty wells were filled with 20 µL of type 1 water mixed with loading buffer. The gel was run at 200 V until the samples were 7-10mm into the gel. Gel running was then halted, and the gel was transferred to a sterile petri dish containing type 1 water. Fixation of the gel was performed in 40% (v/v) ethanol + 10% (v/v) acetic acid for 15 minutes with gentle shaking. The gel was then rinsed with type 1 water and stained with colloidal Coomassie blue G-250 stain (Biorad) overnight, at room temperature, under gentle agitation. After staining, the gels were washed with type 1 water and photographs were taken of the gel lanes before the lanes were excised with a clean scalpel and transferred to individual 2 mL protein lo-bind tubes (Eppendorf). For de-staining, the gel lane was immersed in 1 mL of extraction buffer (50% (v/v) ethanol and 50% (w/v) 100 mM ammonium bicarbonate). The extraction buffer was changed every 30-60 minutes until the solution became light blue to clear in colour. The gel lanes were then left in extraction buffer overnight at 4 °C to completely destain.

For protein deglycosylation (of N-linked glycans), PNGase F (New England Biolab) was diluted in 100 mM ammonium bicarbonate and added to the gels, ensuring that each piece of gel was fully immersed. As per the manufacturer's recommendation, 500 units of PNGase F was used for every 20 μg of protein. The gels were left in PNGase F solution overnight at 37°C then washed thoroughly in type 1 grade water. Then, 500 μL of reduction and alkylation solution (100 mM TCEP and 40 mM 2-chloroacetamide in 100 mM of ammonium bicarbonate) was added to each gel and incubated for 10 minutes at 70 °C in a thermomixer set to 300 rpm. The samples were then cooled and rinsed thoroughly with 100 mM ammonium bicarbonate then washed with HPLC grade water. The samples were then transferred to the Francis Crick Institute for trypsin digestion and mass spectrometry by Mr Steve Howell. In brief, the gel lanes were digested in modified sequencing grade trypsin (V5111, Promega) overnight at 37 °C. The digests were loaded onto Evotips (Evosep, Odense, Denmark) following the manufacturer's protocol and peptide elution was carried out via an Evosep One HPLC into a Lumos Tribrid Oribitrap mass spectrometer (Thermo Scientific) fitted with a nanospray emitter. The Orbitrap was set to "Data Dependent Acquisition" mode with precursor ion spectra acquired at 1.2 x 10^5 resolution. MS/MS spectra in the ion trap was acquired at 35% collision energy in "TopS" mode. The following data acquisition parameters were also used; "Auto" setting for Automatic Gain Control, 20 seconds for dynamic exclusion and the manufacturer's "universal method" for scheduling the ion trap accumulation times.

2.3.3.4.2 Proteomics data processing and analysis

Raw data was processed using Maxquant (Cox & Mann 2008) (maxquant.org) and Perseus [186] software version 1.4.0.2 (maxquant.net/perseus), correlating to the Uniprot Sus scrofa and Homo sapiens reference proteome databases, alongside a common contaminants database. A decoy database of reversed sequences was also used to filter false positive hits and a false detection rate of 1% was set for both peptides and proteins. Gene ontology (GO) analysis was performed using the list of gene names for all proteins identified in fractions 4 or 5 of either biological replicate. The gene list was submitted to open-source, online gene ontology and bioinformatics resources DAVID (2021 update) [187] (https://david.ncifcrf.gov) and ShinyGO [188], version 0.76 (http://bioinformatics.sdstate.edu/go/) for analysis of GO enrichment relevant to biological processes (GO_BP), cellular components (GO_CC) and molecular functions (GO_MF). In both resources, the gene list was searched against the homo sapiens species as this yielded more comprehensive GO terms enrichment data. DAVID was used primarily for its functional annotation clustering tool to identify all

genes relevant to ECM components, processes and functions. ShinyGO was used primarily for automated plotting of enriched gene ontology pathways. The ShinyGO platform determines gene ontology enrichment based on annotations from Ensembl, a large genome database from the European Bioinformatics Institute, and Stringdb, a database for protein-protein interactions and functional enrichment analysis.

The full gene list for endometrial ECM was submitted to ShinyGO, using default settings (FDR cutoff 0.05), to see the top 20 most enriched GO_BP and GO_MF pathways and automated plots were generated within ShinyGO to show this data. In DAVID, functional annotation clustering was performed for the groups GO_BP_Direct, GO_CC_Direct and GO_MF_Direct, using default settings. This generated 40 clusters of associated functions and processes ranked by enrichment score. The cluster with the second highest enrichment score corresponded to genes related to various ECM components, processes and functions. A Benjamini-Hochberg FDR of 0.05 was applied to determine significance of enrichment for GO term inclusion. The list of ECM-related genes was then submitted to ShinyGO to explore and plot the top 20 most enriched GO_BP and GO_MF pathways relevant to ECM.

2.3.4 Isolation and characterisation of matrix-bound vesicles (MBV)

2.3.4.1 Digestion of ECM and MBV isolation

Lyophilised and milled ECM was weighed (150 mg per sample) and digested with 2 mL of Collagenase I 0.06% (w/v) (Sigma-Aldrich, SCR103) in a buffer containing 50 mM tris (pH 8), 5 mM $CaCl_2$ and 200 mM NaCl, at 37^{o}C for 16 hours. If any undigested fragments of ECM remained, the digest solution was vortexed and digested for a further 4 hours at 37 ^{o}C. The digested solution was then diluted to 5 mL with buffer and passed through a 100 μm cell strainer. The ECM solution was centrifuged at 1000 rcf for 5 minutes, then the supernatant was collected and centrifuged at 5000 rcf for 15 minutes. The supernatant was then filtered through a 0.45 μm syringe filter and subsequently concentrated to approximately 500 μL using a 100 kDa Amicon® Ultra-15 Centrifugal Filter Unit (Merck Millipore). The concentrated supernatant was then loaded onto a size exclusion chromatography column packed with sepharose CL 2B beads (Sigma-Aldrich, CL2B300) in PBS. Using a reservoir, 30 mL of 1x PBS was added to the column and 30 consecutive fractions of 1 mL each were eluted from the column into 1.5 mL

microcentrifuge tubes. The fractions were aliquoted and stored at -80 °C for later analysis. Figure 2.6 shows a schematic summarising the MBV isolation protocol.

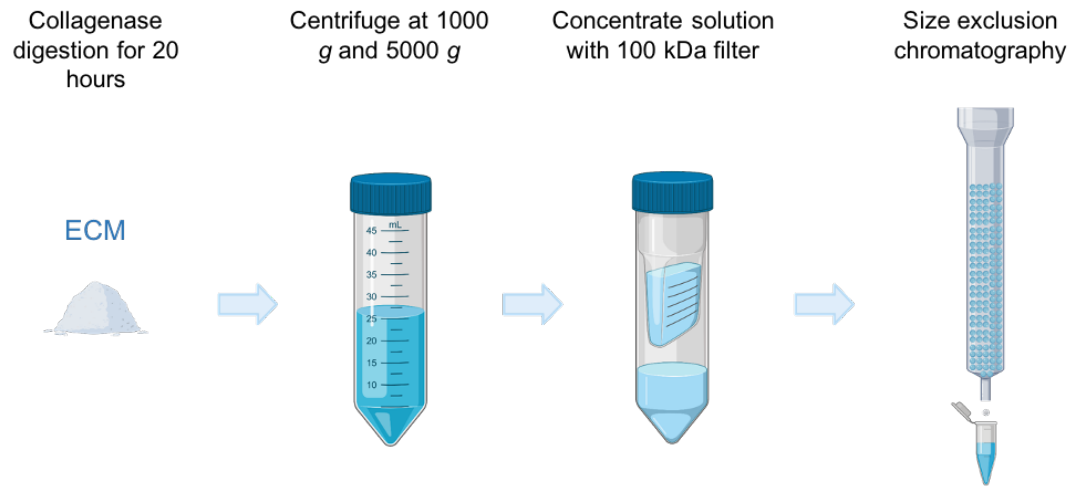


Figure 2.6 Schematic of MBV isolation protocol Lyophilised and ground ECM was digested with collagenase for 20 hours until no solid particles were visible. The solution was centrifuged at 1000 *g* and the supernatant was collected then centrifuged at 5000 *g*. The collected supernatant was concentrated down to 500 µL using a 100 kDa centrifugal filter unit and then loaded onto a size exclusion chromatography column to collect 30x 1 mL fractions. Figure created with BioRender.com.

2.3.4.2 Micro-BCA assay

The protein concentration of each of the 30 fractions was measured using a commercially available Pierce™ micro-BCA assay (Thermo Fisher Scientific) following the manufacturer's instructions. Fractions 15-25 were diluted 1:10 in 1x PBS due to their higher protein content whilst the other fractions were measured undiluted. The working reagent was prepared by mixing solutions A, B and C at a 25:24:1 ratio (v/v/v). The BSA standards and samples were added to a 96 well plate with the working reagent (150 µL of sample and 150 µL of working reagent in each well) and incubated for 2 hours at 37 °C. The plate was then read at 562 nm absorbance in a 96-well plate reader (SpectraMax M5) and the concentrations of the fractions were calculated based on the linear regression curve of the standards.

2.3.4.3 Nanoparticle Tracking Analysis

The nanoparticle concentration of each fraction was quantified using a Nanosight NS300 with a 532 nm laser and sCMOS camera module (Malvern Instruments, Salisbury, UK). Fractions 1-6 and 15-30 were diluted 1:5 whilst fractions 7-14 were diluted 1:25 in Type 1 (18.2 MΩ·cm) ultrapure water, to aim for a particle concentration range of 10^8 to 10^9 at the time of measurement. The measurements were made using the NTA v.3.1 software, with camera level 14 and screen gain 1 in the capture mode, and detection threshold 5 and screen gain 10 in the process mode. Three 60 second videos were captured and analysed for each sample and the average particle concentration was subsequently plotted.

2.3.4.4 Dot Blotting

Dot blotting was performed to detect the presence of EV markers CD9, CD63 and CD81 in the eluted fractions. First, a 0.45 μm nitrocellulose membrane (Bio-Rad, 162-0117) was equilibrated in 1x Tris-buffered saline (TBS) for 10 minutes and then loaded into a 96-well Bio-Dot® microfiltration system (Bio-Rad 1703938). Each well was filled with 100 μL of TBS and drained under vacuum, taking care not to fully dry out the membrane. 150 μL of each fraction was added, undiluted, to the wells and in the wells containing no samples 150 μL of TBS was added. The samples and TBS were allowed to drain by gravity for 1 hour then the wells were washed 3 times with TBS with vacuum-assisted drainage. The membrane was then retrieved from the device and labelled to ensure the orientation of the samples could be identified during imaging and analysis. The membrane was blocked with 5% (w/v) skimmed milk in TBS + 0.1% (w/v) Tween buffer for 1 hour at room temperature and incubated overnight at 4°C overnight in primary antibody solution (CD9, CD163 or CD81 diluted 1:500 in TBS-T with 5% (w/v) BSA) (see table 2.3). The membrane was then washed 3 times with TBS-T and incubated for 1 hour at room temperature with secondary antibody (see table 2.3) diluted 1:10,000 in TBS-T. Finally, the membranes were washed 3 times with TBS-T and imaged with a Li-COR Odyssey® near infrared imaging system.

Table 2.3: Primary and secondary antibodies used for MBV dot blots

Primary antibodies	Secondary antibody
CD9, polyclonal rabbit IgG, 1:500 (Proteintech 25682-1-AP)	Goat anti-rabbit IgG, IRDye® 800CW, 1:10,000 (Li-COR 926-32211)
CD163, polyclonal rabbit IgG, 1:500 (Proteintech 20597-1-AP)	
CD81, polyclonal rabbit IgG, 1:500 (Biorbyt, orb378210)	

2.3.4.5 Single particle Raman spectroscopy analysis of MBV

Using the single particle automated Raman trapping analysis (SPARTA®) technique [131], MBVs isolated from endometrial ECM were analysed by Raman spectroscopy for their biochemical composition and specifically to observe for the presence of nucleic acids. All samples were run and analysed by Dr Jelle Penders. To prepare the samples for SPARTA® analysis, fractions 7-14 (MBV fractions) from 3 biological replicates were first pooled. The pooled MBV sample was then concentrated to 1 mL volume with an Amicon® Ultra-15 Centrifugal Filter unit (Merck Millipore) and the particle concentration was re-assessed by NTA measurement to be 2.9 x 10^9 particles/mL. The pooled MBV was aliquoted and stored at -80 ^oC. Prior to SPARTA® analysis, 400 μl of pooled MBV was thawed and concentrated 10-fold using an Amicon® Ultra 0.5 mL Centrifugal Filter (Merck Millipore). A 24 μL volume of sample was then placed in a confined volume trapping setup with beam expander, and serial dilutions (neat, 1:2 and 1:4) were assessed for optimal single particle trapping and Raman signal. The optimal signal was determined at 1:4 dilution in 1x PBS and Raman spectra were acquired from multiple single trapped particles. Three technical replicates were performed (nI = 102, nII = 41, nIII = 116) and spectra from a total of 259 particles were acquired for analysis. An average endometrial ECM MBV Raman spectrum was obtained and comparison was made to the SPARTA® Raman spectra of MBVs derived from porcine Dura ECM (fabricated by Charlotte Lee-Reeves) and EVs derived from a HEK293F cell line (isolated and analysed by Dr Jelle Penders). The Raman peaks were normalised to the sum of the total Raman intensity under the curve.

2.3.4.5.1 Multivariate analysis

To visualise differences between endometrial MBVs and other MBVs or EVs, two different multivariate analysis techniques models were used to analyse the spectral data sets from endometrial MBVs, dura

MBVs and HEK293 EVs. All data analysis was performed by Dr Jelle Penders. Principal component analysis (PCA) is an unsupervised technique where all the data, here the spectral data from each sample, is fed into the model without assigning any information about the sample origin of the data. PCA generates principal components (PC) which represent the greatest variance within the data sets, and these are ranked in order of variance (PC1 is greatest variance). Each principal component relates to a pseudo-spectrum and scrutiny of the main peaks within the spectrum helps to identify which biochemical components differentiate the data sets. Plotting the principal component scores for each data set (typically for PC1, PC2, PC3 and PC4) allows for visualisation of how the data clustering corresponds to the different principal components. Partial least squares discriminant analysis (PLSDA) is a supervised technique which relies on *a priori* knowledge of the sample origin of each spectrum. The PLSDA latent variables (LV) are generated to maximise cluster separation and are ranked in order of greatest variance. Similar to PCA, each LV corresponds to a pseudo-spectrum.

2.3.5 Production and characterisation of ECM hydrogels

2.3.5.1 Preparation of ECM hydrogels

ECM hydrogels were prepared according to a standard method [173] (Figure 2.7). In earlier experiments with sow decellularised endometrium, decellularised and lyophilised ECM was frozen in liquid nitrogen then ground to small particles using a commercially available ceramic burr coffee grinder. Later, access to a cryogenic mill (Spex 6775 Freezer/Mill®) was granted and lyophilised ECM was milled to a powder. To prepare ECM digests, a defined mass of ground ECM was solubilized with Pepsin 1 mg/mL (Sigma) in 0.01 N hydrochloric acid (pH 2) for 24-48 hours at room temperature, under constant agitation on a magnetic stirrer platform (Stuart UC151 Magnetic Stirrer, dial setting 1.5). As a standard, either 10 mg/mL or 15 mg/mL ECM digests were prepared. The ECM digests were stored at -80 ^{o}C in aliquots to avoid multiple freeze-thaws. To prepare thermo-responsive hydrogels, thawed digests were neutralised to pH 7.4 with 0.1 N sodium hydroxide (1/10th of digest volume), mixed with 10x PBS (1/9th of digest volume) to adjust the salt content and diluted to desired final volume and concentration with cold 1x PBS or cell culture media. The neutralised and diluted ECM pre-gel solutions were kept at 4 ^{o}C until ready for use and were prepared fresh for each experiment. The pre-gel solution was liquid, allowing it to be easily injected and to fill a cavity. Gelation was achieved by incubation at 37 ^{o}C for a minimum of 10 minutes.

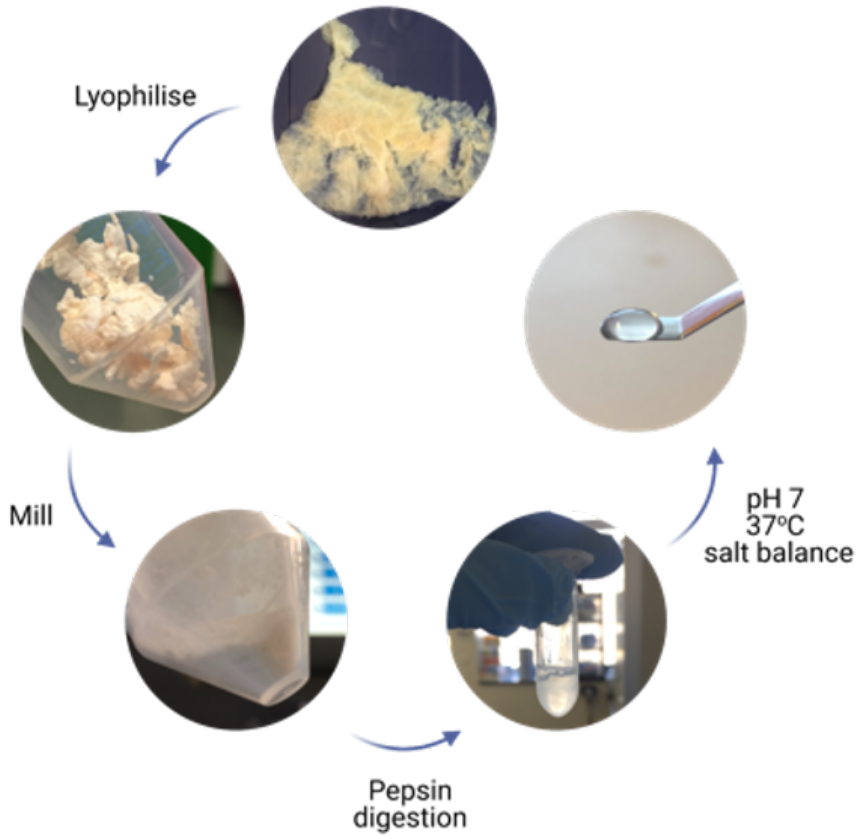


Figure 2.7 Steps for ECM hydrogel fabrication ECM hydrogels were prepared by 1) lyophilisation of decellularised ECM, 2) grinding or milling of lyophilised ECM to a powder, 3) digestion of ECM powder with 1 mg/mL pepsin in 0.01 N hydrochloric acid, 4) neutralising and adjusting the salt concentration of ECM digest and diluting to desired concentration, 5) heating the pre-gel solution to 37°C to achieve a stable gel.

2.3.5.1.1 Preparation of sow endometrial ECM hydrogel for experiments

Decellularised sow endometrium were the first ECM samples to be prepared and converted into hydrogels for rheological testing and subsequent *in vitro* experiments. Each batch of sow endometrial ECM digest was prepared from a single batch of lyophilised, decellularised endometrial ECM, from derived from a single animal and from one decellularisation experiment (protocol version 1). Therefore, each sow endometrial hydrogel tested represented a single biological replicate.

2.3.5.1.2 Preparation of pig endometrial ECM hydrogel for experiments

The preparation of pig endometrial ECM hydrogels was modified, compared to sow, to reduce the risk of batch-to-batch variability. Each batch of pig endometrial ECM digest was prepared from a combination of two or three individual batches of lyophilised endometrial ECM, from two or three different animals, prepared through separate decellularisation experiments following protocol version 2. An equal proportion of lyophilised and milled ECM from each batch was weighed out and combined to prepare a single digest, as per the method described in 2.3.5.1. An ECM hydrogel was then made from a single batch of digest. Therefore, each batch of pig endometrial ECM hydrogel represents a pooling of two or three biological replicates. Table 2.4 summarises the composition of different batches of pig endometrial ECM digests or hydrogels used in subsequent experiments. Table A1 in Appendix 1 summarises all the decellularisation experiments performed to make pig endometrial ECM and includes the pig uterus ID assigned to each animal.

Table 2.4: Pig endometrial ECM digest batches.

Batch of ECM digest	Pig Uterus IDs and composition	Subsequent experiments
A	Uterus 1 (1/3) Uterus 3 (1/3) Uterus 4 (1/3)	Rheology, collagen and GAG assays
B	Uterus 1 (1/3) Uterus 3 (1/3) Uterus 4 (1/3)	Rheology, collagen and GAG assays
C	Uterus 1 (1/2) Uterus 3 (1/2)	Rheology, collagen and GAG assays, cell proliferation studies, *in vitro* angiogenesis assays, *in vitro* endometrial fibrosis assay, *in vitro* macrophage studies, *in vivo* studies

2.3.5.2 Collagen quantification of ECM digests

The collagen content of ECM digests was measured using the commercially available Sircol™ collagen assay (Biocolor, S1000), following the manufacturer's protocol. Collagen standards ranging from 0 μg to 50 μg were prepared in 1.5 mL microcentrifuge tubes. ECM digests were diluted to 1 mg/ml with PBS and then 100 μg, 50 μg and 25 μg of ECM was added to microcentrifuge tubes. Type 1 water was used as reagent blanks. All standards and samples were tested in duplicates. To each standard and sample, 1 mL of Sircol™ dye reagent was added and the contents of the tubes were mixed by inverting

then gentle mechanical agitation for 30 minutes. The tubes were centrifuged at 12,000 rpm for 10 minutes and the supernatant was drained by inverting the tubes, leaving a pellet of collagen-dye complex. Cold acid-salt wash (750 μL) was then added on top of the pellet to remove any unbound dye and the tubes were centrifuged again at 12,000 rpm for 10 minutes. The supernatant was removed and 250 μL of alkali reagent (proprietary, Biocolor) was added to the reagent blanks, standards and samples. The tubes were vortexed to release the collagen bound dye, until no visible particles were seen. To measure the absorbance, 200 μL of each standard, sample or blank was transferred to a 96-well microplate and the plate was read on a SpectraMax M5 plate reader at 555 nm. The collagen content of the samples were calculated by linear regression fitting to the standard curve.

2.3.5.3 Glycosaminoglycan quantification of ECM digests

The sulphated proteoglycan and glycosaminoglycan (GAG) content of ECM digests were measured with the commercially available Blyscan™ sGAG assay (Biocolor, B1000), following the manufacturer's protocol. GAG standards (0 μg to 5 μg) were prepared in 1.5 mL microcentrifuge tubes and deionised water was used as reagent blanks. ECM digests (500 μg and 250 μg) were added to microcentrifuge tubes and diluted with deionised water to make up 100 μL volume. To each sample, 1 mL of Blyscan™ dye reagent was added and the contents of the tubes were mixed by inverting and continuously gently agitated on a shaker, at room temperature, for 30 minutes. The tubes were centrifuged at 12,000 rpm for 10 minutes to result in a pellet of GAG-dye complex. After draining the supernatant, 500 μL of dye dissociation reagent was added to each pellet and the tubes were vortexed to release the dye. A 200 μL aliquot of each sample and standard were transferred to each well of a 96-well microplate, which was read on a SpectraMax plate reader at 656 nm absorbance. All standards and samples were plated in duplicates. The GAG content of the samples was calculated according to a standard curve.

2.3.5.4 Rheology of ECM hydrogels

The rheological properties of ECM hydrogels were characterised using a AR2000ex rheometer (TA Instruments) fitted with a 40 mm parallel plate and an MCR 302 rheometer (Anton Paar) fitted with a 25 mm parallel plate. Pre-gel solutions were prepared at different concentrations according to the method in section 2.3.5.1. The peltier was set to 10°C, to prevent premature initiation of gelation and the pre-gel solution was loaded onto the centre of the peltier. The volume of pre-gel loaded for a 40 mm parallel plate and a 25 mm parallel plate was 1 mL and 0.5 mL respectively. The parallel plate was

lowered to a gap of 500 μm (40 mm plate) or 1 mm (25 mm plate) and to minimise evaporation during the experiment, the gel was surrounded by mineral oil.

Oscillatory rheological tests were performed in the following order: time sweep, frequency sweep and strain sweep. For the time sweep, the temperature was set at 37 °C and measurements were taken for ≥45 minutes once this temperature was reached, typically within 30 seconds of starting the experiment. A constant strain of 0.1%, which lies within the linear viscoelastic region, and a frequency of 10 rad/s were used. Preliminary strain sweeps, at different gel concentrations, had been performed to identify the linear viscoelastic region for oscillatory time sweeps. The frequency sweep step was carried out immediately after the time sweep, at 37 °C and 0.1% constant strain across an angular frequency range of 0.1-100 rad/s. Following this, the strain sweep was performed across a range of 0.001 – 100% strain at 37 °C and a frequency of 10 rad/s.

To test gelation properties after injection or spraying of ECM hydrogels, SIS pre-gels were prepared at 5mg/mL as described in section 2.3.5.1. The cold pre-gels were loaded into a 3 mL syringe with either a 18G needle (Figure 2.8a) or mucosal atomisation device (MAD Nasal™) (Figure 2.8c) fitted to the syringe tip and kept on ice until ready to load. To test post-injection rheological properties, the pre-gels were directly injected onto the peltier set to 10 °C. It was not possible to directly spray the gel onto the peltier, as spraying does not allow for adequate control of the volume, area and positioning of gel under the parallel plate to run the rheological tests and would have also led to excessive wastage of material. Therefore, to test post-spray properties, the pre-gel was first sprayed into a 2 mL microcentrifuge tube. The tube was briefly centrifuged to remove air bubbles and then transferred, by pipette, onto the peltier set to 10 °C. Oscillatory time sweeps, frequency sweeps and strain sweeps were performed as described above.

2.3.5.5 Demonstration of sprayable ECM hydrogel

Neutralised and diluted, cold ECM pre-gel solutions were loaded into a 3 mL Luer Lock syringe with a mucosal atomisation device (MAD Nasal™) fitted to the syringe tip (Figure 2.8c). The atomisation device generates a spray of particles (Figure 2.8d) that are 30-100 μm in size. The syringe containing pre-gel solution was kept on ice until ready to use. The ECM pre-gel was sprayed onto a surface pre-warmed to 37 °C to initiate gelation where the spray was applied. Further incubation of the gel at 37 °C was necessary to complete the gelation process. To aid visualisation of the gel, Alexa Fluor™ 546 C5 Maleimide (Invitrogen) was added to the pre-gel solution at 1:1000 and the solution was mixed

overnight in a foil-covered 15 mL falcon tube on a tube roller platform (Stuart™ Cole-Parmer™ SRT6) at 4 °C. This turns the pre-gel solution bright pink in visible light. To simulate the *in vivo* spray-application of gel to tissue surfaces, endometrial ECM 5 mg/mL pre-gel was sprayed into a mould on the surface of pre-warmed chicken meat and incubated at 37 °C for 15 minutes (Figure 2.9 e-f).

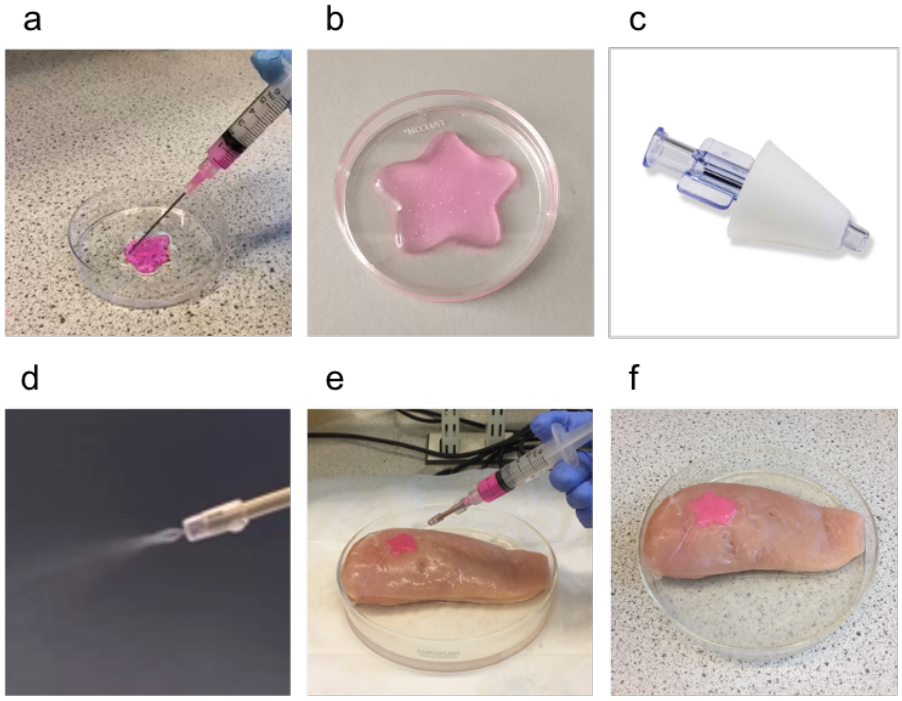


Figure 2.8 Injection and spray of ECM hydrogel Photographs demonstrating the process of testing ECM gel injection and spray. ECM pre-gel solutions were dyed pink for easy visualisation. **A** Cold, 5 mg/mL SIS ECM pre-gel solution was injected through an 18 gauge needle into a star-shaped mould. **B** After heating the pre-gel in **a** at 37 °C for 15 minutes, the mould was removed and a shape-retaining, stable hydrogel was observed. **C** Image of a MAD Nasal™ device that would be attached to the end of a syringe. **D** Still image from a video of cold ECM pre-gel solution being sprayed through the mucosal atomisation device. **E** Still image from a video of cold ECM pre-gel solution being sprayed into a mould placed on top of a piece of chicken warmed on a hot plate to 37 °C. **f** After heating **e** at 37 °C for 15 minutes, a shape-retaining hydrogel was left on the surface of the chicken.

2.3.5.6 Demonstration of ECM gel adherence to endometrial tissue

ECM gels should adhere gently to tissue due to formation of covalent bonds between free thiol groups in the ECM gel and on the surface of tissues. In order to demonstrate ECM gel adherence post gelation, SIS 7 mg/mL pre-gel solution was prepared containing 1:9 F8BT nanoparticles (suspended in H_2O),

which fluoresce green under a 365nm UV light. F8BT fluorescent nanoparticles were synthesised and donated by Dr Adam Creamer in the Stevens Group, Imperial College London. The pre-gel, incorporating fluorescent nanoparticles, was pipetted into a rectangular mould on top of the endometrial surface of a piece of porcine uterus laid flat. The gel and tissue were incubated at 37 ^{o}C for 20 minutes. The tissue was then suspended vertically and imaged at 0, 15 and 30 minutes post-gelation to demonstrate that the gel remain adhered and there was no obvious gel deformation. As a control, fluorescent F8SBT nanoparticles were mixed in 1x PBS at 1:9 dilution and the same volume of fluorescent PBS was added to a piece of endometrial tissue and incubated at 37 ^{o}C.

2.3.6 Statistical analysis

All statistical analysis was performed in GraphPad Prism software version 9.3.1. All data was first assessed for normal distribution before selecting the statistical test to perform. Where the data was normally distributed, student t test was performed if comparing two groups and ordinary one-way ANOVA with Tukey's multiple comparisons test was used for comparing three or more groups. There were no data sets with non-normally distributed data in this chapter. Statistical analysis was not performed where one group contained less than N = 3.

2.4 Results

2.4.1 Histology of pig and sow endometrium

Figure 2.9 shows H&E-stained histological sections of pig endometrium (Figure 2.9a-c) and sow endometrium (Figure 2.9d). The luminal surface of the endometrium is lined by pseudostratified columnar epithelium. The endometrial stroma contains numerous endometrial glands (blue arrows) and blood vessels. The blood vessels in the sow endometrium were larger in diameter and thicker walled than blood vessels seen in pig endometrium. Macroscopically the sow endometrium appeared to be a more vascular tissue than pig endometrium, most likely reflecting the extra vascularisation acquired through pregnancies.

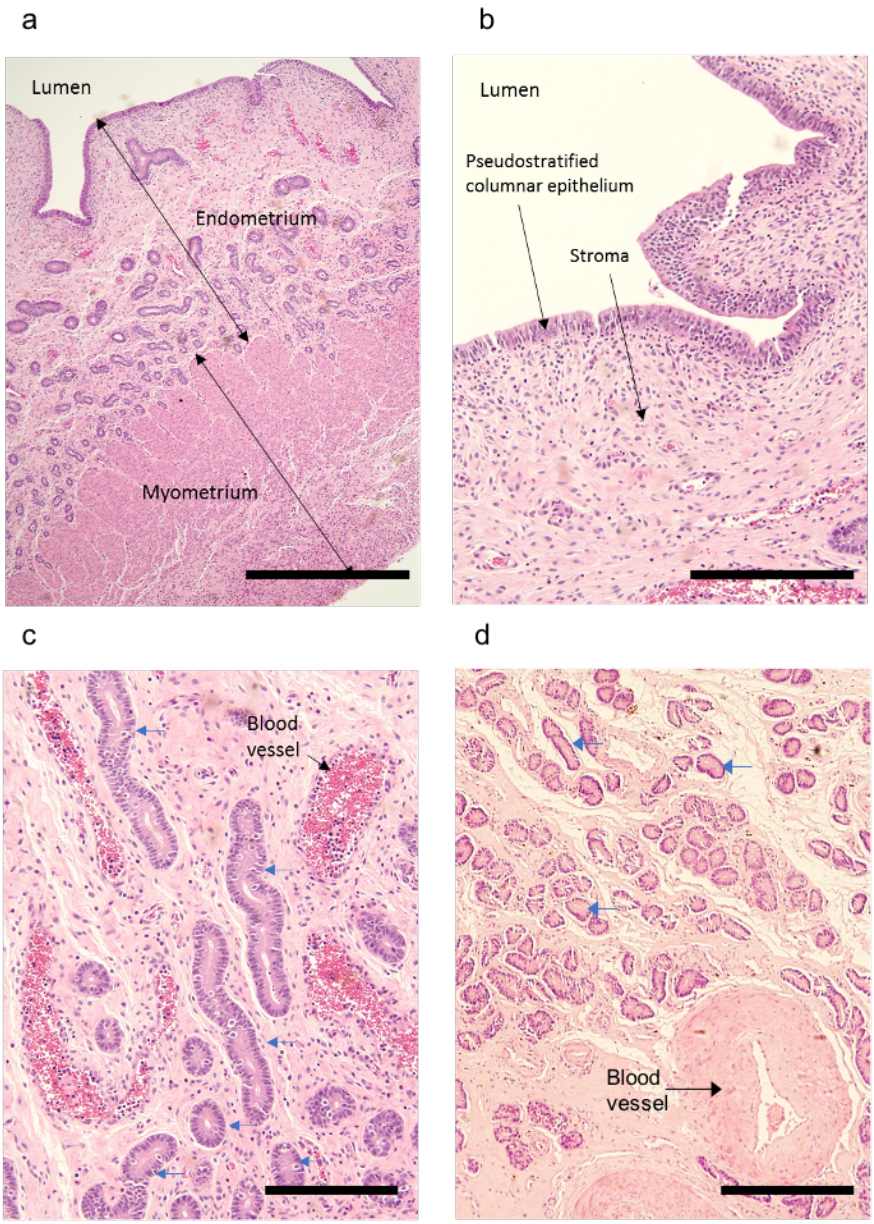


Figure 2.9 Histology of pig and sow endometrium (H&E stained). **a** Full thickness cross-section of pig uterine wall showing endometrial and myometrial layer (4x lens objective). Scale bar = 1 mm. **b** Pig endometrial stroma with overlying pseudostratified columnar epithelium (4x lens objective). Scale bar = 1 mm. **c** Pig endometrial stroma containing endometrial glands (blue arrows) and blood vessels (10x lens objective). Scale bar = 500 µm. **d** Sow endometrial stroma containing endometrial glands (blue arrows) and a thick-walled blood vessel (10x lens objective). Note: an image could not be obtained of the full thickness cross-section of sow uterine wall as the tissue was too thick to be imaged in full, even at the lowest magnification. Scale bar = 500 µm.

2.4.2 Evaluating decellularisation efficiency

2.4.2.1 Histology and DAPI staining of native and decellularised sow endometrium

Sections of native sow endometrium and endometrial tissue after each cycle of the decellularisation protocol were stained with haematoxylin and eosin (H&E), Masson's trichrome or DAPI (Figure 2.10). After day 1 (first cycle) of decellularisation, there was already a dramatic difference in the histological appearance of the endometrial tissue. Whilst the ECM architecture of the tissue was preserved, the cellular component was largely absent after the first cycle of decellularisation. By the end of day 3 (third cycle), there were no visible nuclei on H&E staining and DAPI staining showed very scanty and weak fluorescent signal, in contrast to the abundant nuclear staining seen in the native endometrium.

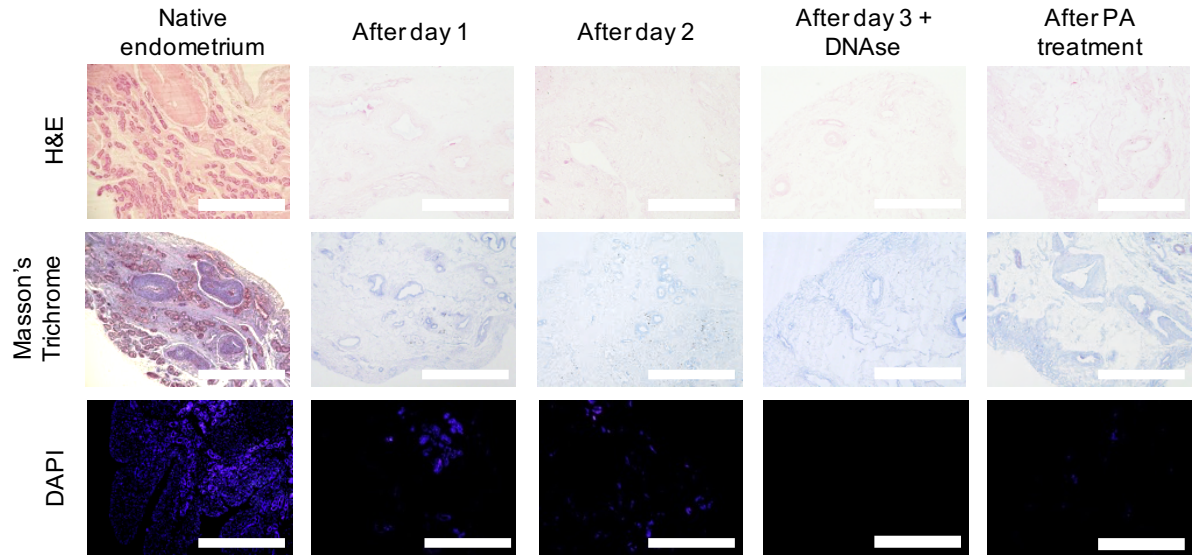


Figure 2.10 H&E, Masson's Trichrome and DAPI staining of native and decellularised sow endometrium. **Top row**: Representative H&E-stained sections of native sow endometrium and sow endometrial ECM after day 1, day 2 and day 3 of decellularisation protocol (version 1) and following peracetic acid (PA) treatment. Even after day 1, there were significantly reduced visible nuclei. Images captured with 4x lens objective, scale bars = 1 mm. **Middle row**: Representative Masson's trichrome stained sections of native sow endometrium and sow endometrial ECM after day 1, day 2 and day 3 of decellularisation protocol and following PA treatment. The collagen matrix was clearly maintained throughout the decellularisation process. Images captured with 4x lens objective, scale bars = 1 mm. **Bottom row**: Representative DAPI stained sections of native sow endometrium and sow endometrial ECM after day 1, day 2 and day 3 of decellularisation protocol and following PA treatment. By the end of the protocol, minimal to no DAPI staining was seen. Images captured with 10x lens objective, scale bars = 500 μm.

2.4.2.2 DNA content of sow endometrial ECM

DNA content was measured by Picogreen assay for native sow endometrium and decellularised sow endometrial ECM and was expressed as ng per mg of dry weight. Native sow endometrium had a mean DNA content of 19523 +/- 6092 ng/mg, whilst decellularised sow endometrial ECM had a DNA content of 522.9 +/- 325.7 ng/mg (Figure 2.11a). This correlated to an average reduction in DNA content of 96.64 +/- 3.304 % (Figure 2.11b).

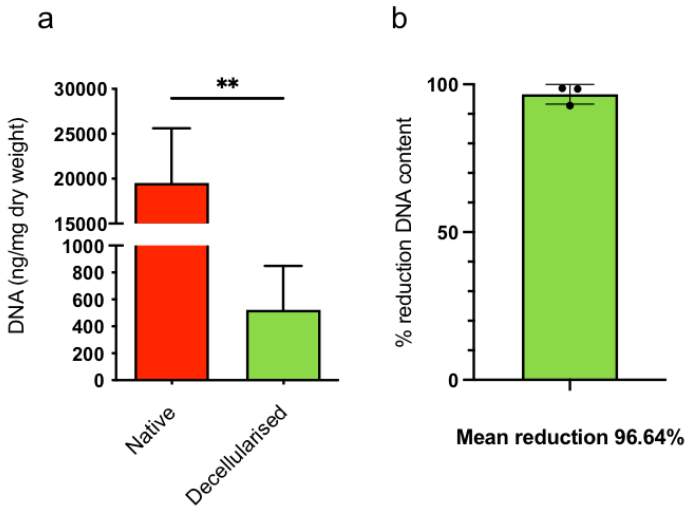


Figure 2.11 DNA content and decellularisation efficiency of sow endometrial ECM. a DNA content (ng/mg dry weight) of native sow endometrium (N = 3, n = 3) compared to decellularised sow endometrial ECM (N = 3, n = 3), prepared with decellularisation protocol version 1. The mean DNA content of decellularised ECM was significantly reduced compared to native (p = 0.0057). **b** The mean reduction in DNA content between native sow endometrium and decellularised endometrial ECM was 96.64 +/- 3.304 %. N = biological replicates, n = technical replicates per Picogreen experiment.

2.4.2.3 Histology and DAPI staining of native and decellularised pig endometrium

Sections of native pig endometrium and pig endometrial ECM at the end of the full decellularisation protocol were stained with H&E, Masson's trichrome or DAPI (Figure 2.12). Abundant nuclei were seen throughout the native endometrium in the H&E and DAPI stained sections. By contrast in the decellularised endometrial ECM sections, no visible nuclei were seen in the H&E stain and scanty DAPI staining was detected. In the Masson's trichrome stained sections, blue staining correlates to collagen and it can be clearly seen that the collagen matrix was preserved in decellularised endometrial ECM.

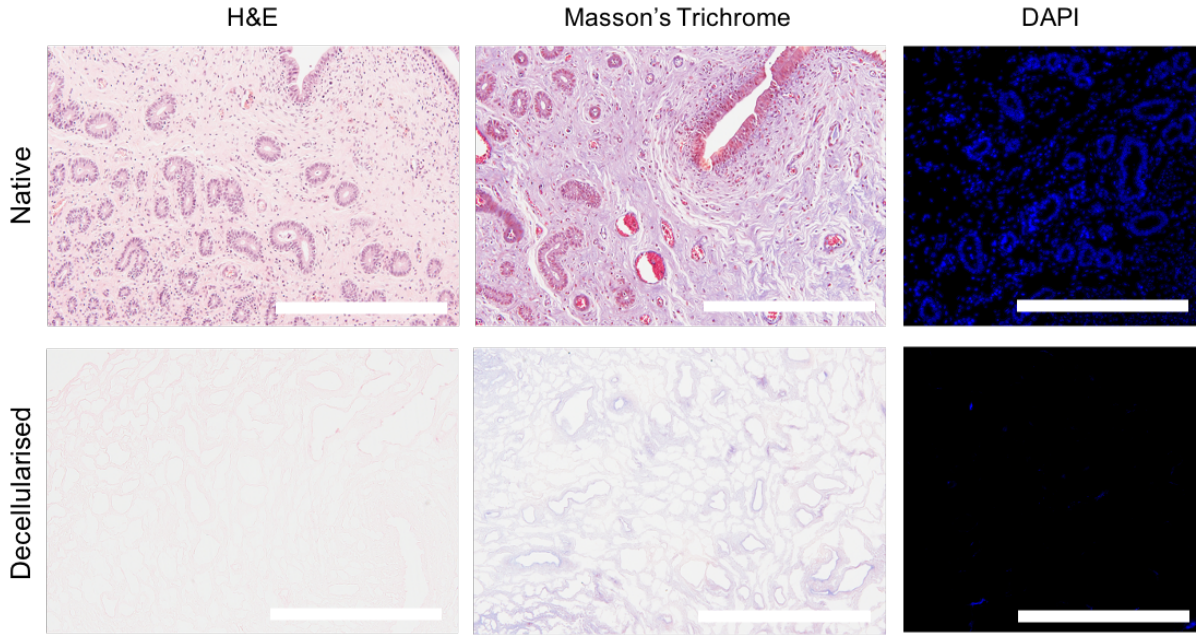


Figure 2.12 H&E, Masson's Trichrome and DAPI staining of native and decellularised pig endometrium. **Top row**: Representative H&E, Masson's trichrome and DAPI staining of native pig endometrium. Abundant nuclei are seen throughout the tissue section. **Bottom row**: Representative H&E, Masson's trichrome and DAPI staining of decellularised pig endometrial ECM showing scanty or no visible nuclei. Decellularised ECM were prepared following decellularisation protocol version 2. Images captured with 10x lens objective. Scale bars = 500 μm.

2.4.2.4 DNA content of pig endometrial ECM

Native pig endometrial ECM had a mean DNA content of 19793 +/- 7530 ng/mg dry weight and decellularised pig endometrial ECM had a mean DNA content 170.4 +/- 190.2 ng/mg dry weight (Figure 2.13a), corresponding to an average 98.85 +/- 1.004 % reduction in DNA (Figure 2.13b). Optimising the decellularisation protocol for pig endometrial ECM, by performing all reagent steps under intense agitation and carrying out the DNAse I step at 37 ^{o}C, improved the decellularisation efficiency compared to the original sow endometrial decellularisation protocol (Figure 2.13c).

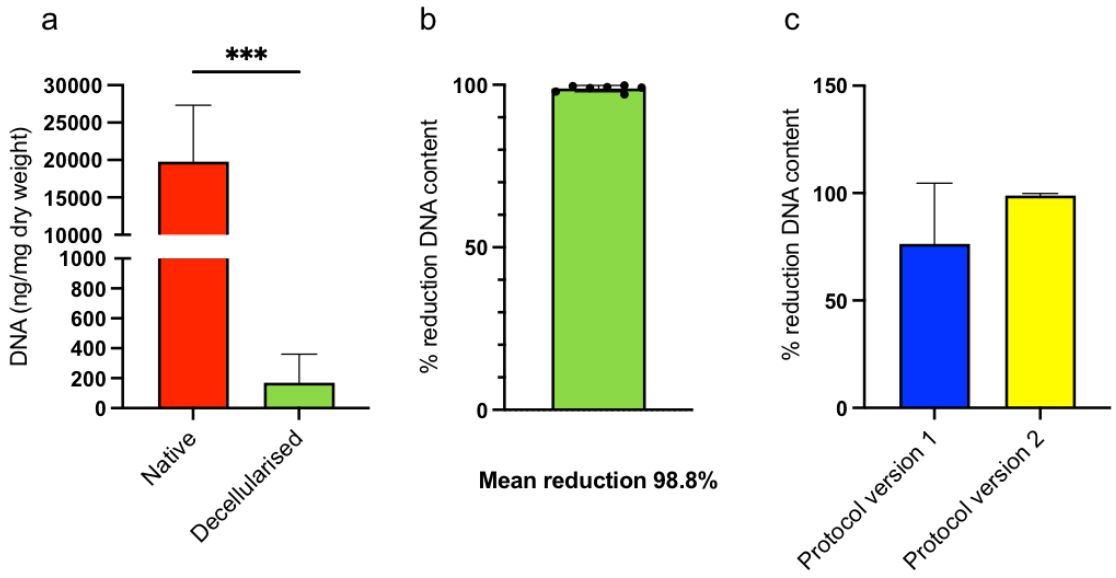


Figure 2.13 DNA content and decellularisation efficiency of pig endometrial ECM. a DNA content (ng/mg dry weight) of native pig endometrium (N = 3, n = 3) compared to decellularised pig endometrial ECM (N = 6, n = 3), prepared following decellularisation protocol version 2. The mean DNA content of decellularised ECM was significantly reduced compared to native (p = 0.0002). **b** The mean reduction in DNA content between native pig endometrium and decellularised endometrial ECM was 98.85 +/- 1.004 %. **C** Reduction in mean DNA content was improved from 76.39% using decellularisation protocol version 1 (N = 2, n = 3) to 98.95% with protocol version 2 (N = 6, n =3). N = biological replicates, n = technical replicates per Picogreen experiment.

2.4.3 Characterisation of decellularised endometrial ECM

2.4.3.1 Immunofluorescence of ECM proteins

Although the optimized endometrial decellularization protocol was highly effective at removing cells and nuclear material, each step in the process can cause protein denaturation. It was therefore important to assess whether key ECM proteins were preserved in the decellularized tissue. Sections of native sow endometrium and sow endometrial ECM were stained with collagen I, fibronectin, collagen IV and laminin antibodies then counterstained with a secondary fluorescent antibody. Figure 2.14 shows the presence of these ECM proteins in the native sow endometrial tissue, which were retained in the decellularized sow endometrial ECM. Collagen I and fibronectin are abundant and ubiquitous ECM proteins in endometrial tissue. In the decellularised sow endometrium, the

immunostaining demonstrated the preservation of the collagen I and fibronectin matrix. Collagen IV and laminin are key components of the basement membrane. In the native endometrium, positive staining for collagen IV could be seen clearly around blood vessels and laminin staining was seen surrounding the endometrial glands (Figure 2.14a). Collagen IV and laminin were preserved in the decellularised endometrial ECM, which is important as these basement membrane proteins play an important role in cell attachment, proliferation and differentiation [189]. Figure 2.14b shows a comparable panel of immunostaining for the four ECM proteins in native and decellularised pig endometrium showing similar patterns of protein distribution in the native tissue as in the sow endometrium, and good preservation of the proteins in the decellularised ECM.

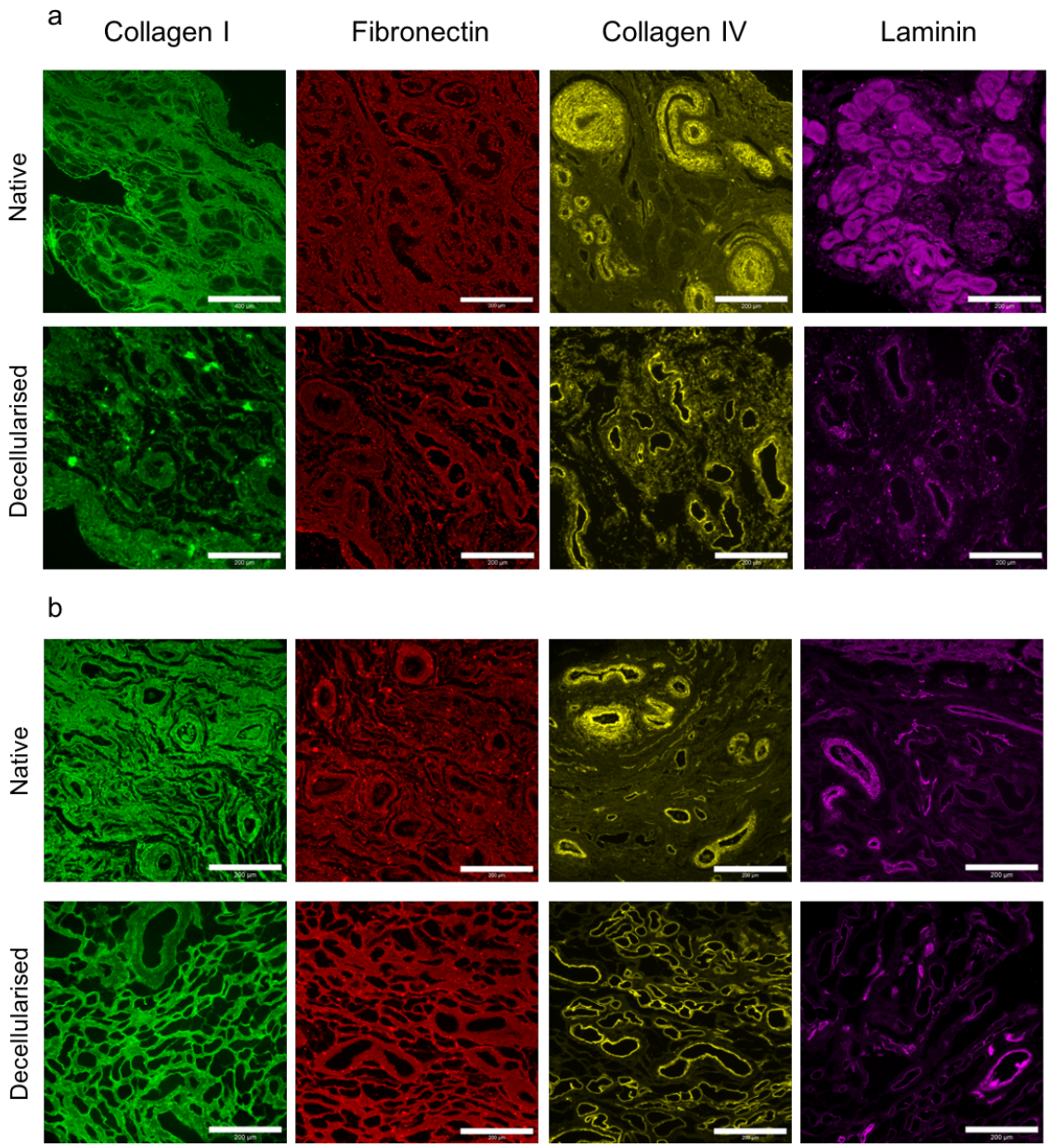


Figure 2.14 Immunofluorescence of ECM proteins in native and decellularised sow and pig endometrium. **a** Sow endometrium and decellularised ECM. **b** Pig endometrium and decellularised ECM. Collagen I, fibronectin, collagen IV and laminin were stained for in the native endometrium and decellularised endometrial ECM in sow (**a**) and pig (**b**). However, the staining abundance and intensity of collagen IV and, particularly, laminin appear lower in the decellularised ECMs in both sow and pig, suggesting some compromise to these proteins during the decellularisation process. Images captured with 20x lens objective. Pseudo-colour applied in ImageJ. Scale bar = 200 μm

2.4.3.2 Raman spectroscopy of endometrial ECM

Raman spectroscopy was performed on decellularised sow and pig endometrial ECM. Raman spectroscopy is a label-free vibrational technique, where Raman scattered light generates a spectrum with peaks that correspond to different molecular bonds. Peaks at different Raman shifts give information about the functional groups within biomolecules and the spectrum serves as a biochemical fingerprint of a biological sample.

The Raman spectral information was assessed to gain insight into the biochemical composition of the ECM and a qualitative comparison was made between the Raman spectra of sow endometrial ECM and other decellularised ECM types (Figure 2.15). A speculative comparison was drawn between sow and pig endometrial ECM (Figure 2.16). Quantitative and multivariate analyses could not be performed to compare sow and pig endometrial ECM as the data was acquired with different lasers in two separate experiments. Raman peak assignments (Table 2.5) were cited from Movasaghi et al. (2007), who published a comprehensive list of spectral assignments relevant to biological tissues [190].

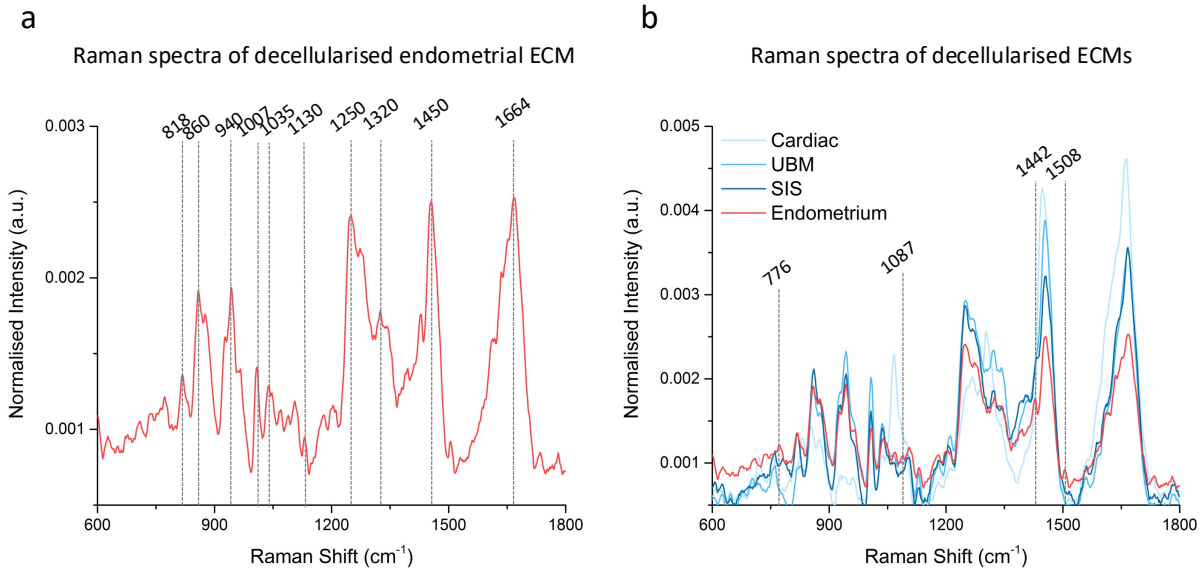


Figure 2.15 Raman spectra of decellularised endometrial sow ECM and other decellularised ECMs. **a** Raman spectra of sow endometrial ECM. Highlighted peaks are those common to other ECMs (818 cm^{-1}, 860 cm^{-1}, 940 cm^{-1}, 1007 cm^{-1}, 1035 cm^{-1}, 1130 cm^{-1}, 1250 cm^{-1}, 1320 cm^{-1}, 1450 cm^{-1}, 1664 cm^{-1}) (see table 2.5 for peak assignments). **B** Raman spectra of sow endometrial ECM overlaid with the spectra of SIS, UBM and cardiac ECMs. Highlighted peaks are those unique to sow endometrial ECM (776 cm^{-1}, 1087 cm^{-1}, 1442 cm^{-1}, 1508 cm^{-1}). Data collected by Dr Conor Horgan.

The Raman spectra of sow endometrial ECM had many similarities to SIS and UBM ECMs, sharing common peaks assigned to collagen (818 cm^{-1}, 1035 cm^{-1}, 1319/1320 cm^{-1}), phosphate (860 cm^{-1}), polysaccharides (940 cm^{-1}), phenylalanine (1007 cm^{-1}), lipids (1130 cm^{-1}, 1450 cm^{-1}) and protein (1250 cm^{-1}, 1664 cm^{-1}) (Figure 2.15a). Endometrial, SIS and UBM were more closely alike in Raman spectra than cardiac ECM, which was distinctly different (Figure 2.15b). This perhaps represents the difference in type of tissue, as cardiac ECM is derived from the muscular myocardium, whilst the endometrium, SIS and UBM are all mucosal tissues. Several peaks were unique to sow endometrial ECM and these mostly corresponded to lipids, such as phosphatidylinositol or fatty acids (776 cm^{-1}, 1087 cm^{-1}, 1442 cm^{-1}) (Figure 2.15b). Interestingly these peaks that were unique to sow endometrial ECM, when compared to other ECMs, were not seen in pig endometrial ECM (Figure 2.16). Figure 2.16 shows the Raman spectra of decellularised pig endometrial ECM. Highlighted in black are the peaks common to both sow and pig endometrial ECM and in blue are peaks that appeared to be unique to pig endometrial ECM only. The peaks that were seen in pig endometrial but not sow endometrial ECM corresponded to tryptophan (760 cm^{-1}) and palmitic acid or fatty acid (1065 cm^{-1}).

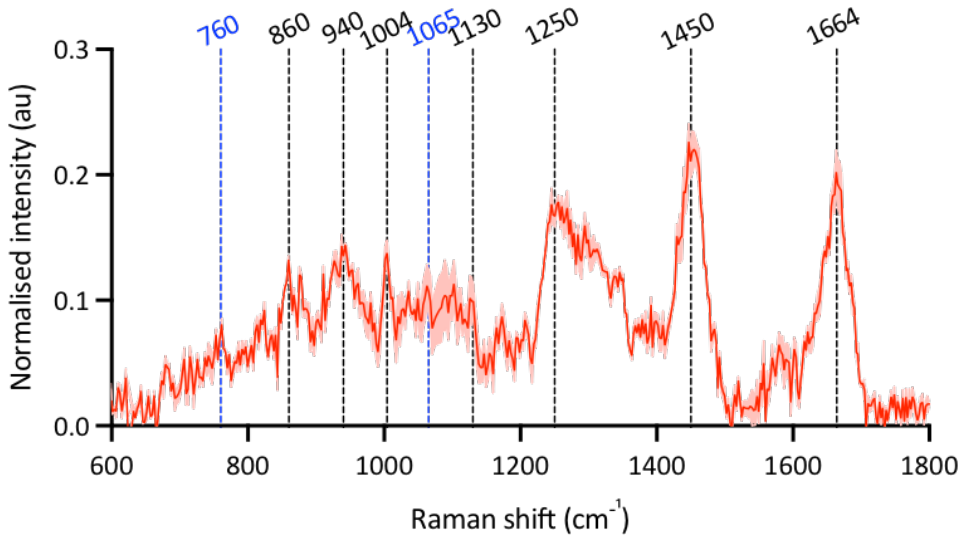


Figure 2.16 Raman spectra of pig endometrial ECM. Highlighted peaks in black are those common to both sow and pig endometrial ECM (860 cm^{-1}, 940 cm^{-1}, 1004 cm^{-1}, 1130 cm^{-1}, 1250 cm^{-1}, 1450 cm^{-1}, 1664 cm^{-1}). In blue are peaks that are unique to pig endometrial ECM (760 cm^{-1}, 1065 cm^{-1}) See table 2.5 for peak assignments. Data collected with the assistance of Dr Vernon Lalone.

Table 2.5: Tentative Raman peak assignments relative to biological tissues, from Movasaghi et al. (2007) [190]

Peak (cm^{-1})	Tentative assignment	Peak (cm^{-1})	Tentative assignment
760	Tryptophan	1087	Lipid
776	Phosphatidylinositol	1130	Phospholipid structural changes
818	Collagen	1250	Amide III, guanine, cytosine (NH_2)
860	Phosphate group, phosphatidic acid	1319/1320	Guanine, CH_3CH_2 twisting (Collagen)/G (DNA/RNA), CH deformation (proteins)
940	Skeletal modes (polysaccharides amylose), (polysaccharides, amylopectin)	1442	Fatty acids/ Triglycerides (fatty acids)/ CH_3, CH_2 deformation (collagen)
1007	Phenylalanine	1450	Lipids
1035	Collagen	1508	Cytosine
1065	Palmitic acid/fatty acid	1664	Amide I

2.4.3.3 Proteomics

Two pig endometrial ECM samples were prepared for proteomics analysis as described in section 2.3.3.4. In total, 370 proteins were identified with a combination of cellular and extracellular proteins and of these 98 proteins were common to both fractions 4 and 5 and in both biological replicates.

A few proteins were unidentified within the UniProt Homo Sapiens and Sus Scrofa databases. In total 367 proteins had corresponding gene names and these were submitted to ShinyGO to determine the top 20 most enriched GO_BP (Figure 2.17) and GO_MF terms (Figure 2.18). The most enriched GO biological process for all the genes was the term “SRP-dependent cotranslational protein-membrane targeting”, followed by the term “ribosomal large subunit biogenesis” (Figure 2.17). These relate to cellular processes involved in protein translation and ribosome synthesis. The third and sixth most enriched GO_BP terms were “collagen fibril organisation” and “extracellular matrix organisation”, showing that these matrisome-related processes are also highly relevant amongst all of the proteins identified in the endometrial ECM samples (Figure 2.17). Amongst the top 10 most enriched biological processes was “wound healing”, which is important considering the intended uses for decellularised endometrial ECM. For GO molecular functions, the most enriched term was “structural molecule activity conferring elasticity” and the third most enriched was “extracellular matrix structural

constituent conferring tensile strength" (Figure 2.18). Amongst the top 10 most enriched GO_MF terms, there was also "extracellular matrix structural constituent", indicating that the proteins identified within endometrial ECM are highly related to ECM functions.

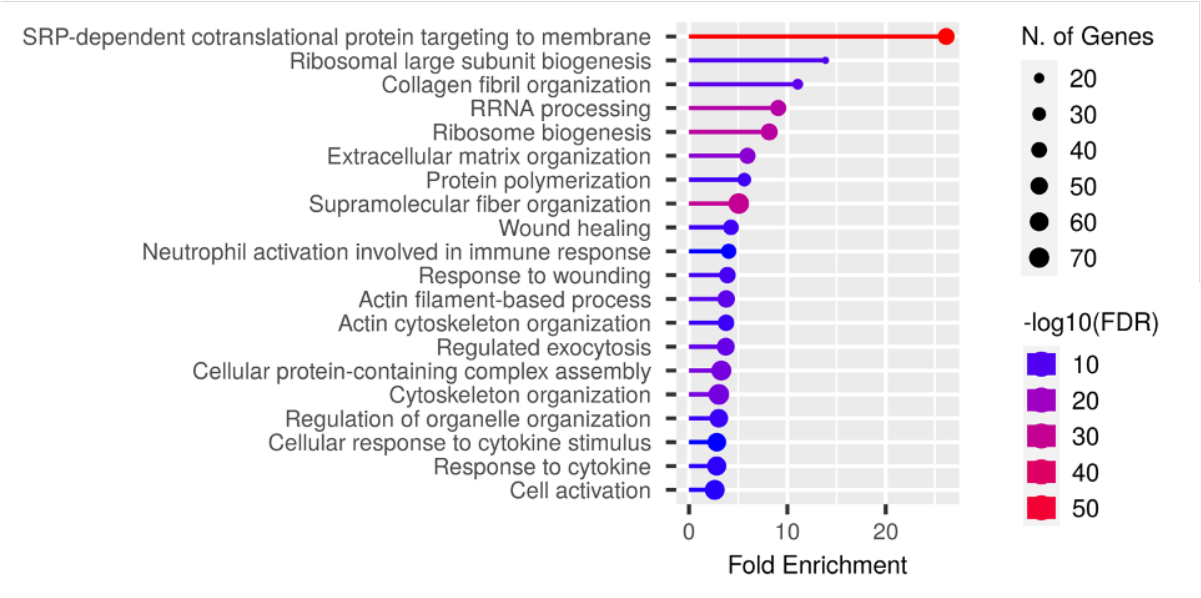


Figure 2.17 GOBP gene ontology enrichment analysis of full list of endometrial ECM proteins. Top 20 gene ontology biological process terms that were enriched for the endometrial ECM proteins were ranked from most (top) to least (bottom) enriched. The size of the circle correlates to the number of genes identified that were related to that GOBP term. Figure produced in ShinyGo (version 0.76), an open-source gene ontology analysis platform.

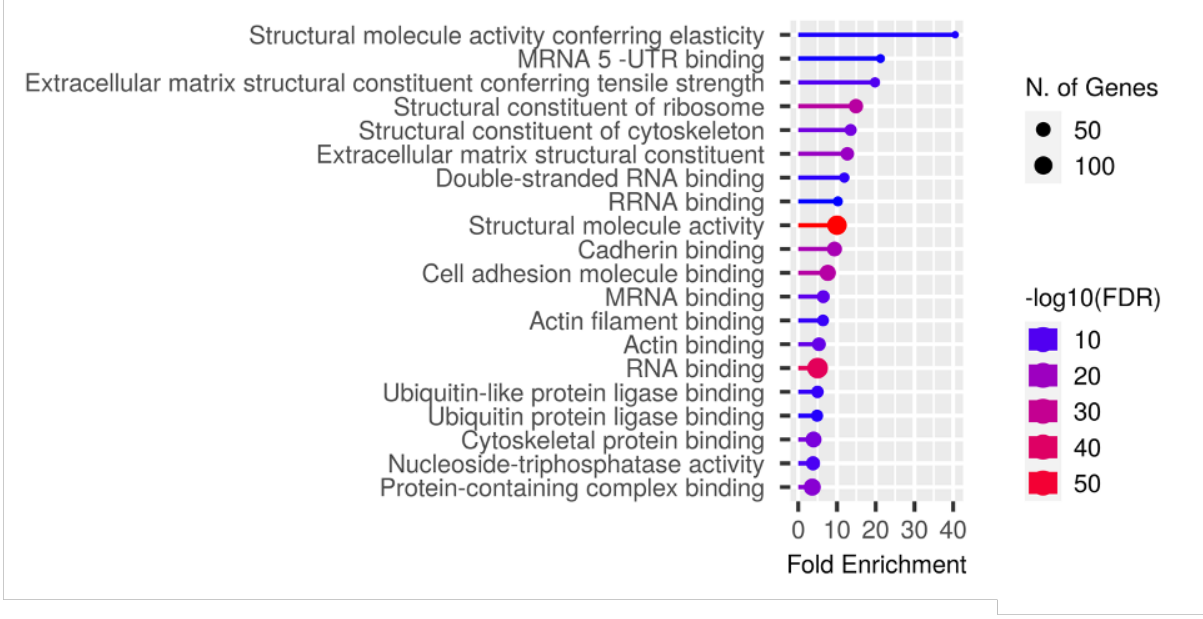


Figure 2.18 GOMF gene ontology enrichment analysis of full list of endometrial ECM proteins. Top 20 gene ontology molecular functions terms that were enriched for the endometrial ECM proteins were ranked from most (top) to least (bottom) enriched. The size of the circle correlates to the number of genes identified that were related to that GOBP term. Figure produced in ShinyGo (version 0.76), an open-source gene ontology analysis platform.

After performing functional annotation clustering of all genes in DAVID, 52 genes were initially identified in the gene ontology cluster of ECM-related cellular components, biological processes and molecular functions. Unexpectedly, this cluster also included genes relevant to endoplasmic reticulum lumen; these were excluded as it was felt that they were unrelated to ECM constituents and processes, leaving 43 genes with direct relevance to the matrisome (Figure 2.19). Among these were core ECM structural proteins; collagens, fibronectin and laminin and elastin. There were also genes corresponding to proteoglycans such as heparan sulfate and small leucine-rich proteoglycans including biglycan, lumican, decorin and fibromodulin. Figure 2.19 lists the ECM-related genes and the functions they relate to, such as collagen fibril organisation and ECM matrix organisation, as determined by DAVID functional annotation clustering analysis. The matrisome genes list was submitted to ShinyGO to visualise the top 20 most enriched GO_BP (Figure 2.20) and GO_MF terms (Figure 2.21).

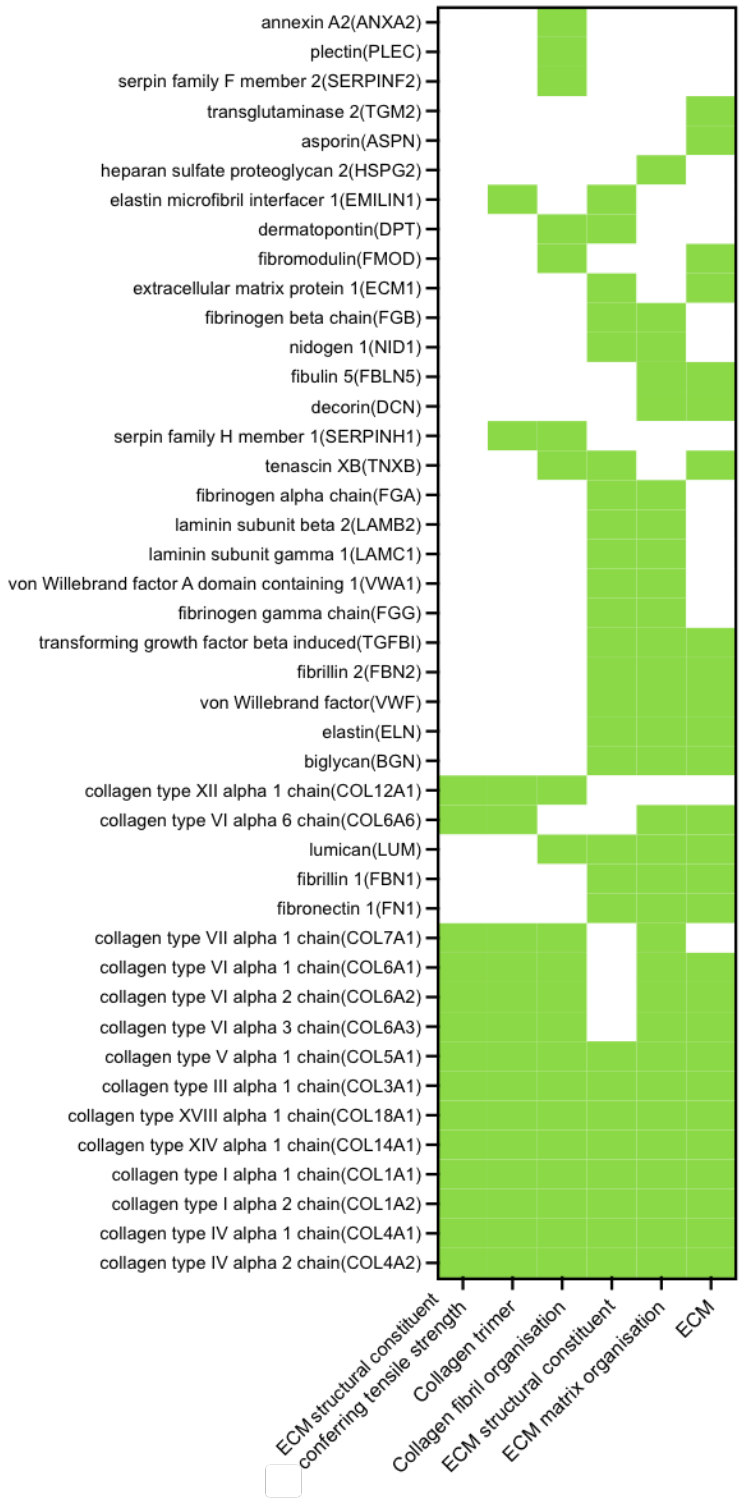


Figure 2.19 Proteomics analysis – gene list of matrisome proteins. Matrisome proteins were identified by functional annotation clustering of all endometrial ECM genes in DAVID, to select the cluster that was enriched for ECM-related GOBP, GOMF and GOCC terms. All the genes within that cluster were considered the matrisome genes / proteins. The x-axis shows the ECM-related processes, and the y-axis shows the full list of matrisome genes. Correlation between the gene and an ECM-related process is denoted by a box shaded in green.

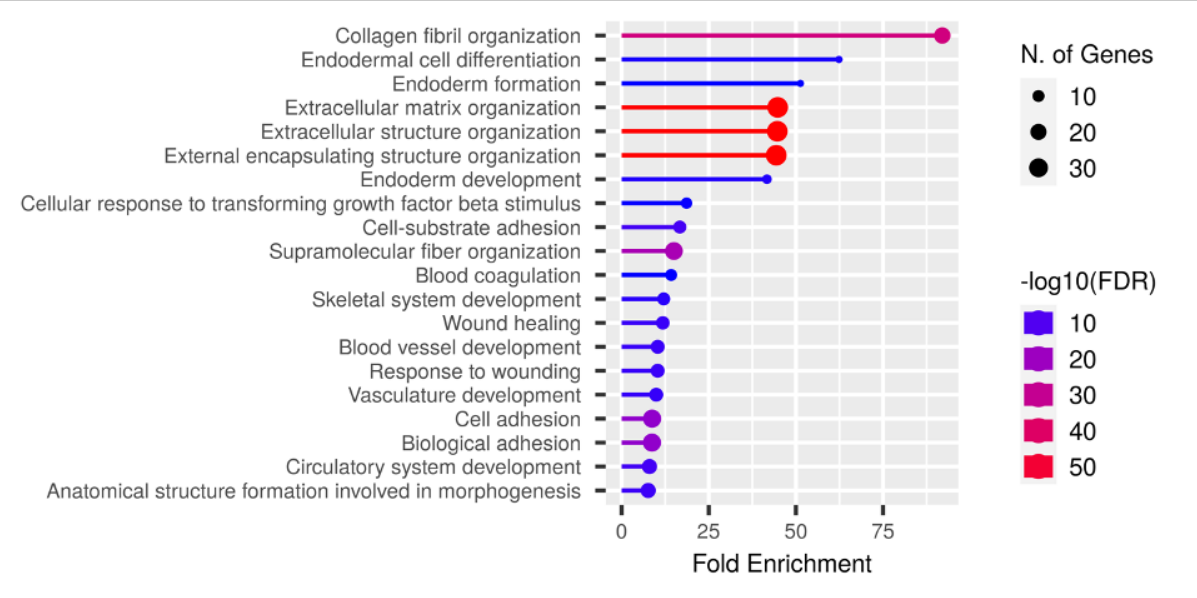


Figure 2.20 GOBP gene ontology enrichment analysis for endometrial ECM matrisome proteins. Top 20 gene ontology biological process terms that were enriched for the matrisome proteins were ranked from most (top) to least (bottom) enriched. The size of the circle correlates to the number of genes identified that were related to that GOBP term. Figure produced in ShinyGo (version 0.76), an open-source gene ontology analysis platform.

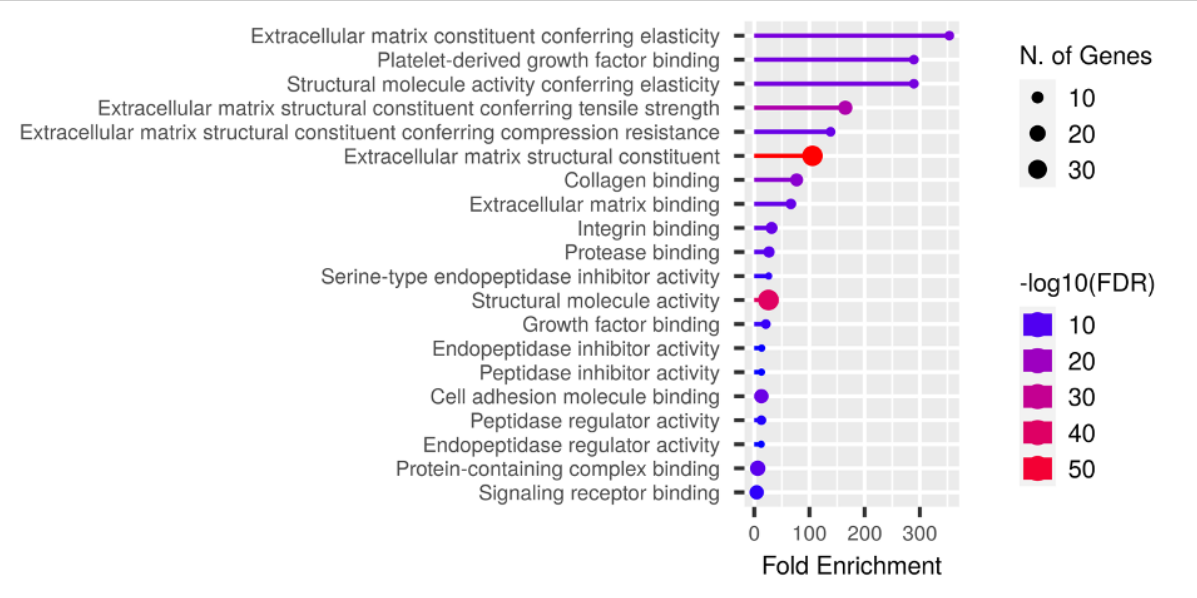


Figure 2.21 GOMF gene ontology enrichment analysis for endometrial ECM matrisome proteins. Top 20 gene ontology for molecular functions terms that were enriched for the matrisome proteins were ranked from most (top) to least (bottom) enriched. The size of the circle correlates to the number of genes identified that were related to that GOBP term. Figure produced in ShinyGo (version 0.76), an open-source gene ontology analysis platform.

2.4.4 Matrix-bound vesicles

2.4.4.1 Decellularised endometrial ECM contains exosome-like matrix-bound vesicles

Decellularised and lyophilised endometrial ECM was digested with collagenase and a SEC-based method was used to collect 30 fractions. Each fraction was then assessed for nanoparticle concentration by NTA, protein concentration by micro-BCA assay and for presence of CD63, CD81 and CD9 by dot-blotting (Figure 2.22). Three different biological replicates (endometrial ECM from 3 different pigs) were analysed. The NTA results showed that there was a large peak in particle concentration between fractions 8-13, with the highest mean total particle count at fraction 9 (1.89×10^{10} +/- 5.77×10^{9}) (Figure 2.22a). The particle peak at fractions 8-13 correlated with low protein concentrations (26.06 +/- 8.708 μg/mL), whilst the expected protein-rich fractions (18-24) displayed high protein concentrations (332.6 +/- 115.9 μg/mL) (Figure 2.22a). The separation between the particle peak and the protein peak is a pattern characteristic of EV isolation by size exclusion chromatography, where the protein contaminants are separated from the EV fractions [182]. In fractions 9 and 10 (the height of the EV peak), the majority of particles were between 50 to 250 nm in size (Figure 2.22b) and in fractions 8-13, the mean particle size was 197 +/- 33.36 nm. This fits with the size range for exosomes and microvesicles in typical EV classifications [174]. Dot blotting revealed that in fractions 8-16, there was expression of exosome markers CD63, CD9 and CD81, which were not detected in the low and high fraction numbers (Figure 2.22c).

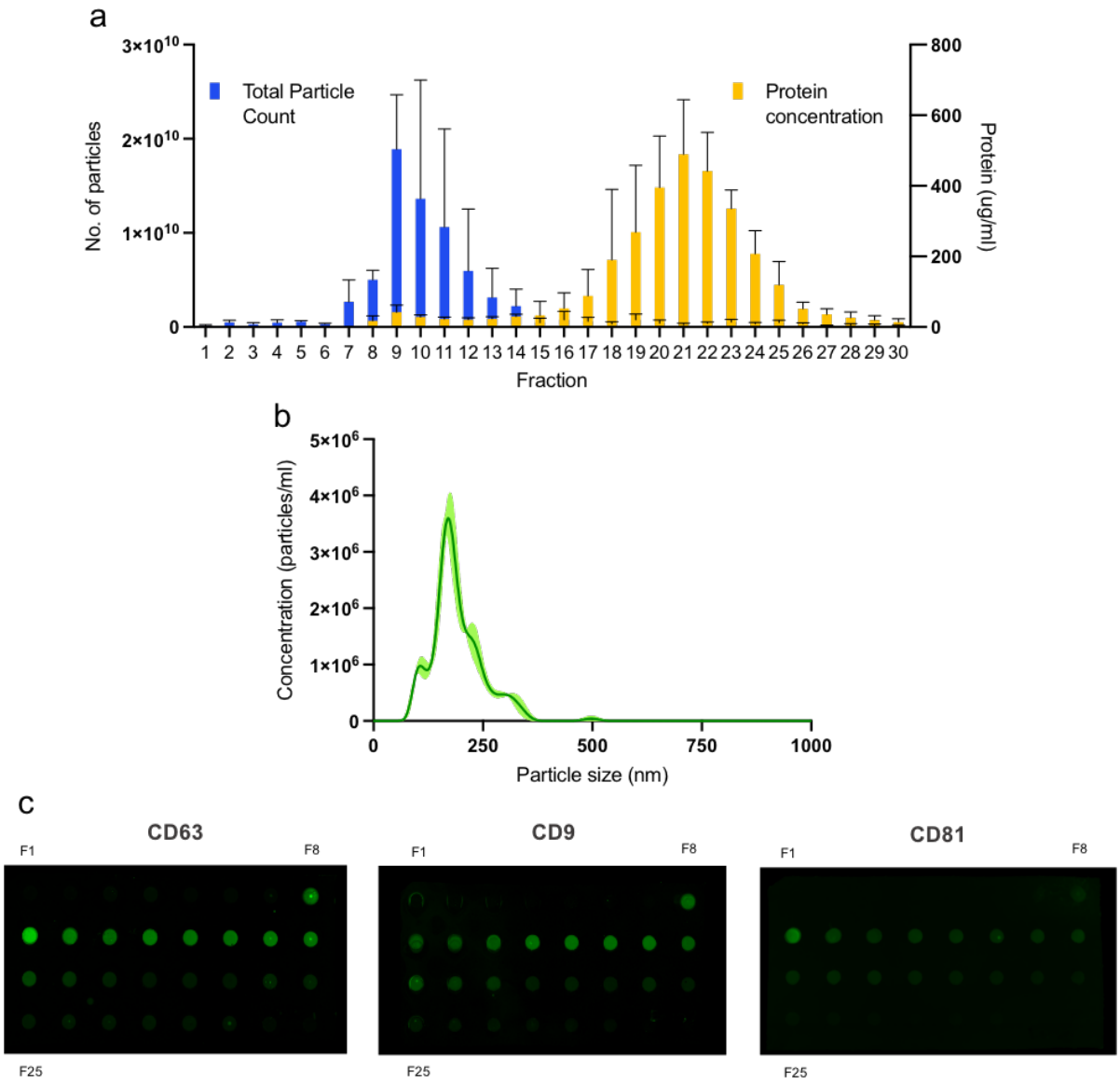


Figure 2.22 Endometrial MBV analysis. **A** NTA analysis and micro-BCA protein assay for fractions 1-30 (N = 3). In blue is the particle count (left y-axis) and in yellow is the protein concentration (right y-axis). The MBV fractions are identified as the peak in particle concentration from fractions 8-13. **B** The distribution of particles from 0 – 1000 nm for fraction 10 (N = 3). **C** CD63, CD9 and CD81 dot blots for pooled EV fractions for all 3 biological replicates. Positive staining is seen in fractions 8-16.

2.4.4.2 Raman spectroscopic analysis of endometrial MBV

The MBV fractions were pooled and analysed by Raman spectroscopy using single particle automated Raman trapping analysis (SPARTA®) (Figure 2.23). The Raman spectra for endometrial ECM-derived

MBVs showed the presence of a number of significant peaks that correspond to nucleic acids, lipids and protein (Figure 2.23a). Key protein signals include bands at 851 cm^{-1} (proline/tyrosine), 1004 cm^{-1} (phenylalanine), 1128 cm^{-1} (C-N stretch), 1245-68 cm^{-1} (amide) and 1667 cm^{-1} (amide). The main lipids bands are at 1062 cm^{-1} (C-C stretch), 1296 cm^{-1} (CH2 twist) and 1445 cm^{-1} (CH2 bend) and nucleic acid signatures at 828 cm^{-1} (O-P-O stretch, 1085 cm^{-1} (PO2-), 1321-44 cm^{-1} (guanine) (Figure 2.23a). When compared with the Raman spectra for HEK293F Evs, mostly the same peaks are observed, though with different signal intensities (Figure 2.23b). A notable difference between the endometrial MBV spectra and EV spectra is the absence of the cholesterol (698 cm^{-1}) and phosphatidylcholine (715 cm^{-1}) peaks in the MBVs, which could signify differences in the membrane composition between the Evs and MBVs. Another point of interest is that the Evs have lower average signal at the 927 and 1268 cm^{-1}, peaks which may correspond to collagen content. This could indicate the stronger presence of collagen in MBVs and may relate to the differences in source of Evs versus MBVs.

The Raman spectra of endometrial MBV were also compared to that of dura MBV (Figure 2.23c), to observe for potential biochemical differences in MBV isolated from different tissue sources. The peaks observed were mostly similar between the two different MBV types, however there were differences in some of the peak intensities, such as at 877 cm^{-1} which was higher in dura MBV and likely corresponds to positively charged lipid content. Compared to dura MBV, endometrial MBV had higher signal intensity at 1004 cm^{-1} (phenylalanine) and lower signal intensities at 1085 cm^{-1} (PO_2^- nucleic acids, lipid) and 1296 cm^{-1} (CH2 twist, lipid). Dura MBV also had a peak at 1372 cm^{-1} (nucleic acids) which was absent in endometrial ECM. The spectral data suggests that there are some biochemical differences between endometrial and dura MBVs and that endometrial MBVs are potentially less lipid-rich and contain lower amounts of nucleic acids. These differences could also reflect differences in decellularisation protocol.

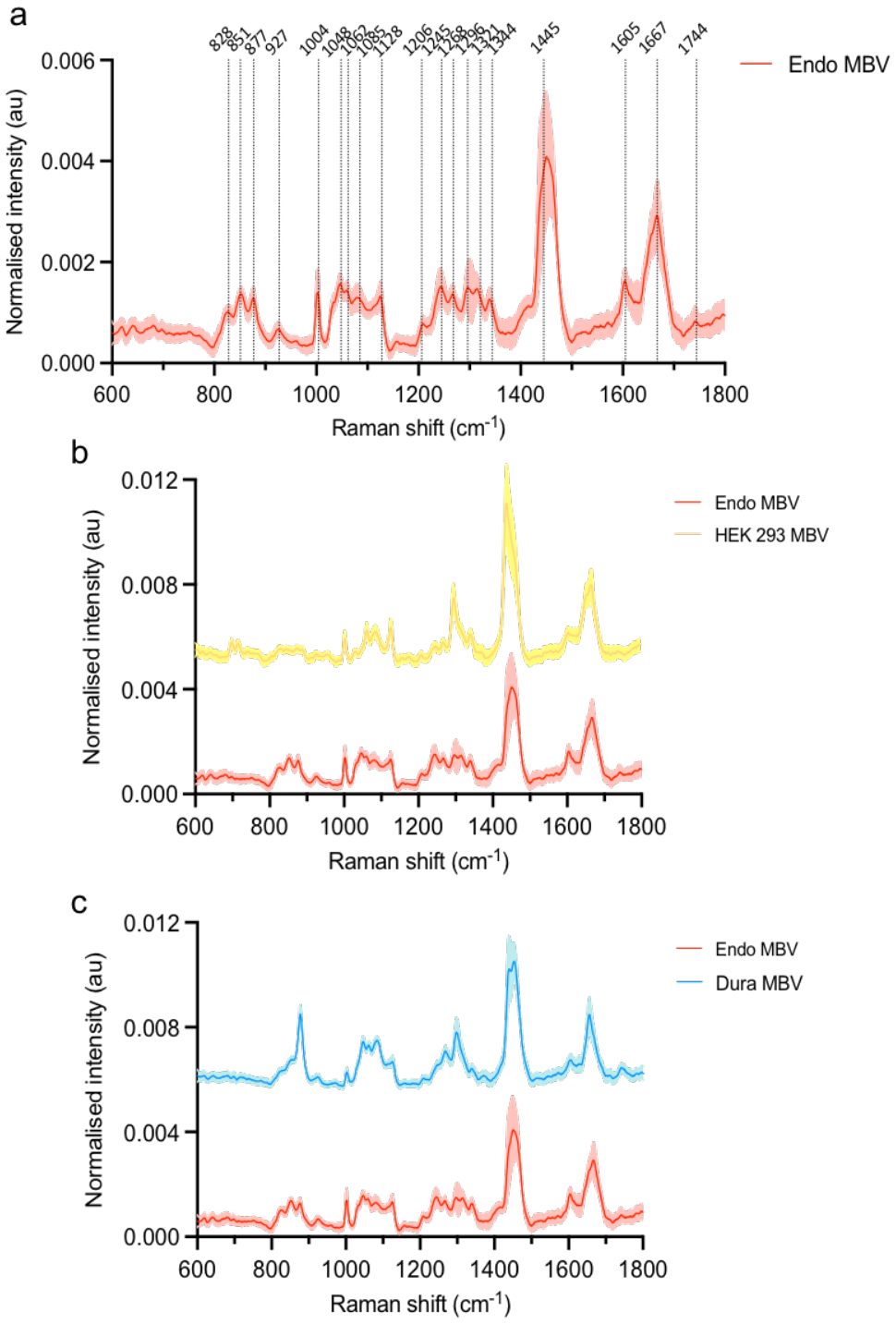


Figure 2.23 Raman spectra of MBVs acquired by single particle automated Raman trapping analysis (SPARTA®). A Raman spectrum of endometrial ECM MBV. The solid line represents the mean spectrum and the shaded area represents the standard deviation (N = 3). The main peaks are highlighted (828 cm^{-1}, 851 cm^{-1}, 877 cm^{-1}, 927 cm^{-1}, 1004 cm^{-1}, 1048 cm^{-1}, 1062 cm^{-1}, 1085 cm^{-1}, 1128 cm^{-1}, 1206 cm^{-1}, 1245 cm^{-1}, 1268 cm^{-1}, 1296 cm^{-1}, 1321 cm^{-1}, 1344 cm^{-1}, 1445 cm^{-1}, 1605 cm^{-1}, 1667 cm^{-1}, 1744 cm^{-1}). See table 2.6 for peak assignments. **B** Raman spectra of endometrial ECM MBV (red) and HEK 293 cell-derived EV (yellow). **C** Raman spectra of endometrial ECM MBV (red) and Dura ECM MBV (blue).

Table 2.6: Tentative Raman peak assignments relative to MBVs, from Movasaghi et al. (2007) [190]

Peak (cm^{-1})	Tentative assignment	Peak (cm^{-1})	Tentative assignment
698	Cholesterol	1206	Collagen, A,T ring, tyrosine
715	C-N phospholipid head, choline	1245	Amide III
828	O-P-O stretch DNA/RNA	1268	Amide III, collagen
851	Protein (proline/tyrosine)	1296	CH_2 twist
877	C-C-N+ lipid, C-O-C, tryptophan	1321	Guanine, amide III protein
927	Proline C-C stretch, collagen	1344	Guanine, nucleic acid
1004	Phenylalanine	1372	T,A,G ring breathing DNA/RNA
1048	Phosphate stretch	1445	CH_2 bend,lipids
1062	C-C stretch, lipid, PO_2^- stretch DNA	1605	Phenylalanine, cytosine, tyrosine
1085	PO_2^- nucleic acids, lipid	1667	Amide I, collagen carbonyl stretch
1128	C-N stretch proteins	1744	Carbonyl, ester

Principal component analysis (PCA) and partial least squares discriminant analysis (PLSDA) were performed on the spectral data sets from endometrial MBV, dura MBV and HEK293 Evs (Figure 2.24). PCA revealed distinct clustering of the three different samples, with greatest cluster separation according to the PC2 scores. The PC2 pseudo-spectrum has prominent peaks at 877 cm^{-1} (lipid), 1048 cm^{-1} (phosphate, glycogen) and 1455 cm^{-1} (lipid), indicating that these are the main biochemical differences between the samples (Figure 2.24). Visually, the two MBV clusters appear closer to each other and more distinct from the EV cluster, suggesting that there are greater similarities between the MBVs compared to the MBV and Evs. The PLSDA model, a supervised technique, was able to distinguish between the three samples with a greater than 99% sensitivity and specificity. Similar to PCA, obvious clustering of the three samples was seen and the clusters were most differentiated by LV2, which has a close resemblance to the PC2 pseudo-spectrum (Figure 2.25). Of note, the pseudo-spectra of LVs in PLSDA can appear inverted and feature negative peaks but the Raman shift of the peaks remain the same and peak intensity can be interpreted as the size of negative or positive deflection from 0 at the y-axis.

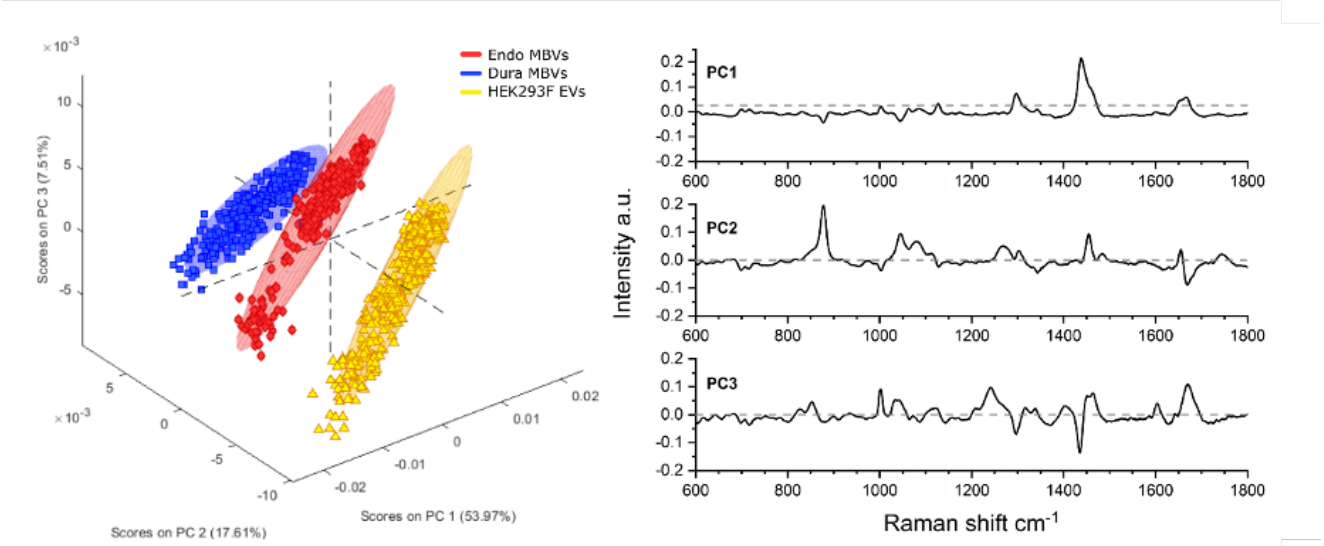


Figure 2.24 Principal component analysis of MBV Raman spectral data. Right: Three-dimensional PCA plot of PC1, PC2 versus PC3. Red points correspond to endometrial MBV spectral data, blue points correspond to dura MBV spectral data and yellow points correspond to EV spectral data. Each data point relates to a single Raman spectrum acquired from a single MBV or EV. PC1 accounted for 53.9% of the overall variability within the spectral data sets, PC2 accounted for 17.61% of overall variability and PC3 accounted for 7.5% of overall variability. The greatest cluster separation was seen along the PC2 axis. **Left**: PC1, PC2 and PC3 pseudo-spectra. The PC2 pseudo-spectrum has prominent peaks corresponding to lipid signals (877 cm^{-1} and 1455 cm^{-1}). Data acquisition and analysis performed by Dr Jelle Penders.

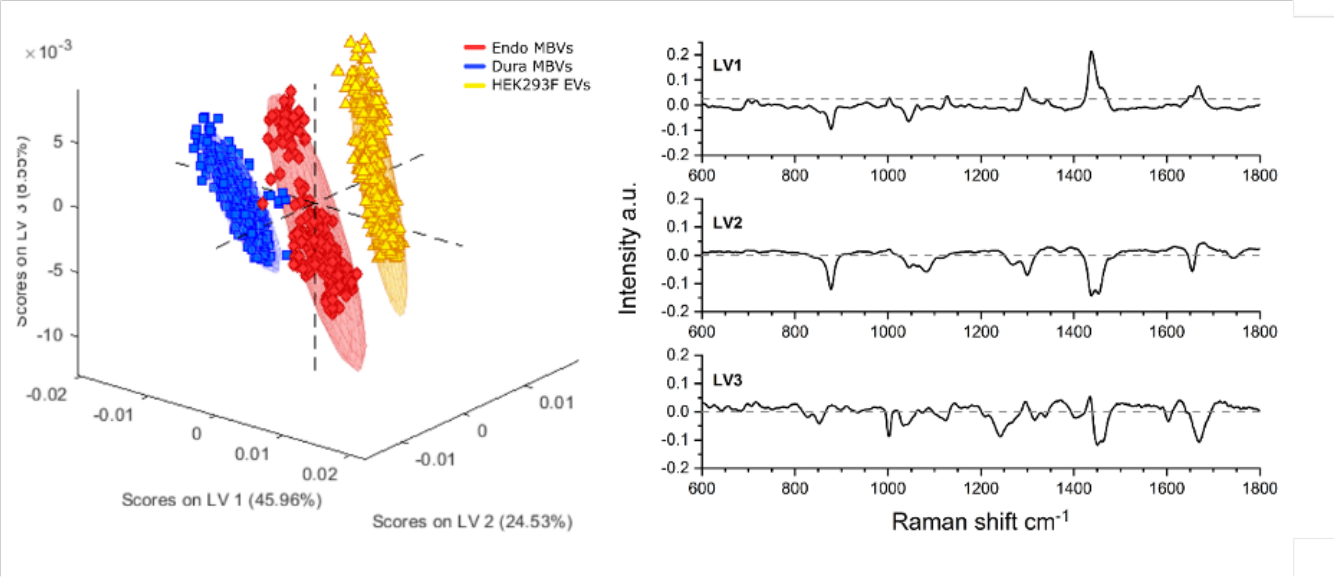


Figure 2.25 Partial least squares discriminant analysis of MBV Raman spectral data. Right: Three-dimensional plot of LV1, LV2 versus LV3. Red points correspond to endometrial MBV spectral data, blue points correspond to dura MBV spectral data and yellow points correspond to EV spectral data. Each data point relates to a single Raman spectrum acquired from a single MBV or EV. LV1 accounted for 45.96% of the overall variability within the spectral data sets, PC2 accounted for 24.53% of overall variability and PC3 accounted for 8.55% of overall variability. Similar to the PCA data, the greatest cluster separation was seen along the LV2 axis. **Left**: LV1, LV2 and LV3 pseudo-spectra, which closely resemble the pattern of the PC1, PC2 and PC3 pseu-spectra. Again, the LV2 pseudo-spectrum has prominent peaks corresponding to lipid signals (877 cm^{-1} and 1455 cm^{-1}). Data acquisition and analysis performed by Dr Jelle Penders.

2.4.5 Characterisation of endometrial ECM hydrogel

2.4.5.1 Collagen and GAG content

The collagen content was very similar between sow and pig endometrial ECM digests and between porcine endometrial, SIS and UBM digests (Figure 2.26a). However, the GAG content of pig endometrial ECM digests (0.3490 +/- 0.0028 µg / 100 µg digest, N = 3) was much lower than SIS and UBM. SIS digest had the highest GAG content (4.126 +/- 0.4569 µg / 100 µg digest, N = 2), more than twice the GAG content of UBM digest (1.844 +/- 0.5649 µg / 100 µg digest, N = 2) and more than 10 times that of endometrial ECM (Figure 2.26b). Statistical analysis was not performed as not all groups had N = 3. Unfortunately, due to insufficient samples, the GAG content of sow endometrial ECM was not measured.

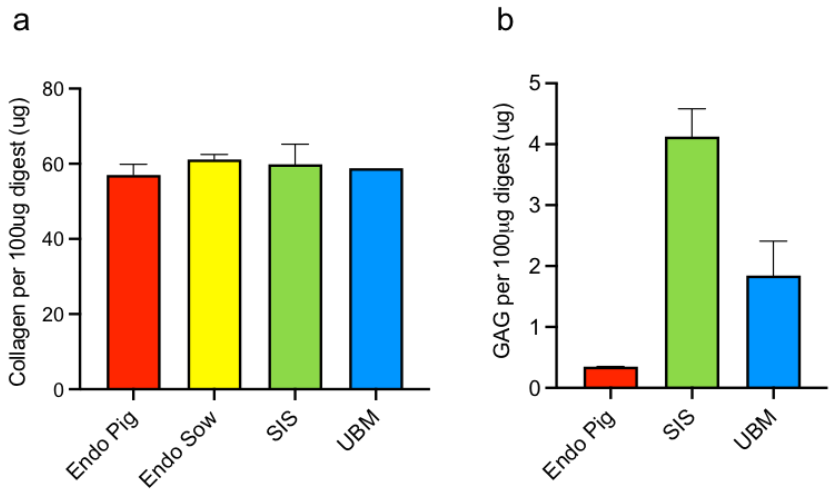


Figure 2.26 Collagen and sGAG content of ECM digests. **A** The collagen content of pig endometrial ECM (N = 3), sow endometrial ECM (N = 2), SIS ECM (N = 2) and UBM ECM (N = 1) digests is very similar. **B** The sulphated GAG content in pig endometrial ECM (N = 3) was lower than UBM (N = 2) and much lower than SIS ECM (N = 2). Statistical analysis was not performed due to there being fewer than N = 3 in some groups.

2.4.5.2 Rheology

Rheology is the study of how a material deforms and flows. Rheological experiments are commonly used to characterise the material properties of viscoelastic hydrogels. Using a parallel plate rheometer to perform oscillatory shear tests, the gelation properties of ECM hydrogels were determined and compared. G' is the storage modulus and G" is the loss modulus. When the storage modulus is significantly higher than the loss modulus, a material has more elastic properties and is gel-like. Vice versa and the material is more viscous and has properties of a fluid. Figure 2.27a shows a representative strain sweep performed on pig endometrial ECM 5 mg/mL gel at 37 °C. A strain sweep applies increasing oscillatory strain at a constant temperature and frequency. Materials have gel-like properties when the storage modulus (G') is significantly higher than the loss modulus (G") in the linear viscoelastic region, denoted by the shaded in area of the graph (Figure 2.27a). With gels, the G' starts to fall above a certain percentage strain and the gel-like structure becomes disrupted through shearing [191]. The point at which G' crosses G" is when the material transitions to being more fluid-like [191]. Figure 2.27b shows a representative frequency sweep of 5 mg/mL sow endometrial ECM hydrogel where G' remains higher than G", indicating that the material remains a gel across a range of frequencies.

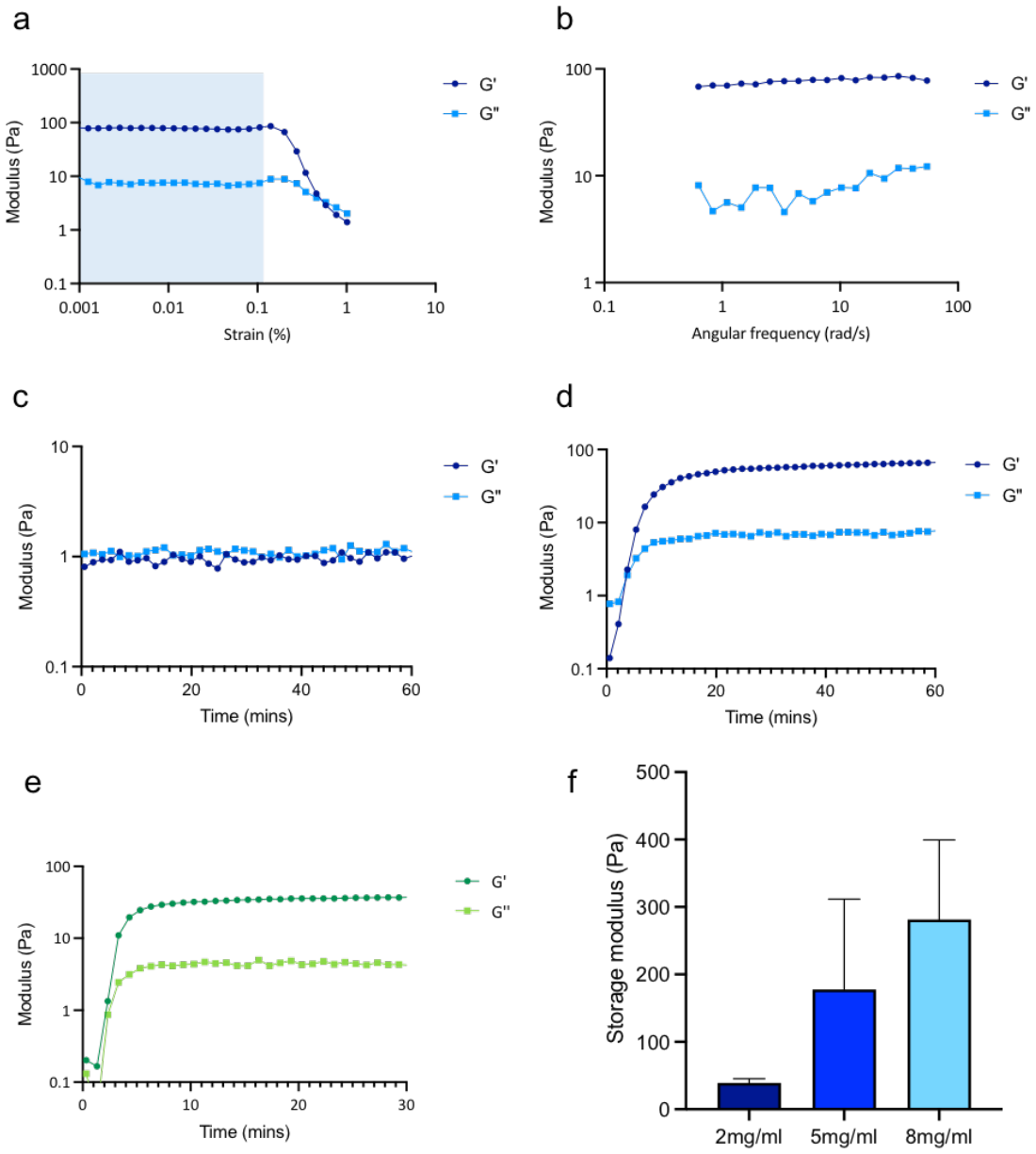


Figure 2.27 Rheology of sow endometrial ECM hydrogel. **A** Representative strain sweep of 5 mg/mL sow endometrial ECM hydrogel performed at constant frequency of 10 rad/s and constant temperature of 37°C. **b** Representative frequency sweep of 5 mg/mL sow endometrial ECM hydrogel performed at constant strain (0.1%) and constant temperature (37 °C). **c** Representative time sweep of 5 mg/mL sow endometrial ECM hydrogel performed at constant strain (0.1%) and frequency (10 rad/s) at 10°C. No gelation occurs at this low temperature over time, as the initiation of gelation only occurs at higher temperatures. **D** Representative time sweep of 5 mg/mL sow endometrial ECM hydrogel performed at constant strain (0.1%) and frequency (10 rad/s) at 37 °C. G' crosses G" within the first 5 minutes and a stable gel forms after 20 minutes. **E** Representative time sweep of 5 mg/mL SIS ECM hydrogel performed with the same parameters as for endometrial ECM hydrogel. **F** Storage modulus of sow endometrial ECM hydrogel at 2 mg/mL (N = 2), 5 mg/mL (N = 4) and 8 mg/mL (N = 2), showing concentration-dependent increase.

The temperature-dependent gelation of ECM gels is demonstrated in Figure 2.27c-d, with oscillatory time sweep tests of sow endometrial ECM 5 mg/mL gel at 10°C and at 37°C. Oscillatory time sweeps are performed at constant temperature, strain and frequency. At 10°C, the loss modulus (G") is not significantly different from the storage modulus (G') and there is no change in either G' or G" with time, indicating a viscous material (Figure 2.27c). At 37 °C, initially the material is liquid and G" is higher than G', but both the storage and loss modulus increase with time and G' then far exceeds G" (by an order of magnitude), indicating the formation of a gel (Figure 2.27d). The gelation point is the point at which the material transitions from fluid-like to solid-like and is determined by the time at which G' exceeds G" (when G' and G" cross) [192]. This measure can be used to determine the speed of initiation of gelation. After a certain duration at 37 °C, the storage and loss modulus reach a maximum level and plateaus, indicating the formation of a stable gel (Figure 2.27d). Figure 2.27d and figure 2.27e show that endometrial ECM hydrogel and SIS ECM hydrogel behaved similarly, with gelation occurring within the first few minutes of a constant 37 °C temperature and a stable gel forming after 10 minutes.

The maximum storage modulus changed with varying concentrations of endometrial ECM gel (Figure 2.27f). The maximum storage modulus was determined as the value reached within the linear plateau region of G' in the time sweep. Figure 2.27f shows the differences in gelation time and storage modulus of sow endometrial ECM hydrogel at 2 mg/mL, 5 mg/mL and 8 mg/mL. With increasing ECM hydrogel concentration, the maximum storage modulus increased. Due to batch-to-batch variability, creating large error bars, the differences in storage modulus were not statistically significant. However, in principle, the stiffness of ECM gel can be tuned by altering the gel concentration whilst maintaining a constant temperature.

After some pilot experiments to determine injectability and retention of endometrial ECM gel for intrauterine application in the mouse *in vivo* model, it was decided that 8 mg/mL of pig endometrial ECM gel would be a suitable concentration to use for the animal study. Rheological studies enabled the recognition of significant variability between different batches of 8 mg/mL pig endometrial ECM hydrogels. This helped with the identification of an optimal batch of endometrial ECM gel to use for the *in vivo* studies. Table 2.4 outlined the details of the three different batches of pig endometrial ECM digests that were made and tested. Figure 2.28 shows time and strain sweeps of three different batches of pig endometrial ECM, which contained pooled, decellularised endometrial ECM from 2 or 3 different pigs (refer to Table 2.4). Each batch was prepared in an identical way using decellularisation protocol version 2, but at different times and containing different combinations of animals. The time

and strain sweeps (Figure 2.28) show that all three batches formed hydrogels, however, there were differences in the plateau storage moduli and the rate at which this plateau was reached. Batch C of the hydrogel had significantly higher mean maximum storage modulus (652.173 ± 42.410 Pa) than batches A (228.565 ± 73.914 Pa) or B (208257 ± 8.068) (Figure 2.28g). Although all three batches had similar gelation points, after gelation is initiated the slope of the G' and G" curves vary dramatically (Figure 2.28a,c,e). Figure 2.28h compares the time taken to reach 50% of maximum storage modulus across the three batches of gels. On average, batch C took less time (9.5 ± 1.887 minutes) than batch B (23.28 ± 8.430 minutes) and significantly less time than batch A (29.05 ± 4.950 minutes).

Based on the rheological findings, it was decided that batch C was the most reliable batch of ECM hydrogel to use for *in vivo* experiments. The time sweep graph for batch C (Figure 2.28e) shows a mean gelation point at 4 minutes. However, it was observed from the rheological measurements that a stable 37 ^{o}C temperature was not reached until 1 minute. Therefore, the true time for gelation to be initiated at 37^{o}C was 3 minutes. The storage modulus starts to reach a plateau in G' around 13 minutes and reaches a mean maximum G' of 647 Pa (Figure 2.28e). For *in vivo* applications, this gelation time would be quick enough to help the gel be retained within the space of intended delivery, whilst not being so fast that it would impede gel injection or filling of the intrauterine cavity.

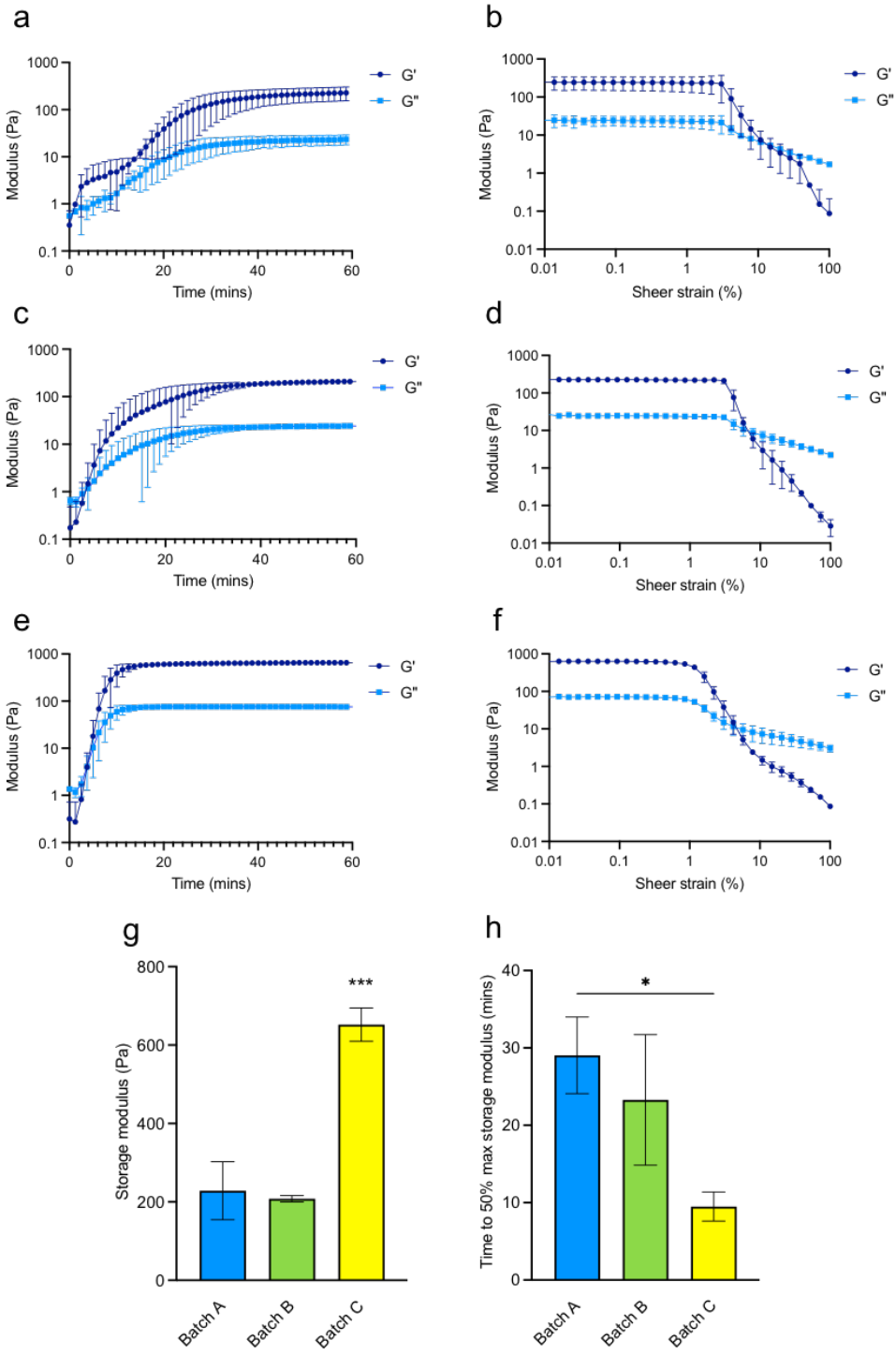


Figure 2.28 Rheology of different batches of pig endometrial ECM hydrogel. **a-b** are time sweep and strain sweep of batch A. **c-d** are time sweep and strain sweep of batch B. **e-f** are time sweep and strain sweep of batch C. **g** Comparison of storage moduli for the three batches of endometrial ECM hydrogel at 60 minutes into a time sweep performed at 37 °C. Batch C had significantly higher storage modulus than batch A ($p = 0.003$) and batch B ($p = 0.001$). **h** Batch C exhibited significantly shorter time to reach 50% of maximum storage modulus compared to Batch A ($p = 0.0336$). The statistical test performed for **g** and **h** was ordinary one-way ANOVA with Tukey's multiple comparisons test.

2.4.5.3 Injectable and sprayable endometrial ECM hydrogel

For *in vivo* and clinical applications, the ECM gel could be injected or sprayed. It was therefore important to determine whether injecting and spraying would significantly alter the rheological properties of the gel. Using 5 mg/mL SIS ECM gel, time sweep experiments were performed on gel that had been injected through an 18 gauge, 5cm long needle and after spraying the gel through an atomisation device (Figure 2.29). The SIS ECM gel was able to form a stable ECM gel at 37 ^{o}C after injecting and spraying (Figure 2.29 a-b) and there were no statistically significant differences in the storage modulus or the gelation point compared to ECM gel that had been pipetted onto the rheometer (Figure 2.29 d-e).

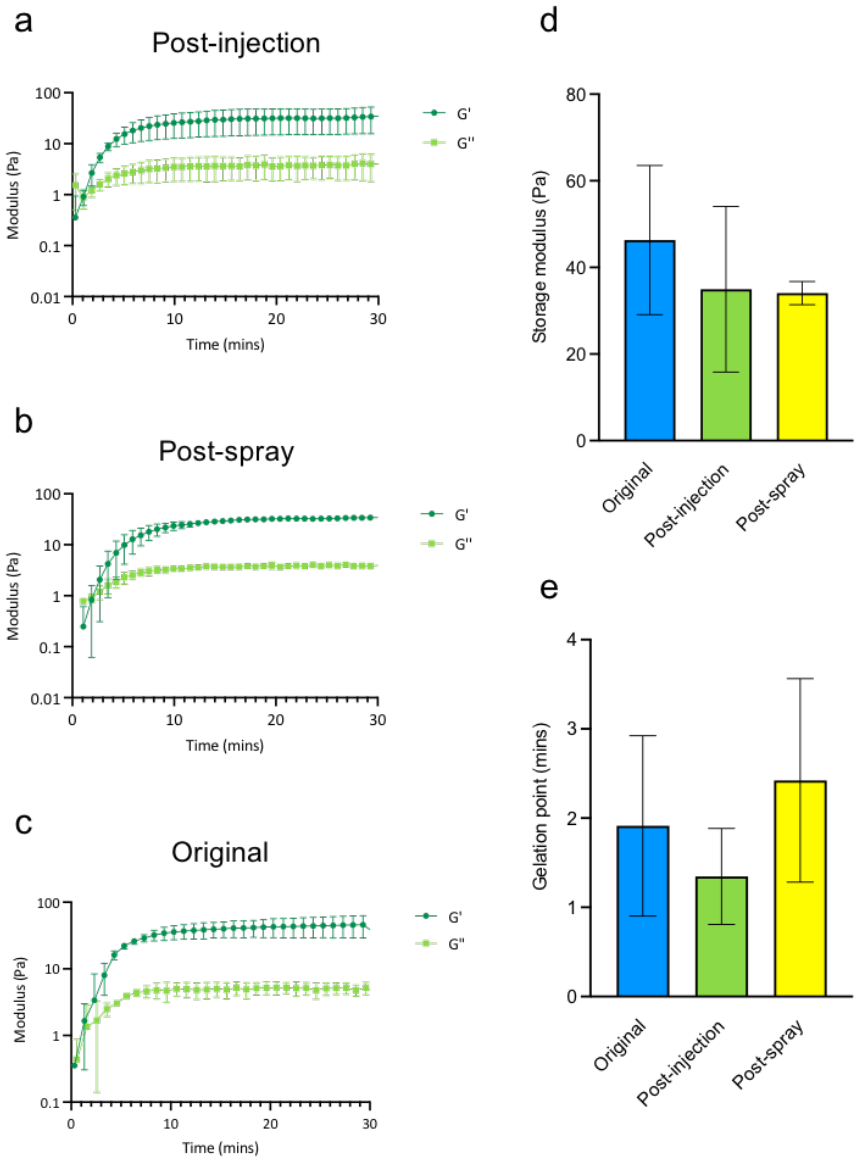


Fig 2.29 Rheology of ECM hydrogel after injecting and spraying. **a** Time sweep of 5 mg/mL SIS ECM hydrogel after injecting through 18G needle (N = 3). **b** Time sweep of 5 mg/mL SIS ECM hydrogel after spraying (N = 2). **c** Time sweep of 5 mg/mL SIS ECM hydrogel pipetted onto peltier (control) (N = 3). **d** Storage modulus at 30 minutes of time sweep for original (pipetted), injected and sprayed 5 mg/mL SIS ECM hydrogel. **e** Gelation points, determined by the point when G' crosses G" in the time sweeps, for original (pipetted), injected and sprayed 5 mg/mL SIS ECM hydrogel.

2.4.5.4 ECM hydrogel adherence to endometrial tissue

In a qualitative experiment to visibly demonstrate ECM hydrogel adherence to porcine endometrial tissue, SIS ECM hydrogel containing fluorescent nanoparticles (Figure 2.30a) was applied to porcine

endometrium and incubated at 37 °C for 15 minutes to enable gelation (Figure 2.30b). As a control, 1x PBS containing the same ratio of fluorescent nanoparticles was applied to porcine endometrium (Figure 2.30b). After gelation the endometrial tissue was suspended vertically, and a 365 nm UV light shone onto the tissue revealed brightly fluorescent gel on the endometrial surface. There was no gel displacement with gravity after 30 minutes, demonstrating that the ECM gel adhered to the tissue upon gelation (Figure 2.30c).

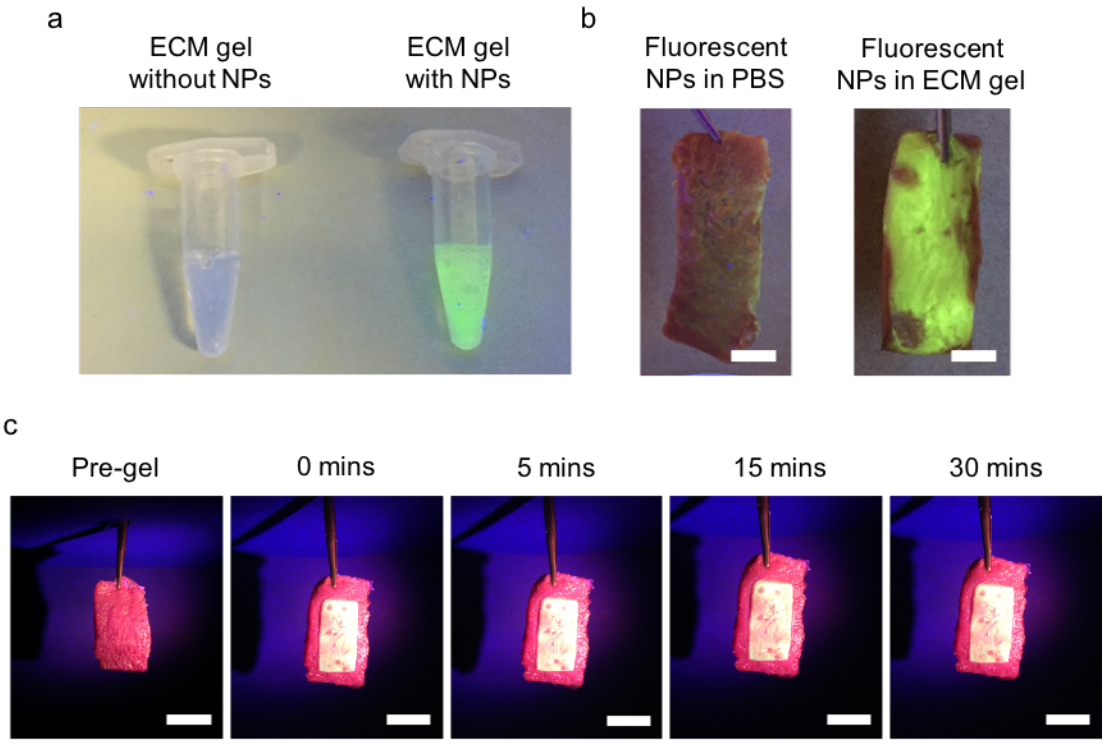


Figure 2.30 ECM hydrogel adherence to endometrial tissue. Photographs of qualitative experiment to demonstrate SIS ECM gel adherence to porcine endometrial tissue. **a** Aliquots of ECM hydrogel under 365nm UV light, without fluorescent nanoparticles and with fluorescent nanoparticles. **b** ECM hydrogel containing fluorescent nanoparticles was pipetted onto porcine endometrial surface and incubated at 37 °C for 15 minutes. Under UV light, brightly fluorescent gel can be seen coating the tissue (image on far right, top row). As a control, the same concentration of fluorescent nanoparticles was mixed in PBS and pipetted onto porcine endometrial tissue. Under UV light, there is no obvious fluorescent layer on the tissue surface (image second from right, top row). **c** Fluorescent ECM hydrogel was applied to a rectangular mould on top of the endometrial surface and incubated at 37 °C for 15 minutes. The mould was carefully removed leaving a clearly defined layer of gel on the tissue when visualised by UV light. The tissue was then suspended vertically for up to 30 minutes and no gel displacement was seen, showing that the ECM gel was adhered to the surface of the tissue. Scale bars = 1 cm.

2.5 Discussion and future work

The work presented in this chapter demonstrates an approach to developing and validating a protocol for effective decellularisation of porcine endometrium, followed by comprehensive characterisation of the decellularised ECM and endometrial ECM hydrogel. Initially, sow endometrial tissue was used for optimising a decellularisation protocol, ECM analysis and testing the gelation properties of an endometrial ECM gel. This was because this tissue was more readily available at the time and early concepts of developing an endometrial ECM biomaterial for fertility restoration prompted the use of tissue from animals with proven reproductive capacity. However, experiments using sow endometrial ECM hydrogel to culture endometrial organoids, the results of which are presented in chapter 3, section 3.2.3, showed significantly inferior performance to Matrigel. Subsequently, a paper published by Giobbe et al. (2019) on ECM hydrogels for endodermal organoid culture emphasised the use of ECM from young piglets [112]. Direct communication with Giobbe confirmed that their experience of working with ECM derived from older pigs included observing greater levels of organ fibrosis, more batch-to-batch variability and less optimal experimental outcomes. In the limited literature on large animal uterine decellularisation, adult animals have always been used but the age of the source animal is often not specified [59], [60], [104] or animals of a wide age range (8-24 months) were used [61]. To investigate the feasibility of obtaining endometrial ECM from piglets, uteri were retrieved from pigs of 7 days and 21 days of age and it was established that piglets have very underdeveloped uteri (Figure 2.3), unsuitable for deriving endometrial ECM. Therefore, a decision was made to fabricate decellularised endometrial ECM from the uterine tissue of 5-month-old pigs. The decellularisation protocol was further optimised for pig endometrium to improve the decellularisation efficiency and pig endometrial ECM was characterised in the same way as sow endometrial ECM, by histology, immunostaining, Raman spectroscopy, collagen assay and rheology. Additional characterisation was performed on pig endometrial ECM only, which included isolation and analysis of matrix bound vesicles and proteomics. Subsequent *in vitro* and *in vivo* experiments (presented in chapters 3 and 4) were also carried out with pig endometrial ECM hydrogel.

Using a protocol that combined chemical and enzymatic decellularisation methods, it was demonstrated that porcine endometrium could be efficiently decellularised, as determined by histological and immunofluorescent assessment of depleted nuclei as well as quantification of reduction in dsDNA content between the native and decellularised tissue. The protocol described in section 2.3.1.4 differs to any other published protocol on fabrication of porcine endometrial ECM, in that the endometrium is isolated from the rest of the uterine tissue prior to decellularisation and the

method does not involve the detergent SDS. A conscious decision was made not to use SDS due to the potential risk of cytotoxicity [148]–[150] and reports of its destructive effect on collagen [148], [152], GAGs [150], and the basement membrane [152]. Santoso et al. reported the lack of cellular migration into implanted uterine ECM scaffolds that were decellularised with SDS, whilst this was not an issue with high hydrostatic pressure [165].

Here, it was demonstrated that decellularised sow and pig endometrium had 96.6% and 98.8% reduced DNA content respectively. This degree of decellularisation is more thorough than the 92.4% reduction in DNA content reported by another group who published on decellularised porcine endometrium [104]. The DNA content of pig endometrial ECM presented here (170.4 ± 190.2 ng/mg dry weight) is similar to that reported by Lopez et al. (2021) (0.15 μg/mg dry weight), who used a reliable DNA quantification method and the same units for DNA concentration [104]. Efficient decellularisation must be balanced against the destruction of proteins and loss of bioactivity of the ECM. Immunostaining of native and decellularised endometrial tissue showed the preservation of key ECM proteins following decellularisation. The biological effects of decellularised endometrial ECM are probed in Chapters 3 and 4. Further experiments could be performed to evaluate the thoroughness of cellular clearance and potential immunogenicity of the endometrial ECM, such as by measuring the level of α-gal epitope.

Raman spectroscopy was used to qualitatively characterise and compare decellularised sow and pig endometrial ECMs and to compare endometrial ECM with other types of decellularised ECM. When the Raman spectra of endometrial ECM was overlaid with the spectra of SIS, UBM and Cardiac ECM, it was possible to appreciate that endometrial ECM was biochemically unique. Interestingly, the Raman spectra of endometrial, SIS and UBM ECMs had many more similar peaks between them compared to Cardiac ECM, possibly reflecting the stark difference in tissue type. Speculative comparison of the Raman spectra of sow and pig endometrial ECMs revealed many similarities, however, the differentiating peaks appeared to correspond mostly to lipids. Given that an almost identical decellularisation protocol was used for producing both endometrial ECMs, this finding may point to key differences in the lipid profile of endometrial tissue from older, parous animals versus younger animals. A limitation of the work presented here is that Raman spectra were not acquired from native endometrial tissue to demonstrate, in more detail, the preservation of biochemical components in decellularised ECM. Several studies have been published where Raman spectroscopy was used as an analytical tool for characterising decellularised ECM [113], [172], [193], [194]. Typically, Raman spectra of decellularised and native tissues have been compared for their analogy, to show

that the biochemical composition is preserved following decellularisation, as well as to highlight the efficiency of decellularisation with the absence or reduction of DNA peaks in ECM scaffolds [113], [172], [194]. This technique can also be used to probe for subtle changes to the ECM structure with different decellularisation methods. For example, Nara et al. (2016) used Raman spectroscopy to identify an optimal decellularisation technique, by observing which protocol generated the least alteration to collagen structures in decellularised corneal scaffolds [193].

Two studies have been identified where Raman spectroscopy was used to analyse decellularised uterine ECM [172], [194]. Arezoo et al. (2021) studied the Raman spectra of native, decellularised and recellularised mouse uterine tissue [194]. The authors demonstrated similarities across all scaffolds in the peaks corresponding to collagen type I, functional groups that contribute to collagen and amino acids [194]. In the decellularised uterine scaffolds, there was a lack of peaks correlating to DNA, whilst in the recellularised uterine scaffolds peaks relevant to cellular material could be seen [194]. Sargazi et al. (2021) described the decellularisation of human endometrial fragments and reported on the use of Raman spectroscopy to identify and quantify the preservation of collagen I, collagen IV, fibronectin, GAGs and elastin in the decellularised endometrium [172]. However, the validity of these results is slightly questionable. The authors attributed these ECM proteins to peak assignments obtained from several different publications where the Raman spectra were acquired using different Raman spectroscopic methods, from either pure protein extracts or diverse tissues, such as cartilage or skin [172]. Also, the authors have merely compared peak intensities as a way to quantify amounts of ECM proteins in the native and decellularised endometrium and have not commented on whether all data were acquired, processed and normalised in the same way [172]. Further work using Raman spectroscopy to characterise decellularised and native sow and pig endometrium, including multivariate analyses, would yield interesting findings on key biochemical differences resulting from decellularisation, as well as between old and young animals.

To characterise the specific composition of decellularised endometrial ECM in more detail, proteomics analysis was performed on 2 biological replicates of ECM. The data revealed 370 peptides and the presence of a combination of extracellular and cellular proteins, with 43 of the 370 peptides identified as matrisome proteins. This is comparable to other studies on proteomics analysis of decellularised ECM where the majority of peptides were non-matrisomal [195], [196]. However it is known that the process of decellularisation helps to enrich the matrisomal proteins, enabling more to be identified compared to proteomics analysis of native tissue [195], [196].

Gene ontology enrichment analysis for the 43 matrisome proteins showed relevance to processes and functions such as ECM organisation, cell adhesion, growth factor binding and wound healing. The matrisome proteins included, as was expected for endometrial ECM, 9 different collagens, fibronectin, laminin, elastin, glycoproteins such as fibrillin and fibrinogen and proteoglycans, including heparan sulfate and various small leucine-rich proteoglycans (SLRP). SLRPs play an important role in controlling ECM assembly, including regulating collagen fibrillogenesis, and mediating interactions between cells and the matrix [197]. Abnormal expression of SLRPs can lead to ECM dysfunction and has been implicated in different diseases. SLRPs have been found in the endometrium and are thought to play a role in endometrial ECM organisation [198], [199]. Expression of SLRPs has been associated with normal and fertile endometrium, whilst low or absent expression of SLRPs have been found in endometrial pathologies [198].

One other academic group has reported, in detail, on proteomics of decellularised endometrial ECM, although this group analysed endometrial ECM hydrogel as opposed to lyophilised decellularised ECM [104], [106]. Whilst there were some similarities between their reported matrisome peptides and the data presented here, there were also some interesting disparities. Common to both matrisome data sets were collagens, laminin, fibronectin, fibrillin, fibrinogen, annexin and von Willebrand factor [104]. However, what was noticeably missing from their list of matrisomes were proteoglycans [104], which were detected in the endometrial ECM proteomic analysis presented in section 2.4.3.3. Another prominent difference was the number and types of collagen; 4 types of collagen were reported by Lopez-Martinez et al. amongst the endometrial ECM hydrogel peptides [104], whilst 9 different collagens were detected within the endometrial ECM peptides presented here. Of note, collagen IV, which should be abundantly present in endometrial ECM (as demonstrated by the immunostaining in section 2.4.3.1) was detected in this matrisome data set but not amongst the peptides listed by Lopez-Martinez et al [104]. It is likely that the differences in identified proteoglycans between these two bodies of work is attributable to the use of PNGase F in the protocol presented here, which deglycosylates proteins by removing N-glycans and allows for better detection of proteoglycans by mass spectrometry [200]. Another potential explanation for the matrisome differences could be the analysis of an ECM hydrogel versus non-digested ECM. In order to prepare an ECM hydrogel, lyophilised ECM is digested with pepsin, a process which cleaves proteins and peptides in a way that may alter which peptides are detectable by mass spectrometry. Alternatively, the lack of collagen IV and proteoglycans in the proteomics results reported by Lopez-Martinez et al. could reflect differences in decellularisation method, as SDS is used in their protocol [104]. SDS has been shown to

disrupt collagen structures and remove more GAGs compared to other decellularisation methods [148], [152].

There is no standardised approach to sample preparation and analysis of proteomics for ECM biomaterials, and methods reported in the literature are highly variable. Significant challenges were experienced in attempting to develop and optimise a protocol for successful proteomics analysis of endometrial ECM. Many attempts were undertaken of several different methods and techniques to try to achieve a solubilised ECM protein extract for mass spectrometry processing. Urea and guanidine are the most commonly used reagents for protein solubilisation during proteomics sample preparation but on their own, these were not sufficient to solubilise freeze-dried endometrial ECM samples. The challenges of solubilising ECM for proteomics have been discussed by another academic group, who have developed tailored methods for extracting insoluble proteins from decellularised ECM scaffolds for mass spectrometry analysis [184], [185]. The final proteomics protocol, outlined in section 2.3.3.4, features an amalgamation of two different protocols from two publications by the same group on ECM proteomics [184], [185] and a third protocol provided by Steve Howell at the Francis Crick Institute for in-gel protein digestion. A key limitation to the proteomics work presented in this chapter was the lack of expert input with regards to ECM sample preparation for mass spectrometry and lack of bioinformatics expertise for proteomics analysis. Therefore, future work on refining ECM proteomics would benefit hugely from an academic collaboration.

The characterisation of endometrial ECM was extended to an area that has not yet been explored in decellularised uterine tissue, nor most other types of ECM; matrix bound nanovesicles (MBV). In recent years it has been postulated that functional, exosome-like MBVs, which are preserved in decellularised ECM scaffolds, play an important role in the bioactivity of acellular ECM. The results presented in section 2.4.4 demonstrate that MBVs can be isolated from decellularised endometrial ECM, using a method that involves size exclusion chromatography (SEC). These MBVs have exosome-like properties and carry protein, lipid and nucleic acid cargo. The detection of nucleic acids by Raman spectroscopy corroborates the published findings that MBVs are enriched with bioactive microRNAs, although the Raman data cannot specify the nature of the nucleic acids. SPARTA® Raman trapping analysis is a method that has been used to characterise and compare EVs derived from cancer cells [201]. It is a non-destructive, high throughput and sensitive approach that enables the identification of variations in biochemical composition of different EV samples. The use of SPARTA® validated the method described in section 2.3.4.1 for extracting exosomes from ECM, demonstrating that the particles were not simply protein contaminants, as we can see the close resemblance between the

Raman spectra of MBVs and secreted EVs harvested from a cell-line. Interestingly, the detection of CD63, CD81 and CD9 expression in the endometrial MBVs contradicts with the findings reported by Huleihel et al. (2016) of an absence of these markers in MBVs derived from UBM, SIS and commercially available ECM products [164]. Whilst Hussey et al. (2020) reported the weak expression of these markers in MBVs compared to liquid-phase EVs [178]. These differences are perhaps attributable to different methods used to isolate MBVs; both Huleihel et al. (2016) and Hussey et al. (2020) used ultracentrifugation followed by filtration through a 0.22 μm filter [164], [178]. Certainly, SEC has been recognised as an optimal technique for MBV isolation in terms of enhanced purity and the preservation of EV properties [177], [183]. There could also be tissue-specific differences in the MBV expression of EV markers. Therefore, in future work the SEC methodology used in this project can be used to extract MBVs from SIS and UBM to facilitate a more direct comparison with the literature. This would be highly complemented by SPARTA® biochemical analysis of MBVs from SIS, UBM and endometrial ECM. TEM imaging was not performed on the endometrial MBVs, due to time constraints, but can be included in further analysis. Although it was felt to be beyond the scope of this thesis, future work should also include investigating the biological effects of isolated endometrial MBVs, as other authors have reported on the immunomodulatory properties of MBVs independent of the other ECM components [176], [179].

Finally, as endometrial ECM is intended to be applied as an injectable hydrogel, the ECM gel properties were characterised by rheology. Oscillatory time sweep studies confirmed that endometrial ECM pre-gel solutions form stable hydrogels at 37 ^{o}C at concentrations between 2 and 8 mg/mL and do not gel at temperatures $\leq$10 ^{o}C. Typically, gelation is initiated within minutes and a maximum plateau storage modulus is achieved in under 20 minutes. The storage modulus appears to be positively correlated with gel concentration, although the rheological experiments highlighted significant batch-to-batch variability amongst the ECM gels, such that the differences in storage modulus with varying concentration were not statistically significant. Batch-to-batch variability is common challenge in working with ECM hydrogels and this can affect the biological effect and *in vivo* impact of ECM gels [202].

Through rheological testing, it was possible to screen multiple batches of ECM gels and identify an optimal concentration and batch for subsequent *in vivo* studies. To decide which concentration of gel to use in the planned animal experiments, a key desirable characteristic was fast gelation time as this would aid gel retention within the uterine lumen and minimise gel leakage, particularly when it is important to minimise operating times to prevent adverse effects in the animals. Time sweeps

identified a specific batch of pig endometrial ECM hydrogel, at 8 mg/mL, as having the most consistent gelation, the shortest time to reach half of the maximum storage modulus and significantly higher storage modulus than other batches of the same concentration. It was felt that these properties would make this batch of gel most suitable for the *in vivo* model.

Whilst the work presented in this chapter represents a thorough examination of a decellularised ECM biomaterial, a limitation of the work presented here is the insufficient comparison of endometrial ECM derived from sow and pig. When the project was first conceived, there was no specific consideration given to the age of the source animal and it was not an original aim of this project to compare tissue from young versus old animals. However, as the project and the literature evolved, the concept of using endometrial tissue from younger pigs became more relevant. Time constraints prevented the investigation of both sow and pig endometrial ECM by proteomics and the comparison of sow and pig endometrial MBVs, which would have likely yielded interesting findings on the biochemical and functional differences of young versus old endometrium. This would lead to important considerations regarding the tissue source when translating ECM biomaterials for clinical use. In addition, more work can be done, particularly with proteomics, to compare the properties of endometrial ECM with other commonly used and studied ECM types such as SIS. This may help to determine whether endometrial ECM has tissue-specific properties that are more relevant for reproductive tissue engineering. These concepts should be explored in future experiments.

2.6 Summary of key findings

The method described in this chapter is the first to decellularise isolated porcine endometrium, as other published protocols on porcine and ovine uterine tissue decellularisation use the whole organ perfusion technique. The method presented here would also be suitable for human endometrial decellularisation where, due to the shape of the human uterus and the thickness of the uterine wall, it would be more practical to separate the endometrium from the myometrium before decellularising. In addition, isolating the endometrium, prior to decellularisation, is potentially more appropriate for scaling up the manufacture of porcine endometrial ECM biomaterials as it does not require labour-intensive microdissection of the endometrium from full thickness uterine rings, as reported in the whole organ perfusion technique [104].

Evaluation of decellularisation efficiency confirmed significant reduction in the DNA content of endometrial ECM. The DNA concentration of pig endometrial ECM demonstrated in this work is comparable to that reported in the literature, when measured and normalised in the same way. Immunofluorescence and proteomics showed the conservation of collagens, laminin, fibronectin, elastin and small leucine-rich proteoglycans in decellularised endometrial ECM, demonstrating that the decellularisation protocol preserves important ECM constituents that may influence cell adhesion, cell migration and ECM bioactivity. Further work could be done to elucidate important biochemical and functional differences between sow and pig endometrial ECM, or endometrial ECM from pigs of different age ranges to identify the optimal age of source animal to produce an ECM hydrogel for endometrial regeneration and fertility restoring purposes. Biomolecular differences in sow and pig endometrium were suggested by Raman spectroscopy, but future work should include more thorough comparative analyses of Raman spectral data and proteomics.

The results presented in this chapter on matrix-bound vesicles represents one of few known bodies of work in this area. Of complete novelty is the use of single particle Raman trapping analysis (SPARTA®) to analyse the MBVs, which revealed some biomolecular similarities to cell-derived EVs and confirmed the presence of nucleic acid cargo.

Rheological characterisation of endometrial ECM hydrogels highlighted considerable batch-to-batch variability, which is a well-recognised limitation of working with ECM-derived biomaterials. Assessing the rheological properties of endometrial ECM hydrogels aided in the identification of an optimal batch of gel to carry forward for *in vivo* experiments.

Chapter 3 – Characterising the *in vitro* effect of endometrial ECM hydrogel

3.1 Chapter aims

In this chapter, the effects of endometrial ECM hydrogel on various cells were assessed through different *in vitro* studies. To begin, a literature review on topics that are pertinent to the methods and methodology was conducted. This includes an overview of different endometrial *in vitro* models and the significance of TGF-β1 as a stimulator and regulator of fibrosis, as TGF-β1 was used in this work to model endometrial fibrosis. Following that, a review of publications on the effects of ECM biomaterials on macrophage polarisation and angiogenesis was performed, as these are important features of ECM bioactivity and were explored in the *in vitro* experiments described in this chapter.

The methods and results sections are each are divided into five subsections, representing the different themes of *in vitro* studies that were carried out. The first section describes the experiments to explore the effect of ECM hydrogel on primary and immortalised endometrial cells. The second section describes assays that were performed to determine the angiogenesis potential of ECM hydrogel. The third section includes preliminary work on endometrial organoids, involving ECM hydrogels as a culture substrate. Next, different techniques for developing an endometrial fibrosis model are described and the effect of ECM hydrogel on a cell-derived matrix-based *in vitro* scarring model was tested. The last section explores the immunomodulatory properties of ECM hydrogel through macrophage culture, RT-qPCR and flow cytometry studies.

It was hypothesised that endometrial hydrogel would maintain high cell viability, enhance endometrial cell proliferation, increase angiogenesis, support endometrial organoid growth, reduce endometrial fibrosis and modulate macrophage responses to favour an M2 (pro-regenerative) phenotype, whilst shifting away from an M1 (pro-inflammatory) phenotype.

The challenges of experimenting with primary endometrial cells are presented in the results section and subsequently discussed. The results presented in section 3.4 highlight the bioactive properties of endometrial ECM hydrogel, including supporting cell proliferation, promoting angiogenesis, mitigating the fibrosis-stimulating effect of TGF-β1 and altering macrophage polarisation in response to inflammatory stimulants. Section 3.5 discusses the relevance, similarities and contradictions of the results presented in this work compared to published studies and explores opportunities for future work.

3.2 Introduction to *in vitro* assays

3.2.1 Endometrial *in vitro* models

Endometrial *in vitro* models have been used to investigate physiological and pathological reproductive processes such as endometrial-embryo interactions, endometrial receptivity, implantation failure and endometriosis [203]. *In vitro* endometrial modelling ranges from simple 2D culture of endometrial epithelial or stromal cells, to more complex 3D co-cultures of epithelial and stromal cell layers [203], [204]. More recently endometrial organoid models have been developed and have been shown to closely resemble endometrial epithelial glands in morphology and behaviour [205], [206].

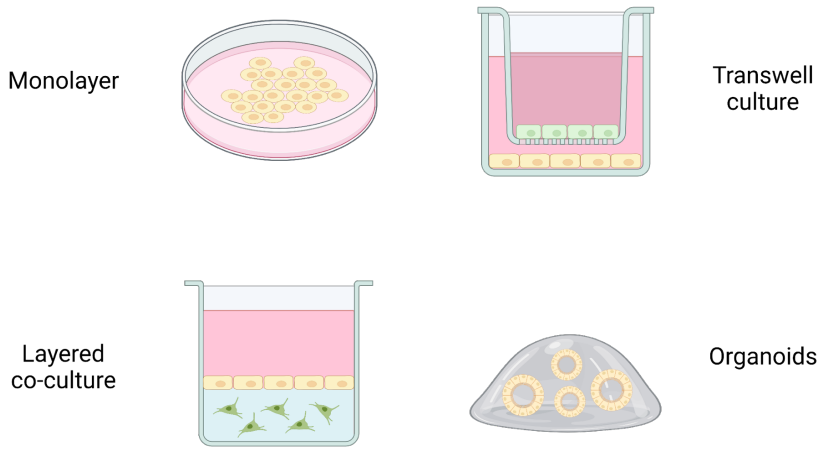


Figure 3.1 Endometrial *in vitro* models. Representative images of endometrial *in vitro* models. 2D endometrial *in vitro* models include monolayer cell cultures or transwell cultures of more than one cell type [203]. 3D *in vitro* models have included layered co-cultures, usually with stromal cells encapsulated in a hydrogel and endometrial cells cultured as a single layer on top [203], [204]. More recent and more biomimetic 3D *in vitro* models include endometrial organoids, involving primary endometrial epithelial cells which self-organise into 3D gland-like structures when cultured in Matrigel and a chemically defined medium [205], [206]. Figure created with BioRender.com.

3.2.1.1 Traditional endometrial *in vitro* models

Two-dimensional endometrial *in vitro* models typically consist of culturing individual endometrial cell types in monolayers on tissue culture plastic. Whilst endometrial stromal cells can be studied easily in

2D cell culture, this is often a poor system for studying endometrial epithelial cells, as epithelial cells do not preserve their essential traits when cultured in 2D [203]. Typically, 2D cell culture lacks ECM, which is necessary for epithelial cells to exhibit apicobasal polarity and form tight junctions [203]. Epithelial cells cultured by themselves in 2D are also not hormonally responsive therefore they are not physiological *in vitro* models [203]. It has also been reported that non-cancerous endometrial epithelial cells are difficult to expand and maintain and could only be cultured on tissue culture plastic for a limited period of time [207]. In addition, it has been demonstrated that paracrine factors released by stromal cells are important for regulating endometrial epithelial cell growth and differentiation [207], [208] and enable the formation of a basement membrane layer [209]. Therefore, 3D human endometrial culture models, consisting of a co-culture of endometrial and stromal cells [207], [209], [210], were found to be more representative and sophisticated. Typically, these 3D models have involved endometrial stromal cells encapsulated in a matrix substrate, such as collagen gel, Matrigel or fibrin, with a monolayer of epithelial cells on top [209], [210]. Alternatively, transwell co-culture systems have been utilised to speculate on the paracrine effect of stromal cells on epithelial cells [207], [211]. Challenges that these types of 3D endometrial models have faced include the rapid remodelling of the matrix by endometrial stromal cells and difficulty culturing epithelial cells long-term [203].

3.2.1.2 Endometrial organoids

Although several papers in the last few decades had described 3D spherical or tubular endometrial epithelial structures forming when epithelial cells were grown in contact with basement membrane extract [207], [212], in 2017 two different academic groups formally described the culture of endometrial epithelial organoids derived from primary endometrial cells [205], [206]. These organoids are formed by culturing isolated endometrial epithelial cells in Matrigel and a chemically defined growth medium that contains specific growth factors, including Wnt, R-spondin 1, Epidermal growth factor (EGF), Fibroblast growth factor (FGF) and Noggin [213]. The epithelial cells then self-assemble into 3D structures consisting of cells aligned with apical-basal polarity, resembling endometrial glands. Endometrial organoids can be grown from a single cell, demonstrate clonogenicity and can be expanded long term, suggesting the presence of stem or progenitor cells within the endometrial biopsies from which the organoids are derived [205]. They can be cultured over a long period of time, withstanding multiple passages and cryopreservation with genetic stability [205]. Endometrial organoids have been demonstrated to be hormonally responsive and can recapitulate the dynamic changes that occur in the human endometrium during the menstrual cycle [205], [206]. They have

also been found to be made up of a heterogenous population of epithelial cell types, such as ciliated, unciliated and secretory cells [214].

Recently, Rawlings et al. reported on the development of endometrial assembloids, consisting of endometrial epithelial organoids surrounded by stromal cells. By culturing assembloids in a differentiation medium that contained medroxyprogesterone acetate, 8-bromo-cAMP and estradiol, a decidualisation response could be promoted, with cellular responses that mimic the midluteal endometrium [215]. Using this model, the authors demonstrated the ability to study early embryonic implantation events by co-culturing human blastocysts with the endometrial assembloids.

The ability to culture and expand endometrial organoids from endometrial biopsies means the possibility of creating a biobank and developing personalised medicine. This could help to overcome the challenges of culturing endometrial epithelial cells in 2D, such as lack of hormone responsiveness [203] and poor expandability [207]. Endometrial organoids also allow for *in vitro* disease modelling using cells from patients with diagnosed endometrial disorders. Boretto et al. (2019) reported on the culture of endometrial organoids from patients with endometrial cancer, precancerous diseases such as endometrial hyperplasia, and endometriosis [216]. Endometrial disease organoids, resembling their original pathologies and maintaining associated genetic traits, allow for biomimetic *in vitro* modelling of diverse human endometrial disorders that is not possible with traditional cell culture methods [216].

3.2.1.3 *In vitro* modelling of endometrial fibrosis

The majority of experimental work on endometrial fibrosis has been conducted *in vivo* and there are limited studies on modelling endometrial fibrosis *in vitro*. Most likely this is because fibrosis is a tissue pathology, involving tissue injury and inflammation and characterised by aberrant ECM deposition and destruction of normal tissue function [217]. Nevertheless, *in vitro* studies may help to isolate and elucidate key mechanisms involved in the pathogenesis of fibrosis and are often complementary to animal models and patient studies. For example, treatment of endometrial stromal cells with TGF-β1 *in vitro* has been reported to stimulate fibrogenic processes, mediated by the TGF-β1/Smad signalling pathway, including myofibroblast transdifferentiation and increase in gene and protein expression of α-SMA and Collagen I [218], [219]. Having found an increased level of high mobility group AT-hook 2 (HMGA2) protein in patients with intrauterine adhesions as well as TGF-β1-treated endometrial epithelial cells, Song et al (2021) demonstrated that HMGA2 knockdown prevents epithelial-to-

mesenchymal transition (EMT) in epithelial cells whilst overexpression of HMGA2 stimulates EMT [220].

3.2.2 TGF-β1 as a fibrosis stimulator

There are three transforming growth factor-β (TGF-β) isoforms; TGF-β1, TGF-β2 and TGF-β3. They act as key drivers in the pathogenesis of fibrosis and TGF-β signalling pathways are always activated when tissue injury occurs and fibrosis ensues [221]. This has been demonstrated abundantly in *in vitro* studies, animal experiments and also by studying clinical biological samples [221]. TGF-β is synthesised and secreted in latent form by a variety of different cell types, including fibroblasts, epithelial cells and immune cells such as macrophages and T Cells [221]. Stores of latent TGF-β are also sequestered in ECM, being released and activated when there has been tissue injury [221]. Activation of TGF-β is spatially controlled and can happen by several different mechanisms, which are influenced by the type of injury and the cellular composition of the injured tissue [221]. Latent-TGF-β is cleaved by proteases, such as serine proteases and matrix metalloproteinases (MMP) and can also be activated non-proteolytically by integrins, particularly the αν integrin subunit [222]. TGF-β activation can also occur via mechanotransduction [223]. It has been demonstrated that matrix strain and stiffening, factors inherent to fibrotic scar formation, can activate latent TGF-β [223]. Chemical factors that can trigger TGF-β activation include reactive oxygen species and a mildly acidic (pH 4.5) environments, events that are common in tissue inflammation and damage [224].

Active TGF-β induces intracellular signalling via the Smad2/3 pathway, which regulate the transcription of profibrotic proteins, such as collagens, α-smooth muscle actin (α-SMA) and tissue inhibitor of matrix metalloproteinases (TIMP) [26] (Figure. 3.2). These in turn provoke myofibroblast activation and deposition of matrix [26]. Of the three TGF-β isoforms, TGF-β1 is the predominant regulator of fibrotic processes and disease [26]. In response to injury, TGF-β1 stimulates the transdifferentiation of fibroblasts into myofibroblasts, which are the key "effector" cells in all fibrotic diseases [225]. Myofibroblasts are contractile cells that express α- smooth muscle actin (α-SMA) and produce pathological ECM proteins and proteoglycans [225]. Excessive accumulation of ECM leads to tissue fibrosis and organ damage and failure. TGF-β1 is also responsible for promoting myofibroblast survival and persistent activation of myofibroblasts is a hallmark of tissue fibrosis [225]. TGF-β1 has also been shown to trigger epithelial-to-mesenchymal transition (EMT), a process whereby epithelial cells lose their epithelial characteristics, gain myofibroblast traits and migrate from the epithelial layer to the interstitium [226]. Endothelial-to-mesenchymal transition (EndMT), which involves the

differentiation of endothelial cells to mesenchymal cells that can give rise to fibroblasts, is also implicated in organ fibrosis and is similarly induced by TGF-β1 [227].

TGF-β1 has been used in *in vitro* studies to induce cellular changes that model the fibrosis process [228]–[231]. Treating epithelial cells with TGF-β1 prompted cells to undergo EMT and adopt a pro-fibrotic phenotype [228]. Fibroblast cell cultures exposed to TGF-β1 undergo differentiation into myofibroblasts, with associated transcriptomic and protein increases in collagens I, III and IV [229]. Coupled with macromolecular crowding, achieved by culturing fibroblasts at high density, TGF-β1 has also been used to generate an *in vitro* "scar-in-a-jar" model, whereby fibroblast activation occurs, and ECM production is significantly increased and accelerated [230]–[232]. This model has been used to screen anti-fibrotic agents, by measuring changes in biomarkers of ECM synthesis and α-SMA [230]–[232].

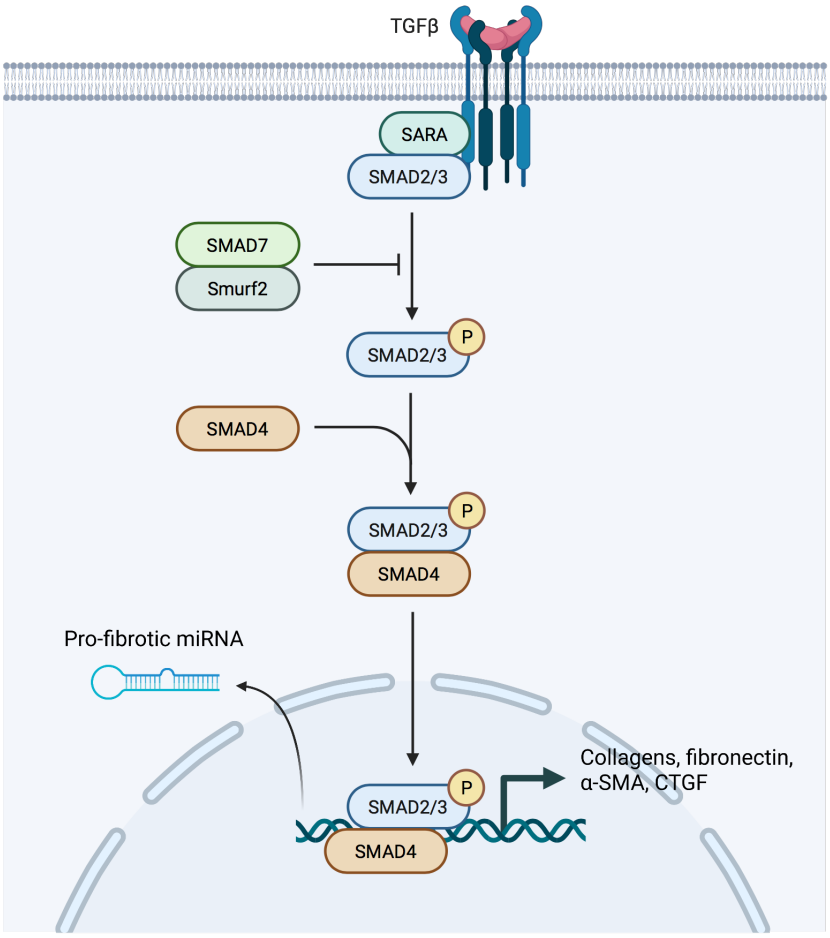


Figure 3.2 Schematic of TGF-β1/Smad pathway. TGF-β1 mediates the transcription of fibrosis-related proteins such as collagens, fibronectin, α-SMA, CTGF, as well as upregulating pro-fibrotic miRNAs. Figure adapted from a BioRender.com template.

3.2.2.1 TGF-β1 in intrauterine fibrosis

TGF-β1 and its downstream signalling pathways have been implicated in Asherman's syndrome and endometrial fibrosis in studies that have analysed clinical samples from patients [28], [29], in animal experiments [28], [233], [234] and *in vitro* studies [219].

In uterine tissue biopsies taken from patients with Asherman's syndrome, protein and mRNA levels of TGF-β1 and Smad3 have been found to be upregulated compared to control [28], [29]. In animal models of intrauterine adhesions, TGF-β1, Smad2 and Smad3 have been found to be significantly raised in the damaged uterine tissues [28], [233], [234], whilst there has been downregulation of Smad7 [28] and pSmad1/5 [234]. In an *in vitro* model of TGF-β1-mediated endometrial fibrosis [219] and in a rabbit model of intrauterine adhesions [28], treatment with SIS3, a Smad3 inhibitor, led to reduced fibrotic effects. TGF-β1 levels have been found to be positively correlated with an increasing severity of adhesions, as well as with expression of p65, a protein involved in the NF-κB signalling pathway [29].

MicroRNAs (miRNA) that inhibit the TGF-β1/Smad signalling pathway have been studied for their therapeutic effect in cell and animal models of intrauterine adhesions. MiRNA-29b, a potent inhibitor of TGF-β1/Smad has been shown in mitigate the effect of TGF-β1-induced fibrosis in an endometrial stromal cell model [235] and to decrease fibrosis in a rat model of intrauterine adhesions [218].

The use of TGF-β1 to induce an *in vitro* endometrial fibrosis model has been reported in several studies. TGF-β1 has been shown to provoke EMT in epithelial endometrial cells [236] and upregulate production of fibrosis markers, such as Col1a1 and α-SMA, by endometrial stromal cells [219], [235].

3.2.3 Macrophage response to ECM biomaterials

Wound healing and healthy tissue remodelling after injury is dependent on an appropriate immune cell response and requires a favourable immune microenvironment. Macrophages play a crucial role in regulating inflammation and fibrosis and have both pro-fibrotic and anti-fibrotic activities [237]. In general, classically activated macrophages (also known as the M1 phenotype) are pro-inflammatory, whilst alternatively activated macrophages (M2 phenotype) are regulatory and promote tissue healing but also mediate fibrosis [238]. A sequential and balanced activation of M1 and M2 phenotype

macrophages is required for optimal tissue repair [239]. M1-like macrophages are predominant in the early phase of tissue injury [239]. They release pro-inflammatory cytokines, phagocytose foreign debris and necrotic cells, and are necessary to initiate tissue healing [238], [240]. However, an excess of M1-like macrophages leads to chronic inflammation, impaired wound healing and tissue damage [238], [241]. M2-like macrophages play a more dominant role in the later phase of tissue repair. They secrete anti-inflammatory factors, phagocytose apoptotic cells, increase fibroblast proliferation and influence ECM deposition [237], [239], [242], but chronic activation of M2 leads to upregulation of TGF-β, initiating a cascade of pro-fibrotic processes including EMT and fibroblast activation with transdifferentiation to myofibroblasts [239]. The manipulation of macrophage phenotype and behaviour, to enhance constructive tissue repair following injury, has therefore become a focus in regenerative medicine [239]. In general, dampening the M1-like macrophage response and promoting an M2-like phenotype has been widely determined to be favourable for constructive wound healing [240].

In vitro, mouse macrophages can be polarised to an 'M1-like' phenotype with lipopolysaccharides (LPS) and interferon-gamma (IFN-γ) or to an 'M2-like' phenotype with interleukin-4 (IL-4), with or without interleukin 13 (IL-13) (Figure. 3.3) [240]. M1-like macrophages release nitric oxide, secrete TNFα, IL-6 and IL-1β and have upregulated expression of Nos2, CD86 and CD38 [243]. M2-like macrophage markers typically include Arg1, CD206 and Retnla [243]. Macrophages are highly plastic cells and are capable of dynamically shifting their phenotype in response to different stimuli [240], [244]. The adaptive ability of macrophages, in a varying cytokine environment, has important implications for developing immunomodulatory therapies [244].

In the field of ECM biomaterials for tissue regeneration, aiming to reduce M1-like macrophage polarisation, whilst increasing M2-like macrophages has generally been seen as beneficial for improving healthy tissue healing [245], [246]. The general consensus has been that ECM influences macrophage polarisation, causing a shift towards a greater M2:M1 ratio, which in turn has been associated with more constructive tissue remodelling outcomes *in vivo* [245]–[247]. In view of its anti-inflammatory effect, ECM hydrogel has been used to coat polypropylene surgical meshes, which attenuated the M1 macrophage expression within the mesh as well as reducing the deposition of mature type 1 collagen that is characteristic of scar tissue [248]. ECM biomaterials do not all have the same effect on macrophages and some types of ECM produce more favourable macrophage responses than others [249]. The efficiency of decellularisation during the manufacture of ECM biomaterials also

influences the macrophage response, with a greater M2 response observed *in vivo* when more acellular ECM is implanted [142].

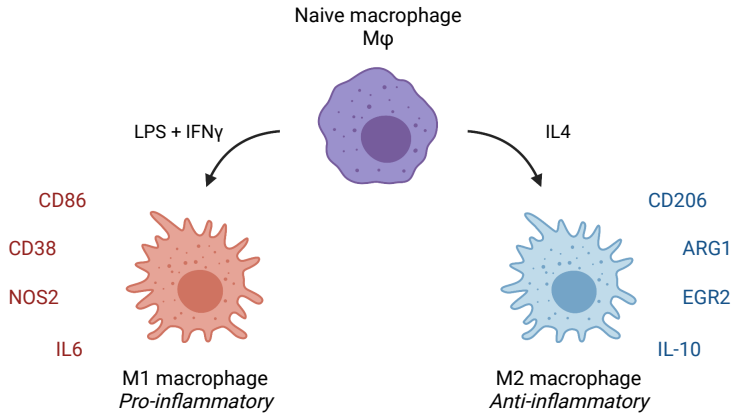


Figure 3.3 Mouse macrophage polarisation *in vitro*. Mouse macrophages can be polarised to an "M1-like" phenotype *in vitro* by stimulation with LPS and IFN-γ. Common markers of M1 phenotype are CD86, CD38, Nos2 and IL6. Treatment of macrophages with IL-4 (+/- IL-13) can polarise the cells to an "M2-like" phenotype, which would be denoted by increased expression of markers such as CD206, Arg1, EGR2 and IL-10. Figure created with BioRender.com.

In vivo, and even *in vitro*, macrophages do not exist as dichotomised populations of M1 and M2 cells but on a spectrum between the two extreme phenotypes and as heterogenous populations of macrophage subtypes [240]. Most ECM biomaterials studies refer only to the M1 and M2 paradigm, with increase in M2 polarisation seen as favourable, and there is a risk of oversimplifying a more complex immune response to biomaterials with this approach. Subtypes of M2 (M2a, M2b, M2c and M2d) have been defined, to differentiate the varied macrophage behaviour, different activation routes and cell surface markers [240], [250]. M2a macrophages are activated by IL-4/IL-13 and play a key role in the initial phase of wound healing as they secrete factors that stimulate fibroblasts and upregulate collagen production [240]. M2c are activated by IL-10, TGF-β and glucocorticoids and appear to have a pro-resolving role as they remodel the matrix through producing matrix metalloproteinases and ECM [240]. Both M2a and M2c express CD206 on their cell surface and secrete high levels of Arginase 1 (Arg1), however they have distinct functions [240]. M2-polarisation *in vitro* is described as the phenotype achieved after IL-4 and IL-13 stimulation and is commonly identified by CD206 expression and Arg1 production [240], however it is yet unclear from existing *in vitro* and *in vivo* studies what proportions of different M2 subtypes are most important for constructive tissue remodelling.

Whilst a predominant M2 phenotype is seen as beneficial for tissue repair, M2-like macrophages are also phenotypically similar to tumor-associated macrophages (TAMs), which play a key role in promoting tumour growth and metastasis [251]. In the context of cancer, an anti-tumour immune microenvironment is one that is more M1-like, where macrophages produce inflammatory cytokines that prevent the invasion of pathogens and cancer cells [252]. Whilst the immune-suppressive and pro-angiogenic nature of M2-like macrophages enable cancer progression [252]. However, implanted ECM biomaterials have experimentally not been shown to promote tumour establishment, growth or metastasis in an animal model [253], or cancer recurrence in humans [254]. In fact, Wolf et al. (2019) demonstrated remarkably that a UBM scaffold implanted in mice generated a tumour-inhibiting immune response and enhanced the action of anti-tumour checkpoint immunotherapies [255].

3.2.4 Angiogenic properties of ECM biomaterials

Neovascularisation is an important process for wound healing and tissue regeneration [256]. The ability to promote angiogenesis is a property that has been demonstrated by decellularised ECM biomaterials both *in vitro* and *in vivo*. Hodde et al. (2001) showed, using human microvascular endothelial cells in an *in vitro* fibrin-based microcarrier bead angiogenesis assay, that addition of SIS ECM extracts to serum-free cell culture medium induced the formation of capillary-like tubes, comparable to the effect seen with the addition of vascular endothelial growth factor (VEGF) [257]. The angiogenesis effect of SIS ECM was attributed to VEGF, as tubes did not form with the addition of an anti-VEGF antibody and VEGF, but not platelet-derived growth factor (PDGF) was detected in the SIS ECM extracts by ELISA [257]. Hoganson et al. (2020) incubated disks of decellularised porcine mesothelium in minimal essential medium to produce an ECM conditioned medium, which was then used for dermal fibroblast culture [258]. VEGF concentration in the cell culture media was then measured by ELISA and was found to be significantly higher when fibroblasts were exposed to mesothelial ECM conditioned media compared to SIS ECM conditioned media and unconditioned medium [258]. The authors suggested that mesothelial ECM likely stimulated VEGF secretion by fibroblasts as the VEGF concentration in the ECM conditioned media alone was minimal [258].

Even after decellularised ECM is pepsin-digested and converted into a hydrogel, it has still been shown to retain and release VEGF upon ECM gel degradation [86]. SIS ECM hydrogel has been shown to promote *in vitro* angiogenesis in a tube formation assay, by culturing endothelial cells directly on top of a layer of SIS ECM hydrogel, and in a mouse aortic ring assay by encasing the aortic ring in SIS ECM

gel [86]. The same authors also studied the *in vivo* angiogenic effect of SIS ECM gel by analysing capillary formation in the tissue surrounding gel implantation [86]. Greater capillary density was found in the tissues surrounding SIS gels compared to control collagen gels and the capillary density was noted to increase with time [86].

In *in vivo* models of diseases characterised by tissue damage, ischaemia and organ failure, improved angiogenesis has been shown when decellularised ECM biomaterials are used for treatment. In murine models of myocardial infarction, injection of SIS ECM hydrogels has led to higher vascular density in as well as improved function [100], [101]. In rat models of hindlimb ischaemia, skeletal muscle ECM promoted endothelial cell infiltration, production of arterioles and improved limb perfusion [135], [259].

3.3 Materials and Methods

3.3.1 Effect of ECM hydrogels on endometrial cells in 2D culture

3.3.1.1 Isolation and culture of primary mouse endometrial epithelial and stromal cells

Primary mouse endometrial cells were isolated following a published protocol [260] from either C57BL/6 strain or CD1 strain female adult mice (≥7 weeks age) (Figure. 3.4). Mouse endometrial epithelial cell (MEEC) medium was prepared with Dulbecco's Modified Eagle Medium, without phenol red (Gibco, Life Technologies) supplemented with 10% (v/v) Fetal Bovine Serum (FBS, Gibco, Life Technologies), 25% (v/v) MCDB-105 medium (Cell Applications), 0.5 μg/mL amphotericin B (Gibco, Life Technologies), 100 μg/mL gentamicin (Sigma-Aldrich) and 5 μg/mL insulin (Gibco, Life Technologies). Mouse endometrial stromal cell (MESC) medium was prepared using Dulbecco's Modified Eagle Medium/Nutrient Mixture F-12 with phenol red (DMEM/F-12, Gibco, Life Technologies), supplemented with 10% (v/v) FBS, 0.5 μg/mL amphotericin B (Gibco, Life Technologies) and 100 μg/mL gentamicin (Sigma-Aldrich). Both media were filtered through a 0.2 μm filter before use.

Mouse uteri were obtained from freshly culled mice. Typically, 3-5 uteri were pooled to obtain enough cells for each experiment. The uteri were rinsed in PBS containing 100 U/mL penicillin and 100 μg/mL streptomycin (PBS+) under a laminar flow hood and the uterine horns were separated from the cervix and any connective tissue or fat. The horns were opened longitudinally and transferred to a solution of PBS+ containing 2.5% (w/v) pancreatin (Sigma-Aldrich) and 0.25% (w/v) trypsin (Sigma-Aldrich). The tissue was incubated in the enzyme mixture for 60 minutes at 4 ^{o}C under gentle agitation, 45 minutes at room temperature without agitation and 15 minutes in a 37 ^{o}C water bath without agitation. After 2 hours, the tissue pieces were transferred to a petri dish containing cold MEEC media to inactivate the enzymes. Then the tissue pieces were transferred to a 15 mL tube containing cold PBS+ and vortexed for 10 seconds to dissociate the epithelial cells. This process was repeated 3 times and the cell suspensions were then pooled and passed through a 100 μm cell strainer. The cells were pelleted by centrifugation at 500 *g* for 5 minutes then resuspended in 12 mL MEEC medium. The solution was allowed to settle for 5 minutes and the top 2 mL was removed to separate any remaining stromal cells. The cells were re-pelleted, then resuspended in MEEC medium and counted manually using a haemocytometer and trypan blue exclusion. After dissociating the epithelial cells, the tissue pieces were transferred to a digestion mixture of 0.05% (v/v) Trypsin-EDTA (Gibco, Life Technologies) containing 10% (v/v) of 10 mg/mL collagenase type IA (Sigma-Aldrich) and incubated at 37 ^{o}C under

vigorous agitation for 30 minutes. The tissue pieces were then transferred to a 15 mL tube containing cold MESC media and the trypsin/EDTA/collagenase digestion mixture was inactivated by adding MESC media. The tube containing the tissue pieces was manually agitated for 10 seconds to release the stromal cells. This process was repeated 3 times and the cell suspensions were then pooled with the inactivated digestion mixture and passed through a 40 μm cell strainer. The cells were pelleted by centrifugation at 500 *g* for 7 minutes then resuspended in fresh MESC media and counted with a haemocytometer. The remaining tissue pieces could be transferred into a fresh trypsin/EDTA/collagenase digestion mixture and the stromal cell isolation process repeated one further time, without agitation during incubation, to obtain more cells.

MEEC were plated on tissue culture plastic pre-coated (1.5 hours at 37 ^{o}C) with 50 μg/mL rat tail collagen I (Corning, Life Sciences) in 0.02 M acetic acid, with the coating solution removed and the surface allowed to dry before cell seeding. MESC were cultured directly on tissue culture plastic. MEEC and MESC were cultured in MEEC or MESC medium, respectively, at 37 ^{o}C and 5% CO_2 overnight then the media was changed to remove any dead or non-adherent cells. The cells were cultured between 24-96 hours depending on the experiment. Epithelial cells could not be successfully passaged, due to poor viability and attachment after passaging. Stromal cells could be passaged, by dissociation with 0.05% (v/v) Trypsin-EDTA (Gibco, Life Technologies), up to 2 times. Three non-genetically modified strains of mice (C57BL/6, Balb-C and CD1) were used for extracting endometrial cells for the *in vitro* studies.

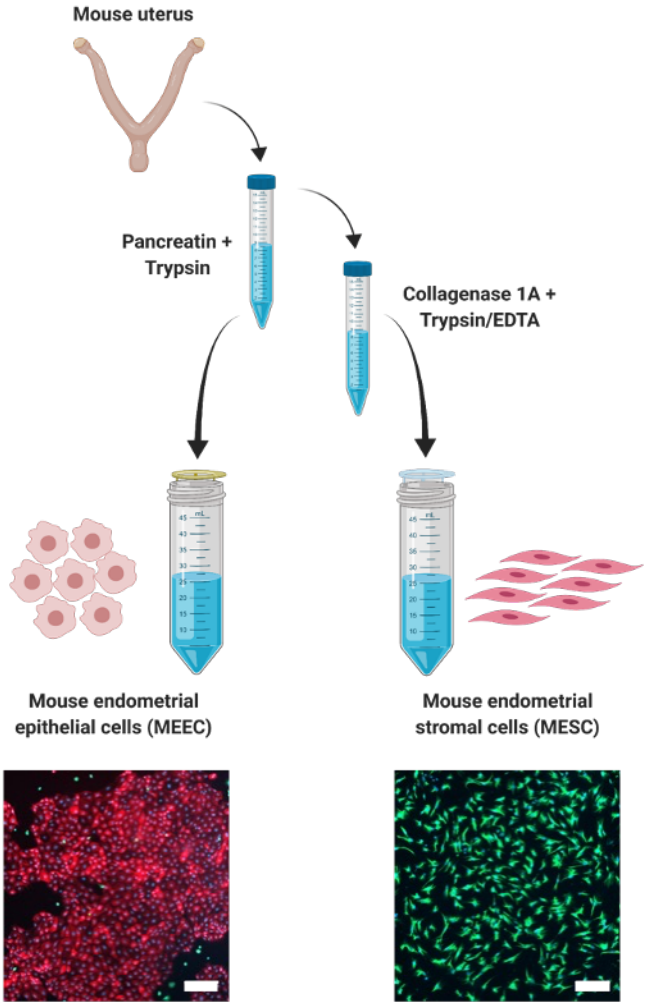


Figure 3.4 Schematic of primary mouse endometrial cell isolation protocol. Following a protocol by De Clercq et al. 2017 [260], involving sequential enzymatic digestion steps, separate populations of MEEC and MESC can be isolated from the mouse uterus. Figure created partly with BioRender.com. The fluorescence microscopy images show MEEC stained with mouse anti-cytokeratin and a fluorescent, anti-mouse secondary antibody (left image) and MESC stained with rabbit anti-vimentin and a fluorescent anti-rabbit secondary antibody (right image). Scale bars = 200 μm.

3.3.1.2 Immunofluorescence of MEEC and MESC

MEECs and MESCs were fixed with 4% (w/v) paraformaldehyde (PFA) then blocked with a buffer containing 0.2% (w/v) BSA, 0.3% (v/v) Triton-X and 5% (v/v) goat serum in PBS for 30 minutes at room temperature. The cells were incubated with mouse monoclonocal anti-cytokeratin 1:1000 (Sigma-Aldrich) and rabbit monoclonal anti-vimentin 1:1000 (Abcam) overnight at 4 °C. The cells were then

co-stained with donkey anti-rabbit Alexa Fluor 488, 1:1000 (ThermoFisher Scientific) and donkey anti-mouse Alexa Fluor 647 1:1000 (ThermoFisher Scientific) in PBS for 1.5 hours at room temperature and DAPI 1:1000 in PBS for 10 minutes (Table 3.1). The cells were washed 3 times with PBS in between each step and as the final step. The stained cells were imaged on a Zeiss Axio Observer Inverted Widefield Microscope (Figure 3.4).

Table 3.1 Primary and secondary antibodies used for immunostaining of MEEC and MESC

Primary antibodies	Secondary antibodies
Mouse monoclonocal anti-cytokeratin (Sigma-Aldrich, C2562), 1:1000	Donkey, anti-mouse Alexa fluor 647 (Invitrogen, A-31571)
Rabbit monoclonal anti-vimentin (Abcam, ab92547), 1:1000	Donkey anti-rabbit Alexa Fluor 488 (Invitrogen, A-21206)

3.3.1.3 Culture of Immortalised Human Endometrial Stromal Cells

Telomerase-immortalised human endometrial stromal cells (ATCC, CRL-4003) were cultured and expanded in growth medium under standard conditions at 37 ^{o}C and 5% CO_2 in a humidified incubator. Human endometrial stromal cell (HESC) growth medium was made from phenol red-free DMEM/F12 with L-glutamine and 15 mM HEPES (Gibco), supplemented with 1% (v/v) Insulin-Transferrin-Selenium (ThermoFisher Scientific), 10% (v/v) fetal bovine serum and 1% (v/v) Penicillin-Streptomycin. The cells were expanded in T175cm^3 culture flasks and the media was refreshed every 3 days until the cells reached 90% confluency. To passage the cells, they were first washed with 5 mL of PBS then detached from the flask using 5 mL Trypsin-EDTA 0.05% (Gibco). Once the cells have detached, 5 mL of growth medium was added to inhibit further enzyme activity and the cell solution was centrifuged at 300 *g* for 5 minutes. The cell pellet was then resuspended in fresh growth medium and cells were counted by Trypan Blue exclusion at a 1:1 ratio, using an automated cell counter.

3.3.1.4 MESC cell viability assay on ECM gel

MESCs were cultured for 48-72 hours until >90% confluence then passaged by trypsinisation. Passage 1 MESCs were used in cell viability experiments. Endometrial (sow) and SIS ECM digests were diluted to a 0.5 mg/mL solution with cold 1x PBS and the solution was used to coat wells in a 24-well plate for 1 hour at 37 ^{o}C. The solution was aspirated from the wells and the wells were left to fully dry before

cell seeding. MESCs were seeded at 30,000 cells per well in the ECM coated wells, or non-coated wells as control, and cultured for 48 hours. The cells were then co-stained with calcein (Invitrogen) and ethidium Homodimer-1 (Invitrogen), both diluted 1:1000 in PBS, for 15 minutes at 37 ^{o}C. The cells were imaged on a Zeiss Axio Observer Inverted Widefield Microscope with a 10x lens objective. For each condition, 3 representative images were taken and the number of live cells and dead cells were quantified using Image-J. An average percentage of live cells was calculated from 3 technical replicates.

3.3.1.5 BrdU ELISA assay

To assess the effect of ECM coatings on the proliferation of endometrial cells, cells were seeded into a 96 well plate coated with 0.5 mg/mL ECM solution and a commercially available BrdU cell proliferation ELISA kit (Abcam, ab126556) was used following the manufacturer's instructions. To prepare the plate, endometrial and SIS ECM digests were diluted to 0.5 mg/mL with cold growth media and triplicate wells in a 96-well tissue culture plate were coated with 100 μL of ECM solution or media alone for 1 hour at 37 ^{o}C. The solutions were aspirated from the wells and the plate was allowed to dry in a laminar flow hood before cell seeding.

To evaluate the proliferation of MEEC and MESC, the primary cells were isolated as previously described and 50,000 cells were seeded per well in a 96 well plate in 100 μL well volume. Triplicate wells were prepared for each ECM coating condition and in these experiments, sow endometrial ECM was compared with SIS ECM. The cells were cultured overnight at 37 ^{o}C and 5% CO_2 to allow attachment and the media was changed the following day to remove dead and non-adherent cells. At the time of media change 1x BrdU was added to the cells, following the manufacturer's protocol, and some extra wells with cells and no BrdU were prepared as background control. The cells were cultured for a further 20 hours before fixing with 200 μL of Fixing Solution for 30 minutes at room temperature.

For HESC, the cells were passaged as previously described and 20,000 cells were seeded per well in 100 μL well volume and 3 technical replicates were plated for each condition. In these experiments, sow endometrial was compared with pig endometrial ECM (batch C – refer to Table 2.4) and pig endometrial ECM (batch C – refer to table 2.4) was compared with SIS ECM. 1x BrdU was added to the cells, as per manufacturer's protocol, and some extra wells containing cells did not have any BrdU added to serve as a background control. The cells were cultured at 37 ^{o}C and 5% CO_2 for 23 hours and then fixed as previously described.

After removing the fixing solution, the plate was thoroughly dried and washed 3 times with 1x Wash Buffer. Anti-BrdU monoclonal detector antibody solution was added to each well (100 μL/well) and incubated for 1 hour at room temperature before washing the wells 3 times with 1x wash buffer. 1x peroxidase goat anti-mouse IgG conjugate was added to each well (100 μL/well) and incubated for 30 minutes at room temperature. The wells were washed 3 times with 1x wash buffer and once with type 1 water, then 100 μL/well of TMB substrate solution was added to each well and incubated for 30 minutes at room temperature in the dark. Finally, 100 μL of Stop Solution was added into each well to stop the reaction and the plate was read at 450nm absorbance on a plate reader (SpectraMax M5). All components used for the BrdU ELISA were supplied with the kit.

3.3.2 Angiogenesis potential of ECM hydrogels

3.3.2.1. Tubule formation assay - cell culture and experimental setup

This protocol was designed and optimised with the assistance of Dr Junyoung Kim and Dr Tom Whittaker. Red fluorescent protein expressing human umbilical vein endothelial cells (HUVEC) were cultured in complete endothelial cell growth medium, containing fetal bovine serum and all supplements supplied by the manufacturer for endothelial cell growth (Table 3.2) under standard culture conditions. Cells lower than passage 8 were used for angiogenesis assays. Six hours prior to the start of the assay, the cells were starved by exchanging the complete media for EBM™-2 Basal Medium (Lonza, CC-3156).

Table 3.2 Components of complete endothelial cell growth medium

Component		**Volume**
EBM™-2 Basal Medium (Lonza, CC-3156)		500 mL
EGM™-2 Endothelial SingleQuots™ Kit (Lonza, CC4176)	FBS	10 mL
	Hydrocortisone	0.2 mL
	h-FGF-B	2 mL
	VEGF	0.5 mL
	R3-IGF-1	0.5 mL
	Ascorbic acid	0.5 mL
	hEGF	0.5 mL
	GA-1000	0.5 mL
	Heparin	0.5 mL

In preparation for cell seeding, 10 μL of ice-cold, undiluted growth factor-reduced Geltrex™ (Gibco) was added to each well of a 96-well angiogenesis plate (Ibidi) on ice. The plate was sealed with parafilm, centrifuged for 1 minute at 50 *g* then transferred to a 37 °C incubator for gelation. Endometrial ECM supplemented media were prepared by mixing cold, pig endometrial ECM digest with cold basal medium or complete medium to a final concentration of 200 μg/mL or 400 μg/mL of ECM. The media were then kept at room temperature until use. Batch C pig endometrial ECM digest was used for these experiments (refer to table 2.4)

HUVECs were passaged by removing the media, washing the cells once with sterile PBS, then incubating the cells with 0.25% (v/v) Trypsin/EDTA (Gibco) for 5 minutes at 37 °C. After confirming cell detachment, basal media was added to the cells to deactivate the enzyme activity and the cell solution was transferred to a falcon tube and centrifuged at 300 *g* for 5 minutes. The cell pellet was resuspended in 1-2 mL of basal media and the cells were counted by trypan blue exclusion using a Countess II FL automated cell counter (Thermo Fisher). The cell solution was mixed thoroughly, then divided equally in volume into 4 new falcon tubes. All tubes were centrifuged to pellet the cells and the cells were resuspended to a concentration of 2 x 10^5 cells/mL in either basal media, basal media + ECM 200 μg/mL, basal media + ECM 400 μg/mL, complete media, complete media + ECM 200 μg/mL or complete media + 400 μg/mL. 50 μL of cell solution (containing 1 x 10^4 cells) was carefully added to each well, on top of the Geltrex™. A minimum of 6 technical replicates were plated to account for experimental variability. The cells were cultured under standard conditions for 21 hours.

3.3.2.2 Tubule formation assay - image acquisition and analysis

Live cells were imaged using a 2.5x objective on a Zeiss Axio Observer inverted widefield fluorescent microscope in the Texas red fluorescence channel. Fixation was not performed to avoid washing the wells and potentially disrupting the gels or tubule network. The images were processed on ImageJ (v1.53c) using the Angiogenesis Analyzer plugin, after cropping the images circularly to exclude the edges of the wells and converting the well images to a binary image by thresholding. Of the multiple readouts generated by the plugin, total tubule length, number of branches and number of junctions were assessed and plotted for each condition.

3.3.2.3 Human VEGF ELISA assay

Endometrial ECM digest (pig, batch C) and SIS ECM digest were first diluted to 500 μg/mL in cold HESC growth medium. Wells of a 96-well plate were then coated with 50 μL of endometrial ECM 500 μg/mL or SIS ECM 500 μg/mL or growth medium alone and incubated for 1 hour at 37 °C. All coating solutions were removed and the wells were allowed to dry in a laminar flow hood before cell seeding. HESCs were passaged as previously described in section 3.2.1.3, resuspended in HESC growth medium and seeded at 2 x 10^4 cells per well in 100 μL well volume. Three technical replicates were plated for each condition. The cells were cultured for 24 hours in standard conditions after which the supernatant was collected from each well and stored at -80 °C until ready for use.

VEGF ELISA was performed by PhD student Aida Abdelwahed, using a commercially available kit (Abcam ab222510) and following the manufacturer's instructions. All reagents required for the assay were supplied within the kit. First, the supernatant was thawed on ice and centrifuged to remove any cell debris. Eight VEGF standards were prepared in sample diluent with enhancer, ranging from 0 pg/mL to 800 pg/mL. A pilot experiment identified 1:4 and 1:8 dilutions as being optimal for the assay. The supernatants were therefore diluted to 1:4 or 1:8 in sample diluent with enhancer. The standard (50 μl/well) and diluted supernatants (50 μL/well) were transferred into a Simple-Step ELISA® pre-coated 96 well plate. Blank wells were also prepared containing just the growth medium. The wells were incubated with an antibody cocktail, containing the capture antibody and detector antibody, for 1 hour at room temperature on an orbital shaker set to 400 rpm. The plate was then washed three times with wash buffer and the wells were then incubated with TMB solution (100 μL/well) for 10 minutes, under agitation, in the dark. Stop solution (100 μL/well) was added to the wells and the plate shaken for 1 minute. The plate was then read straight away on a plate reader (SpectraMax M5) at 450nm absorbance.

To analyse the data, averages were taken for the fluorescence readings for the standard curve and the sample dilutions. After subtracting the blank, a standard curve was plotted from 0 pg/mL to 800 pg/mL and a linear regression was fitted. The VEGF concentrations of the samples were calculated using the linear regression equation and multiplied by the relevant dilution factor. An average concentration was taken across multiple dilutions. Results were excluded if they were outside of the linear portion of the standard curve.

3.3.3 Endometrial organoid culture in ECM hydrogels

3.3.3.1 Endometrial organoid culture

All human endometrial organoid experiments were performed by or with Dr Tom Rawlings in Professor Jan Brosens' laboratory in the Clinical Sciences Research Unit at University Hospitals Coventry and Warwickshire. The endometrial organoids were derived from primary endometrial epithelial cells from patient endometrial biopsies and obtained from Arden Tissue Bank, University Hospitals Coventry and Warwickshire (REC reference 18/SC/0180). Preparation and culture of endometrial organoids were carried out by Dr Rawlings following the published protocol by Turco et al. (2017) [205]. The organoids were first formed in Matrigel and cultured in expansion medium containing the components listed in Table 3.3 [213].

Table 3.3 Components of human endometrial organoid expansion medium [213]

Component	Concentration
Advanced DMEM/F12	1x
N2 supplement	1x
B26 supplement minus vitamin A	1x
Primocin	100 μg/mL
N-Acetyl-L-cysteine	1.25 mM
L-glutamine	2 mM
Recombinant human EGF	50 ng/mL
Recombinant human Noggin	100 ng/mL
Recombinant human Rspondin-1	500 ng/mL
Recombinant human FGF-10	100 ng/mL
Recombinant human HGF	50 ng/mL
A83-01 (ALK-4, -5, -7 inhibitor)	500 nM
Nicotinamide	10 nM

After culturing for 7-10 days, the organoids were passaged (P1 to P2) into Matrigel (control) or ECM hydrogels (Figure. 3.5), following a published protocol [213]. In brief, without removing the medium, the Matrigel droplet containing organoids was mechanically disrupted with a pipette tip and the

contents of each well transferred to 1.5 mL microcentrifuge tubes. The samples were centrifuged at 600 *g* for 6 minutes to pellet, then the supernatant was removed. 200 µL of Advanced DMEM/F12 medium (Gibco) was added to the pellet and pipetted up and down 300 times with a P200 pipette tip, to break up the organoids and Matrigel. Subsequently, 1 mL of Advanced DMEM/F12 medium was added to each tube and the samples were centrifuged again. After removing the supernatant, 200 µL of Advanced DMEM/F12 medium was added again and the pellet disrupted by manually pipetting 80 times. 1 mL of medium was added to each tube and the samples were centrifuged a third time, followed by removal of the supernatant to leave a pellet of organoids with minimal Matrigel. The tubes were then placed on ice and ice-cold Matrigel or neutralised 8 mg/mL ECM hydrogel (prepared as previously described) were added to each tube and gently mixed with the organoids. To plate the organoids, a 20 µL droplet of Matrigel or ECM hydrogel containing the passaged organoids was placed carefully in the centre of a well of a pre-warmed 24-well imaging plate (Ibidi) and the plate was transferred to a 37 °C incubator for 15 minutes to allow gelation to occur. Then, 250 µL of warm expansion medium was added to each well and the organoids were cultured at 37 °C in 5% CO_2, for 7-days with media change every 2-3 days. Three technical replicates and three biological replicates were plated for Matrigel and each of SIS, UBM and Endometrial (sow) 8 mg/mL ECM hydrogel.

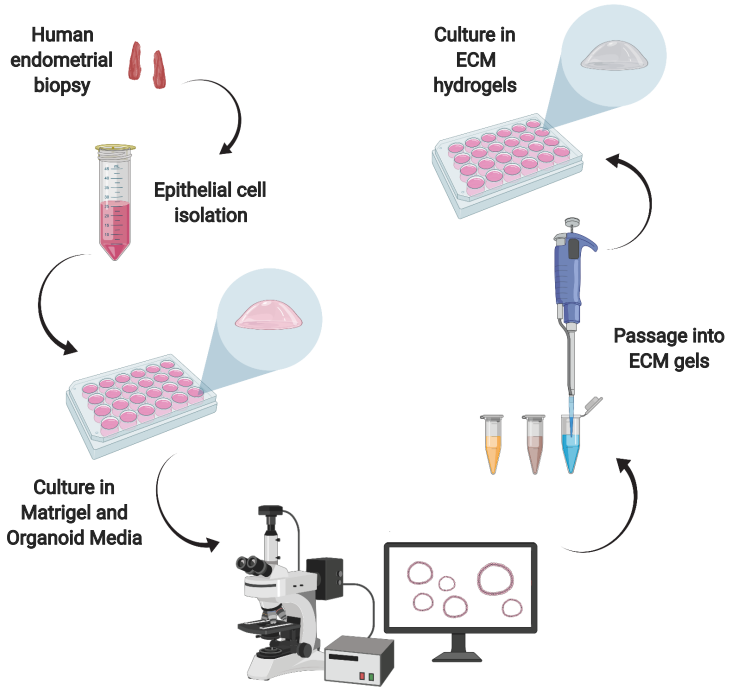


Figure. 3.5 Schematic of human endometrial organoid culture in ECM hydrogels. The protocol is described in section 3.3.3.1. Figure created with BioRender.com.

3.3.3.2 Immunofluorescence staining and imaging of endometrial organoids

After 7 days of culture, the organoids were fixed by immersing the whole gel droplet in 4% (w/v) PFA at room temperature for 30 minutes, followed by 3 washes with 1x PBS. For immunofluorescence staining and confocal imaging, the whole droplet was stained in the well. The organoids were blocked with blocking buffer containing 5% (v/v) goat serum, 0.2% (w/v) BSA and 0.3% (v/v) Triton X-100 in PBS, for 30 minutes at room temperature. Primary antibody staining was performed with mouse monoclonocal anti-cytokeratin 1:200 (Sigma-Aldrich) and rabbit monoclonal anti-vimentin 1:200 (Abcam), (see Table 3.1) at 4 ^{o}C overnight. Secondary antibody staining was performed with goat anti-mouse Alexa Fluor 488, and goat anti-rabbit Alexa Fluor 594, both at 1:400 in blocking buffer for 2 hours at room temperature. DAPI 1:1000 was then added to the gel droplets for 15 minutes, followed by 3 washes in 1x PBS. Fluorescently stained organoids were imaged on a Leica SP8 inverted confocal microscope at 20x magnification.

Table 3.4 Primary and secondary antibodies for immunostaining of endometrial organoids

Primary antibodies	Secondary antibodies
Mouse monoclonocal anti-cytokeratin (Sigma-Aldrich, C2562), 1:200	Goat, anti-mouse Alexa Fluor 488 (Invitrogen, A-11001)
Rabbit monoclonal anti-vimentin (Abcam, ab92547), 1:200	Goat, anti-rabbit Alexa fluor 594 (Invitrogen, A-11012)

3.3.3.3 Organoid formation efficiency assay

For this experiment, the human endometrial organoids were grown initially in Matrigel for 7-10 days following the published protocol [213]. The organoids were then passaged into single cells, following the previously described steps but substituting Advanced DMEM/F12 medium with 200 μL of warm TrypLE^{TM} (Gibco) diluted 1:2 in PBS when disrupting the pellet with manual pipetting. After centrifuging at 600 *g* for 4 minutes and removing the TrypLE^{TM} solution, 200 μL of Advanced DMEM/F12 medium was added to the pellet and pipetted up and down. The tube was centrifuged again and the pellet was resuspended in 500 μL of medium and the cells were counted using an automated cell counter. The cells were first resuspended in medium at 300 cells per μL, then mixed with ice-cold Matrigel or neutralised ECM hydrogels at a concentration of 15 cells per μL of gel. A 20

μL droplet of gel (containing 300 cells per droplet) was placed in the centre of each well in a pre-warmed 24-well imaging plate (Ibidi) and the plate was incubated at 37 °C for 20 minutes to allow the gels to set, before adding 200 μL of media to each well. Three technical replicates and three biological replicates were plated for each of the following conditions: Matrigel (control), endometrial 2 mg/mL gel, endometrial 5 mg/mL gel and endometrial 8 mg/mL gel. Sow endometrial hydrogel was used for this experiment. The organoids were cultured for 7 days under standard conditions then fixed with 4% PFA. The number of organoids in each well was manually counted under a brightfield microscope.

3.3.4 *In vitro endometrial* fibrosis modelling

3.3.4.1 Preparation of TGF-β1 for cell culture experiments

Recombinant human TGF-β1 (Peprotech), which has cross-reactivity with the mouse, was first reconstituted with citric acid 10 mM to 0.5 mg/mL. The solution was then diluted to 50 μg/mL with 0.1% (w/v) bovine serum albumin. Aliquots of TGF-β1 50 μg/mL were stored at -20 °C until required for cell experiments. Multiple freeze-thaws of TGF-β1 were avoided.

3.3.4.2 Stimulation of primary mouse endometrial cells with TGF-β1

Primary mouse endometrial epithelial cells and stromal cells were isolated as previously described in section 3.2.1.1. Freshly isolated mouse endometrial stromal cells (MESC) were plated at 100,000 cells per well in a 24 well plate and cultured in MESC growth medium, which contained 10% serum. After allowing the cells to attach overnight, the media was changed on day 1 to remove any non-adhered and dead cells. TGF-β1 10 ng/mL was diluted in PBS and added to the cells on day 2. For the control condition, no TGF-β1 was added. As serum may contain growth factors that mask or interfere with the activity of additional TGF-β1, the same experiment was performed using MESC medium containing 0.5% serum, with a switch to this low serum medium from day 1. Preliminary studies had been carried out showing that there was adequate cell survival with 0.5% serum in the media, however primary cells died during the experiment when cultured in the complete absence of serum. MESCs were cultured for 24 to 120 hours. Cells were either fixed in 4% PFA for immunofluorescence staining or treated with TRIzol™ reagent at 24-hourly timepoints and stored at -80 °C until ready for RNA extraction.

The same experiment was planned with primary mouse endometrial cells. Unfortunately, due to inadequate yields of primary epithelial cells, sufficient replicates could not be performed for the experiments.

3.3.4.3 Immunofluorescence and imaging

After fixation and washes with PBS, MESCs were blocked with a buffer containing 0.2% (w/v) BSA, 0.3% (v/v) Triton-X and 5% (v/v) goat serum in PBS for 30 minutes at room temperature. The cells were incubated with rabbit monoclonal anti-vimentin 1:1000 (Abcam) in blocking buffer overnight at 4 ^{o}C and secondary antibody staining was performed with donkey anti-rabbit Alexa Fluor 488, 1:1000 (Invitrogen) in PBS (See Table 3.1) for 1.5 hours at room temperature. The cells were then stained with a Cy3-conjugated, anti-mouse antibody against α-SMA (Sigma-Aldrich, C6198) diluted 1:200 in PBS, for 1.5 hours at room temperature. Finally, DAPI staining was performed (1:1000 in PBS) for 10 minutes. The cells were washed 3 times with PBS in between each incubation step and as the final step. The stained cells were imaged on a Zeiss Axio Observer Inverted Widefield Microscope.

3.3.4.4 RNA isolation

Cells in TRIzol^{TM} were transferred to labelled 1.5 mL microcentrifuge tubes and 0.2 mL of chloroform was added per 1mL of TRIzol^{TM} reagent. With the caps closed, each tube was vigorously agitated for 15 seconds and incubated for 3 minutes at room temperature. The samples were then centrifuged at 12,000 *g* at 4 ^{o}C for 15 minutes to phase separate the RNA. The aqueous phase, containing the RNA, was then carefully collected from each sample and transferred to a new 1.5 mL microcentrifuge tube. An equal volume of 70% ethanol was added to the aqueous phase in each tube and mixed by pipetting. RNA purification was then performed using the RNeasy mini kit (Qiagen) following the manufacturer's protocol. In brief, the samples were transferred to spin columns containing a silica membrane and centrifuged. The membranes were washed with RW1 and RPE buffers, supplied in the kit, and the final, pure RNA was eluted from the membrane with 50 μL of nuclease-free water. The RNA concentrations were measured on Nanodrop and the RNA was stored at -80 ^{o}C if not immediately proceeding with cDNA synthesis.

3.3.4.5 cDNA synthesis

RNA samples were first diluted with nuclease-free water so that all samples contained the same quantity (1000 ng or 2000 ng) and concentration (83.3 ng/μL) of RNA. cDNA synthesis was performed using the QuantiTect™ Reverse Transcription kit (Qiagen), following the manufacturer's protocol. All reagents used were supplied within the kit. First, 2 μL of gDNA Wipeout Buffer was added to each 12 μL of diluted RNA sample to make a final volume of 14 μL per reaction inside a 0.5 mL PCR tube. The samples were then incubated for 2 minutes at 42 °C in a thermal cycler (LifePro, Bioer) and immediately transferred to ice. Then a master mix was prepared containing, per reaction, 1 μL of Quantiscript reverse transcriptase, 4 μl of Quantiscript RT Buffer 5x and 1 μL of RT Primer Mix. To each 14 μL of template RNA, 6 μL of master mix was added and incubated for 15 minutes at 42 °C, followed by 3 minutes at 95 °C in a thermal cycler (LifePro, Bioer). The cDNA samples were then stored at -20 °C if not immediately used for RT-qPCR.

3.3.4.6 RT-qPCR

The cDNA was diluted to desired working concentration (10 ng/μL) with nuclease-free water prior to RT-qPCR. RT-qPCR was performed using Taqman Fast Advanced Master Mix (Applied Biosystems) and Taqman gene assays, following the manufacturer's protocol. For MESCs, the TaqMan FAM-MGB conjugated gene assays for *Acta2* and *Cola1a1* were used (Table 3.5). The reactions were run in a 384-well MicroAmp EnduraPlate microplates (Applied Biosystems) using the QuantStudio™ 6 Flex Real-Time PCR system and accompanying software. Each well contained 5.0 μL of Taqman Fast Advanced Master Mix, 0.5 μL of Taqman gene assay, 3.5 μL of nuclease free water and 1 μL (10 ng) of cDNA. Three technical replicates were plated for each sample in each experiment. The following thermal cycling profile was set for each plate run: hold step 2 minutes at 50 °C, hold step 20 seconds at 95 °C, 40 cycles of PCR including denaturing step of 1 second at 95 °C followed by annealing step of 20 seconds at 60 °C. The CT values were automatically calculated by the software and raw values were exported as an Excel spreadsheet. The data was analysed with the delta delta CT (ΔΔCT) method, using the CT mean values with normalisation to the *GAPDH* housekeeping gene (Table 3.4) and experimental controls. Relative fold changes in gene expression were calculated by $2^{-(\Delta\Delta CT)}$.

Table 3.5 Taqman gene assays used for RT-qPCR analysis of MESC treated with TGF-β1

Gene	Taqman assay ID	Protein encoded	Relevance of gene
GAPDH	Mm99999915_g1	Glyceraldehyde-3-phosphate dehydrogenase	Housekeeping gene
Acta2	Mm00725412_s1	α-smooth muscle actin	Myofibroblast marker. Upregulated in fibrosis
Col1a1	Mm00801666_g1	Collagen 1 alpha 1 chain	Upregulated in fibrosis

3.3.4.7 Stimulation of endometrial organoids with TGF-β1

Human endometrial organoids were cultured, as previously described, by Dr Tom Rawlings and the organoid experiment was performed by Dr Rawlings in the Clinical Sciences Research Unit at University Hospitals Coventry and Warwickshire. The aim of this experiment was to see whether stimulating endometrial organoids with TGF-β1 would induce morphological changes to the epithelial cells and induce or increase expression of fibroblast and myofibroblast markers. Human endometrial organoid expansion medium contains A83-01, a TGF-β receptor inhibitor (Table 3.3) [213]. Therefore, to be able to evaluate the effect of TGF-β1 on epithelial organoids it was necessary to culture them in media that omitted A83-01 and contained TGF-β1. Four versions of organoid expansion media were prepared: I) normal expansion medium (control), II) normal expansion medium supplemented with TGF-β1 10 ng/mL, III) expansion medium prepared without A83-01, and IV) expansion medium prepared without A83-01 and supplemented with TGF-β1 10 ng/mL. Passage 1 organoids were cultured from three donors in normal expansion medium in Matrigel as previously described (section 3.2.3.1). After 7 days of culture, the organoids were passaged (passage 2) into Matrigel, as previously described and one 20 μL droplet of Matrigel containing organoids, was added to each well in a 24-well plate. The organoids were cultured for four days in normal expansion medium, then the media was changed to one of the four different versions of expansion media. Technical duplicates of each donor and each condition were prepared. The organoids were cultured for a total of 10 days before being fixed in 4% PFA for staining, as described in section 3.2.3.2. Organoid morphology was inspected by brightfield microscopy before, during and after the experiment. Brightfield images were taken of the organoids at the end of the experiment.

3.3.4.8 Immunofluorescence and imaging of endometrial organoids

Immunofluorescence staining was performed in the plate as previously described in section 3.2.3.2. Primary antibody staining was performed with mouse monoclonocal anti-cytokeratin 1:200 (Sigma-Aldrich) and rabbit monoclonal anti-vimentin 1:200 (Abcam) (see Table 3.4) at 4 ^{o}C overnight. The secondary antibodies used were goat anti-mouse Alexa Fluor 488, and goat anti-rabbit Alexa Fluor 594 (See table 3.4), both at 1:400 in blocking buffer for 2 hours at room temperature. Additional staining was performed with an anti-mouse antibody against α-SMA which was conjugated to Cy3 (Sigma-Aldrich C6198) at 1:400 dilution in blocking buffer for 1.5 hours at room temperature. Finally, DAPI staining was performed for 15 minutes and the wells were then washed 3 times with 1x PBS. The plate was imaged on a Zeiss Axio Observer inverted widefield microscope with a 20x lens objective.

3.3.4.9 Fibrosis modelling with cell-derived matrices

3.3.4.9.1 General Cell Culture

Primary human dermal fibroblasts (ATCC, PCS-201-012) were cultured under standard conditions at 37 ^{o}C and 5% CO_2 in a humidified incubator. The cells were cultured in growth medium consisting of Dulbecco's Modified Eagle Medium with 4.5g/L glucose (Gibco), supplemented with 10% (v/v) fetal bovine serum and 1% (v/v) Penicillin-Streptomycin. The cells were expanded in T175cm^3 culture flasks and the media was refreshed every 3 days until the cells reached 90% confluency. The passaging method was the same as described for human endometrial stromal cells. Only cells that were above 90% viability were used for subsequent experiments.

HESCs (ATCC, CRL-4003) were cultured and passaged as previously described. Only cells that were above 90% viability were used for subsequent experiments.

3.3.4.9.2 Production of Cell-Derived Matrices

Cell-derived matrices (CDM) were prepared from primary human dermal fibroblasts (HDF) and from immortalised human endometrial stromal cells (HESC) using a protocol adapted from Kaukonen et al. (2017) [261] (Figure. 3.6). HDF CDM experiments were performed in collaboration with PhD student, Charlotte Lee-Reeves. HESC CDM experiments were performed independently by this author. In

preparation for cell culture, a 24-well cell imaging plate (Ibidi) was coated with 0.2% (w/v) sterile gelatin solution (Sigma-Aldrich) at 37 °C for 1 hour. The gelatin coating was cross-linked with 1% (v/v) sterile glutaraldehyde for 30 minutes, then the glutaraldehyde was quenched with 1 M sterile glycine for 20 minutes at room temperature. The wells were incubated with growth medium for 1 hour before cell seeding. HDFs or HESCs were cultured at 6 x 10^4 cells per well at 37 °C and 5% CO_2 for 3 days until a confluent monolayer had formed. At this point the media was changed, and the cells were treated with either TGF-β1 10 ng/mL (Peprotech), TGFβ1 10 ng/mL and pig endometrial ECM (batch C) hydrogel 500 μg/mL or growth medium alone (Figure. 3.6). The endometrial ECM hydrogel was added to the wells using Transwell® cell culture inserts with 3.0 μm pore size (VWR). Endometrial ECM digest was diluted to 500 μg /mL with fibroblast growth medium and 250 μL of diluted digest was added to a Transwell® insert and incubated for 20 minutes at 37 °C before transferring to the plate containing cells. The cells were cultured for a further 12 days with media change and fresh TGFβ1 10 ng/mL and ECM hydrogel 500 μg/mL every 2-3 days. At least 2 technical replicates were plated for each experiment and three biological replicate experiments were performed using either consecutive cell passages or the same passage cells expanded in different flasks.

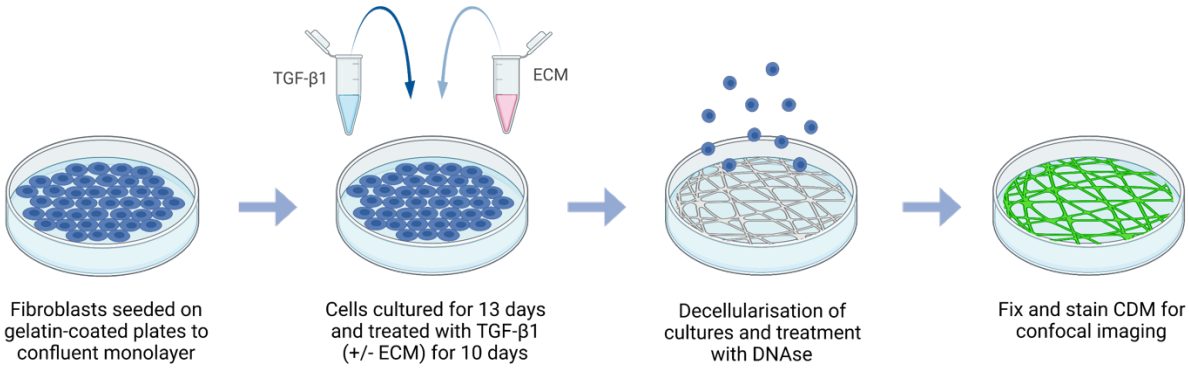


Figure 3.6 Schematic of protocol for production, decellularisation and staining of CDM. Protocol adapted from Kaukonen et al. 2017 [261]. Figure created with BioRender.com.

3.3.4.9.3 Decellularising and Staining Cell-Derived Matrices for Imaging

After five media changes, the CDM were decellularised by treating the cells with warm 2% (v/v) ammonium hydroxide and 0.5% (v/v) Triton X-100 in PBS for 2-3 minutes at room temperature, followed by 2 gentle washes with PBS. Residual cellular DNA was removed by incubating the CDM with DNase I 10 μg/mL (Roche) in PBS for 30 minutes at 37 °C, followed by 2 gentle washes with PBS. The

CDM were fixed in the plate with 4% (w/v) paraformaldehyde for 15 minutes at room temperature before staining for collagen I, fibronectin or a general amine reactive dye (Table 3.6) for image analysis of deposited ECM. For collagen I and fibronectin staining, CDM were blocked with 30% (v/v) goat serum for 30 minutes and then incubated with anti-collagen I antibody diluted 1:300 in PBS at 4 ^{o}C overnight followed with 3 washes with PBS. The CDM were then stained with secondary donkey anti-rabbit Alexa-Fluor 488 for 1 hour at room temperature. For amine staining, Oregon Green™ 488 Carboxylic Acid, Succinimidyl Ester (Invitrogen) (Table 3.6) was resuspended at 10 mg/mL in DMSO then mixed into 50 mM HEPES (pH 8.5) at 1:10 dilution. CDM were incubated with the Oregon Green solution for 90 minutes under gentle agitation at room temperature, then washed 3 times with 50 mM HEPES buffer and stored in 1x PBS.

Table 3.6 Antibodies and amine reactive dye used for staining CDM for fluorescence imaging

Primary antibodies	**Secondary antibody**
Anti-rabbit Collagen I (Novus Biologicals, NB600-408), 1:300	Donkey anti-rabbit Alexa Fluor 488 (Invitrogen, A-21206)
Anti-Rabbit Fibronectin, 1:200 (Abcam ab23751)	
Amine dye	
Oregon Green™ 488 Carboxylic Acid, Succinimidyl Ester (Invitrogen, O6147)	

3.3.4.9.4 Image acquisition and analysis

Stained CDM were imaged with a Leica SP8 inverted confocal microscope using a 63x oil immersion objective. Confocal imaging was performed in collaboration with PhD Student, Charlotte Lee-Reeves. Z-stack scans were taken at 3 random locations in the well for each condition. All image files were processed and analysed in ImageJ (Software version 1.52) and subjected to the same processing steps. The z-stacks were transformed into a single image using maximum intensity projection. The DiameterJ plugin was used to batch process the images, converting each image into a binary mask and segmenting the images for downstream analysis. The segmented images were then analysed using the OrientationJ plugin to measure the alignment of the matrix fibres, output as a coherence score between 0-1. Results were averaged across all images for the same condition. The plugin also generates a histogram showing the distribution of the orientation of the structures (fibres) within the image at each angle of orientation.

3.3.5 Immunomodulatory effects of ECM hydrogels

3.3.5.1 RAW 264.7 cell culture

RAW 264.7 (ATCC® TIB-71™) is a mouse macrophage cell line. The cells were cultured in growth medium consisting of Dulbecco's Modified Eagle Medium with 4.5 g/L glucose (Gibco), supplemented with 10% (v/v) fetal bovine serum and 1% (v/v) Penicillin-Streptomycin, in T-175cm^2 flasks at 37 ^{o}C and 5% CO_2. The cells were passaged when they reached 90% confluence. After removing the media, the cells were washed twice with PBS and then dissociated with 7 mL ice-cold 5 mM EDTA in PBS for 5 minutes and the flask was then manually agitated to aid detachment of the cells. An equal volume of growth medium was then added to the cells before they were collected, pelleted by centrifugation and resuspended in fresh growth medium for subsequent culture. Cells were used for experiments within 1-2 passages after thawing.

3.3.5.2 Macrophage polarisation and ECM treatment of unpolarised macrophages

RAW 264.7 cells were seeded at 1 x 10^6 cells (5 x 10^5 / mL) per well in 6 well plates and allowed to attach overnight. For polarisation to M1-like phenotype, Lipopolysaccharides (LPS) from E.Coli 0111:B4 (Sigma-Aldrich) 100 ng/mL and recombinant mouse interferon-gamma (IFN-γ) (R&D systems) 20 ng/mL were added to the well (M1 control). For polarisation to M2-like phenotype, Interleukin-4 (IL-4) (Peprotech) 20 ng/mL was added to the well (M2 control). Unstimulated (Mφ control) macrophages were cultured in growth medium alone. To assess the effect of ECM hydrogels on Mφ macrophages, ECM hydrogel was added into the wells to a final concentration of 500 μg/mL. All cells were cultured for a further 24 hours from the initial time of cytokine or ECM addition.

3.3.5.3 Macrophage polarisation followed by ECM treatment

RAW 264.7 cells were seeded at 5 x 10^5 cells (2.5 x 10^5 /mL) per well in 6 well plates and allowed to attach overnight to reach 55-60% confluence. For polarisation to M1-like phenotype, LPS 100 ng/mL and IFNγ 20 ng/mL were added to the well. After 2 hours of stimulation, the LPS and IFNγ were removed by changing the media in the wells to fresh growth medium (M1 2 hour control), or fresh growth medium containing pig endometrial ECM hydrogel (batch C) 500 μg/mL. For the unstimulated macrophage (Mφ) control, no cytokines were added to the media, but the media was changed at 2

hours when LPS and IFNγ were removed from the M1 wells. For polarisation to M2-like phenotype, IL-4 20 ng/mL and IL-13 (Peprotech) 20 ng/mL were added to the well (M2 control). IL-13 was used, in addition to IL-4, after observing insufficient M2 polarisation response with IL-4 alone. As an additional comparison, Mφ macrophages were also treated with endometrial ECM hydrogel 500 μg/mL. All cells were cultured for 24 hours from the initial time of cytokine addition. Brightfield images were taken at each time point to track the changes in cell morphology.

3.3.5.4 Flow cytometry

To collect samples for flow cytometry, the media was removed and the cells washed with cold PBS before being dissociated with ice-cold 5 mM EDTA in PBS for 10 minutes on ice. The cells were collected into Eppendorf tubes and pelleted by centrifugation at 400 *g* for 5 minutes. The cells were then washed with PBS, pelleted and resuspended in CD16/CD32 monoclonal antibody (Invitrogen, 14-0161-82) diluted 1:100 in 10% (v/v) FBS for 10 minutes on ice, to minimise non-specific binding. After washing and pelleting, the cells were then stained with APC-conjugated CD86 monoclonal antibody (eBioscience™, 17-0862-82) and PE-conjugated CD206 monoclocal antibody (eBioscience™, 12-2061-82) for 30 minutes on ice. Finally, the cells were washed, pelleted, fixed with 4% PFA for 10 minutes at room temperature, washed again with PBS and resuspended in 500 μL volume PBS. For the compensation panel, ebeads (Thermo Fisher Scientific) were stained separately with each fluorophore-conjugated antibody. The samples were assessed within 48 hours of staining on a Fortessa I flow cytometer and the results were analysed using FlowJo software (Version 9.0.1).

In Flowjo, the macrophage population was first gated manually based on the forward scatter (FSC) versus side scatter (SSC) plot of naïve (Mφ) macrophages and the same gate was applied to all samples in the same experiment but each sample was checked to ensure that the gating was appropriate (Appendix Figure A). Where necessary, the gate was adjusted manually to include the majority of cells. To determine positive staining for CD86 and CD206, a gate was applied around the blank, unstained cells in a CD86 versus CD206 density plot (Appendix Figure A viii). This gate was then applied to all samples in the same experiment and enabled the identification of proportions of CD86+ CD206-, CD86- CD206+ and CD86+ CD206+ cells.

3.3.5.5 Preparation of samples for RT-qPCR

At the end of the experiment, 24 hours after cytokine addition, the media was removed from the cells and TRIzol™ reagent (Invitrogen) was added to each well. The plates were transferred to -80 °C for later RNA isolation.

3.3.5.6 RNA isolation and cDNA synthesis

Cells in TRIzol™ were thawed and RNA isolation was performed as described in 3.3.4.4. RNA concentrations were measured using Nanodrop and then cDNA synthesis was performed as described in 3.3.4.5.

3.3.5.7 RT-qPCR

RT-qPCR was performed as described in 3.3.4.5. Table 3.7 shows a list of the TaqMan FAM-MGB conjugated gene assays used. Preliminary RT-qPCR experiments were performed to test the stability of expression of *GAPDH* and *Actb* across all samples. The expression of *GAPDH* was found to be altered by LPS and IFNγ treatment of macrophages, whilst *Actb* expression remained most stable across all samples, so this was chosen as the housekeeping gene. The data was analysed using the CT mean values with normalisation to the *Actb* and experimental controls, using the delta delta CT (ΔΔCT) method. Relative fold changes in gene expression were calculated by $2^{-(\Delta\Delta CT)}$.

Table 3.7 TaqMan gene assays used for RT-qPCR for RAW 264.7 experiments

Gene	TaqMan assay ID	Protein encoded	Relevance of gene
Actb	Mm00607939_s1	Actin b	Housekeeping gene
Nos2	Mm00440502_m1	Nitric oxide synthase 2	"M1" macrophage marker
IL6	Mm00446190_m1	Interleukin-6	"M1" macrophage marker
IL1-β	Mm00434228_m1	Interleukin-1-β	"M1" macrophage marker
Arg1	Mm00475988_m1	Arginase-1	"M2" macrophage marker

The following macrophage markers were also screened by RT-qPCR for M1 (CD38, TNF-α) and M2 (Retnla, EGR2, IL-10) but were found to not be differentially expressed in their respective polarised

controls. They were therefore not included in the final panel of gene expression assays used to determine the immunomodulatory effect of ECM hydrogels.

3.3.6 Statistical analysis

Data plotting and statistical analyses were performed using GraphPad Prism 9.2.0. The data was first checked for normal distribution, then unpaired student's t tests were run on all normally distributed data where two groups were compared directly. One-way ANOVA was performed with Tukey's multiple comparison's test to determine statistically significant differences more than two groups.

3.4 Results

3.4.1 Cytocompatibility of endometrial ECM hydrogels on endometrial cells

Cytocompatibility of endometrial ECM hydrogels (sow and pig) was tested by cell viability assays and BrdU uptake assays using both primary mouse endometrial cells and an immortalised human endometrial stromal cell line.

3.4.1.1 Effect of endometrial ECM hydrogel on cell viability

Primary endometrial stromal cells were isolated from mice uteri and cultured on a coating of sow endometrial ECM, SIS ECM or uncoated tissue culture plastic. After 48 hours of culture, cell viability was 93.67 +/- 5.774 % on endometrial ECM, 91.67 +/- 4.509 % on SIS ECM and 88.33 +/- 8.145 % in the control wells. There was no significant difference between in viability across any of the conditions (Figure. 3.7a).

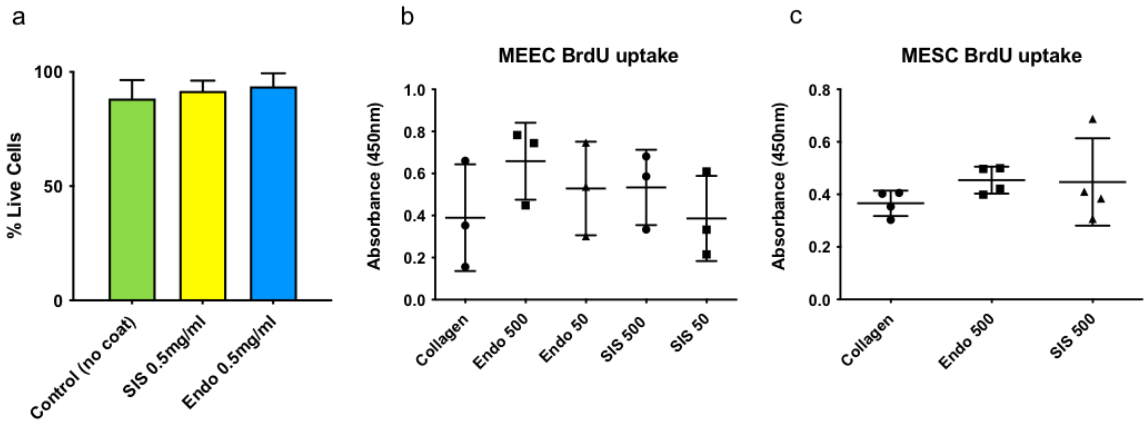


Figure. 3.7 Primary endometrial cell viability and proliferation assays. **a** Cell viability analysis of MESC cultured on coatings of SIS ECM 0.5 mg/mL (N = 3, n = 3) or sow endometrial ECM 0.5 mg/mL (N = 3, n = 3) compared to control (no coating) (N = 3, n = 3). High cell viability was observed at 48 hours with no significant difference between the conditions. **b** Results for MEEC BrdU uptake assay. MEEC were cultured on collagen coating (control) (N = 3, n = 3) or coatings of endometrial ECM 500 μg/mL (N = 3, n = 3), endometrial ECM 50 μg/mL (N = 3, n = 3), SIS 500 μg/mL (N = 3, n = 3) or SIS ECM 50 μg/mL (N = 3, n = 3). No statistically significant difference in proliferation was seen across all the conditions. **c** Results for MESC BrdU uptake assay. MESC were cultured on collagen coating (control) (N = 4, n = 3), endometrial ECM 500 μg/mL (N = 4, n = 3) or SIS 500 μg/mL (N = 4, n =3). No significant difference in proliferation was found between the groups. Statistical analyses were performed using one-way ANOVA. N = biological replicates, n = technical replicates.

3.4.1.2 Effect of endometrial ECM hydrogel on endometrial cell proliferation

BrdU uptake assays were performed to determine whether primary mouse endometrial cells (Figure. 3.7b-c) and immortalised human endometrial stromal cells (Figure. 3.8) changed their proliferative ability in response to ECM hydrogels. Primary mouse endometrial epithelial cells and stromal cells were separately cultured on tissue culture plastic coated with sow endometrial ECM, SIS ECM and collagen (as control). Although a slight upwards trend was observed with endometrial epithelial cells grown on endometrial ECM 500 μg/mL there was no statistically significant difference between any of the ECM conditions and control for either primary epithelial or stromal cells (Figure. 3.7b-c). This could have been due to primary cells having lower proliferative capacity as well as considerable batch-batch-variability with the cells, particularly with endometrial epithelial cells, as exemplified by the large standard deviations.

Due to limited access to more fresh animal tissues for primary cell isolation, the assay was repeated, with minor modifications, with a human endometrial stromal cell line. This time both sow and pig endometrial ECM significantly increased endometrial stromal cell proliferation compared to control ($p < 0.0001$ for both) (Figure. 3.8a). There was no significant difference in cell proliferation between sow and pig endometrial ECM (Figure. 3.8a). In a separate experiment, pig endometrial ECM was compared to SIS ECM. Both significantly increased endometrial stromal cell proliferation and there was no significant difference between these two types of ECM (Figure. 3.8b).

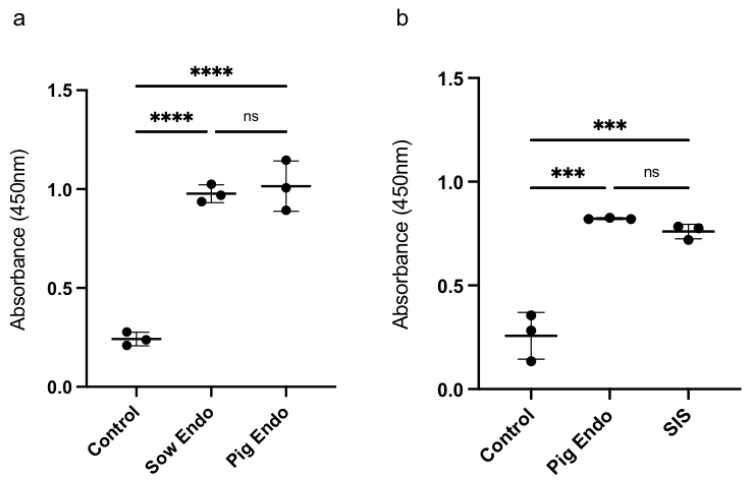


Figure 3.8 Endometrial stromal cell proliferation assays. The graphs show data for BrdU uptake assays with immortalised HESCs cultured on ECM coatings (all 500 μg/mL) or tissue culture plastic only (control). **a** Sow endometrial ECM (N = 3, n = 3) and pig endometrial ECM, batch C (N = 3, n = 3) significantly increased endometrial stromal cell proliferation compared to control (N=3) ($p < 0.0001$ for both endometrial ECMs). There was no significant difference between sow and pig endometrial ECMs. **b** Pig endometrial ECM, batch C (N = 3, n = 3) and SIS ECM (N = 3, n = 3) both significantly increased endometrial stromal cell proliferation compared to control (N = 3, n = 3) ($p = 0.0001$ and 0.0003 respectively). No significant difference was found between endometrial ECM and SIS ECM. Statistical analyses were performed with one-way ANOVA and Tukey's multiple comparisons test. N = biological replicates, n = technical replicates.

3.4.2 Angiogenesis potential of endometrial ECM hydrogels

3.4.2.1 Endometrial ECM hydrogel increases tubule formation

An *in vitro* tubule formation assay was performed to assess the angiogenic potential of endometrial ECM hydrogel (Figure 3.9a). HUVECs cultured on a layer of hydrogel made from basement membrane extract (Geltrex), are capable of migrating to form a network of capillary-like tubules on the surface of the hydrogel. Tubule formation occurs if the cells are cultured in media supplemented with serum and appropriate growth factors. Without growth factors, HUVECs remain viable but do not form tubules. Therefore, cells cultured on Geltrex in fully supplemented growth medium served as positive experimental controls, whilst cells grown in basal medium were negative controls. The extent of tubule formation can be determined through image analysis of the tubule network. Total tubule

length, number of junctions and number of branches were selected as the metrics for comparing angiogenic capacity. Junctions and branches are vectorial objects defined by the Angiogenesis Analyzer software analysis [262]. A junction is defined as a group of nodes forming a bifurcation, whilst a branch is a binary line linked with one junction and one extremity [262].

When HUVECs were cultured in endometrial ECM-supplemented media, angiogenesis was found to be increased, as demonstrated by increased total tubule length (Figure. 3.9a,b). This effect was observed when endometrial ECM digest was added to serum-free and growth factor-deplete basal medium, as well as when endometrial ECM digest was added to complete growth medium. HUVEC cultured in complete medium formed a network of elongated, connecting tubules (Figure. 3.9a,b). In complete media containing 200 μg/mL, there was a slight but non-significant increase in total tubule length. With 400 μg/mL of endometrial ECM, the total tubule length increased significantly compared to complete media alone ($p = 0.0010$) (Figure. 3.9b). The number of junctions increased significantly in complete media with 400 μg/mL of ECM compared with complete media alone ($p = 0.0016$) (Figure 3.9c). Similarly, the number of branches were also significantly increased in complete media with 400 μg/mL of ECM compared with complete media alone ($p = 0.0017$) (Figure 3.9d).

Whilst HUVECs did not form connecting networks of tubules when cultured in basal media, cells cultured in basal media containing 400 μg/mL of endometrial ECM formed more elongated tubules (Figure 3.9a). This was demonstrated by significantly greater total tubule length in basal media with 400 μg/mL ECM compared to basal media alone ($p = 0.02$) (Figure 3.9b). A small but non-signficant increase in total tubule length was observed with 200 μg/mL of ECM. Similarly, small but non-significant increases in number of junctions and number of branches were seen in basal media supplemented with 400 μg/mL endometrial ECM (Figure. 3.9c-d).

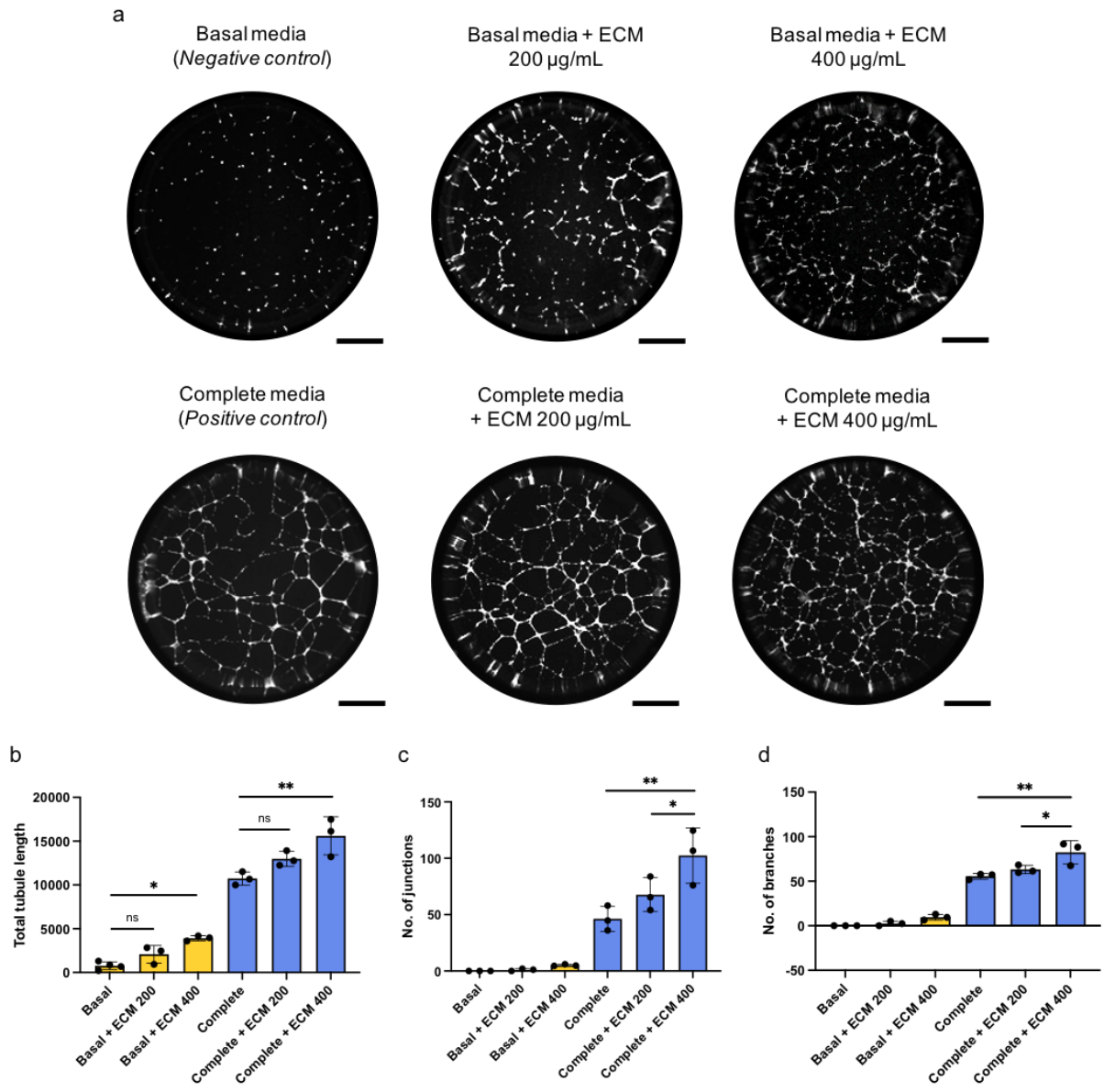


Figure 3.9 Tubule formation assays. **a** Representative fluorescence microscopy images of HUVECs in tubule formation assays under different media conditions. Images captured with 2.5x lens objective on Zeiss Axio Observer widefield microscope. Scale bars = 1 mm. Negative control consisted of cells cultured in basal media only (N = 4). No tubules were formed in the negative control. When basal media was supplemented with pig endometrial ECM 200 µg/mL (N = 3) and 400 µg/mL (N = 3), more elongated tubules and some junctions formed. Positive control consisted of cells cultured in complete growth medium (N = 3). In the positive control, a network of tubules formed with multiple junctions and branches. When the complete growth medium was supplemented with endometrial ECM 200 µg/mL (N = 3) and 400 µg/mL (N = 3), the network of tubules was enhanced and a greater number of branches and junctions could be seen. **b** Total tubule length analysis. **c** Analysis of number of junctions. **d** Analysis of number of branches. Statistical analyses performed with one-way ANOVA and multiple Tukey's comparison tests. ns = non-significant, * $p \leq 0.05$, ** $p \leq 0.01$, *** $p \leq 0.001$, **** $p \leq 0.0001$.

These results indicate that solubilised pig endometrial ECM enhances tubule formation in an *in vitro* angiogenesis model and there is possibly a dose-responsive effect, as greater tubule lengths, number of junctions and number of branches are seen at the higher concentration of ECM. Concentrations ≥ 500 μg/mL were not investigated as they tended to cause the media to gel.

The increase in angiogenesis measures seen when endometrial ECM was added to complete medium suggests that there are components within the endometrial ECM that may act synergistically with the growth factors in the growth medium. However, a more interesting observation was that endometrial ECM stimulated tubule formation even in serum and growth-factor deplete culture conditions, suggesting that endometrial ECM contains pro-angiogenic factors which can independently influence endothelial cells.

3.4.2.2 Human VEGF ELISA

Human endometrial stromal cells were cultured on a coating of ECM for 24 hours and the supernatant was collected and analysed with a commercially available VEGF ELISA kit. The conditions compared were pig endometrial ECM, SIS ECM and no ECM coating (control). There was no statistically significant difference between the three different conditions (Figure. 3.10).

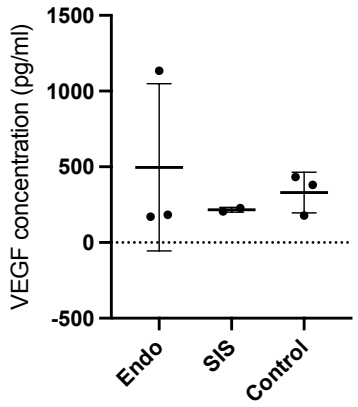


Figure 3.10 Human VEGF ELISA. HESCs were cultured on coatings of pig endometrial ECM 500 μg/mL, SIS ECM 500 μg/mL or uncoated tissue culture plastic (control). No statistically significant difference was found between any of the conditions. All conditions were tested with three biological replicates (N = 3) and plated with three technical replicates (n = 3). Each data point presents the average of n = 3 for one biological replicate. Statistical analysis was performed with one-way ANOVA. VEGF ELISA data was acquired and analysed by Aida Abdelwahed.

3.4.3 Endometrial organoid culture in ECM hydrogels

3.4.3.1 ECM hydrogels can support endometrial organoid culture

Human endometrial organoids were grown from patient-derived endometrial cells in Matrigel and then passaged into either Matrigel or 8 mg/mL ECM hydrogels (sow endometrial, SIS and UBM). This concentration of ECM hydrogels was chosen to allow for direct comparison of the three different ECM types, as UBM formed very weak gels at lower concentrations and often did not gel at 2 mg/mL. A preliminary experiment using 5 mg/mL ECM hydrogels to culture endometrial organoids was also unsuccessful, therefore the decision was made to try a higher concentration. The organoids were cultured for 7 days and then assessed by brightfield imaging and immunofluorescent staining with confocal imaging (Figure. 3.11). Organoids grew in all gel conditions, however it was noticed that objectively far fewer organoids grew in the ECM hydrogels compared with Matrigel. Of the three ECM hydrogels, the organoids that formed in endometrial ECM and SIS gels were the most uniform looking and most similar to organoids grown in Matrigel (Figure. 3.11a). Immunofluorescence staining identified the endometrial organoids in all hydrogel conditions as 3D structures consisting of a single organised layer of epithelial cells staining positively for cytokeratin (Figure. 3.11b).

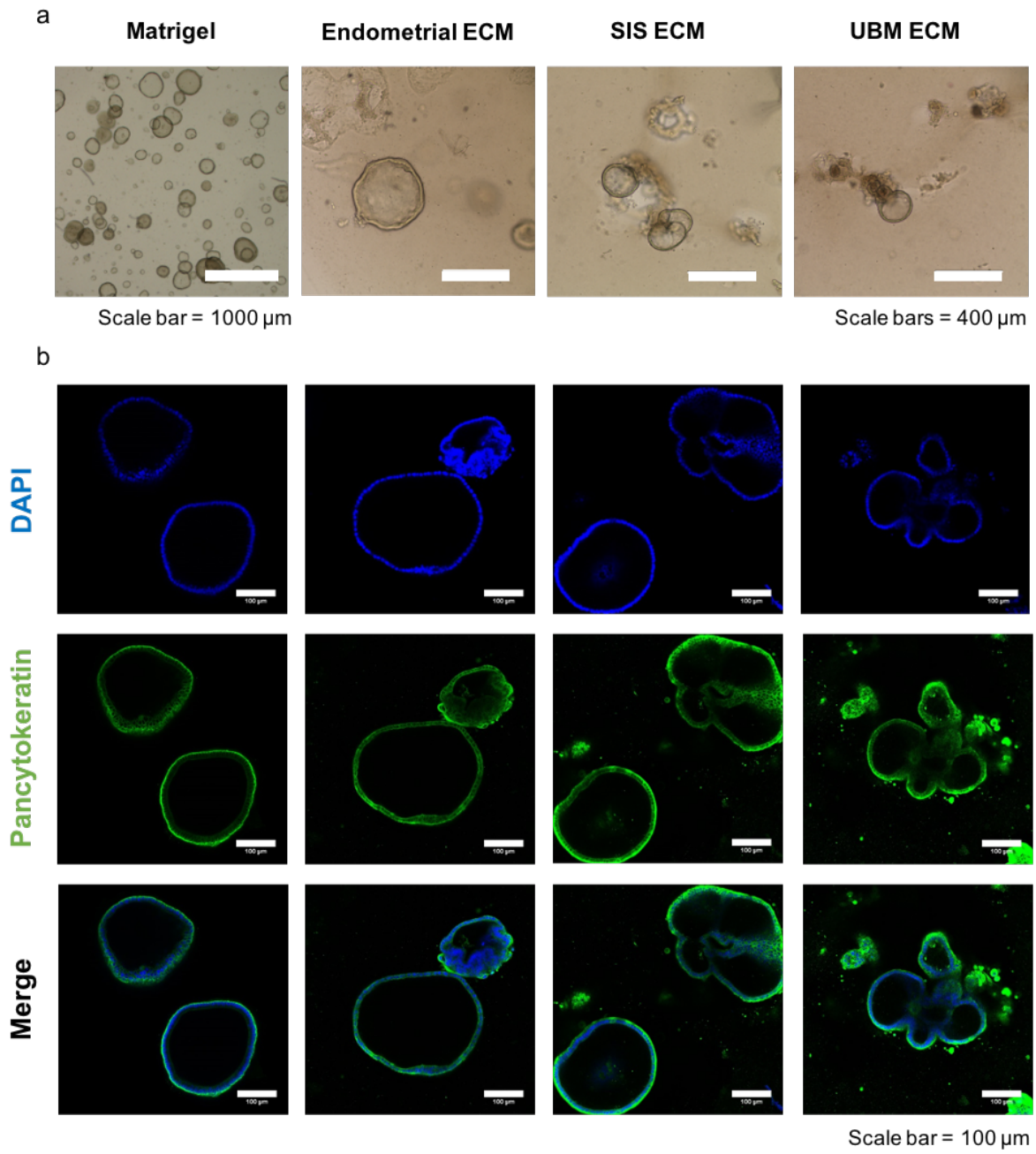


Figure 3.11 Human endometrial organoid culture in ECM hydrogels. Human endometrial organoids were passaged from Matrigel into 8 mg/mL SIS, UBM or sow endometrial ECM hydrogels. Although organoids formed in all gels, only a few organoids formed in the ECM hydrogels compared to abundant organoids in Matrigel. All organoid experiments were performed in collaboration with Dr Tom Rawlings, University of Warwick. **a** Representative brightfield images of endometrial organoids in different gel conditions. Matrigel image taken with a 5x lens objective. Scale bar = 1000 µm. ECM hydrogel images taken with a 10x lens objective. Scale bars = 400 µm. **b** Representative confocal fluorescence microscopy images taken with 20x lens objective. Organoids were stained whole with anti-cytokeratin and DAPI. Scale bars = 100 µm.

3.4.3.2 Organoid formation efficiency in endometrial ECM hydrogel

An organoid formation efficiency assay was performed to assess the performance of Matrigel compared to three different concentrations of sow endometrial ECM hydrogel. Matrigel had significantly greater efficiency compared to all concentrations of sow endometrial ECM (Figure. 3.12). Minimal to no organoids were formed in sow endometrial ECM. Although the mean organoid count was slightly higher for 5 mg/mL, there was no statistically significant difference between any of the three concentrations of sow endometrial ECM (Figure. 3.12).

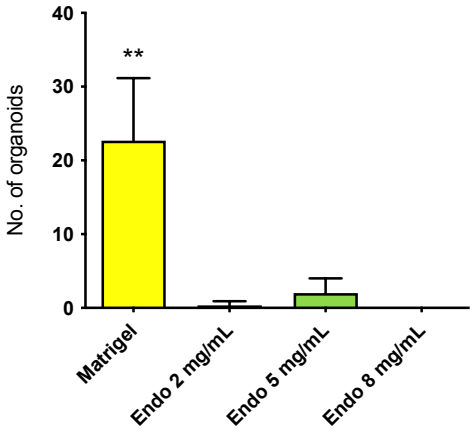


Figure 3.12 Organoid formation efficiency assay. Significantly fewer endometrial organoids grew in all sow endometrial ECM concentrations compared to Matrigel (N = 3, n = 3). One-way ANOVA analysis *** p = 0.0005, with Tukey's multiple comparisons test (Matrigel vs Endo 2 mg/mL (N = 3, n =3) ** p = 0.0011, Matrigel vs Endo 5 mg/mL (N = 3, n = 3) ** p = 0.0019, Matrigel vs Endo 8 mg/mL (N = 3, n = 3) ** p = 0.0010). All organoid experiments were performed in collaboration with Dr Tom Rawlings, University of Warwick. N = biological replicates, n = technical replicates.

3.4.4 *In vitro* endometrial fibrosis modelling

3.4.4.1 Stimulation of primary endometrial cells with TGF-β1

To develop an *in vitro* fibrosis model, primary mouse endometrial epithelial cells and stromal cells were isolated and cultured separately as monolayers. TGF-β1 was then added to the cell culture media for 24-120 hours and cells were collected for immunofluorescence staining or RNA extraction and qPCR.

The aim of treating endometrial stromal cells with TGF-β1 was to observe for fibroblast to myofibroblast transdifferentiation, which would be detected by increased expression of α-SMA and Collagen 1. Freshly isolated primary endometrial stromal cells largely consist of fibroblast-like cells, with spindle-shaped cell bodies, which stain positively for vimentin and negatively for cytokeratin (Figure. 3.13a). When endometrial stromal cells were cultured on tissue culture plastic, it was noted that over several days their appearances changed and the cells adopted a myofibroblast-like morphology with enlarged, spread-out cell bodies with multiple projections and a network of stress fibres within the cytoplasm that stained positively for α-SMA (Figure. 3.13b). This spontaneous transdifferentiation occurred when the cells were cultured in 10% serum as well as low (0.5%) serum conditions and was apparent by 48-72 hours after plating (Figure.3.13b). With TGF-β1 addition to the stromal cell media on day 0 of culture, myofibroblast transdifferentiation was still observed but there was no appreciable difference between the untreated and treated cells at 72 hours (Figure 3.13b).

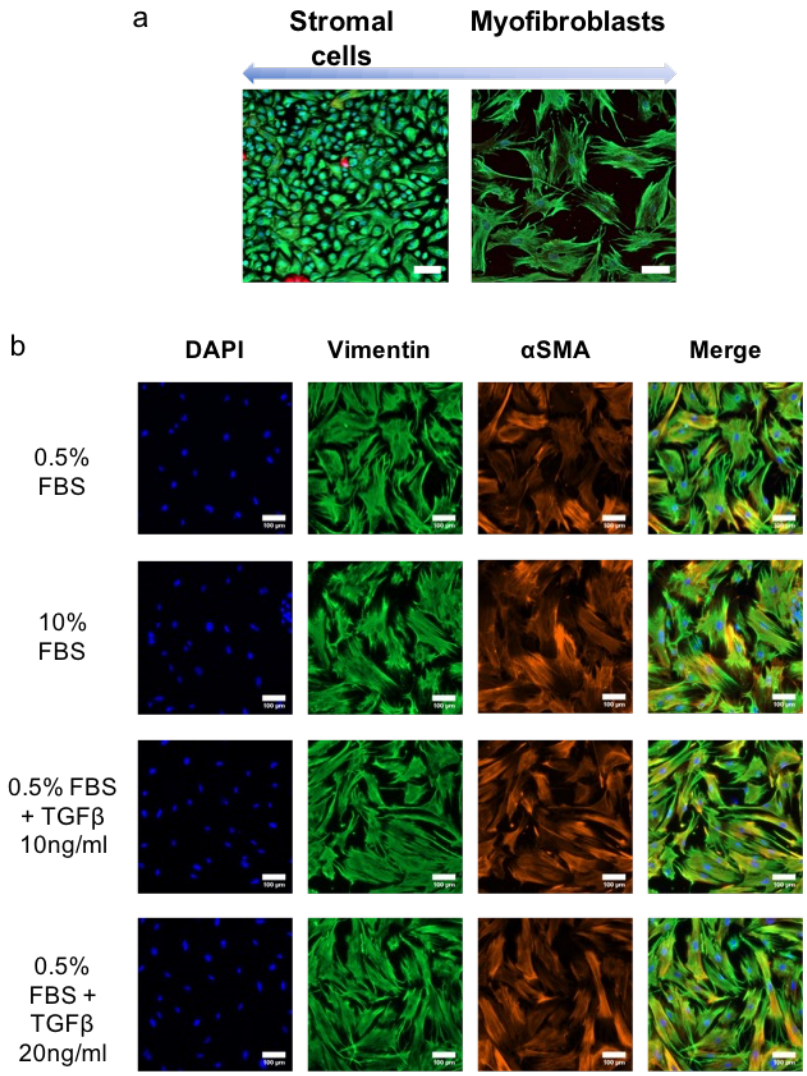


Figure 3.13 Transdifferentiation of primary endometrial stromal cells when cultured. Representative images of MESCs. **a** Freshly isolated MESC are predominantly fibroblast-like. After being in culture for 48 hours, they transdifferentiate into myofibroblast-like cells with enlarged cell bodies and multiple projections. **b** An experiment was performed to see if culturing MESC with or without TGF-β1 and in low or normal serum conditions would affect their transdifferentiation in myofibroblasts. At 72 hours of culture, after primary isolation, the majority of MESC had myofibroblast-like appearances and stained positively for α-SMA regardless of the media type. All images acquired with a 20x lens objective on Zeiss Axio Observer widefield microscope. Scale bars = 100 μm.

Stromal cells were collected for RNA extraction and RT-qPCR every 24 hours after initial plating and TGF-β1 treatment. Gene expression of *Acta2* (mRNA transcription of which leads to production of α-SMA protein) and *Col1a1* were measured with normalisation to non TGF-β1-treated, control stromal cells. In 10% serum and with TGF-β1 treatment, no significant difference in expression of *Acta2* or

Col1a1 was seen at 24 hours, 48 hours or 72 hours (Figure. 3.14). In 0.5% serum, no significant difference was seen in *Acta2* or *Col1a1* expression at 24 and 48 hours and no discernible difference in gene expression could be observed at 72, 96 and 120 hours although insufficient biological replicates were performed at those timepoints to perform statistical analysis (Figure. 3.14).

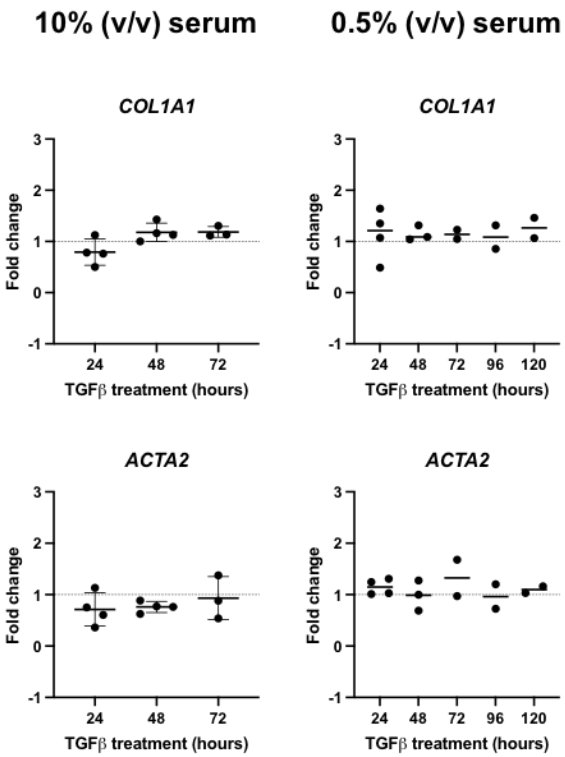


Figure. 3.14 RT-qPCR results for Col1a1 and Acta2 expression in MESC treated with TGF-β1. MESC were cultured in 10% (v/v) serum + TGF-β1 10 ng/mL for 24 hours (N=4). 48 hours (N=4) or 72 hours (N=3). A fold change of 1 denotes no upregulation or downregulation of the target gene. No significant difference was found in Col1a1 or Acta2 gene expression at any timepoint, when normalised to control (no TGF-β1, 10% v/v serum) and the housekeeping gene. Statistical analysis was performed with one-way ANOVA. MESC were also cultured in 0.5% (v/v) serum + TGF-β1 for 24 to 120 hours. No difference in gene expression of Col1a1 or Acta2 were observed at any timepoints and statistical analysis was not performed due to small group numbers.

3.4.4.2 Stimulation of endometrial organoids with TGF-β1

Human endometrial organoids were cultured in four different media conditions: I) normal expansion medium, II) expansion medium supplemented with TGF-β1, III) expansion medium without A83-01

and IV) expansion medium without A83-01 and supplemented with TGF-β1. Brightfield images of the organoids showed no difference in morphology of the organoids across the different media conditions (Figure. 3.15a). Comparing the most TGF-β1-sensitive condition (minus A83-01 plus TGF-β1) with the control, immunofluorescence staining was performed for pan-cytokeratin, vimentin and α-SMA. No obvious differences in any of these three markers were seen between the control and TGF-β1-stimulated organoids (Figure. 3.15b). Surprisingly, there was clear expression of Vimentin in both the control organoids and the organoids cultured with TGF-β1 (Figure. 3.15b). Vimentin is a stromal marker and was not expected to be found in the epithelial organoids cultured in normal medium.

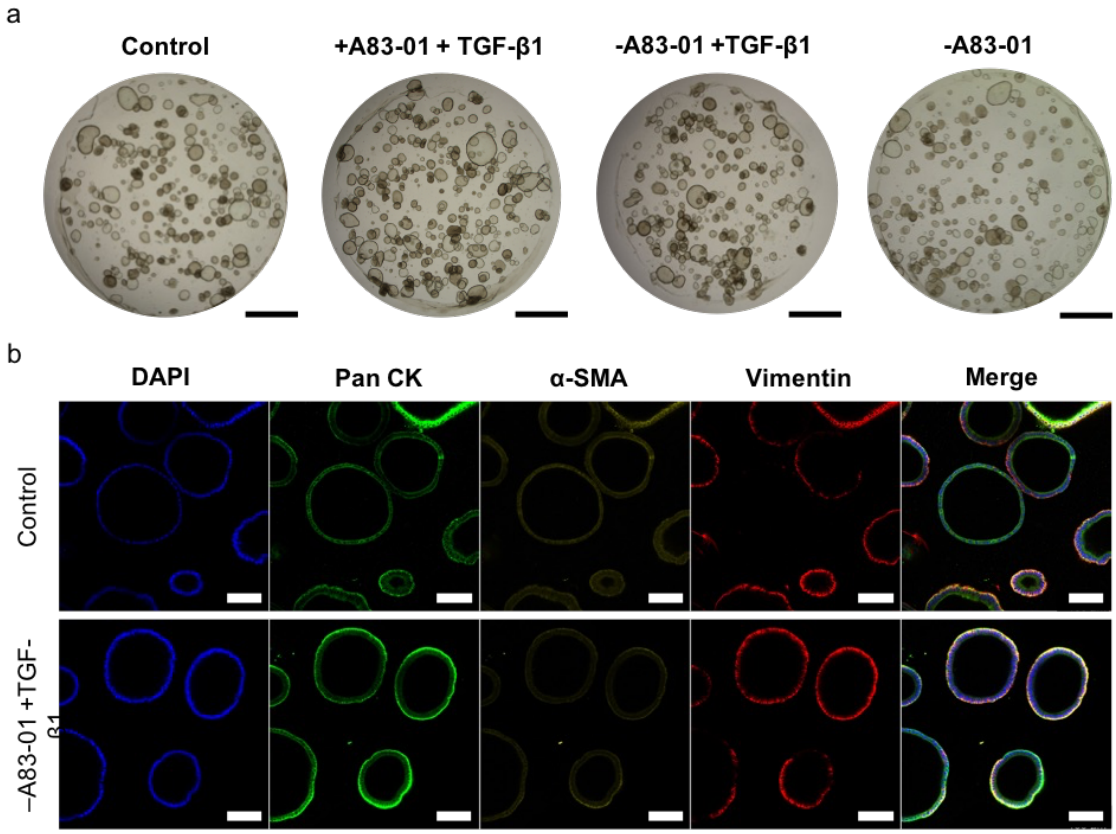


Figure 3.15 Human endometrial organoids stimulated with TGF-β1. **a** Representative Brightfield images taken with a 1.25x lens objective of representative wells of organoids cultured in control (normal expansion) media, media +A83-01 and +TGF-β1, media without A83-01 +TGF-β1 and media without A83-01 or TGF-β1. Scale bars = 500 μm. No obvious morphological differences were seen across the 4 conditions. **b** Organoids grown in control media and organoids grown in media without A83-01 +TGF-β1 were stained with anti-cytokeratin, anti-α-SMA, anti-vimentin and DAPI. There were no obvious staining differences between the two conditions. Vimentin, a mesenchymal marker, was unexpectedly detected in both the control and the TGF-β1 positive condition. Images acquired on a confocal fluorescence microscope with a 20x lens objective. Scale bars = 100 μm. All organoid experiments were performed in collaboration with Dr Tom Rawlings, University of Warwick.

3.4.4.3 *In vitro* fibrosis modelling with cell-derived matrices

Culturing fibroblasts at high density for 15 days resulted in their deposition of a sheet of extracellular matrix beneath the cell monolayer. When cultured in normal growth media, without any other stimulus, the cell-derived matrices (CDM) produced by both human dermal fibroblasts and human endometrial stromal cells (HESC) formed a basketweave-like meshwork of fibres (Figure 3.16). These fibres stained positively for collagen and fibronectin (Figure. 3.16a,b), although are likely to include other ECM proteins, such as collagen III and Laminin, which were not stained for in these experiments. It was found that staining the CDM with a general amine dye achieved the best fluorescence image quality for image analysis (Figure. 3.16c). Using the OrientationJ plugin in ImageJ to analyse pre-processed images of CDM, a coherence score could be generated for each image which correlates with the degree of orientation of the structures within a region of interest. A score of 0 means that the structures within the image are anisotropic, whilst a score of 1 means that the structures have a single angle of orientation [263].

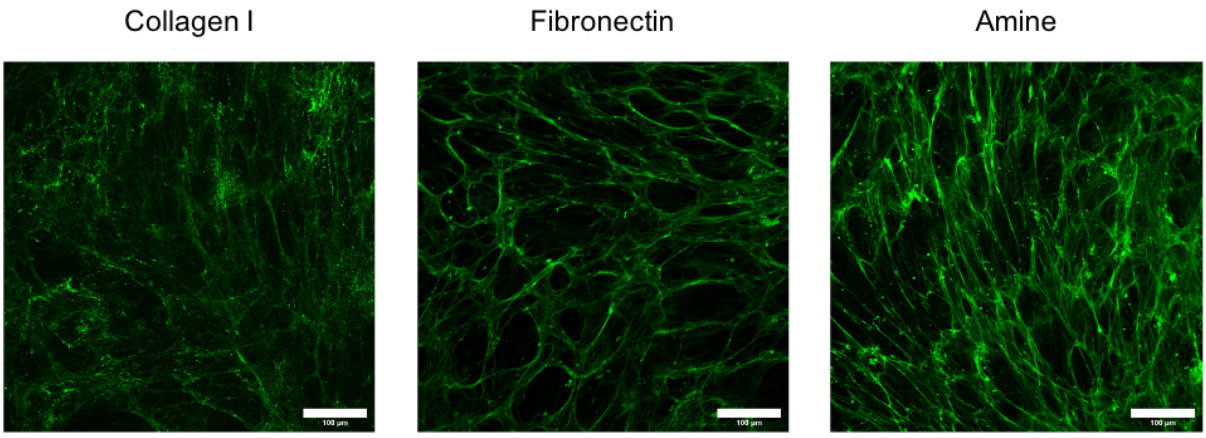


Figure 3.16 Cell-derived matrices stained for collagen I, fibronectin and amine. Representative confocal microscopy images, taken with a 20x lens objective of fibroblast CDM (control condition) stained with anti-collagen I, anti-fibronectin and a general amine dye. The amine dye gave the best staining quality for image analysis. Scale bars = 100 μm

3.4.4.3.1 Endometrial ECM hydrogel attenuates effect of TGF-β1 on fibroblast CDM

When dermal fibroblasts were cultured in the presence of TGF-β1, the morphology of their CDM changed dramatically. The basketweave appearance of the control condition (Figure. 3.17a) was replaced by parallel, aligned bundles of fibres (Figure. 3.17b). The histogram plot of distribution of

fibre orientation, showed that the orientation of fibres in the control was spread over different angles (Figure. 17d), whilst with TGF-β1 treatment the fibres were predominantly concentrated at one angle (Figure 3.17e). The CDM of TGF-β1-stimulated dermal fibroblasts generated a significantly increased mean coherence score of 0.4320 +/- 0.066 compared to control culture conditions (0.1493 +/- 0.030) ($p < 0.0011$) (Figure. 3.17g).

When dermal fibroblasts were co-treated with TGF-β1 and endometrial ECM hydrogel, the basketweave CDM morphology was rescued and the matrix closely resembled the control (Figure 3.17b). The histogram showed fibre distribution across multiple angles of orientation (Figure. 3.17f) and the coherence score was significantly reduced compared to TGF-β1 alone ($p < 0.0016$) (Figure 3.17g).

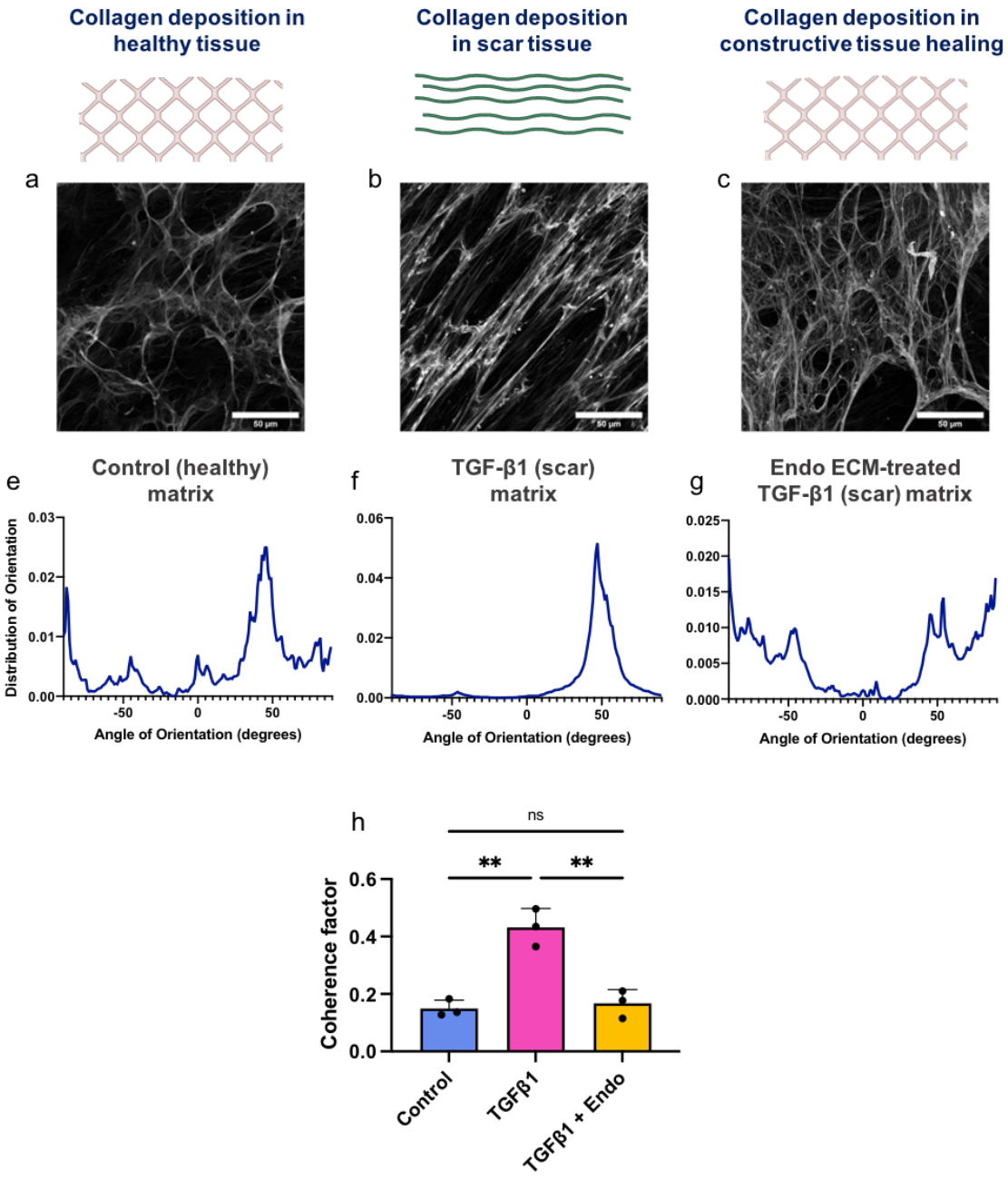


Figure 3.17 An *in vitro* model of TGF-β1-mediated fibrosis using fibroblast cell-derived matrices. In healthy, normal tissues, collagen fibres are organised in a basketweave or randomly orientated pattern. In scar tissue, collagen fibres become aligned. **a-c** Representative confocal fluorescence microscopy images, taken with a 63x lens objective, of fibroblast-derived CDMs stained with a general amine dye. Scale bars = 50 μm. **a** Image of the control condition. Matrix fibres have a mesh-like pattern and appear more randomly orientated. **b** After treating fibroblasts with TGF-β1, the deposited matrix features highly aligned, parallel fibres. **c** When fibroblasts are simultaneously treated with TGF-β1 and ECM hydrogel, the appearance of the CDM closely resembles the control condition. **d-f** Histograms showing the distribution of fibres by angle of orientation. Data generated by the OrientationJ plugin in ImageJ software. **d** The histogram for the control CDM shows fibre distribution across multiple different angles. **e** The histogram for the TGF-β1 CDM

shows the fibres are distributed in one single, dominant angle of orientation. **f** With ECM treatment, the distribution of fibres is spread across multiple different angles. **g** The coherence score of fibres is significantly higher in the TGF-β1 CDM (N = 3) compared to the control (N = 3) (p = 0.0011) and to the ECM-treated CDM (N = 3) (p = 0.0016). Statistical analysis was performed with one-way ANOVA and Tukey's multiple comparisons test.

3.4.4.3.2 Endometrial ECM hydrogel attenuates effect of TGF-β1 on endometrial CDM

Very similar effects were seen with the HESCs. A meshwork of fibres that appear to be orientated at multiple different angles was seen in the control CDM (Figure 3.18a,d), with a mean coherence score of 0.1252 +/- 0.017 (Figure. 3.18g). When HESCs were stimulated with TGF-β1 the CDM featured bundles of parallel fibres aligned in a similar direction (Figure. 3.18b,e), corresponding to a mean coherence score of 0.4206 +/- 0.063, which is significantly higher than the control (p = 0.0004) (Figure. 3.18g).

Treatment with ECM hydrogel appeared to abrogate the effect of TGF-β1 on HESC CDM, with fibres distributed over different angles of orientation (Figure 3.18 c,f), and a significantly reduced mean coherence score of 0.084 +/- 0.035 (p = 0.0002) (Figure 3.18g).

These results demonstrate that TGF-β1 causes fibroblasts and endometrial stromal cells to deposit matrix differently, in aligned fibre bundles that is representative of ECM deposition in scar tissue. This most likely corresponds to fibroblast alignment and elongation. Simultaneous treatment of fibroblasts with endometrial ECM hydrogel appeared to mitigate the effect of TGF-β1 and resulted in matrix deposition that closely resembled control conditions.

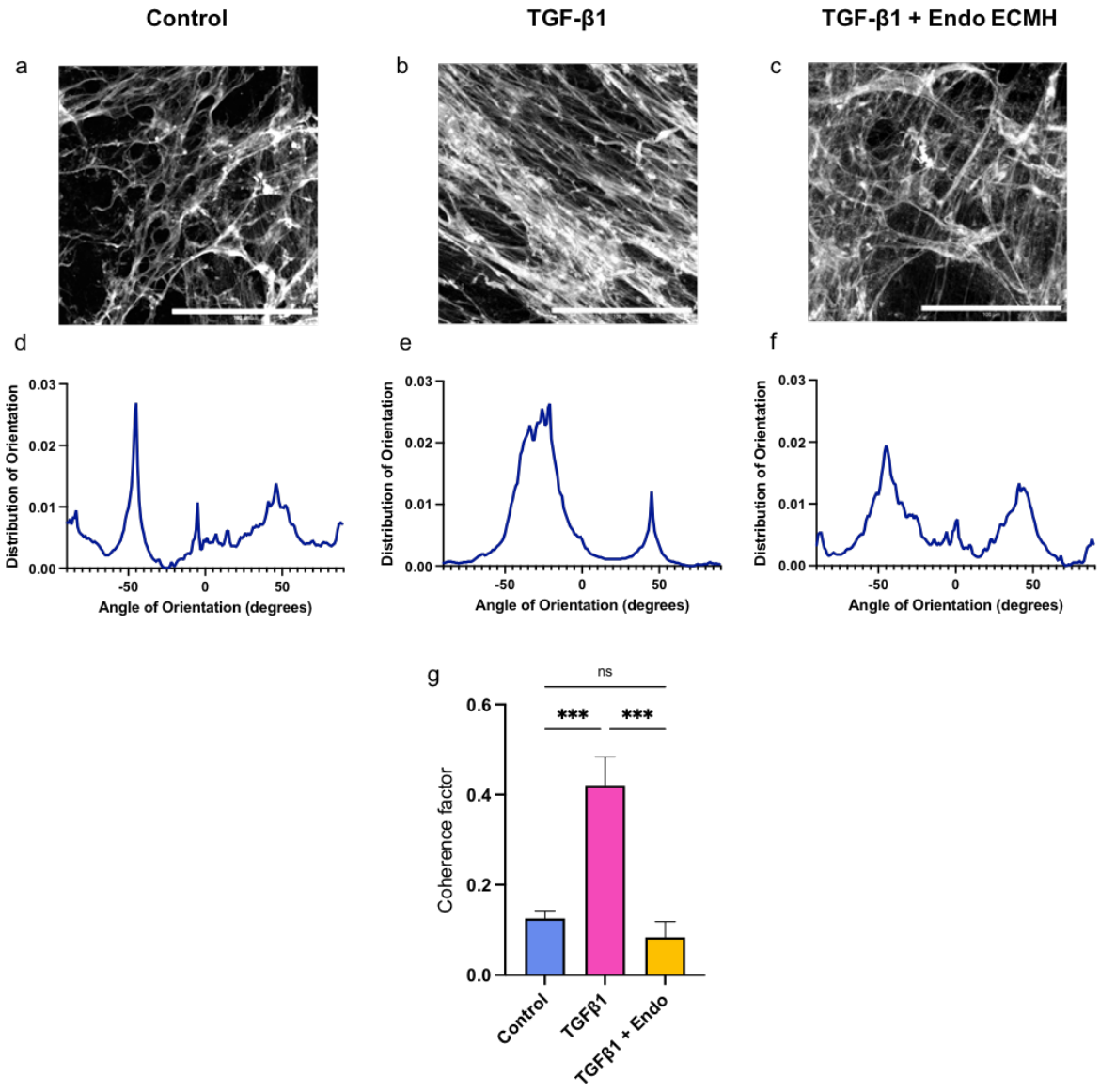


Figure 3.18 An *in vitro* model of endometrial fibrosis using cell-derived matrices. **a-c** Confocal fluorescence microscopy images, taken with a 63x lens objective, of HESC-derived CDMs stained with a general amine dye. Scale bars = 100 μm. **a** In the control condition, the matrix fibres were randomly orientated. **b** After treatment of HESCs with TGF-β1, the CDM shows highly aligned, parallel bundles of fibres. **c** Treatment with endometrial ECM hydrogel appears to abrogate the effect of TGF-β1, resulting in the fibres appearing more randomly distributed and resembling more closely the control CDM. **d-f** Histograms showing the distribution of fibres by angle of orientation. Data generated by the OrientationJ plugin in ImageJ software. The plots corroborate the images, showing distribution of fibres across multiple angles in the control (**d**) and ECM-treated conditions (**f**), whilst the TGF-β1 CDM has one dominant angle of orientation (**e**). **g** The coherence score of fibres is significantly higher in the TGF-β1 CDM (N = 3) compared to the control (N = 3) ($p = 0.0004$) and to the ECM-treated CDM (N = 3) ($p = 0.0002$). Statistical analysis was performed with one-way ANOVA and Tukey's multiple comparisons test.

3.4.5 Immunomodulatory effects of endometrial ECM

3.4.5.1 Polarisation and ECM treatment of macrophages

Figure. 3.19 shows representative brightfield images and flow cytometry plots of RAW 264.7 cells under various different treatment conditions. Unstimulated, naïve (Mφ) macrophages were observed to be predominantly rounded cells (Figure 3.19a). On flow cytometry, Mφ had low expression of CD86+, an "M1" marker, but relatively high CD206 expression, an "M2" marker (Table 3.8). LPS and IFN-γ stimulation of macrophages *in vitro* led to morphological changes in the cells, with the macrophages becoming more enlarged and spiculated in appearance (Figure 3.19b). During flow cytometry analysis, it was noted that with LPS and IFNγ-treatment, the cell population shifted upwards in the FSC and SSC plots, indicating increased granularity in these cells (see Appendix Figure A). LPS and IFN-γ stimulation led to a markedly increased proportion of cells expressing CD86 (99.13%). However, only 3.66 +/- 2.13% of cells were CD86+ CD206- and the majority of cells co-expressed CD86 and CD206 (95.47 +/- 2.25%) (Table 3.8). In fact, the proportion of cells expressing CD206 was far greater in the LPS and IFN-γ-stimulated macrophages than in the IL-4-stimulated macrophages (Table 3.8). IL-4-stimulated macrophages had a similar CD86/CD206 expression profile to naïve macrophages (Figure. 3.19g), but surprisingly had a lower proportion of cells that were CD86- CD206+. This observation highlighted that either CD206 was not a useful marker of M2 macrophages or IL-4 treatment did not reliably produce a shift towards an M2 macrophage phenotype, even though the former is a commonly reported M2 marker and the latter is the dominant method for stimulating an M2 phenotype shift *in vitro* [240].

When SIS, UBM and endometrial ECM digests were added to naïve (Mφ) macrophages, there was minimal change in the morphology of the macrophages (Figure 3.19 d-f) and the ECM hydrogels did not provoke a shift in CD86 and CD206 expression towards an M1 phenotype response (Figure. 3.19j-l). In the ECM-treated macrophages, CD86/CD206 expression closely resembled unstimulated Mφ, but endometrial and UBM ECM treated macrophages showed higher proportions of CD86- CD206+ cells (62.13 +/- 12.65% and 60.87 +/- 13.26% respectively) compared to SIS (46.47 +/- 19.05%).

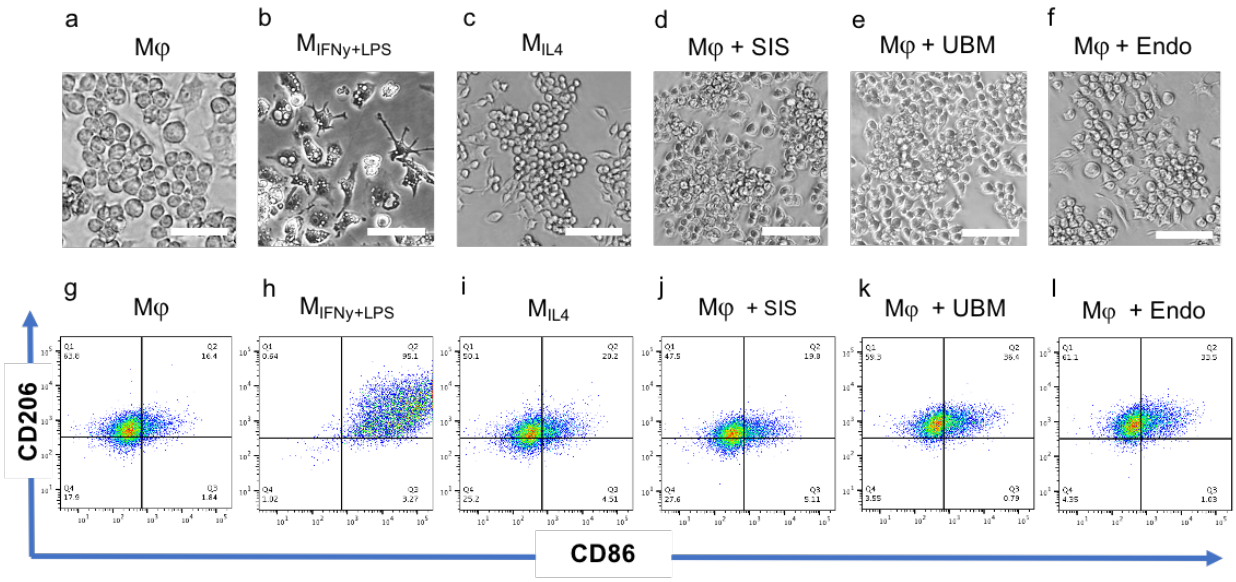


Figure 3.19 RAW 264.7 macrophage polarisation and ECM treatment. **a-f** Brightfield images of macrophages taken with a 20x lens objective. Scale bars = 200 μm. **g-l** Representative flow cytometry density plots of macrophages stained with anti-CD86 (x-axis) and anti-CD206 (y-axis). **a and g** Unstimulated (naïve) macrophages, **b and h** macrophages treated with LPS and IFN-γ, **c and i** macrophages treated with IL-4, **d and j** macrophages treated with SIS ECM, **e and k** macrophages treated with UBM ECM, **f and l** macrophages treated with Endo ECM. Treatment of macrophages with LPS and IFN-γ dramatically changed the cell morphology and increased expression of CD86 and CD206. Treating macrophages with ECMs did not lead to an M1-like phenotype shift and the expression profile of CD86/CD206 remained similar to naïve macrophages.

Table 3.8 Flow cytometry analysis of naïve, cytokine-stimulated and ECM-treated RAW 264.7 macrophages. Average data from N = 3 experiments is shown.

	% (+/- SD) of cells					
	Mφ	**M1**	**M2**	**Mφ + SIS**	**Mφ + UBM**	**Mφ + Endo**
CD86- CD206-	20.00 +/- 9.67	0.53 +/- 0.17	31.10 +/- 11.97	32.73 +/- 17.06	9.23 +/- 10.06	10.28 +/- 9.90
CD86+ CD206-	2.68 +/- 2.26	3.66 +/- 2.13	4.51 +/- 2.28	5.80 +/- 4.16	1.82 +/- 2.17	2.16 +/- 2.34
CD86+ CD206+	15.06 +/- 0.56	95.47 +/- 2.25	15.07 +/- 1.91	14.97 +/- 2.48	28.10 +/- 2.66	25.40 +/- 2.40
CD86- CD206+	62.2 +/- 12.31	0.38 +/- 0.08	49.30 +/- 12.90	46.47 +/- 19.05	60.87 +/- 13.26	62.13 +/- 12.65

Stimulation of macrophages with LPS and IFN-γ caused a significant increase in the gene expression of M1 macrophage markers: Nos2, IL6 and IL1-β (Figure. 3.20a-c). Based on the flow cytometry observation of relatively low CD206 expression in IL-4-stimulated macrophages, compared to unstimulated macrophages, IL-4 was combined with IL-13 stimulation of macrophages to enhance polarisation to an M2-like phenotype for gene expression analysis. Gene expression of Arg1 (a typical M2 marker) was found to be upregulated in the IL-4 and IL-13 stimulated macrophages (M2 control) but not significantly so, when normalised to unstimulated Mφ at 24 hours (Figure. 3.20d). On the other hand, Arg1 expression was significantly upregulated in the LPS and IFN-γ stimulated macrophages (M1 control) (Figure. 3.20d).

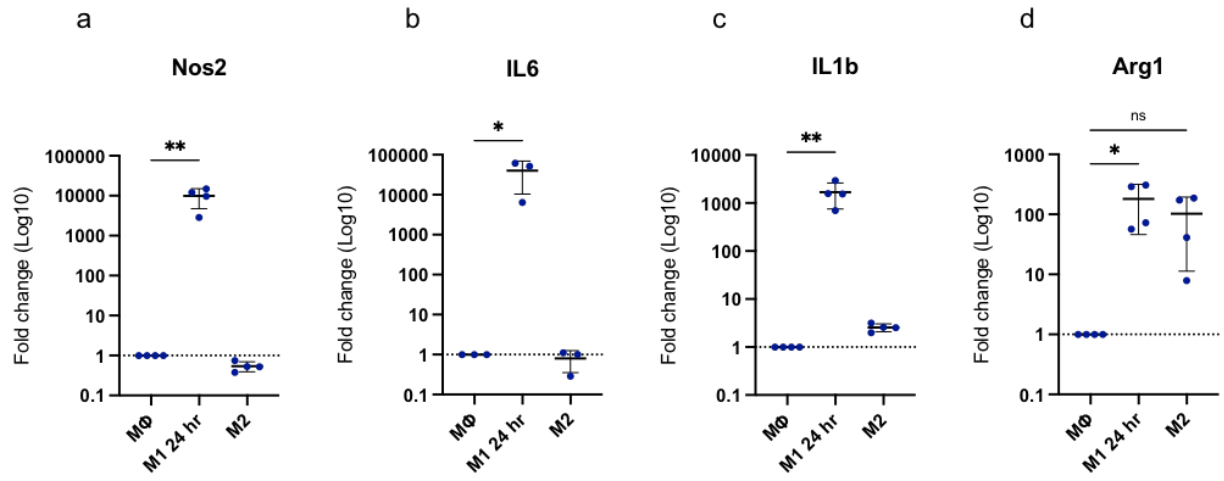


Figure 3.20 RT-qPCR of polarised macrophages. Gene expression was determined with normalisation to experimental control (unstimulated macrophages, MΦ) and the housekeeping gene. **a** Nos2 gene expression was significantly raised compared to MΦ when macrophages were polarised towards M1 phenotype with LPS and IFN-γ for 24 hours (M1 control) ($p = 0.0021$). **b** IL6 ($p = 0.0493$) gene expression was significantly raised in the M1 control compared to MΦ ($p = 0.0021$). **c** IL1-β gene expression was significantly raised in the M1 control compared to MΦ ($p = 0.0031$). **d** Arg1 expression was found to be significantly raised in the M1 control ($p = 0.0481$) but not significantly raised in the M2 control ($p = 0.2682$). N = 4 biological replicates and n = 3 technical replicates were performed for all conditions. Statistical analysis was performed with one-way ANOVA and Tukey's multiple comparisons tests.

3.4.5.2 Effect of endometrial ECM on M1-polarised macrophages

When macrophages were stimulated with LPS and IFN-γ for 2 hours then the culture medium was switched out to fresh medium lacking LPS and IFN-γ (M1 control), the morphology of cells still took on

an obvious M1-like appearance after 24 hours of culture (Figure. 3.21a,b). When LPS and IFN-γ were removed and medium containing endometrial ECM was added, significant downregulation in the M1 markers Nos2 and IL6 was observed when normalised to the M1 control (Figure. 3.21c). The difference in IL1-β between the M1 control and macrophages polarised with LPS and IFN-γ, followed by ECM treatment, was not significant (Figure. 3.21c). Arg1 expression increased in M1-polarised macrophages that were subsequently treated with ECM, but to a lesser degree than the M1 control, however neither were significantly different when normalised to Mφ. Endometrial ECM treatment of macrophages alone did not lead to significant differential expression of Nos2, IL6, IL-1β or Arg1 (Figure. 3.21c).

Differences in whether Arg1 was significantly raised with IL-4/IL-13 stimulation were found between experiments where cytokine treatment occurred for 24 hours and was normalised to Mφ at 24 hours and experiments where cytokine treatment was for 2 hours only and the gene expression was normalised to Mφ with a normal media change at 2 hours. In the former experiments, Arg1 expression was significantly increased in the M1 control but not the M2 (Figure. 3.20), whilst in the latter Arg1 expression was significantly raised in M2 ($p = 0.0328$) but not M1 (Figure. 3.21c).

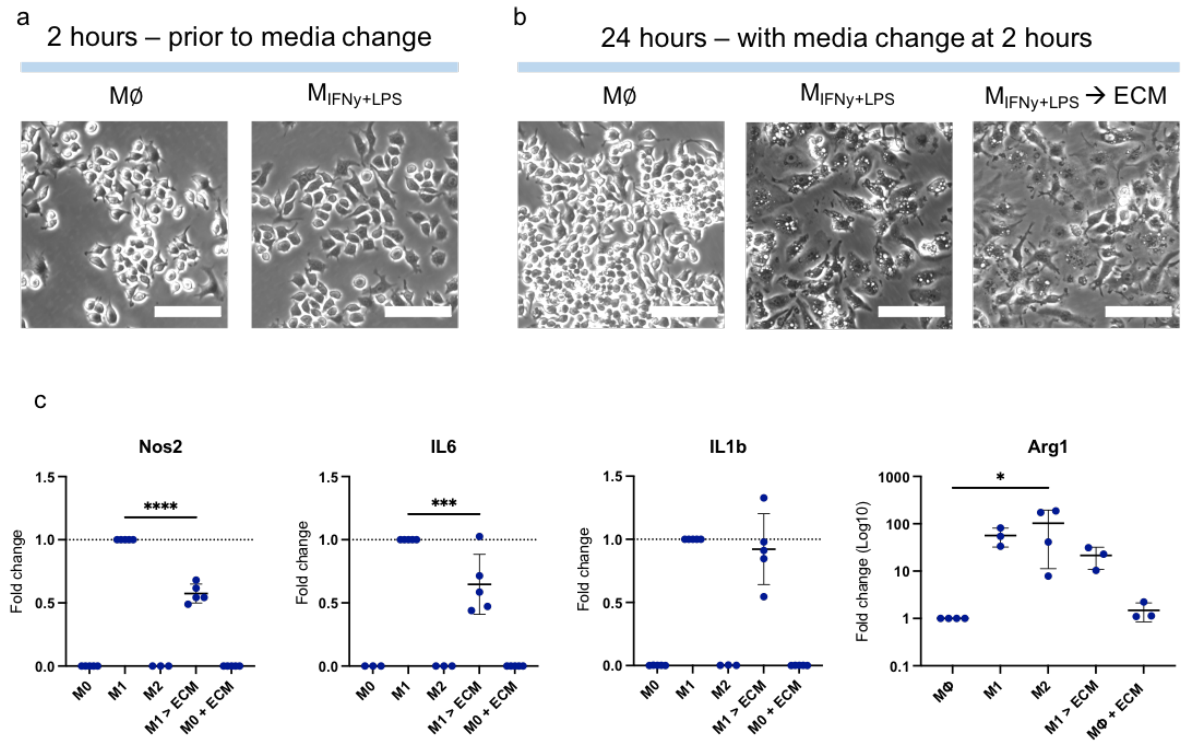


Figure 3.21 Brightfield images and RT-qPCR of RAW 264.7 cells polarised and treated with endometrial ECM. a – b Representative brightfield images of macrophages taken with a 20x lens objective. Scale bars = 200 μm. **a** Macrophages 2 hours after treatment with LPS and IFN-γ or no treatment (unstimulated control, MΦ). **b** MΦ and LPS and IFN-γ-treated macrophages at 24 hours into the experiment, with media changed at 2 hours (to normal growth medium or media supplemented with endometrial ECM). **c** Gene expression analysis of Nos2, IL6, IL1-β (normalised to M1 control and housekeeping gene) and Arg1 (normalised to MΦ and housekeeping gene). Treatment with endometrial ECM significantly reduced the expression of Nos2 ($p < 0.0001$) (N = 5) and IL6 ($p = 0.0009$) (N = 5) in macrophages that were polarised to M1 phenotype, compared to the M1 control (N = 4). No significant difference was seen with IL1-β (N = 4) or Arg1 gene expression (N = 3) after ECM treatment of M1-polarised macrophages. Arg1 gene expression was significantly upregulated in the macrophages treated with IL-4 + IL-13 (M2 control) (N = 4) when normalised to MΦ 2 hour control ($p = 0.0328$). Each data point presents one biological replicate (N). Three technical replicates (n = 3) were plated for each experiment. Statistical analyses were performed with one-way ANOVA with Tukey's multiple comparisons test.

Flow cytometry analysis of CD86 and CD206 was also performed on macrophages that were stimulated with LPS and IFN-γ for 2 hours, followed by treatment with ECM. No change in CD86 or CD206 expression was seen with ECM treatment, compared to the M1 control (data shown in Appendix Figure B). This indicated that CD86 and CD206 were perhaps not ideal markers for this assay

or may suggest that when polarisation has occurred *in vitro*, cells have committed to a change in expression of cell surface markers which is not readily reversed. *In vivo*, this may be less relevant as there would be a constant turnover of macrophages depending on changes in cytokines and other biochemical cues.

3.5 Discussion and future work

The work presented in this chapter investigated the different biological properties of ECM hydrogel by studying the interactions between various cell types and ECM, as well as exploring how an *in vitro* model of endometrial fibrosis could be established for biomaterials testing. The experiments carried out in this chapter were selected for their relevance to cellular events involved in tissue healing. Both sow and pig endometrial ECM hydrogels were used in the in vitro experiments, although a direct comparison of the two was not always performed, due to the chronology of the *in vitro* work relative to when pig endometrial ECM was fabricated and characterised. Sow endometrial ECM was used for cell viability, proliferation and organoid studies, as well as the flow cytometry experiments to assess the impact of ECM on naïve macrophages. Pig endometrial ECM was used for proliferation, angiogenesis and CDM experiments, and to evaluate the immunomodulatory effect of ECM on M1-polarised macrophages.

The biocompatibility of endometrial ECM with endometrial cells was assessed with cell viability testing and cell proliferation studies. It was demonstrated that primary endometrial stromal cells cultured on a coating of endometrial ECM exhibited high viability (94%), comparable to SIS ECM and slightly, but not significantly, higher than control (no ECM coating). Endometrial stromal cells cultured on a coating of endometrial ECM were significantly more proliferative than control (no ECM coating). Interestingly, no significant difference was seen between endometrial ECM from younger pigs compared to ECM from older animals (sows), nor was there any significant difference in cell proliferation between endometrial ECM or SIS ECM, suggesting that it is probably a generic and common component of decellularised ECM that encourages cell proliferation. Cellular interactions with ECM are essential for driving cell fate, such as survival, differentiation and proliferation [264]. Major ECM components, such as collagen I, fibronectin and laminin have been demonstrated to affect cell adhesion kinetics, formation of focal adhesions, cell morphology and proliferative ability [264]. Different ECM proteins have been shown to increase proliferation of various cell types *in vitro*, with fibronectin enhancing the proliferation of fibroblasts specifically [264]. Cell proliferation, in particular stem cell differentiation, is important for tissue regeneration and wound healing. Therefore, the ability of the ECMs tested to increase endometrial stromal cell proliferation suggests an advantageous property for endometrial regeneration.

Angiogenesis is vital for wound healing and tissue regeneration to provide oxygen and nutrients to support the dynamic cellular processes that are involved in tissue repair and growth [256]. Several

studies have demonstrated the pro-angiogenic effect of ECM biomaterials, in particular SIS [257], [258]. In section 3.4.2.1, the results of an *in vitro* tubule formation assay were presented. Adding soluble endometrial ECM to HUVECs cultured on a layer of growth factor reduced basement membrane extract led to increased angiogenesis. Remarkably, this effect was observed both when ECM was added to growth factor and serum supplemented (complete) media, as well as when ECM was added to growth factor and serum replete basal media. In complete media, endometrial ECM promoted the formation of tubular networks with more junctions and branches and overall greater total tubule length compared to the positive control. In basal media, interconnecting tubular networks featuring junctions and branches did not form, even with the addition of endometrial ECM, however ECM stimulated the formation of more elongated tubules in comparison to the negative control. This was reflected in significantly increased total tubule length in the ECM supplemented media. A dose-dependent response was observed in these assays, with significantly increased angiogenesis metrics only seen when 400 μg/mL of endometrial ECM was added to the media, whilst there were non-significant increases with 200 μg/mL of ECM. Further work should involve a comparative study using SIS ECM, to determine if the angiogenic effect is stronger in one ECM type versus another.

The finding that endometrial ECM increased tubule formation, even in the absence of serum or additional supplements, suggested that decellularised endometrial ECM contains angiogenic factors, such as VEGF, EGF or FGF. Indeed, the angiogenic property of decellularised ECM biomaterials has previously been attributed to VEGF [257]. It has also been demonstrated that decellularised ECM can stimulate fibroblasts to produce more VEGF [258]. VEGF is produced by numerous different cell types but in the uterus, endometrial stromal cells have been shown to secrete VEGF [265], [266]. An experiment was therefore setup whereby immortalised human endometrial stromal cells were cultured on a coating of endometrial ECM, SIS ECM or on uncoated tissue culture plastic as a control. After 24 hours of culture and at full cell confluence, the supernatant was collected for human VEGF ELISA. No significant difference in VEGF concentration was found between any of the three supernatants. It is possible that applying a coating of ECM to the tissue culture plastic was insufficient exposure to ECM for the endometrial stromal cells and this experiment could be modified, in future, by preparing conditioned media from ECM as described by Hoganson et al. (2010) [258] or by adding ECM hydrogel to the media via a Transwell insert, as described in section 3.3.4.9.2 for the cell derived matrices experiments.

Challenges with 2D endometrial epithelial cell culture were both anticipated and encountered in the course of trying to establish endometrial *in vitro* models. Although it was possible to isolate primary

endometrial epithelial cells from mice uteri, cell yields were frequently insufficient for experiments and it was discovered that the primary epithelial cells could not withstand being passaged or expanded. Commercially, a benign murine or human endometrial epithelial cell line is not available; most epithelial cell lines are derived from endometrial adenocarcinoma. Therefore, to characterise the effect of ECM on endometrial epithelial cells and to aspire to develop an *in vitro* fibrosis model with endometrial epithelial cells, work was carried out with human endometrial organoids (sections 3.3.3 and sections 3.3.4.7). An experiment was performed whereby human endometrial organoids were passaged from Matrigel into 8 mg/mL SIS, UBM and endometrial ECM hydrogels and cultured for 7 days (section 3.2.3.1). In all three ECM hydrogels, some organoids grew but much less than in Matrigel. Of the three ECM hydrogels, organoids in endometrial and SIS ECM were more uniform and more closely resembled the appearance of organoids grown in Matrigel. To determine the true organoid formation capacity of endometrial ECM hydrogels, an organoid formation assay was conducted with 2 mg/mL, 5 mg/mL or 8 mg/mL endometrial ECM hydrogel. After 7 days of culture, all three concentrations of endometrial ECM hydrogel performed significantly worse than Matrigel, although 5 mg/mL was marginally better than the other two concentrations.

Previous studies have clearly demonstrated the ability of ECM hydrogels to support formation and growth of organoids [94], [105], [112]. Keane et al. (2015) compared oesophageal organoid formation capacity between three different types of porcine ECM hydrogel (oesophageal, SIS and UBM) and between 2 different gel concentrations (2 mg/mL and 6 mg/mL) [94]. The authors identified that tissue-specific ECM was most enabling for oesophageal organoid formation, whilst SIS ECM hydrogel was the worst performing, and more organoids formed in 2 mg/mL ECM hydrogel compared to the higher concentration [94]. Giobbe et al. (2019) compared porcine SIS ECM hydrogel with Matrigel for the growth and culture of gastric, intestinal, liver and pancreatic organoids from both mouse and human cells, including from adult and foetal human donors [112]. The authors used SIS ECM gel at 6 mg/mL, as they found that this concentration had the most similar rheological properties to Matrigel [112]. They reported not only comparable performance between Matrigel and SIS ECM for organoid formation capacity, organoid viability and size, it was also demonstrated that organoids could be formed directly from primary cells in SIS ECM hydrogel, without the need to first culture and passage organoids from Matrigel [112]. RNA sequencing of the organoids cultured in Matrigel versus SIS ECM gel identified both similarities and differences in transcriptomic profile, suggesting that further research into tissue matching between organoids and ECM gel culture substrate would yield interesting and informative findings [112]. Francés-Herrero et al. (2021) took a different approach to exploring the effect of ECM hydrogel on organoid culture, by culturing endometrial organoids in

Matrigel, in a chemically defined expansion medium supplemented with solubilised endometrial ECM [105]. They reported increased organoid proliferation rate when endometrial ECM was added to the media [105].

In considering the reasons for the relatively poor performance of endometrial ECM gel for organoid culture in the results presented in section 3.4.3, it is possible that further optimisation of the gel concentration was necessary. However, another consideration is the source of the ECM. The endometrial organoid culture experiments described in section 3.2.3 were carried out with ECM hydrogel made from sow endometrium, as these were the first batches of decellularised ECM that were optimised and characterised in this project. Giobbe et al. (2019) discussed, in their paper, the observation of batch-to-batch variability between tissues obtained from different animals and their effort to minimise this by consistently using pigs of a specific breed, age and weight to isolate SIS ECM [112]. It was noted that Giobbe et al. isolated SIS from piglets [112], which was unusual as most papers report isolating SIS from adult, market weight pigs. Contact was made with the first author, Giobbe, in order to clarify the importance of using young animals and it was confirmed that their research group specifically use piglets that are 2 weeks old, weighing 3 kg or less, as they have greater experimental inconsistency when older animals were used.

It was the observation of poor organoid growth in sow endometrial ECM gels as well as the conversation with Giobbe that prompted a shift, in this project, to producing ECM hydrogels from decellularised endometrium obtained from younger pigs. Practically, however, piglets are not feasible for isolating endometrial ECM as very young pigs have small and underdeveloped uteri, as was discussed in Chapter 2. Unfortunately, due to time constraints and the disruptions that the COVID-19 pandemic had on logistics and collaborative experimental work, there was insufficient opportunity to repeat and optimise the culture of endometrial organoids in ECM hydrogels. Future work would therefore include growing endometrial organoids in pig endometrial ECM gel and testing a greater range of concentrations to identify the optimum.

In section 3.4.4, the results of different approaches to establishing an *in vitro* endometrial fibrosis model using TGF-β1 were presented. To establish whether treatment of endometrial epithelial organoids with TGF-β1 would result in morphological changes to the organoids and EMT, human endometrial organoids were treated with TGF-β1, with and without the TGF-β1 inhibitor, A83-01, in the chemically defined growth medium. No obvious morphological differences were seen in the organoids treated with TGF-β1, even in the absence of A83-01, compared to the control.

Immunofluorescence staining also revealed no discernible differences between these two conditions although interestingly, both the control organoids and those stimulated with TGF-β1 equally expressed the mesenchymal marker, Vimentin. Vimentin was initially chosen as a marker of EMT and was not expected to be detected in the non TGF-β1-treated organoids. Human endometrial epithelium, which originates from the mesoderm, can co-express vimentin and cytokeratin, and this may relate to the contribution of mesenchymal-epithelial transition to stem or progenitor cell populations in the endometrium [267]. Co-expression of Vimentin with Cytokeratin has been observed in unstimulated dental epithelial organoids and this mesenchymal trait was postulated to be related to the presence of active stem cells [268]. Indeed, it is known, through single cell RNA sequencing analysis, that stem cells are present in endometrial organoids derived from human endometrial biopsies [214], though positive vimentin staining has not previously been described in endometrial epithelial organoids that were not part of a co-culture model.

Previous studies have demonstrated the effect of TGF-β1 on intestinal epithelial organoids in an *in vitro* intestinal fibrosis model. Hahn et al al. (2017) reported significant disruption and death of intestinal epithelial organoids when TGF-β1 was added to the culture media, although a small proportion of the disrupted organoids had increased expression of Vimentin and α-SMA [269]. Estrada et al. (2022) showed that TGF-β1 treatment of iPSC-derived intestinal organoids led to upregulation of EMT genes, including Vimentin and N-Cadherin, as well as evidence of co-expression of Vimentin and Cytokeratin on immunofluorescence staining [270]. Hemeryck et al. (2022) also reported that treatment of dental epithelial organoids with TGF-β1 increased Vimentin expression, attributing this to the EMT process, which is implicated in tooth root development [268]. Whilst a TGF-β1-induced EMT effect was not clearly observed by immunofluorescence staining in the work presented here, it is possible that provocation of EMT and the disruption of the robust integrity of epithelial organoids is time-sensitive. In other studies, TGF-β1 was introduced 24 hours [270] or 48 hours [269] after organoid culture was initiated, whilst in the experiment presented in section 3.3.4.7, TGF-β1 treatment occurred 4 days after organoids were passaged and cultured. Hahn et al. (2017) also highlighted a significant synergistic effect when combining TGF-β1 with TNF-α treatment, demonstrating much greater induction of EMT in intestinal epithelial organoids compared with TGF-β1 alone [269]. Moving forward, the establishment of an *in vitro* endometrial epithelial organoid fibrosis model may involve combinations of pro-fibrotic treatments and optimising the timing of treatments.

It was discovered that culturing primary endometrial stromal cells led to their spontaneous transdifferentiation into myofibroblasts, even in the absence of TGF-β1. This inspired a transition to modelling *in vitro* fibrosis in a different way, by studying the cell-derived matrices (CDM) from a human endometrial stromal cell line. Using a cell line ensured greater experimental reproducibility and eliminated the need to use animals. The method for generating fibroblast-derived CDM was adapted from Kaukonen et al. (2017) [261] and involved culturing fibroblasts at high density for 12 days, with or without TGF-β1, followed by decellularisation to enable staining and imaging of the deposited matrix. The experiment was first optimised with dermal fibroblasts, then the same method was applied to human endometrial stromal cells to study how endometrial matrix deposition is affected by TGF-β1 and ECM treatment. The results presented in section 3.4.4.3 demonstrate that treatment with TGF-β1 led to dramatic change in CDM morphology in both dermal fibroblasts and endometrial stromal cells, with significant increase in fibre alignment and isotropy, measured through image analysis. Addition of endometrial ECM hydrogel abrogated the effect of TGF-β1 and led to CDM consisting of more randomly aligned fibres with a significantly decreased coherence score, comparable to control CDM.

Loss of the anisotropic ECM meshwork in healthy tissue, along with the alignment of collagen fibres is characteristic of fibrosis [271]–[273]. Though CDM have not been used extensively to study fibrosis, Witherel et al. (2021) used CDM to illustrate the influence of different macrophage phenotypes on fibroblast behaviour and reported significantly less CDM fibre alignment when fibroblasts were treated with conditioned media from a pro-reparative macrophage phenotype [274]. The endometrial stromal CDM data presented in this chapter represents the first known reported study of the morphology of matrix deposition by endometrial cells in response to a pro-fibrotic factor and treatment with an ECM hydrogel. The data presented in section 3.4.4.3 implies that TGF-β1 increases scar-like matrix deposition by endometrial stromal cells, whilst simultaneous treatment with endometrial ECM prevents the development of a fibrotic matrix. There are, of course, limitations to this study and caveats to this conclusion. This observation has been made just on image analysis and there was no additional investigation of the biochemical and mechanical characteristics of the CDM. Further work could therefore include analysing the proteomic composition of the CDM with mass spectrometry and measuring the matrix stiffness with atomic force microscopy. Differences in composition and quantities of ECM proteins, as well as increased ECM stiffness, would be anticipated in the fibrotic CDM samples. Due to time constraints, the effect of endometrial ECM on TGF-β1-mediated CDM production was not compared with another type of ECM or another hydrogel control, such as a collagen gel. This could have highlighted interesting differences in the properties of different

types of ECM hydrogel and demonstrated that the effect seen is due specifically to degradation products of decellularised ECM biomaterials.

The favourable tissue regenerative effect of ECM biomaterials has long been attributed to the development of a pro-reparative immune microenvironment when ECM interacts with macrophages. Experimentally, ECM biomaterials that provoke a shift in macrophage polarisation away from the M1-like phenotype and towards an M2-like phenotype have generally been associated with more constructive tissue repair [245]–[247], [249]. It was therefore important to characterise the effect of decellularised endometrial ECM on macrophage phenotype, which was carried out through *in vitro* assays using a mouse macrophage cell line. These results were presented in section 3.4.5. To establish M1 and M2 macrophage controls, RAW 264.7 cells were treated with LPS and IFN-γ (M1) or IL-4/IL-13 (M2) and evaluated for upregulation of M1 markers (CD86, Nos2, IL1-β, IL6) or M2 markers (CD206, Arg1). Whilst M1 markers were reliably upregulated following LPS and IFN-γ stimulation, CD206 and Arg1 were not significantly upregulated with IL-4 and IL-13 stimulation. Instead CD206 expression was markedly increased with LPS and IFN-γ treatment, showing high co-expression with CD86 on flow cytometry. Arg1 gene expression was raised with both LPS/IFN-γ and IL-4/IL-13 treatment. The duration of cytokine treatment appeared to affect Arg1 expression, with higher Arg1 expression in the M1 control after 24 hours of cytokine treatment, whilst Arg1 was more increased in the M2 control after 2 hours of cytokine treatment. These findings highlight the dynamicity of macrophages and their sensitivity to different durations of cytokine exposure. Although Arg1 is often cited as a typical M2 marker, it is also expressed by M1-like macrophages [243], [275], and may not be consistently expressed by all M2-like macrophages [243]. Retnla, EGR and IL10 were also preliminarily screened as M2 markers by RT-qPCR [243] but were not found to be differentially expressed in IL-4/IL-13-treated RAW 264.7 cells (data not shown). As a reliable M2 control could not be determined, it was not possible to evaluate whether ECM hydrogels shifted macrophage polarisation towards an M2-like phenotype. Instead, the immunomodulatory effect of ECM hydrogels was assessed by whether they provoked a shift away from the M1-like phenotype.

In section 3.4.5, it was demonstrated that none of the ECM hydrogels themselves caused a pro-inflammatory macrophage response. Gene expression of M1 and M2 markers did not change significantly when Mφ were treated with ECM alone. When macrophages were first polarised to M1-like phenotype followed by removal of LPS/IFN-γ stimulus and addition of endometrial ECM hydrogel, there was a significant decline in gene expression of M1 markers Nos2 and IL6 compared to the M1 control. This highlighted the plasticity of macrophages and signified that endometrial ECM treatment

can shift macrophage polarisation away from a pro-inflammatory M1-like phenotype. These findings are similar to those reported in *in vitro* and *in vivo* studies, which have found that ECM biomaterials downregulate inflammatory macrophage markers [143]. Recently, Witherel et al. (2021) demonstrated that a hybrid M1/M2 macrophage population, *in vitro*, is more favourable for reducing fibrosis compared to a predominant M2 phenotype or M1 shifted to M2 phenotype, highlighting the relevance of not just focussing on the two ends of the spectrum [274].

There are several limitations and caveats to the macrophage studies presented in this chapter. Firstly, the use of a single macrophage cell line, *in vitro* setup and the dichotomised M1 and M2 macrophage characterisation is an oversimplified approach to determining the immunomodulatory effect of ECM hydrogels. Different types of macrophages, such as primary versus cell line and from different animal sources, respond variably to the same stimulus, including to ECM treatment [276]. Therefore investigating only the RAW 264.7 cell line means that the findings cannot be extrapolated to all macrophages. *In vivo*, the immune microenvironment in the context of tissue repair is much more complex and macrophages are influenced by a multitude of different factors. Therefore, it would be important and more biologically relevant to characterise the macrophage populations that predominate when endometrial ECM interfaces with endometrial tissue *in vivo*.

Characterisation of macrophage response was limited to flow cytometry and gene expression analysis to determine differential expression of M1 or M2 markers. Flow cytometry analysis of CD86 and CD206 expression found that this combination of markers was unhelpful for denoting M1-like and M2-like phenotypes, as after LPS and IFN-γ stimulation, macrophages predominantly co-expressed CD86 and CD206, whilst IL-4-stimulated macrophages did not upregulate expression of either CD86 or CD206. Identification of optimal cell surface markers for M1 and M2-like macrophages is a challenge that has been recognised in the field [277]. Future work would include verifying a better panel of cell surface markers to improve the characterisation of the effect of ECM hydrogels on macrophage polarisation. For example, CD9 and CD36 could be evaluated as M2 markers [277]. Other methods for detecting protein expression of M1 and M2 markers could be used, such as western blot, and functional macrophage behaviour could also be assessed, such as with phagocytic activity, nitric oxide production or effect of macrophage conditioned media on fibroblasts.

3.6 Summary of key findings

Through different cell experiments, this chapter highlighted various biological effects of endometrial ECM hydrogel that would be beneficial for constructive tissue healing after endometrial trauma. The results presented in this chapter correlated with most of the initial hypotheses and were in keeping with published studies on the pro-regenerative properties of ECM biomaterials.

Endometrial ECM hydrogel supported endometrial cell viability and improved endometrial cell proliferation in *in vitro* assays. Endometrial ECM hydrogel also demonstrated a pro-angiogenic effect in a tubule formation assay. A novel *in vitro* endometrial fibrosis model was developed using TGF-β1 to cause scar-like deposition of fibres by endometrial stromal cells. Analysis of the cell-derived matrices showed that treatment with endometrial ECM hydrogel attenuated the effect of TGF-β1. The immunomodulatory properties of endometrial ECM hydrogel were demonstrated by its ability to downregulate the expression of M1 phenotype genes, in LPS and IFNγ-stimulated macrophages.

It would be interesting to determine, in future work, how endometrial ECM performs in relation to other ECM types, such as SIS. In particular, to evaluate whether there is a tissue-specific effect of ECM hydrogels on endometrial cells.

Chapter 4 – *In vivo* effect of endometrial ECM hydrogels

4.1 Chapter aims

Like most *in vivo* disease models, the majority of animal studies on Asherman's syndrome have been done on rodents and rabbits. These species have a bicornuate uterus, involving two uterine horns [278], allowing for one horn to be used for intervention and the other to serve as a control in most studies. Modelling Asherman's syndrome in animals requires a method to generate trauma to the endometrium that successfully replicates the intrauterine scarring that is characteristic of the disease.

This chapter will focus on summarising the literature on mouse models of Asherman's syndrome and describing the work carried out to develop and validate a mouse model of intrauterine fibrosis. Mechanical and chemical injury methods were tested and their efficacy and reliability for generating endometrial damage were assessed by histology, immunohistochemistry and RT-qPCR. The results and learnings from each pilot study are presented and discussed.

Using an optimised model of mouse intrauterine fibrosis, the effect of endometrial ECM hydrogel was tested in a final study for its ability to prevent scarring and support endometrial regeneration. Endometrial ECM hydrogel was applied immediately after intrauterine trauma and tissues were harvested one week later for histological, immunohistochemical and gene expression analysis. In the discussion, the findings from this study are compared to the one other existing publication on endometrial ECM for treatment of IUA in a mouse model.

4.2 Introduction to *in vivo* modelling of intrauterine fibrosis

4.2.1 Mouse models of intrauterine fibrosis

Whilst mice and humans have structurally very different reproductive tracts (Figure 4.1), the mouse uterus and human uterus share many similarities histologically and functionally [278]. Both have an inner, glandular endometrial mucosal lining, overlying smooth muscle myometrium [278] (Figure 4.1). Like the human menstrual cycle, rodents also have a reproductive cycle known as the estrus cycle. Each estrus cycle lasts 4-5 days and has four phases; proestrus, estrus, metestrus and diestrus [279]. Each phase corresponds to anatomical, structural and hormonal changes that prepare a mouse for pregnancy, with estrus being the phase when a female would mate [279], [280]. The morphology of the endometrium varies across each phase of the estrus cycle [279], [280] and some studies have included timing endometrial injury to a specific phase in the cycle [56], [130], [281], [282], although most studies do not.

Several different methods for injuring the endometrium, to generate a mouse of model of intrauterine fibrosis, have been described in the literature. These include mechanical injury methods that abrase the endometrium, chemical injury methods that rely on perfusing the uterine lumen with an agent that causes tissue damage and electrocoagulation to cause thermal endometrial injury. The most commonly reported methods are mechanical trauma and ethanol-induced injury to the endometrium. These are discussed in the subsequent sections. Other techniques for generating murine models of intrauterine fibrosis include electrocoagulation [282], [283] and other chemical methods, such as trichloracetic acid [284], [285]. These are less frequently reported compared to mechanical injury and ethanol injury models.

Various mouse strains have been used for *in vivo* modelling of Asherman's syndrome, including both immunodeficient [286] and non-immunodeficient strains. However, there does not appear to be a consensus within the literature as to whether a particular strain is best for studying this disease. Female mice reach sexual maturity between 6-8 weeks [287] and most studies on murine models of intrauterine fibrosis used mice between the ages of 6 to 12 weeks [282], [288]–[290].

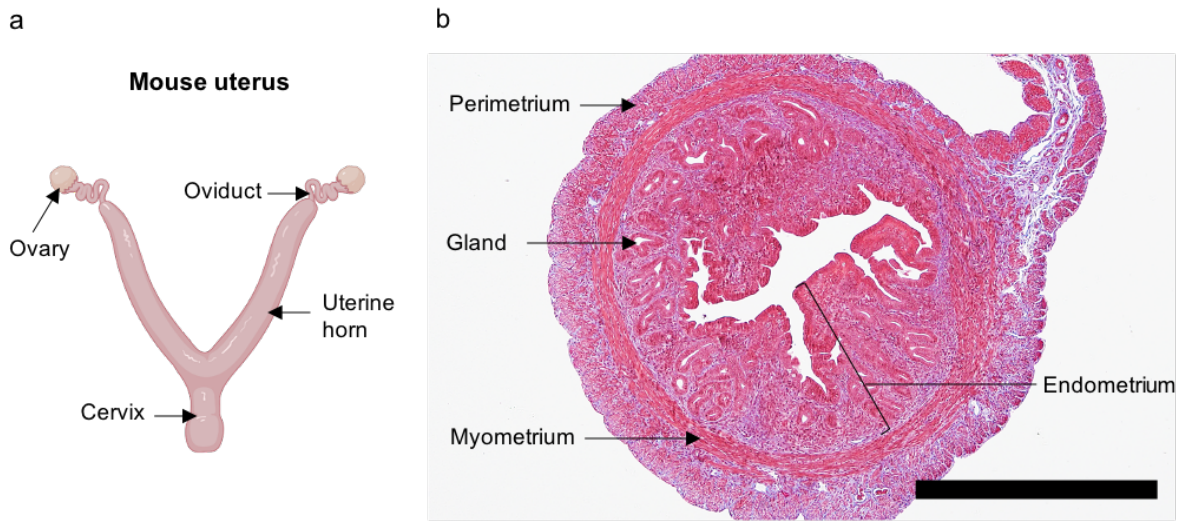


Figure 4.1 Diagram and histology of the mouse uterus. **a** Diagram of mouse reproductive tract with anatomical annotations. The mouse, like most mammals, has two uterine horns, which join to one cervix. This is useful for *in vivo* uterine disease or treatment models, as it allows one horn to receive the intervention and the other horn to serve as a sham control. **b** Masson's trichrome stained cross-section of the normal mouse uterine horn. The perimetrium, myometrium, endometrium and uterine gland have been annotated. The surface of the endometrium is lined with columnar epithelium. The endometrium contains multiple uterine glands surrounded by endometrial stroma. This section was cut from the uterine horn of a healthy, 8-week-old, control mouse that had not received any surgery or intervention. The image was acquired with a 4x lens objective using an Olympus IX71 upright microscope with colour camera. Scale bar = 1 mm.

4.2.2 Mechanical injury models

Murine intrauterine fibrosis can be generated by mechanical injury methods that rely on scraping the endometrium. In rat studies, researchers have reported the use of a mini endometrial curette to traumatise the endometrium, generating reduced numbers of endometrial glands and increased collagen deposition [74], [291]. The mouse uterus is much smaller than that of the rat and therefore a 27-gauge needle is the most commonly reported tool for generating mechanical trauma [289], [292]–[294]. Alawadhi et al. (2014) were the first to describe this method for generating a mouse model of Asherman's syndrome [292]. A needle was inserted into the uterine lumen, rotated and withdrawn repeatedly whilst the tip of the needle scraped the endometrial lining [292]. After 3 estrus cycles, the uterine horns were collected for histological assessment or the mice were mated. The fibrosis rate ranged between 40-80% in the mice that received uterine trauma, by estimating the area

and density of fibrosis on Masson's Trichrome stained sections [292]. The pregnancy rate reduced from 100% to 30% in the mechanical injury group that did not receive therapeutic intervention [292]. Using the 27g needle injury method, Xu et al. (2017) reported a significant increase in the area of fibrosis between the control uteri (12%) and traumatised uteri (90%) ($p < 0.001$) [289]. With the same technique, Hu et al. (2015) showed significantly increased immunohistochemistry scores and mRNA expression for fibrosis markers (CTGF, Collagen I, Collagen III and TGF-β) after 2 estrus cycles [293].

In some studies, mechanical curettage was combined with an inflammatory stimulus, typically lipopolysaccharide (LPS) [295], [296]. Zhu et al. (2016) used a 27g needle to scrape the endometrium, as previously described, then injected 6 mg/L of LPS into the uterine lumen [295]. Using Masson's trichrome staining analysis, a significantly higher rate of fibrosis area was found in the damaged group, than the sham control group, after 1, 2 and 4 estrus cycles, although the greatest fibrosis was seen after 1 estrus cycle [295]. Immunohistochemistry and western blot of TGF-β1, CTGF, Collagen I and Collagen III demonstrated significant upregulation of these proteins in the damaged group after 1 estrus cycle [295]. Ma et al. (2021) did not describe how the endometrium was scraped, but combined mechanical trauma with an LPS-soaked suture left inside the uterine lumen [296]. They reported significant reduction in endometrial glands and significantly upregulated gene expression of TGF-β1, α-SMA and MMP9 in the injured group that received control treatment, compared to the uninjured after 14 days [296].

4.2.3 Ethanol injury model

Since 2018, several papers have reported the use of ethanol perfusion to induce endometrial injury and fibrosis in murine models. Jing et al. (2018) used anhydrous ethanol injected into rat uterine cavities to generate a thin endometrium model, with which the authors assessed the effect of VEGF-transfected bone marrow stem cells on endometrial regeneration [297]. The concentration of ethanol and duration of ethanol exposure were not reported but histological analysis showed significantly reduced endometrial thickness, with extensive endometrial damage including coagulation necrosis and cell death [297].

Kim et al. (2019) compared ethanol injury with mechanical injury of the endometrium in C57BL/6 female mice [298]. The authors tested 50%, 70% and 100% ethanol perfused into the uterine cavity for several minutes, versus a copper scraper to induce mechanical injury. Whilst they only evaluated

gross morphology and H&E-stained histology, they found that all concentrations of ethanol produced endometrial damage, with 100% ethanol being the most effective [298]. However, they did not specify the exact duration of ethanol perfusion. In comparison, the mechanical injury method was more prone to experimental variability and produced inconsistent, moderate endometrial damage [298]. They also compared a blind, vaginal catheterisation approach for ethanol injection versus an open surgical approach which enabled direct visualisation and clamping of the uterine horn. The vaginal approach, whilst enabling shorter anaesthetic times, did not allow for precise insertion of the catheter and resulted in occasional perforation into the abdominal cavity [298]. Clamping of the uterine horns, with the open surgical approach, prevented leakage of ethanol outside of the uterus. Interestingly, shorter anaesthesia was associated with improved efficacy of the model in addition to being safer [298].

Zhang et al. (2020) evaluated the effect of different ethanol exposure times on the extent of uterine fibrosis, inflammation and angiogenesis in Balb/c mice, as assessed by histology and immunohistochemistry staining for CD31 and F4/80 [281]. In this study a vaginal, transcervical perfusion technique was used by injecting 95% ethanol through an intragastric needle inserted into the right uterine horn, after administration of a cervical relaxant [281]. When ethanol was seen to flow back out of the vaginal orifice, this was determined as the ethanol exposure start time [281]. Following ethanol treatment, the horn was rinsed with normal saline. A preliminary screening had revealed that with 95% ethanol, exposure times of longer than 1 minute caused excessive tissue damage, with complete destruction of the endometrium and coagulative necrosis of the endometrial glands [281]. Therefore, in the main study, 10 second, 20 second, 40 second and 1 minute treatment times were compared and mice were sacrificed on day 8 for analysis [281]. The degree of endometrial fibrosis was quantified by image analysis of Masson's trichrome stained histological sections and reported as the percentage of fibrosis [281]. Endometrial fibrosis was significantly increased in ethanol treated uterine horns, compared to sham control [281]. The extent of fibrosis was positively correlated with increasing ethanol exposure times ($p < 0.01$ at 10 seconds, $p < 0.001$ at and above 20 seconds) [281]. Endometrial thickness and number of endometrial glands were significantly reduced with ethanol injury ($p < 0.001$), showing a negative correlation with increasing ethanol treatment time [281]. At 20 seconds or longer there was significant increase in expression of F4/80, a generic macrophage marker, suggestive of an upregulated inflammatory response [281]. At 20 seconds and 40 seconds, CD31 was expressed significantly more than the sham control. However, CD31 was significantly downregulated at 60 seconds, implying that moderate ethanol exposure increases angiogenesis whilst prolonged exposure inhibits vascularisation [281]. Fertility was assessed by comparing the pregnancy rate and number of embryos in mated mice in the sham control group the

40 second ethanol group. The number of pregnant mice was negatively impacted by ethanol treatment and the number of embryos were significantly reduced in the ethanol group ($p < 0.001$) [281]. A key limitation of the methodology in this study is the blind approach to injecting ethanol into the uterus. The authors recognise that whilst they cannulate the right uterine horn, there is no prevention of ethanol flowing into the left uterine horn also [281]. In addition, without clamping the distal end of the horn, ethanol is likely to leak into the peritoneal cavity causing extra-uterine injury that may confound the results or affect animal survival. Another notable limitation with the methodology was the imprecision of determining ethanol exposure time, relying on observing backflow of ethanol out of the vagina [281], which could be affected by variation in sizes of uterine horns.

4.2.4 Evaluating endometrial injury and regeneration

The most consistently reported approach for evaluating the extent of endometrial fibrosis in murine models of Ashermans syndrome is the percentage of fibrosis, measured by image analysis of blue (collagen) staining on Masson's trichrome stained sections [106], [281], [282], [292]–[296]. The method by which this is done is usually not described in detail by the authors, therefore there is unlikely to be a standardised approach to analysing this outcome. The inherent problem with quantifying fibrosis with Masson's trichrome stained images is that it is common for there to be batch-to-batch and inter-image variability in staining intensity, which can affect the accuracy of image analysis. Immunohistochemistry [282], [289], [293], [295] , western blot [282], [289], [295], [296] and qPCR [106], [282], [286], [289], [293], [296] are also often used to quantify the extent of fibrosis or to measure endometrial function. Commonly reported fibrosis markers include Collagen I [282], [293], [295], [296], Collagen 3 [293], [295], TGFb1 [293], [296] and α-SMA [282], [289], [296], which are upregulated when trauma results in scarring. Following therapeutic intervention, endometrial function and receptivity may be assessed by expression of estrogen receptor and progesterone receptor [64], [294], Hoxa10 [64], [299] or LIF [64], [130], [288]. For indicators of tissue regeneration, Ki67 or PCNA are markers of cell proliferation [286], [294], [299] and angiogenesis may be inferred from determining VEGF expression [74], [294]. The timepoints selected for tissue harvesting and histological analysis varies between 1 estrus cycle (4 days) [295] to 90 days [286], though a commonly reported timepoint is 7-8 days post surgery [282], [283], [294], or 2 estrus cycles [293], [295].

4.3 Materials and Methods

4.3.1 *In vivo* experiments – general process

All animal experiments were carried out at University College London, in collaboration with Professor Simon Waddington and postdoctoral researcher, Dr Ashley Boyle. All animal handling and experimental work were performed with ethics approval and in accordance with the UK Home Office Animals Scientific Procedures Act 1986, within the remits of a Home Office approved project licence (PPL no. 14300) and Home Office issued personal licences. All surgeries were performed by Professor Waddington, preparation of treatments and post-surgical recovery was performed by this author and general animal maintenance was carried out by Dr Ashley Boyle. All mice were purchased from Charles River Laboratories and allowed to acclimatise for 7 days before any procedures were carried out. Non-immunodeficient mouse strains, at 8-9 weeks old were used for all the experiments. For pilot study 1 C57BL/6 inbred mice were used, however the mice and their uteri were considered too small for ease of optimising the surgical model. For all subsequent studies, the larger CD1 outbred strain of mice were used. The CD1 mice were chosen because it was noticed that they tended to have slightly larger sized uteri, making it easier to perform the surgical model. The mice were housed in cages in groups of 5 and given food and water ad libitum. Post-surgery the mice were kept in single cages and supplemented with a wet mash diet.

For all surgeries, the mice were anaesthetised with 5% isoflurane inhalation and anaesthesia was maintained with 3% isoflurane throughout the procedure. Adequate anaesthesia was assessed by observing the slowing down of respiratory movements and loss of pedal reflexes. The abdomen of the mice was cleaned with iodine and a small midline laparotomy was performed to allow identification of and intervention to the right uterine horn. No interventions were performed in the left uterine horn, which served as a sham operation control. After uterine injury, the peritoneum and the skin were closed in separate layers by suturing with Mersilk 5.0. The mice were given analgesia by subcutaneous injection of Metacam pre-procedure and topical application of local anaesthetic cream to the laparotomy wound post-procedure. Care was taken to minimise surgery and anaesthesia time. All procedures were carried out on a 37^{o}C heat mat. Immediately after surgery, the mice were placed in a heated recovery chamber and observed until they regained normal movements, before being transferred to a normal cage. At the end of the experiment, or at a humane endpoint, animals were culled by cervical dislocation followed by decapitation as confirmation.

4.3.2 Developing a mechanical injury model for intrauterine fibrosis

In pilot study 1, the right uterine horn was injured with a 25g sterile hypodermic needle by inserting the needle through the uterine wall, just above the uterine bifurcation, into the lumen and advancing the tip of the needle to the distal horn. Using the bevel of the needle the endometrium was scraped by repeatedly rotating and withdrawing the needle until the uterine horn became hyperaemic (Figure 4.2). Mice were culled at day 2, day 5 or day 9 post-surgery (3 mice per timepoint) and the uterine horns were collected for histological assessment.

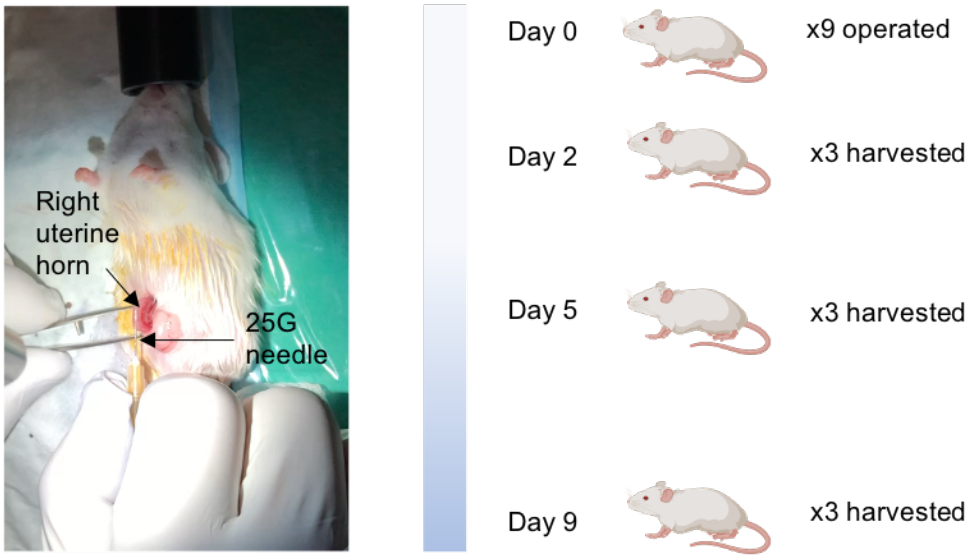


Figure 4.2 Pilot study 1 overview. The photograph on the left shows a mouse under general anaesthetic, with a midline laparotomy and the right uterine horn exteriorised. A 25G hypodermic needle was inserted through the uterine wall into the lumen of the right horn and repeatedly rotated and withdrawn to cause endometrial abrasion. The study involved the same procedure performed on 9 mice at day 0. Three mice were culled to harvest the uterine horns for histology at 3 different timepoints.

In pilot study 2, three different techniques were assessed to generate intrauterine fibrosis: two mechanical injury methods and one method combining mechanical and inflammatory injury (Figure 4.3). In the first method, 1 mm and 1.25 mm diameter 3D-printed scrapers were fabricated, with a barbed design of stacked cones that would cause endometrial abrasion when the scraper was withdrawn (Figure 4.3). A small incision was made at the distal end of the right uterine horn, the scraper was inserted and advanced proximally to the uterine bifurcation and then rotated and

withdrawn. In the second method, the 3D-printed scraper was first dipped in LPS 100 ng/mL, from E.Coli O111:B4 (Sigma-Aldrich, L4391), and the same process was carried out as previous. In the third method, a 0.9 mm diamond-coated drill bit was dipped in LPS 100 ng/mL then inserted into the uterine lumen, rotated and withdrawn several times with gentle counter-pressure on the uterine wall. The mice were culled at day 7 post-surgery and the uterine horns were collected for histological assessment. Day 7 was chosen as the timepoint for tissue collection, based on mouse studies that have identified significant increase in fibrosis by day 7-8 post endometrial trauma [281], [282], [289], [294].

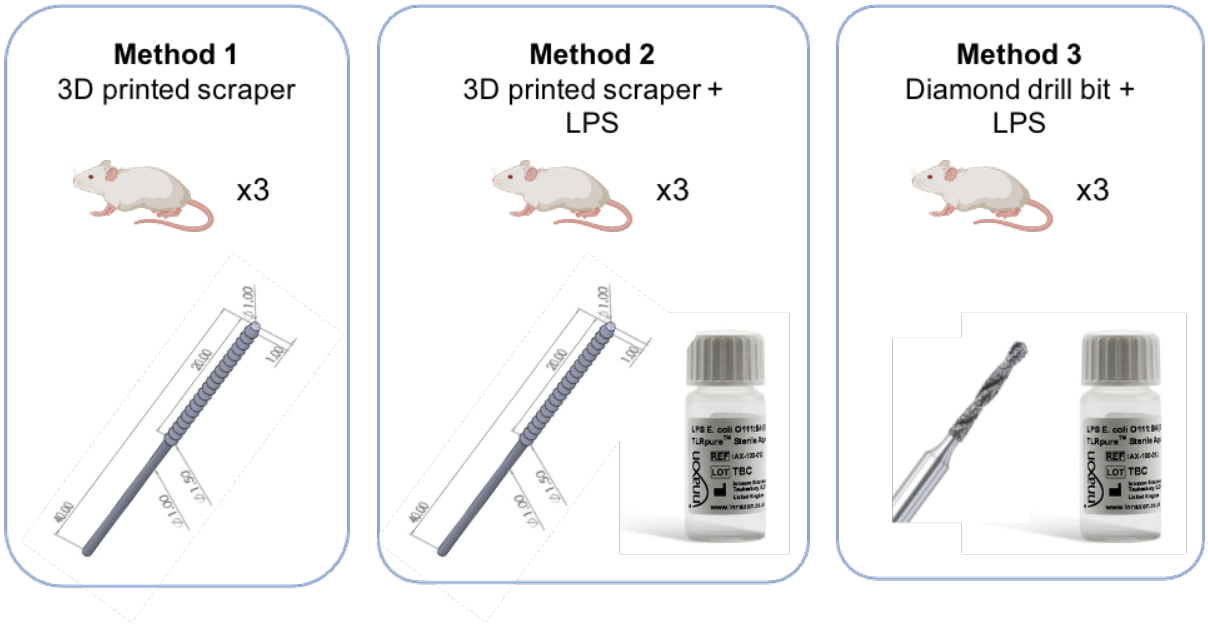
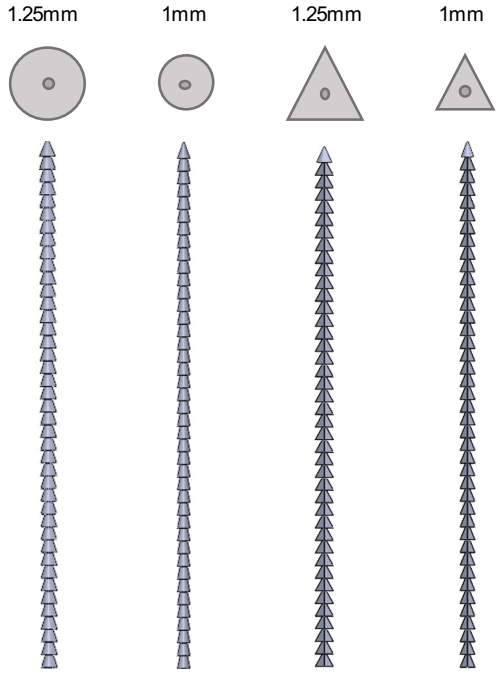
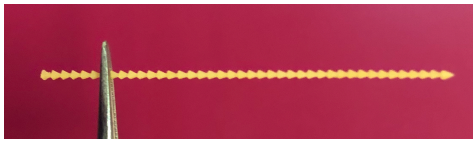


Figure 4.3 Pilot study 2 overview. To evaluate a mechanical injury method for generating intrauterine fibrosis, three mice were assigned to each of three different injury methods. Method 1 involved using a 3D-printed scraper, method 2 combined a 3D printed scraper with LPS 100 ng/mL and method 3 involved a metal diamond-coated drill bit and LPS 100 ng/mL. All mice were culled at day 7 to collect uterine tissues for histology.

In pilot study 3, a mechanical injury method was compared with a chemical injury method. In the mechanical injury group, the 3D-printed scraper design was modified so that instead of stacked cones the barbed scraper was made of stacked pyramids, creating more angular edges to abrase the endometrium (Figure 4.4). The right uterine horn was scraped with a 1 – 1.25 mm diameter 3D-printed scraper in the same manner as pilot 2. No LPS was used, after observing no difference in effect in pilot study 2.





Type	Outer Radius	Side Length	Taper (degrees)
Circle	1	N/A	20
Circle	1.25	N/A	25
Triangle	1	1.15	20
Triangle	1.25	1.44	25

Point tip radius 0.05 mm

Inner radius 0.3 mm

Figure 4.4 Different geometries of 3D-printed endometrial scrapers. The scrapers used in pilot study 2 were designed with stacked cones and the scrapers used in pilot study 3 were designed with stacked pyramids to create a more exaggerated barbed effect. One end of the scraper was tapered, to facilitate insertion into the uterine horn. The scrapers were printed to have an outer radius of 1 mm or 1.25 mm so that they could fit inside the uterine lumen. Graphics of scrapers produced by Lorna Barron.

4.3.3 Developing a chemical injury model for intrauterine fibrosis

In pilot study 3, one group of mice was treated with a chemical injury method and compared to a second group receiving mechanical injury. In the chemical injury group, the right uterine horn was identified, and the proximal and distal ends of the horn were clamped with forceps. 100 μL of 95% ethanol was injected into the uterine lumen via a 27G needle for 45 seconds and then aspirated. The uterine lumen was then washed with PBS before the horn was unclamped. In the ethanol injury group, 3 out of 5 mice had to be culled early (day 1 and day 2 post-surgery) due to adverse effects (pain) or complications (wound dehiscence). Two mice survived until the end of the experiment on day 7 post-surgery. In the mechanical injury group, all mice were culled at day 7 post-procedure. The uterine horns were harvested immediately after culling and one segment of each horn was fixed for histological assessment, whilst another segment was stored in RNAlater™ (Invitrogen) for subsequent

RNA isolation. Uterine tissues were collected for histological assessment only in the mice that were culled on days 1-2.

To minimise adverse effects and complications from the chemical injury model, modifications were made to the technique in pilot study 4. The duration of ethanol treatment was shortened to 30 seconds and 2 different concentrations of ethanol (95% and 90%) were tested. The proximal end of the right uterine horn was clamped with an atraumatic mini vascular clip. A small incision was made at the distal end of the uterine horn and a length of polyethylene tubing, with an outer diameter of 0.61 mm and inner diameter of 0.28 mm, was inserted into the uterine lumen (Figure. 4.5). The distal uterine horn was temporarily ligated around the tubing by tying a suture to create an enclosed segment of the uterine horn where ethanol can be infused without risk of leaking into the peritoneal cavity or through the cervix (Figure 4.5). 100 μL ethanol was injected through the tube for 30 seconds then aspirated and the lumen was then washed with PBS. To unclamp the uterus the vascular clip was removed, and the distal suture was cut. The tubing was removed, and the incision was deemed small enough to be allowed to heal by itself. In this pilot study, 1 out of 5 mice was culled at one-hour post-procedure due to adverse effects (pain and abnormal movement). The remaining mice survived without complication to day 7 when they were culled for harvesting of the uterine horns.

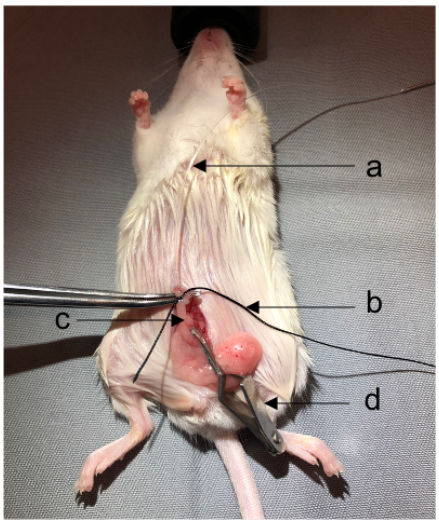


Figure. 4.5 Intrauterine ethanol perfusion setup. Photograph of a mouse under general anaesthetic, with a midline laparotomy and right uterine horn exteriorised. **a** Polyethylene tubing, with one end inserted into the right uterine horn and the other end connected to a syringe containing ethanol or PBS (not shown in photo). **b** Mersilk suture used to temporarily secure the polyethylene tubing, by tying a knot at the distal end of the uterine horn. **c** Right uterine horn. **d** Atraumatic vascular clip applied to temporarily clamp the proximal uterine horn to prevent leakage of ethanol through the cervix.

4.3.4 Evaluating effect of ECM hydrogel on ethanol-induced intrauterine fibrosis

In the final study, the ethanol injury model was modified slightly to limit the severity. The same technique was applied as described in pilot 4 but this time 90% ethanol was infused for only 15 seconds, followed by PBS wash. One group received ethanol treatment and PBS only in the right uterine horn and was considered the injury only control group. The second group received ethanol injury and PBS wash, followed by delivery of 50 μL of 8 mg/mL endometrial ECM hydrogel into the lumen of the injured right horn, using gel-loading pipette tips designed for gel electrophoresis (Biorad) (Figure 4.6). The ECM gel was prepared 30 minutes before surgery (as described in Chapter 2, section 2.3.5.1) and was kept at room temperature prior to injection, to minimise cooling of the animal and to speed up gelation. Preliminary tests showed that ECM gel could still be easily injected at room temperature. All mice recovered without complication and were culled at day 7 post-surgery. Three, age-matched, same strain, female mice that did not receive any surgical intervention were used as the true, unoperated experimental controls. The uterine horns were collected and cut into 3 segments. One segment was fixed for histological assessment, one segment was transferred to RNAlater™ (Invitrogen) and stored at 4°C and the remaining segment was snap frozen on dry ice and stored at -80°C for subsequent protein isolation.

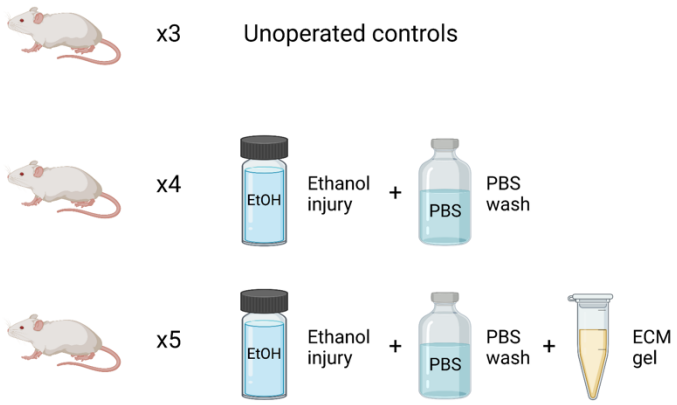


Figure 4.6 Final *in vivo* study overview. Three mice did not receive any surgery or treatment and was used as the true experimental controls. Four mice received 90% ethanol for 15 seconds to cause endometrial damage, followed by a PBS wash (injury only group). Five mice received 90% ethanol for 15 seconds, followed by a PBS wash, followed by treatment with endometrial ECM hydrogel. All mice were culled at day 7 to collect uterine tissues for histology and RNA extraction.

4.3.5 Tissue collection and histology

Tissues were collected immediately after the animals were culled. The uterine horns were either kept whole or cut into 3 segments (proximal, middle and distal) and fixed in 10% (v/v) Neutral Buffered Formalin for 6-24 hours at room temperature, depending on the thickness and size of the tissue. The tissues were then transferred to 70% ethanol. Each segment was embedded in paraffin separately and 4 μm sections were cut to reveal the circular cross-section of the uterine horn. The sections were mounted on glass slides and, as a standard, stained with Haematoxylin and Eosin or Masson's Trichrome. Some sections were also stained with Picrosirius Red to assess specifically for presence of collagen. All histology processing and staining were performed by Miss Lorraine Lawrence (LL) in the core histology facility at Imperial College London. All image acquisition and data analysis was performed by this author.

4.3.6 Histological analysis of degree of collagen deposition

The degree of fibrosis was quantified by image analysis using Image J software (version 1.52) and the Colour Deconvolution plugin, which unmixes dyes in images by colour subtraction. Masson's trichrome-stained histological sections were imaged with a 40x lens objective on a Zeiss Axio Observer widefield microscope with a colour camera. Three separate areas were captured for each sample. The images were loaded into Image J and the Colour Deconvolution plugin was used to first define new colour vectors based on the Masson's trichrome stained images. The vectors were saved so that the same parameters could be used for analysing all images. The plugin was then run to generate an RGB version of the original image, which was then separated into three colour channels (purple, blue and white). Selecting the blue channel and the all-colour RGB image only, both images were converted to 8-bit grayscale then manual black and white thresholds were set, referring back to the original image for accuracy. An area selection was created and saved as a region of interest, then each region was measured as an area in relation to the original image file. The blue area was divided by the all-colour area to determine the percentage of blue-stained area. As blue staining in Masson's trichrome correlates to collagen, the percentage of blue staining infers the degree of collagen deposition. In the literature, this output is often referred to as the degree of fibrosis [295], [300]. Comparisons and statistical analysis was performed between the sham control and injured horns and, in the final study, between the injured horns and injury + ECM horns.

4.3.7 Histological analysis of number of endometrial glands

The number of endometrial glands were counted manually by reviewing the H&E and Masson's trichrome stained sections imaged with a 4x lens objective on a microscope with colour camera (Olympus IX71). Glands are easy to recognise as round or tubular structures lined by simple columnar or cuboidal epithelium found within the endometrial layer [301]. The total number of glands in a whole section were counted for each sample. Comparisons and statistical analyses were performed between the injured horns and the control horns and, in the final study, between the injured horns and injury + ECM horns.

4.3.8 Immunohistochemistry

Unstained 4 μm sections of tissue were deparaffinised with Histo-Clear™ (Fisher Scientific) and rehydrated. The slides were immersed successively in Histo-Clear™ (3 minutes), Histo-Clear™ (3 minutes), 100% Ethanol (2 minutes), 90% Ethanol (2 minutes), 70% Ethanol (2 minutes) and type 1 ultrapure water (2 minutes). Antigen retrieval was performed by placing the slides in boiling hot sodium citrate buffer (sodium citrate 10 mM, 0.05% Tween 20, pH 6.0) for 20 minutes. The slides were then rinsed with cold PBS and dried. A border was drawn around each tissue section with a Pap pen and the ink was allowed to fully dry. The sections were blocked with hydrogen peroxide blocking solution for 10 minutes at room temperature then washed once with TBS containing Tween 0.1% v/v (TBS-T). The sections were then blocked in a blocking buffer (2% (v/v) goat serum, 1% (w/v) BSA, 0.1% (v/v) Triton X-100, 0.1% (v/v) Tween) for 1 hour at room temperature and washed 3 times with TBS-T for 5 mins each time. The sections were incubated with primary antibodies (see Table 4.1) diluted in blocking buffer overnight at 4^{o}C in a humidified chamber. After 4 washes in TBS-T (5 mins each wash), DAB staining was performed using a commercially available HRP/DAB detection IHC kit (Abcam, ab64264), following the manufacturer's protocol. Biotinylated goat anti-polyvalent solution, supplied with the kit, was applied to the sections and incubated for 10 minutes at room temperature, followed by 4 washes with TBS-T. Streptavidin peroxidase solution, supplied with the kit, was then added to the sections and incubated for 10 minutes at room temperature, followed by 4 washes with TBS-T. DAB chromogen was mixed with DAB substrate (supplied with the kit) at a 1:50 v/v ratio and then added to the tissue sections for 30 seconds to 10 minutes, ensuring the same duration of DAB staining time was used for all control and injured sections in the same experiment. The sections were then washed 4 times with TBS-T and Haematoxylin was applied for 1 minute as a counterstain. Finally, the slides

were rinsed with type 1 water then dehydrated and cleared by proceeding in reverse through the initial deparaffinisation and rehydration steps. DAB-stained slides were mounted with glass coverslips and DPX-new. The sections were imaged on a Zeiss Axio Observer Inverted Widefield Microscope with a colour camera, ensuring that the same camera settings were used for all sections in one experiment.

Table 4.1 Primary antibodies used for immunohistochemistry

Antibody	Dilution
Rabbit polyclonal anti-collagen I (Abcam, ab34710)	1:100
Rabbit polyclonal anti-collagen III (Abcam, ab7778)	1:200
Rabbit polyclonal anti-CTGF (Abcam, ab6992)	1:400
Rabbit monoclonal anti-TGF-β1 (Abcam, ab215715)	1:300

Note: Staining for Ki67 (cell proliferation marker) and VEGF (angiogenesis marker) was also performed for selected sections in the final study but no difference in expression was observed between control, injured and ECM-treated groups. As there was insufficient time to optimise the staining for these markers, the results were not presented here.

4.3.9 Analysis of immunohistochemistry

Four independent, blinded assessors were asked to grade the immunohistochemistry by reviewing images of the DAB-stained sections, captured with a 10x lens objective on a widefield microscope with a colour camera (Zeiss Axio Observer), with the same settings used for each image capture. Each assessor was asked to assign each image a score between 0 to 3 for intensity of DAB staining, with 0 correlating to absent staining and 3 for strong staining. The scores from each assessor were averaged for each image and plotted. Comparisons and statistical analyses were performed between the sham control and injured horns and, in the final study, between the injured horns and injury + ECM horns and between the sham control horns in the injury only group and injury + ECM group.

4.3.10 RNA isolation from uterine tissue and cDNA synthesis

The uterine tissue pieces were removed from RNAlater™ and transferred to a 2 mL microcentrifuge tube containing 500 μL of TRIzol™. The samples were frozen at -80°C then thawed, before being homogenised using a TissueRuptor device and probe (Qiagen), using a fresh probe for each sample. RNA isolation was then performed as previously described (Chapter 3, 3.3.4.4), by chloroform-mediated phase separation and using the RNeasy Mini Kit (Qiagen) following the manufacturer's protocol. RNA concentrations were measured by Nanodrop and all RNA samples were diluted to the same concentration prior to cDNA synthesis using the QuantiTect Reverse Transcription Kit (Qiagen) following the manufacturer's protocol. The method for cDNA synthesis was described in detail in Chapter 3, 3.3.4.5. cDNA was stored at -20°C until use in qPCR.

4.3.11 RT-qPCR

The cDNA was diluted to desired working concentration with nuclease-free water prior to RT-qPCR. RT-qPCR was performed using Taqman Fast Advanced Master Mix (Applied Biosystems) and Taqman gene assays, following the manufacturer's protocol. Table 4.2 shows a list of the gene assays used. The reactions were run in 384-well MicroAmp EnduraPlate microplates (Applied Biosystems), with 10 ng of cDNA per well. The plate was processed using the QuantStudio™ 6 Flex Real-Time PCR system and accompanying software, as previously described (Chapter 3.3.4.6). The CT values were automatically calculated by the software and raw values were exported as an Excel spreadsheet. The data was analysed using the CT mean values with normalisation to *Actb*, as the housekeeping gene, and experimental controls. Relative fold changes in gene expression were calculated using the delta delta CT ($\Delta\Delta$CT) method and expressed as $2^{-\Delta CT}$, when CT values were normalised only to the housekeeping gene, or $2^{-(\Delta\Delta CT)}$, when CT values were normalised to both the housekeeping gene and the true experimental (unoperated) controls.

For comparison of the injured horns with true experimental controls, gene expression was determined by $2^{-(\text{CT target gene} - \text{CT housekeeping gene})}$, which is $2^{-\Delta CT}$. These values were plotted and student t-tests were performed to determining statistical significance between the control and injured.

To analyse fold change in expression of various genes in the injured horns compared to the ECM-treated injured horns, the following calculation was performed $2^{-[(\text{CT target gene A} - \text{CT housekeeping gene A}) - (\text{CT target gene B} - \text{CT housekeeping gene B})]}$, where A was the horn that received injury or ECM treatment and B was the true experimental control. Each mouse was normalised to the average true experimental controls.

Table 4.2 Taqman gene assays used for RT-qPCR analysis in this chapter and their relevance

Gene	Taqman assay ID	Protein encoded	Relevance of gene
Actb	Mm00607939_s1	Actin b	Housekeeping gene
Acta2	Mm00725412_s1	α-smooth muscle actin	Myofibroblast marker. Expect to be upregulated in fibrosis
Col1a1	Mm00801666_g1	Collagen 1 alpha 1 chain	Upregulated in fibrosis
Col3a1	Mm00802296_g1	Collagen 3 alpha 1 chain	Upregulated in fibrosis
CTGF	Mm01192933_g1	Connective tissue growth factor	Upregulated in fibrosis
Essra	Mm00433143_m1	Oestrogen receptor alpha	Marker of normal endometrial function
Hoxa10	Mm07295769_m1	Homeobox A10	Marker of endometrial receptivity
Igf1	Mm00439560_m1	Insulin-like growth factor 1	Marker of normal endometrial function
IL6		Interleukin-6	Inflammatory marker
LIF	Mm00434762_g1	Leukaemia-inhibitory factor	Marker of endometrial receptivity
MMP9	Mm00442991_m1	Matrix metalloproteinase 9	Downregulated in fibrosis
PCNA	Mm00448100_g1	Proliferating cell nuclear antigen	Cell proliferation marker. Expect to be upregulated in tissue regeneration.
TGF-β1	Mm01178820_m1	Transforming growth factor beta 1	Upregulated in fibrosis
VEGFA	Mm01281449_m1	Vascular endothelial growth factor alpha	Angiogenesis marker. Expect to be upregulated in tissue regeneration.

4.3.12 Statistical analysis

All graph plotting and statistical analyses were performed using GraphPad Prism 9.2.0. Data was first checked for normal distribution, then unpaired student's t tests were run on all normally distributed data where two groups were compared directly. Where more than two groups were analysed at once, one-way ANOVA was performed with Tukey's multiple comparison's test to determine statistically significant differences between paired groups.

4.4 Results

4.4.1 Mechanical injury does not reliably produce a murine model of intrauterine fibrosis

In pilot studies 1, 2 and 3, we assessed different mechanical methods for generating intrauterine fibrosis, relying on the use of abrasive implements to scrape the endometrium. Uterine horns were collected and prepared for histology and Masson's trichrome staining was performed for all mice to assess for endometrial damage. Masson's trichrome staining of histological sections is the most commonly reported method for assessing intrauterine fibrosis in animal models. Collagen stains blue and the area of blue staining can be measured and expressed as a percentage of the total area of the endometrium. Increased collagen deposition, or blue staining, represents tissue fibrosis.

4.4.1.1 Pilot study 1 findings

In pilot study 1, a hypodermic needle tip was used to scrape the endometrium. The Masson's Trichrome stained uterine sections showed no clear differences between the injured and control uterine horns at three different timepoints; 2 days post-surgery (N = 3), 5 days post-surgery (N = 3) and 9 days post-surgery (N = 3) (Figure. 4.7). There was subjectively no difference in blue (collagen) staining (Figure 4.7 a-c) and objectively no difference in no. of endometrial glands (Figure 4.7d) between control and injured horns.

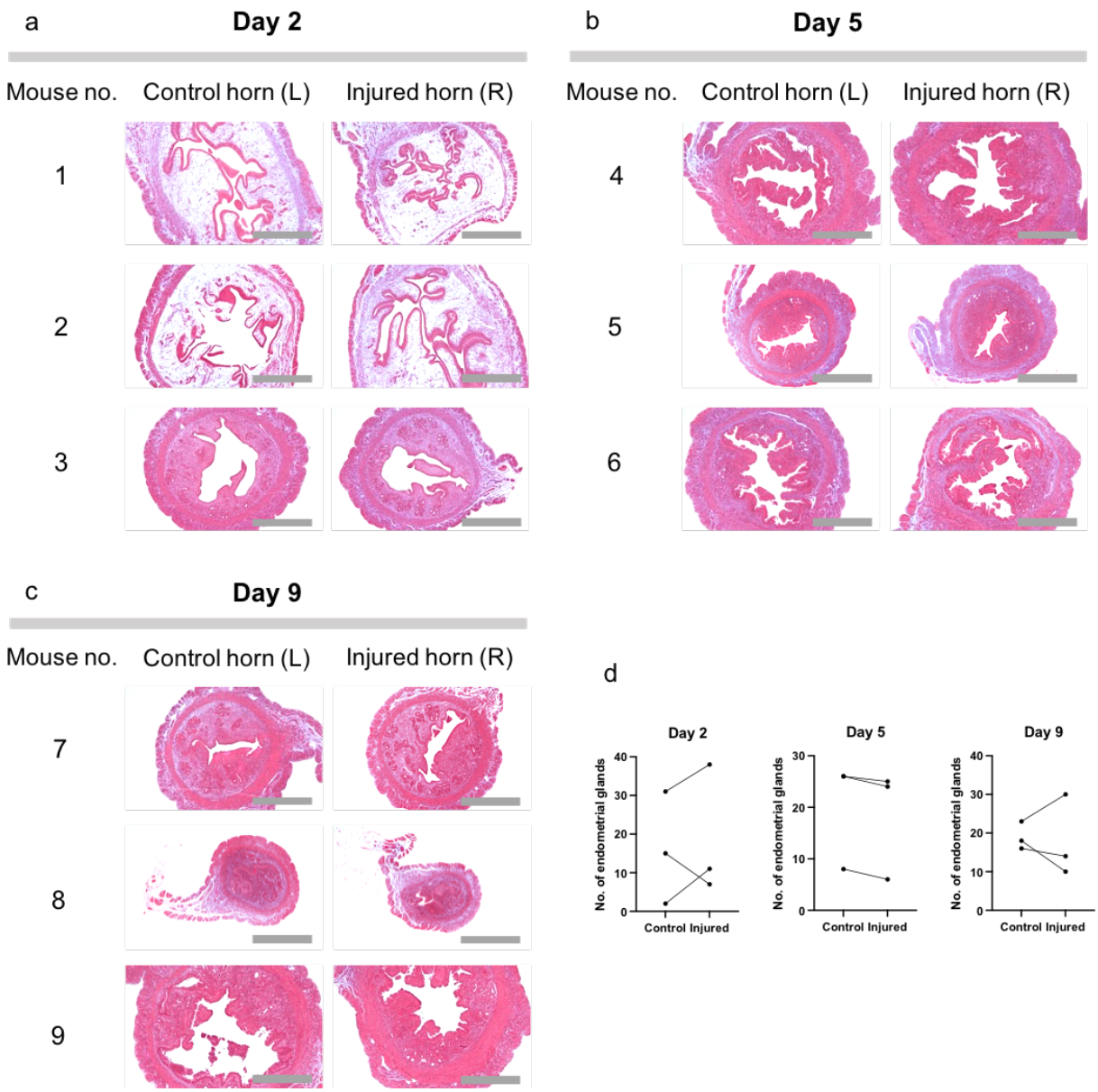


Figure 4.7 Pilot study 1 results: Masson's trichrome staining. All mouse uteri sections were stained with Masson's trichrome (performed by LL, Imperial College London) and images were captured with a 4x lens objective on an Olympus IX71 upright microscope with colour camera. Scale bars = 1 mm. **a** Control and injured horns for mouse 1-3, at day 2 post-surgery. **b** Control and injured horns for mouse 4-6, at day 5 post-surgery. **c** Control and injured horns for mouse 7-9, at day 9 post-surgery. No obvious differences were seen between the control and injured horns at all timepoints. **d** Endometrial gland count was performed using Masson's trichrome stained sections of injured horns and paired sham control horns at day 2 (N = 3), day 5 (N = 3) and day 9 (N = 3). No significant differences were found at any timepoint, as determined by student's t-test.

4.4.1.2 Pilot study 2 findings

The mechanical injury technique was modified in pilot study 2 by using different instruments. A scraper was designed and 3D-printed from Prusa tough resin. The scrapers were made to be 1-1.5 mm in diameter, so that they could fit inside the lumen of the mouse uterus and featured a design of stacked cones, which created a barbed effect. The orientation of the cones allowed for the instrument to be easily inserted into the uterine lumen and on withdrawing the instrument the cones would scrape the endometrium circumferentially. Mechanical scraping was tested alone and in combination with an inflammatory trigger, by dipping the scraper into a solution of LPS before inserting it into the uterine lumen. An alternative method, using diamond-coated twisted metal drill bits, dipped in LPS solution, were also tested. Three mice were assigned to each of the injury groups and tissues were collected at 7 days post-surgery (Figure 4.8). Masson's trichrome staining of the histological sections showed some signs of endometrial damage and focal areas of fibrosis in the injured horns in the 3D-printed scraper group (Figure 4.8g,h,i). Picrosirius red staining also revealed increase in periglandular collagen deposition in the injured horns in the 3D-printed scraper group (Figure 4.8 j,k,l). There was a significantly increased percentage of collagen blue staining in the injured horns compared to control ($p = 0.0081$) in the Masson's trichrome stained sections (Figure 4.8m). The number of endometrial glands in the injured horns was also reduced compared to control horns, although this difference was not statistically significant (Figure 4.8n). Interestingly, addition of the LPS inflammatory stimulus did not result in any signs of obvious fibrosis in the injured horns (Figure 4.8o,p,q). This could be because there were variations in the abrasiveness of the 3D printed scrapers. It was noted that the endometrium appeared to have been stripped away by the scraper in the left horn of mouse 5, and it was suspected that the right and left horns were accidentally switched during tissue harvesting for histology. There were no clear differences between the injured and control horns in the drill bit and LPS group (Figure 4.8r,s,t). Based on the visual comparison of the Masson's trichrome stained sections in the LPS and Diamond drill bit group, quantitative analysis was not performed for these sections. These findings suggested that addition of an LPS-mediated inflammatory stimulus did not contribute to fibrosis and the success of generating a mechanical injury model using a scraper depended on how reliably abrasive the implement was.

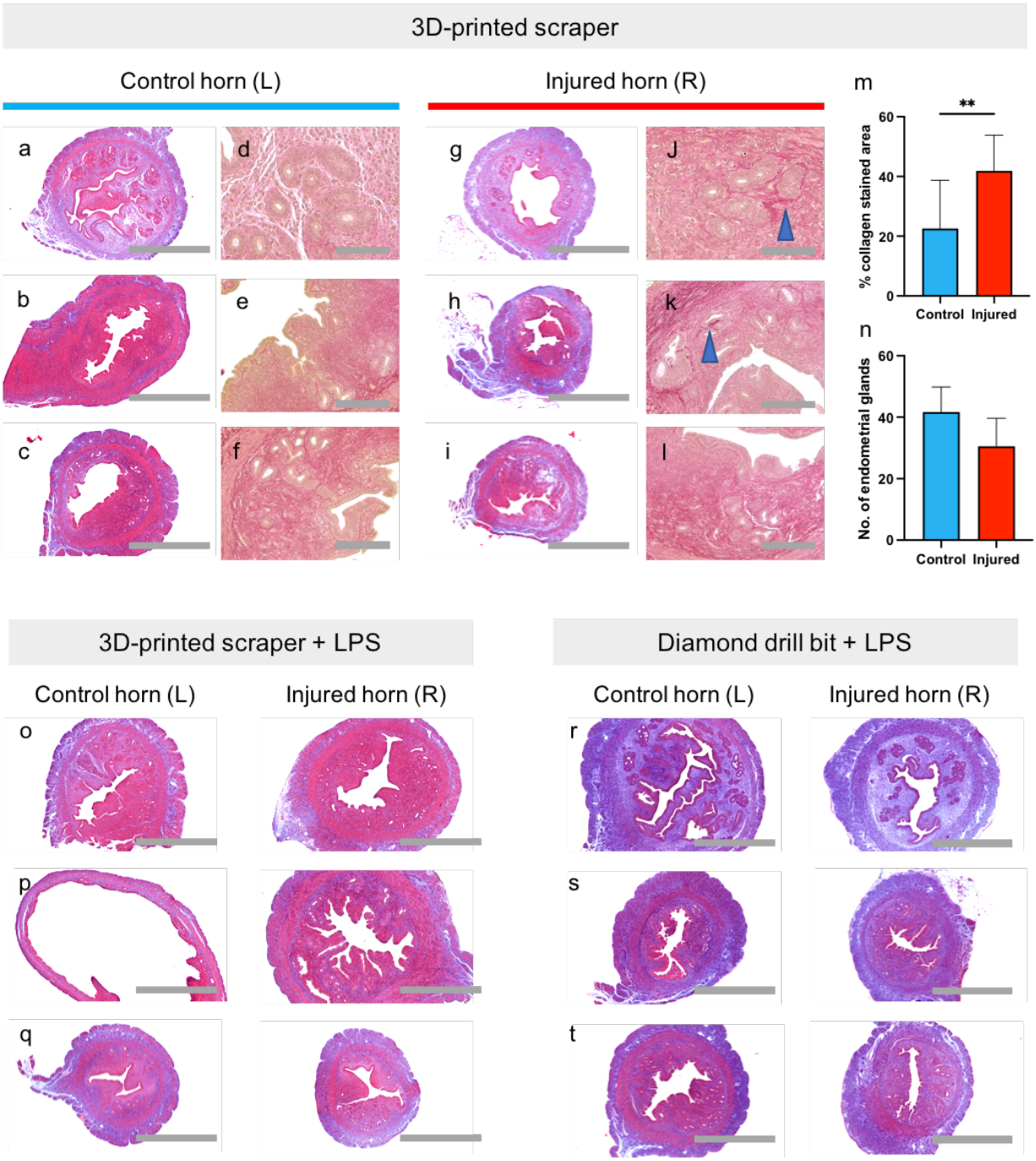


Figure 4.8 Pilot study 2 findings: Masson's trichrome and Picrosirius red staining. Three different methods were assessed for mechanical injury of the endometrium: 3D-printed scraper, 3D-printed scraper + LPS and Diamond drill bit + LPS. Three mice were assigned to each group. All Masson's trichrome images were acquired with 4x lens objective with Olympus IX71 upright microscope. Scale bars = 1 mm. Picrosirius red images were acquired with 10x lens objective on Zeiss Axio Observer widefield microscope with colour camera. Scale bars = 250 μm. **a,b,c** Masson's trichrome stained sections of sham control (left) uterine horns from three mice in the 3D-printed scraper group. **d,e,f** Picrosirius red stained sections of sham control (left) uterine horns from three mice in the 3D-printed scraper group. **g,h,i** Masson's trichrome stained sections

of injured (right) uterine horns from three mice in the 3D-printed scraper group. Focal areas of increased blue (collagen) staining can be seen. **j,k,l** Picrosirius red stained sections of injured (right) uterine horns from three mice in the 3D-printed scraper group. Increased red staining was seen around the uterine glands in the injured horns (blue arrowheads), indicating excess collagen deposition. **m** Analysis of the percentage of collagen (blue)-stained area (in Masson's trichrome stained sections) in control and injured horns, in the 3D-printed scraper group. A significant increase was found in the injured horns (41.87 +/- 11.97%) compared to control (22.55 +/- 16.18 %) ($p = 0.0081$), when assessed by student's t test. Control horns N = 3, injured horns N = 3. **n** Endometrial gland count in sections of control and injured uterine horns in 3D-printed scraper group. The mean number of glands appears reduced in the injured horns but this difference is not statistically significant ($p = 0.1192$), when assessed by student's t test. Control horns N = 3, injured horns N = 3 **o,p,q** Masson's trichrome stained sections of sham control (left) and injured (right) uterine horns from three mice in the 3D-printed scraper + LPS group. No obvious differences were seen. **r,s,t** Masson's trichrome stained sections of sham control (left) and injured (right) uterine horns from three mice in the Diamond-coated drill bit + LPS group. No obvious differences were seen. All histological staining was performed by LL, Imperial College London.

4.4.1.3 Pilot study 3 findings – mechanical injury group

In pilot study 3, changing the design and geometry of the 3D-printed scrapers, from stacked cones to stacked pyramids, to increase the abrasiveness of the scraper, did not result in successful and reproducible intrauterine scarring Figure 4.9). This was evidenced by similar appearances of the endometrium in the injured and control horns on Masson's Trichrome staining (Figure 4.9a) and immunohistochemistry (Figure 4.9 b-e). There was no statistically significant difference in the immunohistochemistry DAB intensity scoring for the fibrosis markers, Collagen I, Collagen III, CTGF and TGF-β1 between the injured and control horns in the mechanical injury group (Figure. 4.9f).

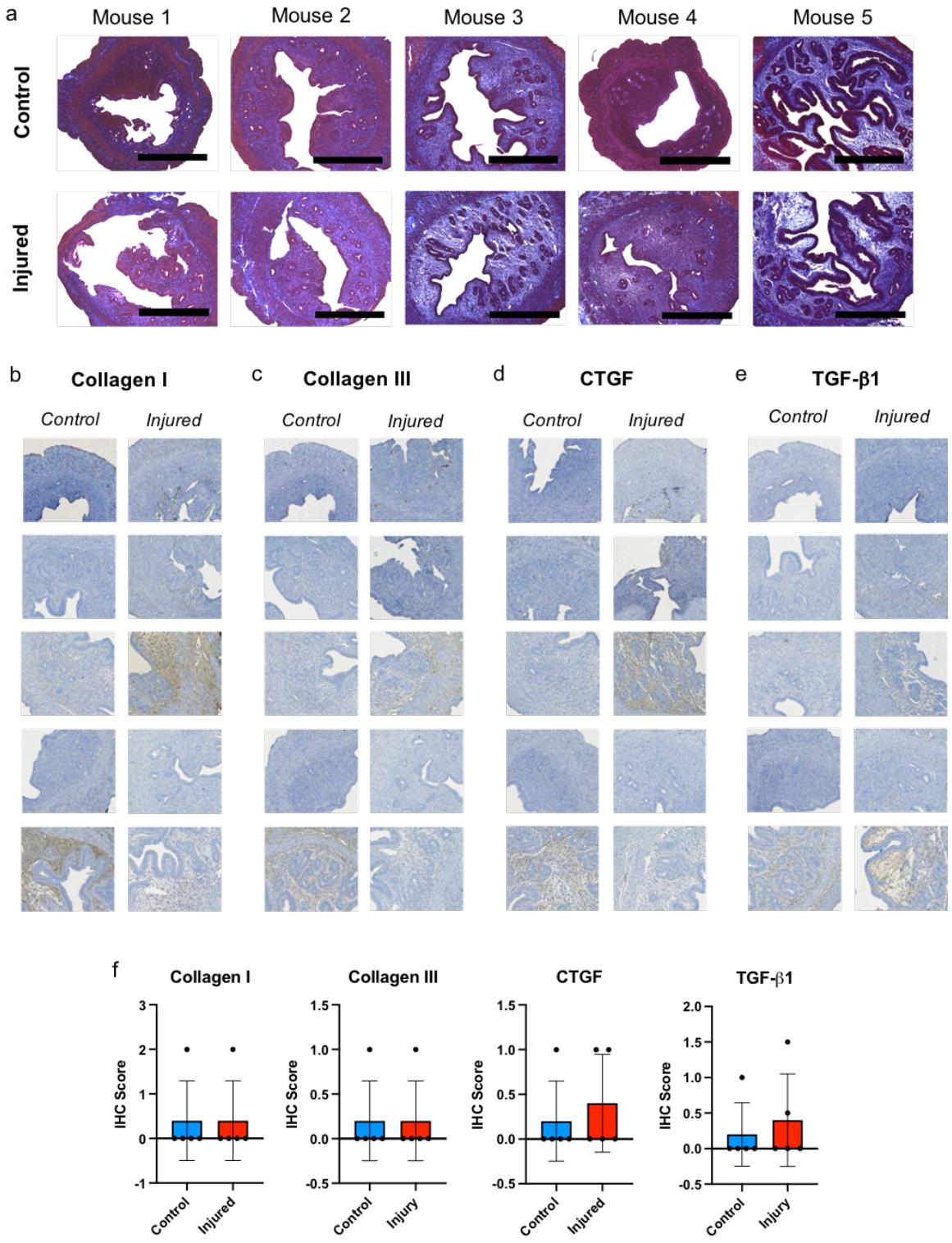


Figure 4.9 Pilot study 3 findings – mechanical injury group: Masson's trichrome staining and immunohistochemistry. a Masson's trichrome stained sections of sham control (top row panels) and injured (second row panels) uterine horns from mouse 1 to 5 (mechanical injury group). Masson's trichrome staining performed by LL, Imperial College London. Images were captured with a 5x lens objective on a Zeiss Axio Observer inverted widefield microscope with a colour camera. Scale bars = 1 mm.

b-e Immunohistochemistry of Collagen I (**b**), Collagen III (**c**), CTGF (**d**) and TGF-β1 (**e**) in sham control and injured uterine horns for mouse 1 to 5 (mechanical injury group). Images were captured with a 10x lens objective on the same microscope. **f** Analysis of immunohistochemistry. The images in **b** were scored (from 0-3) for intensity of DAB staining, by 3 independent assessors. The scores were plotted for control horns (N = 5) vs. injured horns (N = 5) for Collagen I, Collagen III, CTGF and TGF-β1. No significant differences were found in the immunohistochemistry (IHC) scores between control and injured horns in any of the markers, when assessed by student's t tests.

4.4.2 Ethanol-induced injury effectively generates intrauterine fibrosis

4.4.2.1 Pilot study 3 findings – ethanol injury group

In pilot study 3, 95% ethanol injected into the uterine lumen and maintained within the lumen for 45 seconds caused extensive and uniform tissue damage and intrauterine fibrosis, as demonstrated by Masson's Trichrome staining (Figure 4.10a) and immunohistochemistry for fibrosis markers (Figure 4.10b-e). Although 3 out of 5 mice (mouse 2, 4 and 5) in the ethanol injury group had to be culled early at day 1 and day 2 post-surgery, due to adverse outcomes, all the mice were found to have severely damaged endometria where the stroma was replaced by collagen deposition with few recognisable endometrial glands in the injured horns (Figure 4.10a). Scoring of the DAB staining intensity for antibodies against Collagen I, Collagen III, TGF-β1 and CTGF showed significantly increased expression of these fibrosis markers in the ethanol injured horns compared to the control, uninjured horns ($p < 0.001$ for Collagen I, Collagen III and CTGF, $p < 0.0001$ for TGF-β1) (Figure 4.10f). By contrast, there were minimal observable differences in Masson's Trichrome staining and no significant differences in immunohistochemistry scoring of injured versus control horns in the mechanical injury (3D-printed scraper) group (Figure 4.9).

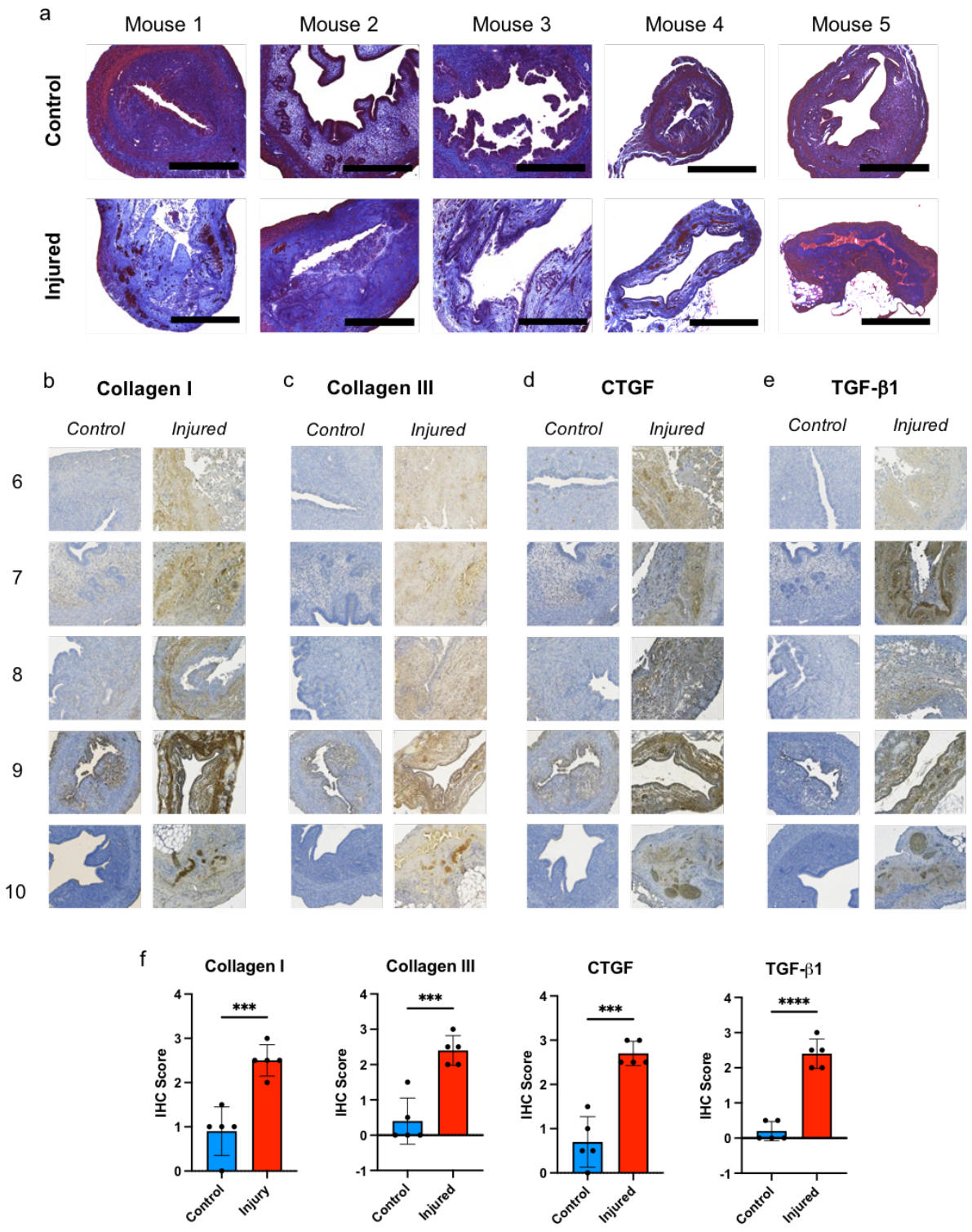


Figure 4.10 Pilot study 3 findings – ethanol injury group: Masson's trichrome staining and immunohistochemistry. a Masson's trichrome stained sections of sham control (top row panels) and injured (second row panels) uterine horns from mouse 1 to 5 (ethanol injury group). Histology was assessed at day 7 for mouse 1 and 3. Mouse 2, 4 and 5 had to be culled at day 1 or day 2 post-surgery, therefore the histology represents day 1 and day 2 changes. Dramatic differences can be seen between the sham control

and injured horns in all mice. The injured horns show loss of normal endometrial stroma and glands coupled with excess deposition of collagen (blue staining). In the injured horn of mouse 5, there is no recognisable endometrium at all. Masson's trichrome staining performed by LL, Imperial College London. Images were captured with a 5x lens objective on a Zeiss Axio Observer inverted widefield microscope with a colour camera. Scale bars = 1 mm. **b-e** Immunohistochemistry of Collagen I (**b**), Collagen III (**c**), CTGF (**d**) and TGF-β1 (**e**) in sham control and injured uterine horns for mouse 1 to 5 (ethanol injury group). Obvious increased DAB staining can be seen in the control horns for all 4 markers. Images were captured with a 10x lens objective on the same microscope. **f** Analysis of immunohistochemistry. The images in **b** were scored (from 0-3) for intensity of DAB staining, by 3 independent assessors. The scores were plotted for control horns (N = 5) vs. injured horns (N = 5) for Collagen I, Collagen III, CTGF and TGF-β1. Statistically significant increases in IHC score were found in Collagen I ($p = 0.0006$), Collagen III ($p = 0.0004$), CTGF ($p = 0.0001$) and TGF-β1 ($p = <0.0001$), when assessed by student's t tests.

Uterine tissues from pilot study 3 were also processed for RNA isolation and qPCR analysis (Figure 4.11). RNA was isolated from 4 out of 5 mice in the mechanical injury group. Unfortunately, in the ethanol injury group, tissue collection for RNA was only performed for the 2 mice that survived to the day 7 timepoint. Therefore, statistical analysis was not performed, due to the small group size. The genes Acta2, Col1a1 and TGF-β1 were selected as markers of fibrosis and relative gene expression in the injured horns was calculated by normalisation to the average sham control horns and the housekeeping gene. A fold change <1 implied downregulation of the gene, a fold change of 1 implied no change in expression and a fold change >1 implied upregulation. When all mice in the mechanical injury group were pooled, Acta2 does not appear upregulated in the mechanical injury group and appears, in fact, downregulated in the ethanol injury group (Figure 4.11). However, Col1a1 gene expression appears upregulated 2.5 fold in the ethanol injury group and a clear difference is seen when compared to the mechanical injury group, in which on average there appears to be no upregulation of Col1a1 (Figure 4.11). Similarly, TGF-β1 seems to be upregulated about 4-fold in the ethanol group, whilst it is not upregulated in the mechanical injury group (Figure 4.11).

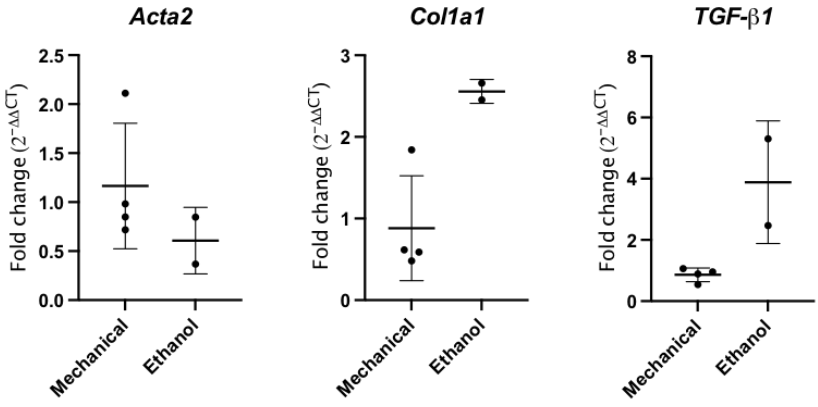


Figure 4.11 Pilot study 3 RT-qPCR results. Gene expression analysis for Acta2, Col1a1 and TGF-β1, with normalisation to sham controls and housekeeping gene. Each data point represents one mouse. In the mechanical injury group, RNA was extracted from the uterine tissues of 4 mice at day 7. In the ethanol injury group, tissues were collected from the 2 mice that survived to day 7. The fold change of Col1a1 and TGF-β1 appear increased in the ethanol injury group (N = 2, n = 3) compared to the mechanical injury group (N = 4, n =3). Statistical analyses were not performed due to a small number of biological replicates in the ethanol injury group. N = biological replicates, n = technical replicates.

4.4.2.2 Pilot study 4 findings

To minimise the adverse outcomes on the mice and improve animal survival from the ethanol injury model, 4 mice in pilot 4 were exposed to 30 seconds of 90% or 95% intraluminal ethanol. In one mouse (mouse 1), the ethanol administration failed due to technical error and the tip of the polyethylene tubing broke and was retained inside the uterine horn. Ethanol was successfully administered to the other four mice. The proportion of mice which thrived at 7 days improved from 40% to 80% between pilot 3 and pilot 4, though this could also have been attributable to better surgical technique. All mice that received ethanol injury displayed damaged and fibrosed endometria in their injured horns on Masson's Trichrome staining (Figure 4.12). Quantitative analysis was not performed.

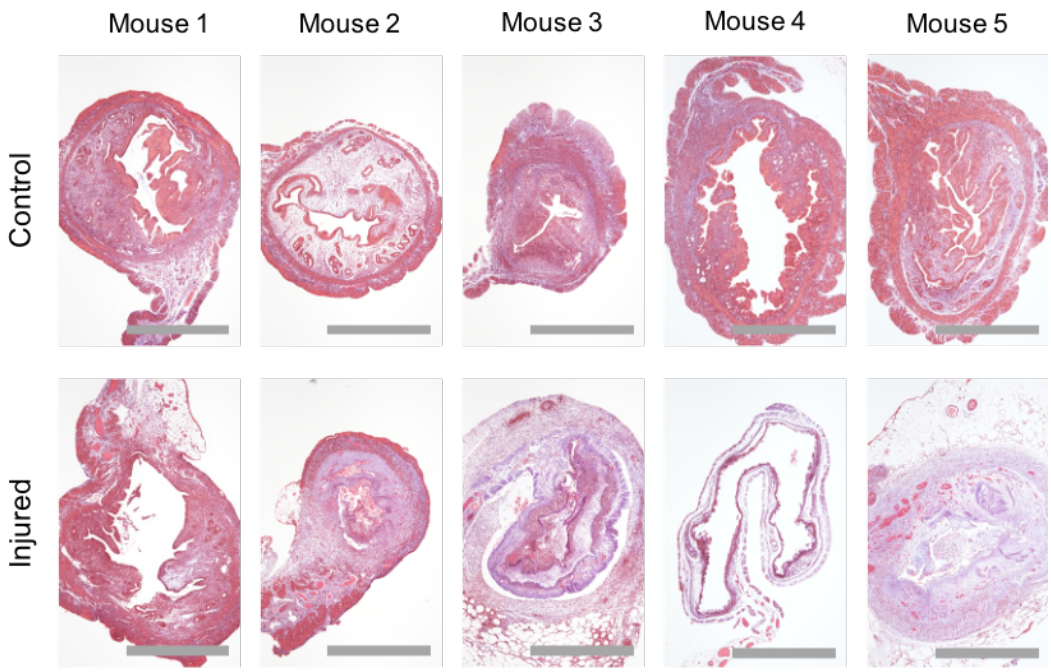


Figure 4.12 Pilot study 4 Masson's trichrome stained sections. Five mice were included in this pilot study. For mouse 1, ethanol was not successfully administered to the injured horn. As a consequence, there was no obvious increase in fibrosis in the injured horn compared to sham control. Mouse 2 and 3 received 95% ethanol for 30 seconds in the injured horn and mouse 4 and 5 received 90% ethanol for 30 seconds. Mouse 4 was culled 1 hour after surgery due to pain, therefore the histology represents endometrial damage immediately after ethanol treatment. A technical error had occurred during mouse 4's surgery which meant that the PBS wash was not properly given. For all other mice, tissue was collected for histology at day 7. Masson's trichrome staining was performed by LL, Imperial College London. These images were captured with a 4x lens objective on an Olympus IX71 upright microscope with a colour camera. Scale bars = 1 mm.

4.4.2.3 Final study findings

4.4.2.3.1 Histological assessment of injury vs. sham control horns

In the final study, where the effect of endometrial ECM hydrogel was evaluated, 90% ethanol was used, and the exposure time was reduced to 15 seconds. This amount of ethanol injury was sufficient to generate intrauterine fibrosis and endometrial damage, whilst enabling all mice to survive to the day 7 experimental endpoint. In the four mice that received ethanol injury only (mouse 6, 8, 9 and 10), the injured right horns were morphologically different to the sham control left horns at a

macroscopic level (Figure 4.13 top panels), with the injured horn appearing more constricted and the tissue feeling hardened. On histology, the differences between injured and control were dramatic (Figure 4.13 middle and bottom panels). In the Masson's trichrome stained sections, the injured horns of mouse 8, 9 and 10 showed extensive fibrous collagen deposition replacing normal endometrial stroma, a paucity of cells in the endometria, absence of endometrial glands and a loss of epithelia lining the lumen (Figure 4.13 middle and bottom panels). Mouse 6 had less severe appearances of endometrial damage and fibrosis in the injured horn compared with the other mice in the injury-only group, although there was a clear reduction in normal endometrial area and luminal epithelial surface area (Figure 4.13 bottom panels). Of note, during the surgery, mouse 6 sustained a small perforation in the uterine wall during ethanol perfusion and this may have reduced the ethanol exposure and therefore the severity of the endometrial injury.

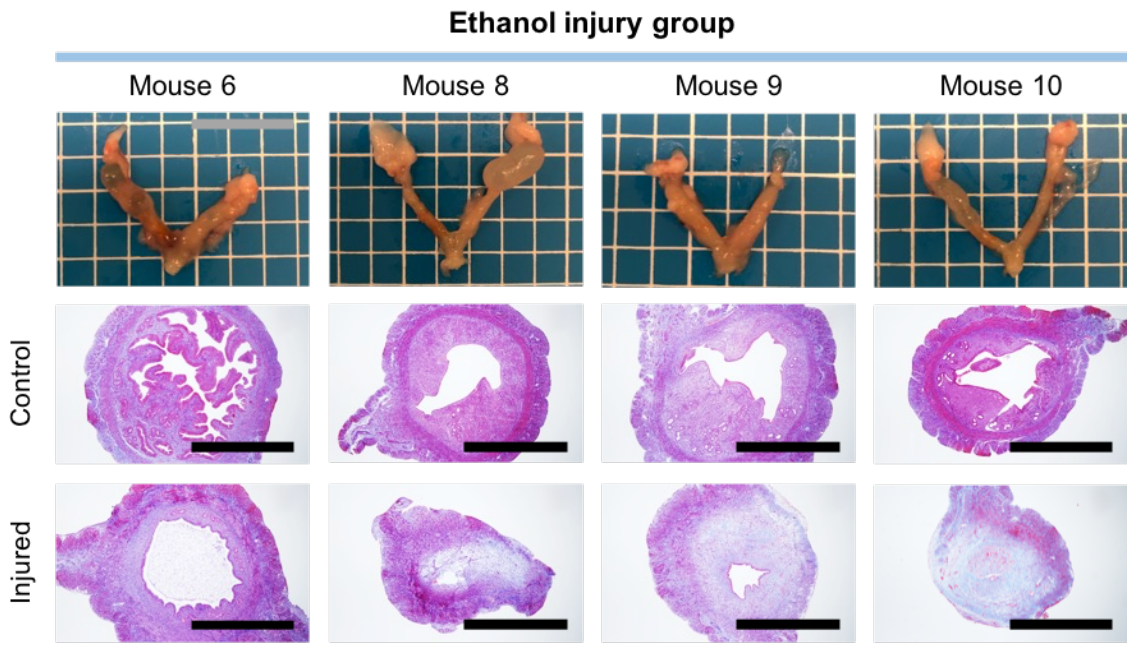


Figure. 4.13 Final *in vivo* study: injury group - macroscopic observations and Masson's trichrome stained sections. Top row panels Photographs of mouse uteri harvested on day 7 post surgery (ethanol injury group). The injured horns (left horn in the images) appeared narrowed and felt sclerosed compared to the contralateral sham control horn. **Middle row panels** Masson's trichrome stained sections of sham control uterine horns, showing normal endometrial stroma with abundant glands. Variations in the endometrial appearance most likely related to different phases of the estrus cycle. **Bottom row panels** Masson's trichrome stained sections of contralateral injured horns. Obvious differences are seen in the injured horns compared to their paired sham controls. In mouse 8, 9 and 10 there was loss of endometrial stroma, epithelia and glands, accompanied by excess collagen deposition (blue staining). Mouse 6 had a less severe response to ethanol treatment although the endometrial area appeared dramatically reduced compared to control and there were fewer glands. Masson's trichrome staining was performed by LL, Imperial College London. Images were acquired with 4x lens objective on Olympus IX71 upright microscope. Scale bars = 1 mm.

When pooling all the ethanol-injury only mice for quantitative analysis, statistically significant differences can be found between the injured horns and the sham control horns. When evaluating the degree of Masson's trichrome blue-stained area in the injury-only mice, the percentage of blue-stained area was significantly higher in the injury only horns (62.3 +/- 5.3%) than in the sham control horns (36.7 +/- 12.9%) ($p = 0.0211$) (Figure 4.14a,c). The number of endometrial glands was significantly decreased in the injured horns (6.5 +/- 10.34) compared with the paired sham control (48.25 +/- 12.79) ($p = 0.0026$) (Figure 4.14b,c).

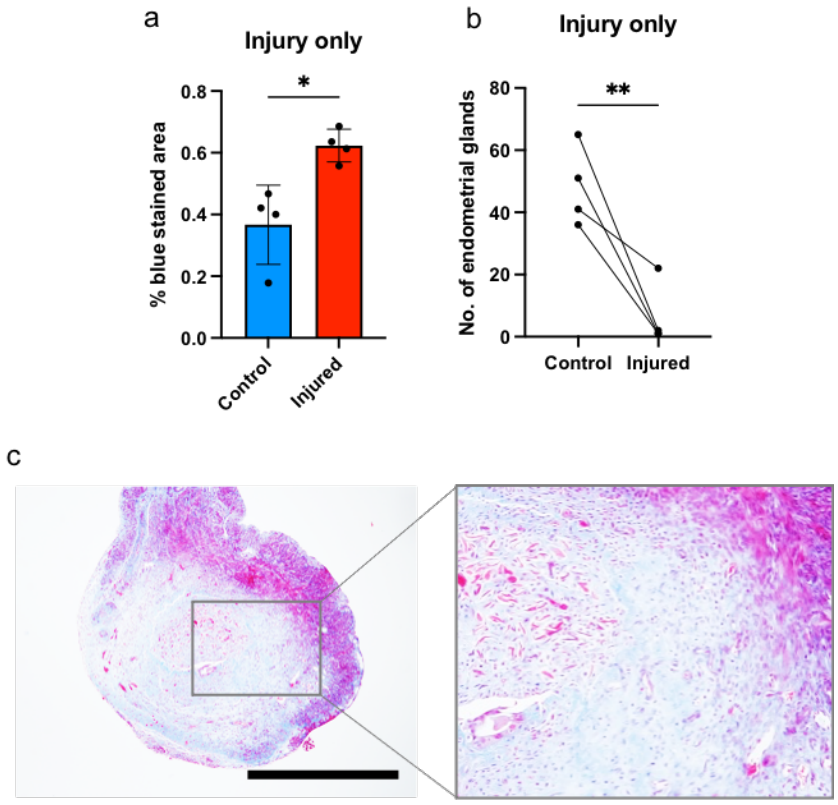


Figure 4.14 Final *in vivo* study: injury group – analysis of Masson's trichrome staining. **a** Analysis of percentage of blue (collagen)-stained area, as a proportion of the total endometrial area. This serves as a representative measure of the area of fibrosis. The percentage of collagen-stained area was significantly higher in the injured horns (62.3 +/- 5.3%) (N = 4) than the paired sham control horns (36.7 +/- 12.9%) (N = 4) (p = 0.0211), when assessed by student's t test. **b** Endometrial gland count in the sham control horns (N = 4) and paired injured horns (N = 4). The no. of endometrial glands was significantly reduced in the injured horns (p = 0.0023), when assessed by student's t test. **c** Masson's trichrome staining of mouse 10's injured endometrium, showing lack of endometrial glands, paucity of cells and excess collagen (blue) deposition. Staining performed by LL, Imperial College London. Image acquired with 4x lens objective on Olympus IX71 upright microscope. Scale bar = 1 mm.

4.4.2.3.2 Immunohistochemical analysis of injury vs. control horns

In the immunohistochemistry scoring, the expression of Collagen I (Figure. 4.15a,b) and CTGF (Figure. 4.15c,d) were both significantly higher in the injured horns compared to the sham control horns (p = 0.0008 and p = 0.0114 respectively).

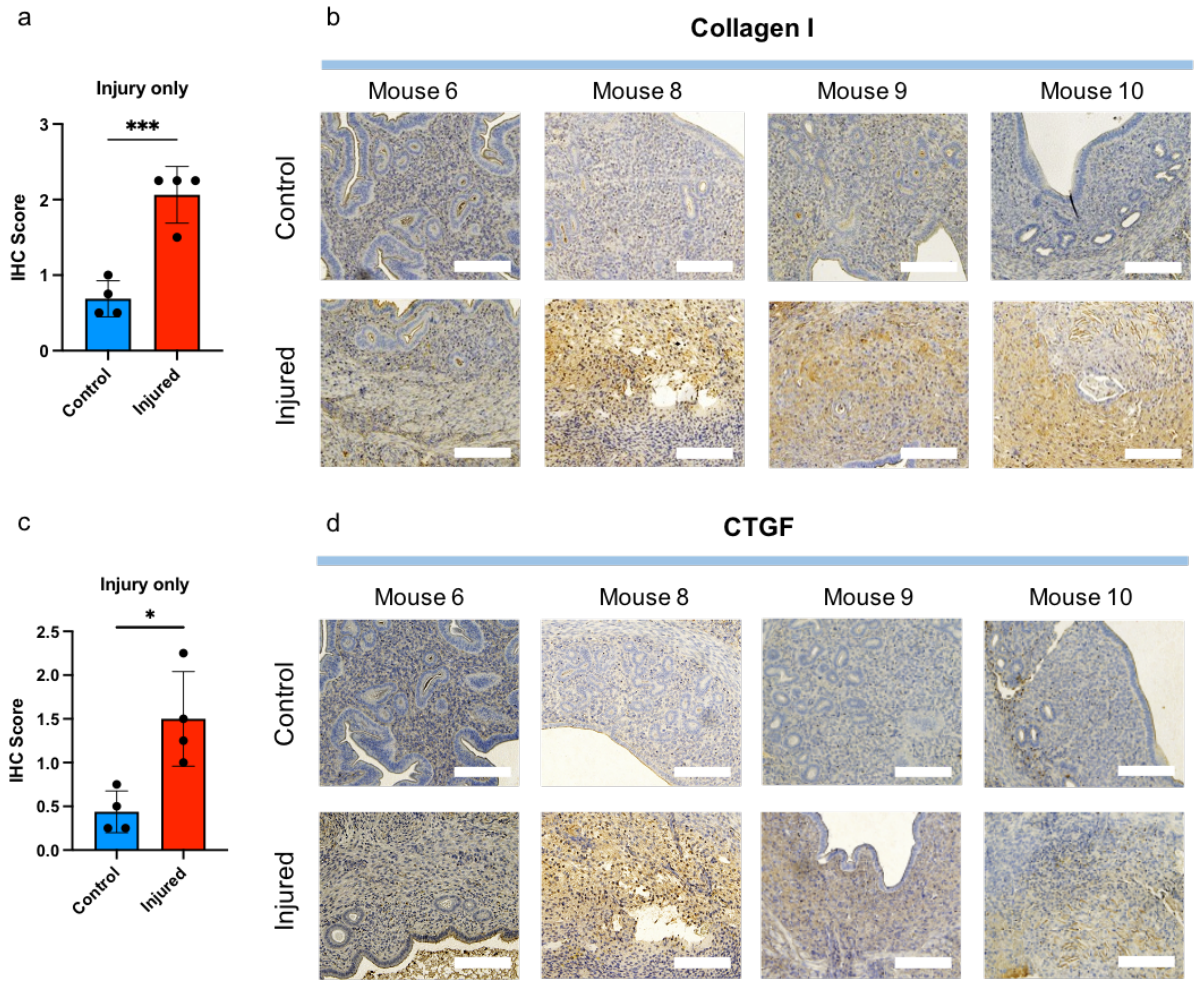


Figure 4.15 Final *in vivo* study: injury group – immunohistochemistry. a Analysis of immunohistochemistry score for Collagen I in the sham control and injured horns. The images in **b** were scored (from 0 - 3) for intensity of DAB staining, by 4 independent, blinded assessors. The scores were plotted for sham control horns (N = 4) vs. injured horns (N = 4). Collagen I expression was significantly increased in the injured horns compared to the paired sham control ($p = 0.0008$). **c** Analysis of immunohistochemistry score for CTGF in the sham control and injured horns. The images in **d** were scored for intensity of DAB staining by 4 independent, blinded assessors. CTGF expression was significantly increased in the injured horns (N = 4) compared to the paid sham control horns (N = 4), ($p = 0.0114$). Student's t tests were performed for statistical analysis. Images acquired with 10x lens objective on Zeiss Axio Observer widefield microscope with colour camera. Scale bars = 250 μm.

4.4.2.3.3 RT-qPCR analysis of injury vs. control horns

Analysis of relative gene expression showed significantly increased expression of fibrosis markers Col1a1 ($p = 0.028$), TGF-β1 ($p = 0.0131$) and Col3a1 ($p = 0.0243$) in the injured horns compared to true control horns, when normalised to the housekeeping gene (Figure 4.16a). IL6, a marker of inflammation, was also expressed significantly higher in the injured compared to true control ($p = 0.0405$) (Figure 4.16a). The qPCR results validate Col1a1, TGF-β1, Col3a1 and IL6 as markers of fibrosis and inflammation in the ethanol-injury model. Whilst not statistically significant, MMP9 showed an increased trend in the injured horns compared to true control horns. (Figure 4.16a). Additionally, non-significant downward trends were observed in the expression of the regeneration markers PCNA and VEGFA in the injured horns compared with the true control horns (Figure 4.16b). Expression of Hoxa10, LIF, ESSRA and IGF-1 were also assessed as markers of endometrial function. None of these markers were significantly different in the injured horns compared with the unoperated control horns (Figure 4.16c). Given the clear histological differences between the healthy endometrium in the control horns and the damaged endometrium in the injured horns, it was surprising that Hoxa10, LIF, ESSRA and IGF-1 expression were not significantly decreased. The possible explanations for this are discussed in section 4.5.

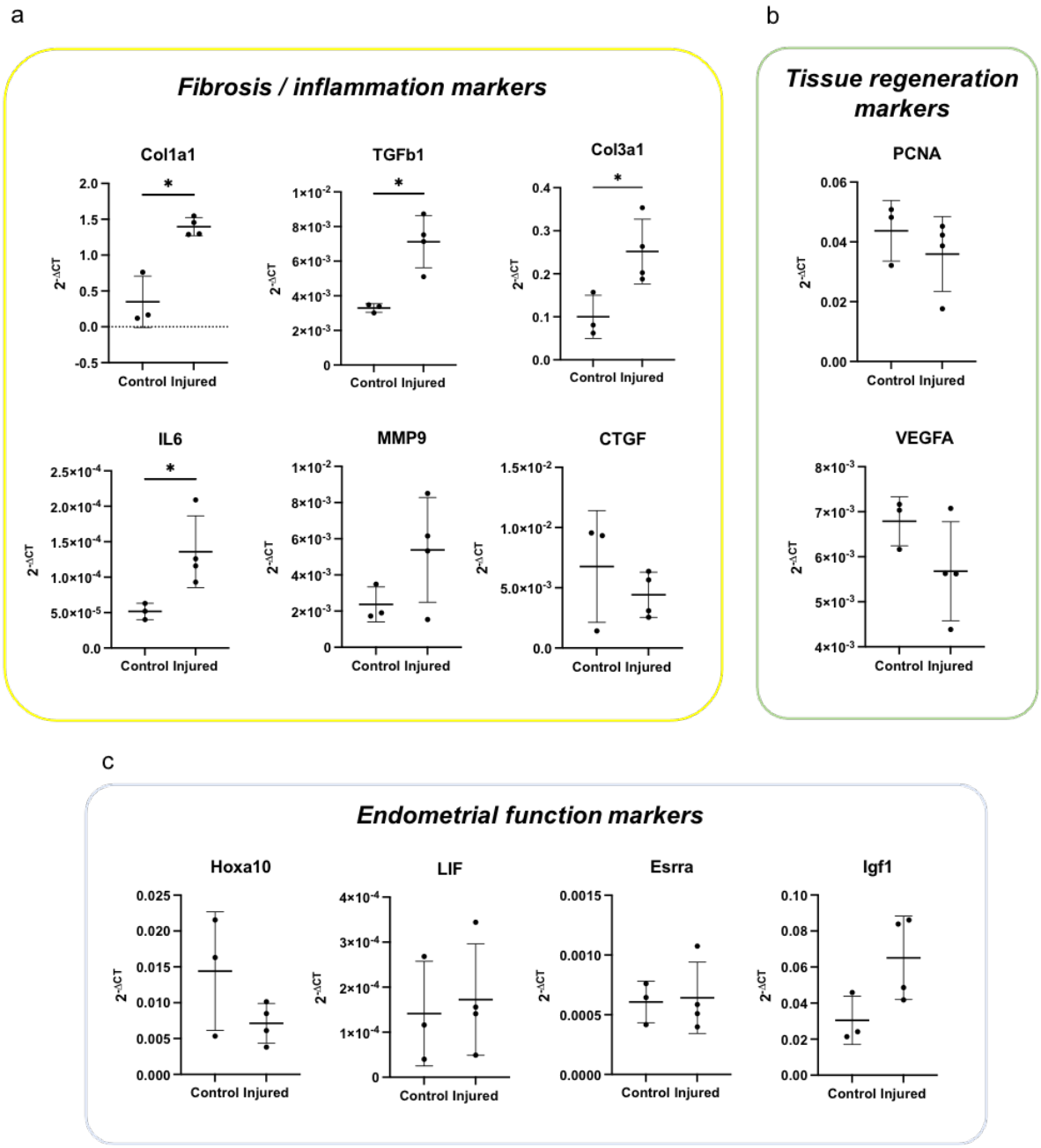


Figure. 4.16 Final *in vivo* study: injury group – RT-qPCR results. **a** Gene expression analysis for fibrosis and inflammation markers Col1a1, TGF-β1, Col3a1, IL6, MMP9 and CTGF in the true experimental controls (N = 3, n =3) versus injured horns (N = 3, n =3), with normalisation to the housekeeping gene. Data expressed as $2^{-\Delta CT}$. **a** Significant increases were seen in the injured horns for Col1a1 (p = 0.028), TGF-β1 (p = 0.0131), Col3a1 (p = 0.0243) and IL6 (p = 0.0405). MMP9 and CTGF expression were not significantly different between control and injured horns. **b** Gene expression analysis for tissue regeneration markers PCNA and VEGFA. No significant differences were seen between control and injured horns. **c** Gene expression analysis for markers of endometrial function and receptivity: Hoxa10, LIF, Essra and IGF1. No significant differences were seen between control and injured horns. Statistical analyses were performed with student t tests.

4.4.3 Effect of endometrial ECM hydrogel on intrauterine fibrosis

4.4.3.1 Histological analysis

In the final study, five mice (mouse 2, 3, 4, 5 and 7) received ethanol injury in the right horn, followed by PBS wash and delivery of endometrial ECM hydrogel into the injured uterine lumen. At 7 days post-surgery, the histological evaluation of the Masson's trichrome stained sections showed that 2 of the mice (mouse 3 and 5) had extensive endometrial fibrosis with loss of normal endometrial stroma, endometrial glands and epithelia; appearances that were consistent with the ethanol-injury only controls (Figure 4.17 middle and bottom panels). However, 3 of the 5 mice (mouse 2, 4 and 7) had comparable endometrial morphology between the injured and control horns, with preservation of normal endometrial stroma, glands and epithelia in the injured and ECM-treated horns (Figure 4.17 middle and bottom panels). From these observations, it appears that in the ECM-treated mice with extensive fibrosis (mouse 3 and 5), the ECM hydrogel either had no effect or was not successfully delivered. On reviewing the surgery notes (Appendix Table A1), the latter is a plausible explanation as mouse 3 was noted to have a large uterus, which may have meant that not enough gel was delivered to the cavity, whilst mouse 5 had gel leak back out of the uterine lumen immediately after application.

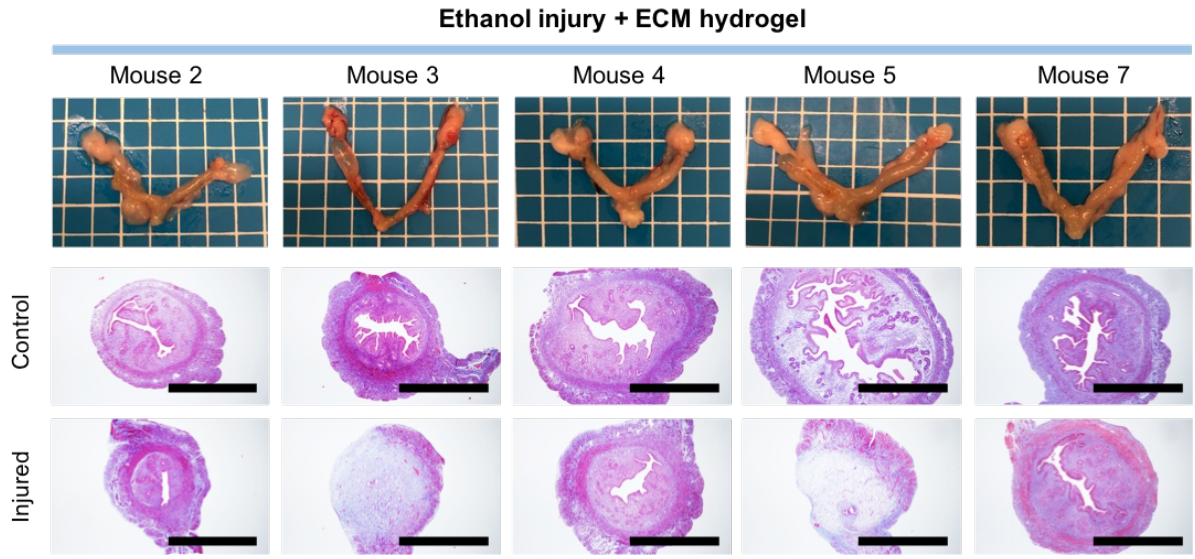


Figure. 4.17 Final *in vivo* study: injury + ECM treatment group - macroscopic observations and Masson's trichrome stained sections. Top row panels Photographs of mouse uteri harvested on day 7 post surgery (injury + ECM treatment group). **Middle row panels** Masson's trichrome stained sections of sham control uterine horns, showing normal endometrial stroma with abundant glands. **Bottom row panels** Masson's trichrome stained sections of contralateral injured horns. The ECM-treated injured horns of mouse 2, 3 and 7 had very similar histological appearances to their paired sham control horns. The endometrial stroma, epithelia and glands were preserved and there appeared to be minimal collagen (blue) deposition. In contrast, mouse 3 and 5 had dramatically different injured horns compared to the sham controls. In these ECM-treated injured horns, there was excess collagen deposition, which had replaced the normal endometrial stroma, and there was a paucity of glands and endometrial epithelia. These appearances were similar to the injured horns in the non-ECM-treated group. Mouse 3 and 5 both had potentially insufficient or ineffective delivery of ECM hydrogel after ethanol injury. Masson's trichrome staining was performed by LL, Imperial College London. Images were acquired with 4x lens objective on Olympus IX71 upright microscope. Scale bars = 1 mm.

To avoid bias, all mice in the ECM-treated group were pooled for analysis. Evaluating the percentage of blue-stained (collagen) area in the Masson's trichrome stained sections for the ECM-treated group, there was a statistically significant increase in the blue (collagen)-stained area in the injured horns compared to pooled sham controls ($p = 0.0316$) (Figure 4.18a). No statistical difference was found in the percentage of blue-stained area between the ECM-treated injured horns and the injury-only horns. (Figure 4.18a). If mouse 3 and 5 were omitted from the analysis, then the percentage of blue-stained area in the ECM-treated injured horns became significantly reduced compared to the injury-only horns ($p = 0.0293$) (data shown in Appendix Figure C).

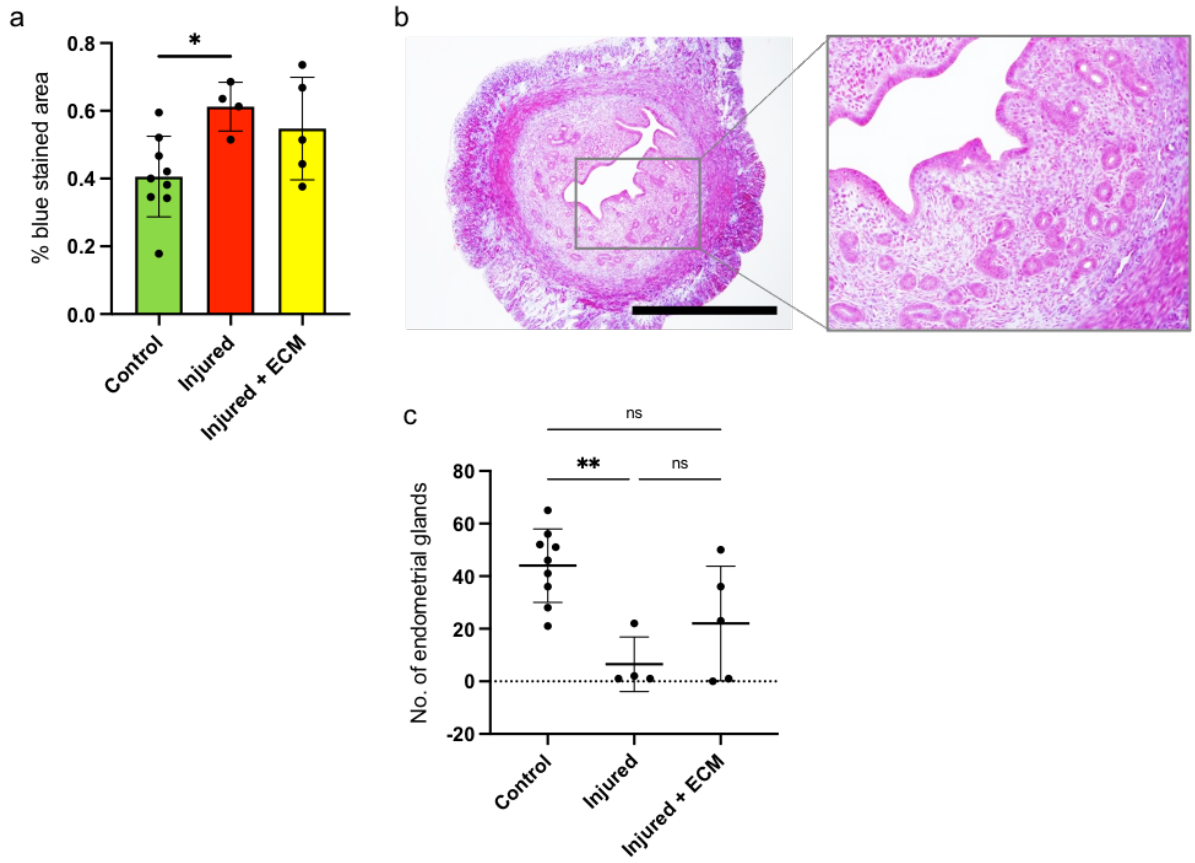


Figure 4.18 Final *in vivo* study: injury + ECM group – analysis of Masson's trichrome staining. **a** Analysis of percentage of blue (collagen)-stained area, as a proportion of the total endometrial area. The percentage of collagen-stained area was significantly higher in the injured horns (62.3 +/- 5.3%) (N = 4) compared to the pooled sham control horns (40.59 +/- 11.8%) (N = 9) (p = 0.0215). No significant difference was found between the injured horns and ECM-treated injured horns (N = 5). **b** Masson's trichrome staining of mouse 4's ECM-treated injured horn, showing preserved endometrial stroma and glands with minimal collagen deposition. **c** Endometrial gland count in the pooled sham control horns (N = 9), injured horns (N = 4) and ECM-treated injured horns (N = 5). The number of endometrial glands was significantly reduced in the injured compared to control (p = 0.0036) but not significantly different between the control and injured + ECM or between injured and injured + ECM. Statistical analyses were performed with one-way ANOVA and Tukey's multiple comparisons test. Masson's trichrome staining performed by LL, Imperial College London. Images were acquired with 4x lens objective on Olympus IX71 upright microscope. Scale bars = 1 mm.

4.4.3.2 Endometrial gland count

With all mice pooled for analysis, in the ethanol-injured, ECM-treated group there was no statistically significant difference between the number of endometrial glands in the sham control horns versus

the injured and ECM-treated horns (p = 0.062) (Figure 4.18c). This suggested a protective effect of ECM hydrogel for endometrial gland preservation. When the endometrial gland number was compared between injury only horns and ECM-treated injured horns, there was no statistically significant difference when all mice were included in the analysis. Omitting mouse 3 and 5 led to a significant increase in endometrial glands in the ECM-treated horns compared to the untreated, injured horns (p = 0.027) (data shown in Appendix Figure C).

4.4.3.3 Immunohistochemistry analysis

Only Collagen I and CTGF were analysed for the final study as staining for Collagen III and TGF-β1 were unsuccessful for these sections and could not be optimised. As previously reported, expression of Collagen I and CTGF were both significantly increased in the injury-only horns compared to the sham control, validating the ethanol-injury model for inducing intrauterine fibrosis. In the pooled, ECM-treated mice, there was no statistical difference between the sham control and injured horns in the Collagen I IHC scores (Figure 4.19a), nor the CTGF IHC scores (Figure 4.19d). However, when comparing the injury-only horns and the ECM-treated injured horns, there was also no significant difference in Collagen I (Figure 4.19b), nor CTGF expression (Figure 4.17e). These findings imply that overall, when all mice are pooled, ECM hydrogel treatment following ethanol injury did not reduce the expression of Collagen I and CTGF. Even with mouse 3 and 5 omitted, the differences between the injured and ECM treated injured horns were not significant (data shown in Appendix Figure C).

Of important note, there were significant differences between the sham control horns in the injury only group versus the ECM-treated injured group. Both Collagen I (Figure 4.17c) and CTGF (Figure 4.17f) were significantly increased in the control horns of the ECM-treated group, compared to the control horns of the injury-only group, even though these horns did not receive any direct intervention or treatment. However, the histological appearances of the control horns in both groups were highly similar (Figure. 4.13 middle panels and Figure. 4.17 middle panels), with the presence of normal endometrial stroma, glands and epithelia, and there was no statistical difference between the number of endometrial glands in either sham control group (data show in Appendix Figure C). This suggests that treatment with ECM hydrogel encourages upregulation of Collagen I and CTGF in the whole uterus, but this does not necessarily represent tissue damage and scarring.

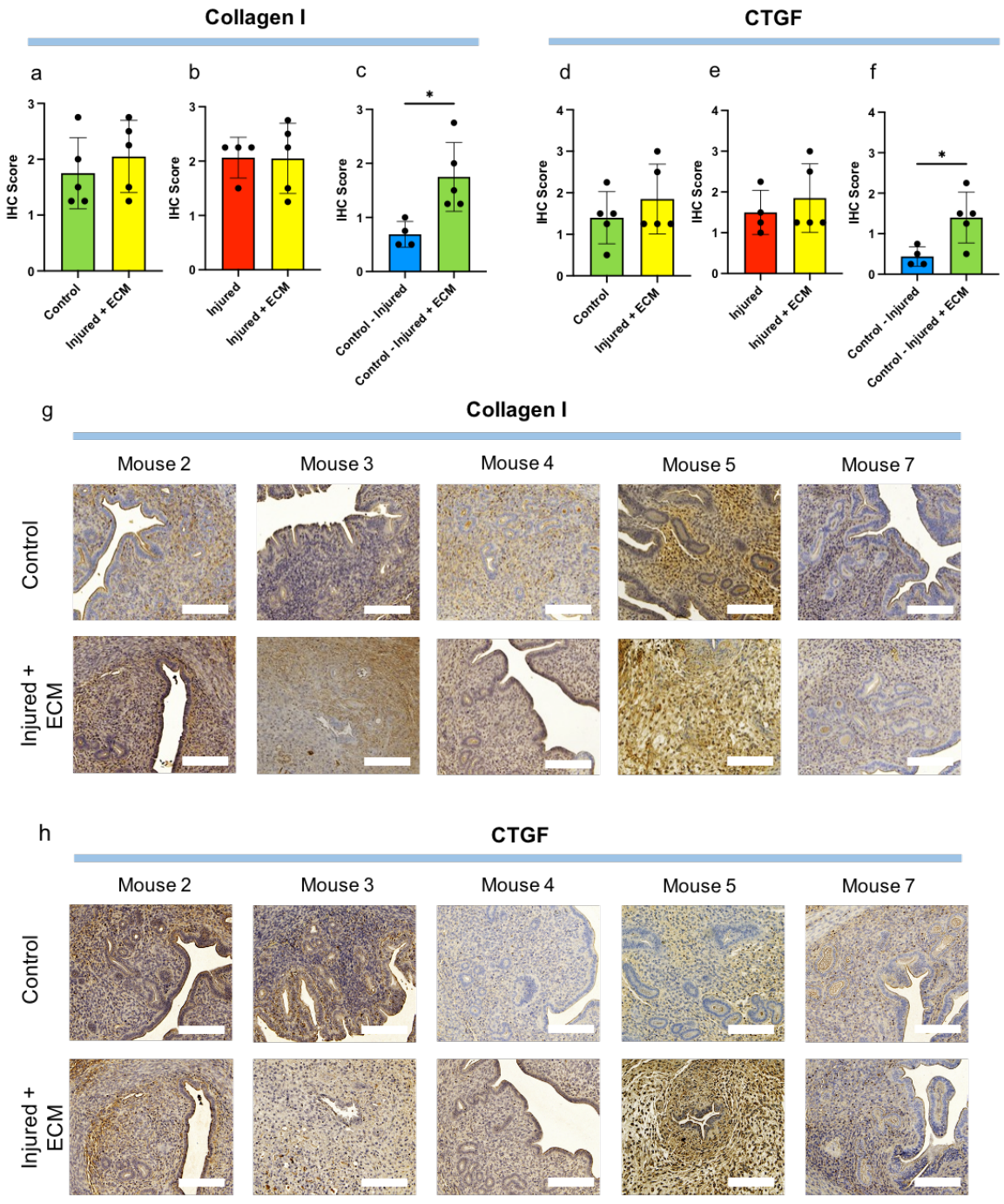


Figure 4.19 Final *in vivo* study: injury + ECM treatment group – immunohistochemistry. a-f Analysis of IHC score for Collagen I and CTGF in the injured horns (N = 4) and ECM-treated injured horns (N = 5), sham control horns in injured group (N = 4) and sham control horns in the ECM-treated injured group (N = 5). Significant differences in Collagen I ($p = 0.0168$) and CTGF ($p = 0.0239$) expression were seen only between the sham controls in the injured group and sham controls in the ECM-treated injured group. The images in **g** and **h** were scored (from 0-3) for intensity of DAB staining, by 4 independent, blinded assessors to generate the graphs in **a-f**. Statistical analyses were performed with student's t tests. Images acquired with 10x lens objective on Zeiss Axio Observer widefield microscope with colour camera. Scale bars = 250 μm.

4.4.3.4 RT-qPCR analysis

Of all the fibrosis and inflammation markers assessed, only Col1a1 was significantly different between the injury-only horns and the ECM-treated injured horns (Figure 4.20a). When normalised to the unoperated control horns, expression of Col1a1 was downregulated with ECM treatment (relative fold change 3.589 +/- 1.211) compared to injury only (relative fold change 5.658 +/- 0.5114) ($p = 0.0154$). TGF-β1, Col3a1 and IL6, which were upregulated in the injury only horns compared to the unoperated controls (Figure 4.16a), were not significantly different between the injury-only and ECM-treated injured horns (Figure 4.20a). Whilst there were slight upward trends in the regeneration markers, PCNA and VEGF, in the ECM-treated horns compared to injury-only, this difference was also not significant (Figure 4.20b). Hoxa10, LIF, Essra and Igf1, which were selected as markers of endometrial function, were not significantly different between the injury only and ECM-treated horns (Figure. 4.20c, although these markers were also not differentially expressed in the injured horns compared to control (Figure 4.16.c). For all the genes without significant difference between the injured and ECM-treated horns, omitting mouse 3 and 5 from the analysis did not make any of the data significant (data not shown).

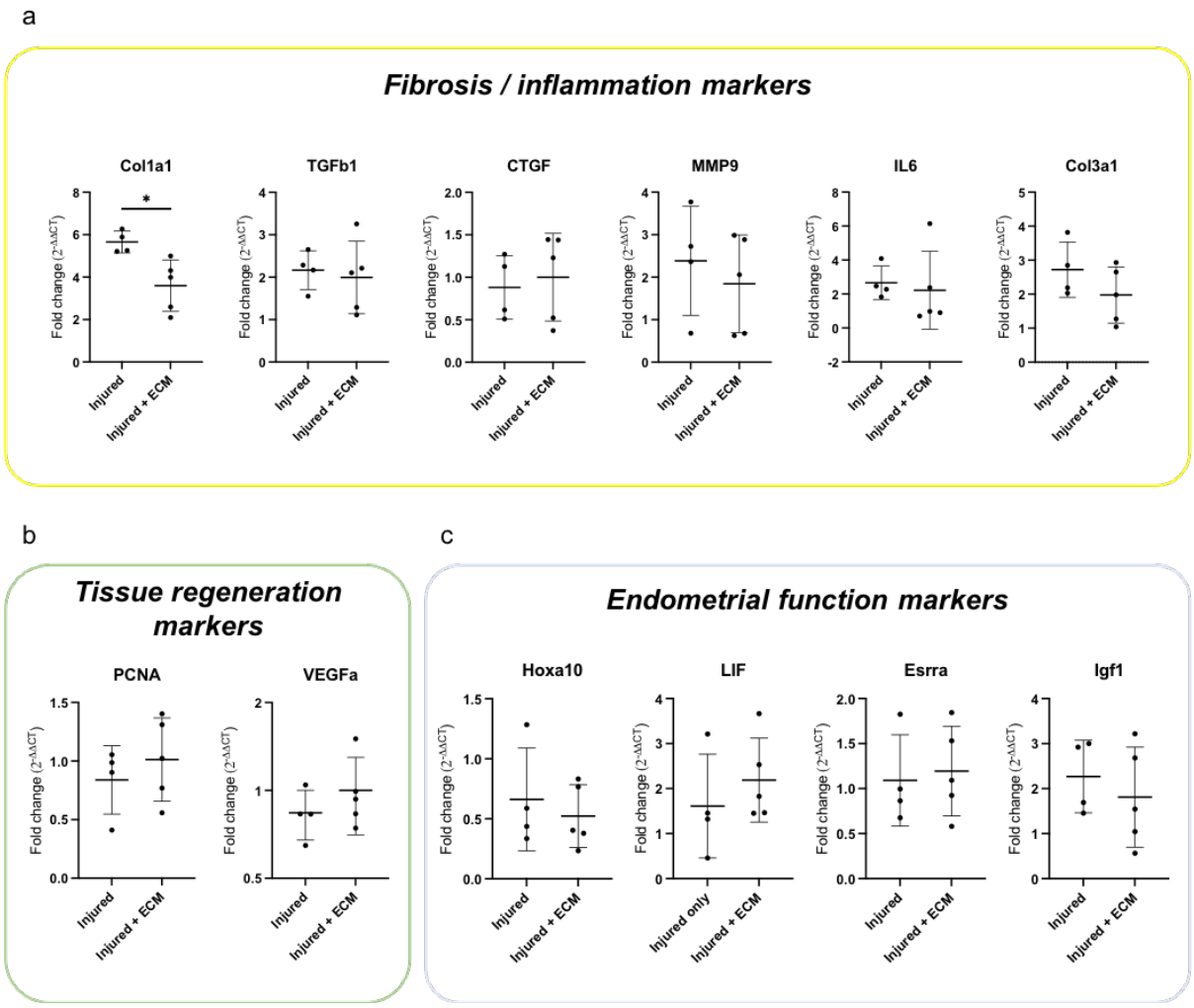


Figure. 4.20 Final *in vivo* study: injury + ECM treatment group – RT-qPCR results. **a** Gene expression analysis for fibrosis and inflammation markers Col1a1, TGF-β1, Col3a1, IL6, MMP9 and CTGF in the injured horns (N = 4, n =3) versus ECM-treated injured horns (N = 5, n =3), with normalisation to the true experimental controls and housekeeping gene. a Col1a1 had a significantly higher fold change in the ECM-treated injured horns compared to the injury only horns (p = 0.0154). There were no significant differences in TGF-β1, Col3a1, IL6, MMP9 and CTGF expression. **b** Gene expression analysis for tissue regeneration markers PCNA and VEGFA. No significant differences were seen in the injured horns versus ECM-treated injured horns. **c** Gene expression analysis for markers of endometrial function and receptivity: Hoxa10, LIF, Essra and IGF1. No significant differences were seen between the injured horns versus ECM-treated injured horns. Statistical analyses were performed with student t tests.

4.5 Discussion and future work

The work presented in this chapter explored the development of a reliable mouse model of Asherman's syndrome. In pilot studies 1 to 3, various mechanical injury methods were tested, beginning with the use of a small-gauge needle inserted and rotated within the uterine lumen to cause endometrial trauma. This method was one of the most commonly reported in the literature for generating intrauterine scarring in mice [289], [292]–[294]. However, no differences were seen on Masson's Trichrome staining between the uninjured horns and the injured horns at days 2,5 and 9 post-surgery. Other abrasive implements were then resourced or designed to be used as endometrial scrapers to mechanically generate intrauterine fibrosis. These included diamond-coated twisted drill bits and 3D-printed, barbed scrapers with different geometries. The results presented in section 4.4.1 showed that none of these alternative methods for mechanical injury were able to reliably generate fibrosis. Furthermore, the addition of LPS as a pro-inflammatory stimulus did not make any difference to the success of the mechanical injury method. Mice have small uteri, causing many technical limitations to mechanical injury methods. It is highly likely that similar to the human endometrium, the murine endometrium is very efficient at healing. Indeed, in human patients one in five women develop intrauterine adhesions following a miscarriage and of those 41.9% have moderate to severe adhesions [23]. Therefore, it is possible that the outcomes of mechanical intrauterine injury models in mice are quite representative of human outcomes. However, this does not make for a useful *in vivo* model of disease, as large numbers of animals would be required to determine the efficacy of a disease-limiting treatment.

The ethanol-induced, chemical injury method has been described in more recent papers on murine models of intrauterine fibrosis, as a way to produce a more robust, uniform and reproducible endometrial scarring [106], [281], [288], [302]. In the literature, increasing ethanol exposure time correlates with more severe endometrial damage [281]. This was also noted when comparing the histological appearance and immunohistochemistry of ethanol-injured uterine horns in pilot 3, where 45 seconds of ethanol was used, compared to injured horns in the final study, which were only exposed to 15 seconds of ethanol. The findings of pilot studies 3 and 4 also indicated that longer duration of ethanol exposure increased the likelihood of adverse outcomes and the need for humane culling of animals before the designated endpoint of the study. By reducing the ethanol exposure time from 45 seconds to 15 seconds, the survival of animals at day 7 post-surgery improved from 40% to 100%. In the final study, 15 seconds of ethanol was sufficient to generate gross morphological changes on histological assessment. In the injured horns there was significant endometrial scarring, with

destruction of normal endometrial stroma, obliteration of luminal epithelia and loss of endometrial glands. Masson's trichrome staining showed significant increased fibrosis area and significantly decreased endometrial glands in the injured horns compared to sham control. On immunohistochemistry, Collagen I and CTGF were increased in the ethanol-injured horns compared to the contralateral sham control horns and qPCR results showed significantly higher expression of Col1a1, Col3a1, TGF-β1 and IL6 in the injured horns. These findings validate the use of 90% ethanol for 15 seconds to generate a mouse model of intrauterine fibrosis. Interestingly, despite the undeniable appearances of severe endometrial damage in the ethanol-injured horns, there were no significant differences in the regeneration markers PCNA and VEGFA between the injured and unoperated control horns. PCNA is a nuclear antigen that is upregulated with cell proliferation and given the relative paucity of cells in the scarred endometrium of the injured horns, it was surprising that PCNA gene expression was not significantly reduced. Gene expression of VEGFA was also not significantly downregulated in the ethanol-injured horns, as might be expected with severe tissue damage. Here, it is worth noting a phenomenon that has been described in the uterus [281] and in other tissues [303], that mild ethanol exposure can in fact promote angiogenesis whilst severe ethanol exposure, which causes too extensive tissue damage, inhibits angiogenesis.

Hoxa10, LIF, ESSRA and IGF-1 were also screened as potential markers of normal endometrial function and receptivity, based on other studies that evaluated these genes as indicators of endometrial regeneration [64], [288], [299], [304], [305]. On qPCR, there was no significant difference in expression of these genes between the unoperated controls with healthy endometrium and the ethanol-injured horns with damaged endometrium. Of note, the expression of Hoxa10 and LIF showed marked variation in the control mice. In both human and mice, the Hoxa10 gene regulates endometrial receptivity and is important for embryo implantation [306], whilst LIF expression is essential for embryo implantation [307]. Mutation of these genes have resulted in infertility in mouse studies [306], [307].The expression of both Hoxa10 and LIF is known to fluctuate throughout the mouse estrus cycle and the human menstrual cycle [306], [307]. Hoxa10 expression peaks in response to sex steroids in the midscretory phase of the menstrual cycle, in preparation for implantation [306]. Similarly, LIF expression is highest around the time of ovulation and just before implantation [307]. The variation seen in Hoxa10 and LIF expression in the control mice could be attributable to the animals being in different phases of the estrus cycle at the time of tissue harvesting. Therefore, identifying or artificially synchronising the estrus cycle of the mice may be an important modification for future studies, in order to determine differential expression of endometrial receptivity markers.

The results presented in section 4.4.3 demonstrate, to some degree, the effect of 8 mg/mL endometrial ECM hydrogel in preventing endometrial damage and fibrosis. This particular batch and concentration of gel was chosen for its optimal gelation properties as determined by rheology (chapter 2, section 2.4.5.2), which would aid gel retention within the uterine lumen. Of the five mice that received ethanol-injury in the right horn, followed by application of endometrial ECM hydrogel, three mice had clear responses to treatment whilst two mice (mouse 3 and 5) failed to respond to the ECM gel. In the mice that did not respond to treatment, the histological appearances of the endometrium were similar to the injured horns in the injury-only group and showed replacement of the endometrial stroma with fibrous collagen, with loss of endometrial epithelia and glands. When the surgery notes were reviewed (Appendix Table A1), the two mice that did not respond to ECM hydrogel treatment had either a particularly large uterine horn or was noted to have gel leakage from the horn immediately after the treatment was delivered. These factors imply that there was inadequate delivery of ECM hydrogel to the injured horns, as all mice in the ECM treatment group received an equal volume of gel during the experiment. Therefore, it is plausible to attribute the findings in those two mice to insufficient treatment rather than ineffectiveness of the ECM hydrogel. Of the other three mice in the ECM treatment group, the histological appearance of the injured horns looked very similar to the sham control horns. The endometrial stroma, endometrial glands and luminal epithelia were preserved in these three ECM-treated injured horns. Quantitative analysis of Masson's trichrome stained sections found no significant different in the fibrosis area or number of endometrial glands in the ECM-treated injured horns and their paired sham control horns, suggesting a beneficial effect of ECM hydrogel on limiting endometrial damage. However, when the fibrosis area and endometrial gland count were compared between the injury only horns and the ECM-treated injured horns, the difference was not significant, unless mouse 3 and 5 were excluded.

Excessive production and aberrant deposition of collagen I is a hallmark of tissue fibrosis [225] and appears to be one of the the most commonly reported marker of intrauterine fibrosis in animal studies. In the final *in vivo* study, when all mice were pooled within their groups for analysis, there was no difference in the expression of collagen I on immunohistochemistry between the ECM-treated injured horns and injury-only horns. Even with exclusion of the two mice that were presumed to have inadequate gel treatment, the difference between ECM-treated and injury-only remained non-significant (data shown in Appendix Figure C). However, on qPCR, Col1a1 was significantly downregulated in the ECM-treated horns compared to the injury-only horns. The differences between the immunohistochemistry findings and qPCR results for collagen I suggest that whilst there was increased production of the collagen I protein in all injured horns, greater upregulation of Collagen I

is sustained at a transcriptional level when the injury correlates with severe tissue damage and in the absence of ECM hydrogel, which may be tempering the fibrosis response.

CTGF is a secreted matricellular protein that acts as a key mediator in cell signalling pathways implicated in tissue remodelling and fibrosis [308]. It acts as a downstream effector for TGFβ to promote myofibroblast activation and ECM deposition or remodelling, leading to fibrosis [308]. Increased expression of CTGF has been shown in intrauterine adhesions [29] and it has been used as a marker of endometrial fibrosis in a mouse model of Asherman's syndrome [295]. In the results presented in section 4.4.2.2, CTGF was found to be increased on immunohistochemistry in injured uterine horns compared with the sham control horns, however gene expression of CTGF was not upregulated in the injured horns. When comparing the injury-only horns and ECM-treated injured horns, no difference was found in CTGF expression at a protein or gene transcription level. An interesting observation was made when analysing the contralateral sham control horns in the final *in vivo* study. The sham control horns in the ECM-treated group had significantly higher expression of collagen I and CTGF than the injury-only group. These findings suggest that endometrial ECM hydrogel upregulates production of collagen I and CTGF in both uterine horns, even though only one horn was injured and received gel treatment. However, increases in collagen I and CTGF are not necessarily synonymous with endometrial damage or perhaps even tissue fibrosis, as, histologically, the sham control horns and 60% of the ECM-treated injured group closely resembled the appearance of an unoperated control horn (See Figure 4.1). Indeed, excess collagen I and CTGF production are observed in the normal wound healing process [309], [310]. Collagen I synthesis and remodelling are required for tissue repair following trauma, however when the rate of collagen production by myofibroblasts exceeds its rate of degradation, then collagen I accumulates in excess over time and results in tissue fibrosis [309]. CTGF has been suggested to play a non-pathological and vital role in the early wound healing process, however fibrosis occurs when there is persistent overexpression of CTGF in [310]. The *in vivo* work presented in this chapter only evaluated a single timepoint, 7 days post-surgery. Further work could involve a later timepoint to compare the relative expression of collagen I and CTGF at early and late stages of tissue repair. At a later stage, greater differences may be revealed between the injury-only and ECM-treated injured groups.

A panel of genes were analysed for differential expression between the injured and ECM-treated injured horns. These genes correlated to markers of fibrosis and inflammation (Col1a1, Col3a1, CTGF, TGF-β1, MMP9), cell proliferation, (PCNA), angiogenesis (VEGFA) and endometrial function or receptivity (Hoxa10, LIF, Essra, Igf-1). Other than Col1a1, none of the genes analysed showed

significant difference in expression between the injured horns and ECM-treated injured horns at day 7 post-surgery. Due to time constraints, other timepoints were not evaluated. Detection of gene expression is time-sensitive and sampling of RNA outside of the transcription window may result in inaccurate evaluation of genes of interest [311]. In other words, collecting RNA from tissue samples earlier or later than 7 days may show significantly different results. Another potential source of error was that RNA was extracted not just from the endometrium but from the full thickness of a segment of the uterine horn. Although great care was ensured to sample tissue from a visibly affected region, it is possible that some uninjured or untreated tissue could have been included in the sample for RNA extraction. Additionally, extracting RNA from cells in the myometrium and perimetrium may have diluted the RNA target from cells in the affected endometrium. Appropriate tissue sectioning can greatly influence the RNA data and significant alterations of gene expression can be seen between whole tissue extracts and dissected regions of interest [311].

Only one other group has studied endometrial ECM hydrogel in an *in vivo* model of intrauterine adhesions [106]. In 2021, an academic group led by Cervello published a method to produce porcine endometrial ECM hydrogels and characterised the effect of this material on endometrial cells *in vitro*, on endometrial organoid cultures and as a treatment to regenerate the endometrium [104]–[106]. There were differences in the endometrial decellularisation protocol and the proteomics results between Cervello's group and the work presented in this thesis, which was discussed in greater detail in Chapter 2. Lopez-Martinez et al. also used an ethanol-induced IUA mouse model (70% ethanol for 3 minutes) but explored the effect of ECM treatment at a delayed timepoint, 4 days after endometrial injury, and evaluated the tissue healing response 2 weeks after treatment [106]. This group also studied 2 different treatments; endometrial ECM hydrogel alone and endometrial ECM combined with PDGF, bFGF and IGF-1 [106]. The concentration of endometrial ECM hydrogel used was 6 mg/mL and PBS was used as their control [106]. As indicators of endometrial damage, they evaluated endometrial thickness, gland concentration, percentage of fibrosis as determined by Masson's trichrome blue staining and gene expression of Col1a1 [106]. To determine endometrial regeneration, immunostaining for Ki67, α-SMA and GSL-1 was performed to gauge cell proliferation and neoangiogenesis [106]. All mice were mated after treatment and the uteri were harvested to establish the number of embryos and gestational sacs [106]. Interestingly, Lopez-Martinez et al. only reported significant differences in the ECM plus growth factor treatment group, where a significant downregulation in Col1a1 was observed and Ki67 and angiogenesis were significantly increased. No significant effects were found in endometrial thickness, gland concentration and collagen deposition between the control and either treatment groups [106]. Endometrial ECM alone did not significantly

increase the marker of cell proliferation or staining for new blood vessels. In the PBS and endometrial ECM treatment groups, the pregnancy rate was significantly reduced compared to the non-damaged horns, however there was no significant difference between the ECM and growth factor treatment group and non-damaged group [106].

The results of the final *in vivo* study presented in this chapter, when all mice were analysed, were similar to the findings reported by Lopez-Martinez et al. (2021) [106], where no difference in fibrosis area or endometrial gland count was found between the injured group that received saline and the ECM-treated group. However, unlike the data shown by Lopez-Martinez et al. (2021), Col1a1 gene expression between the ECM-gel treated and injury only group was significantly reduced here. This possibly reflects the different timepoints that were evaluated. In future experiments it would be enlightening to determine whether the endometrial ECM hydrogel produced in this work is effective for treating established intrauterine fibrosis, which could be achieved by administering ECM hydrogel at a delayed timepoint, when endometrial scarring has already occurred. Challenges to delayed hydrogel administration include the requirement for a second anaesthetic and the potential need for repeat laparotomy to deliver the treatment, which would increase the likelihood of adverse outcome for the animal, unless an approach could be developed for transvaginal gel administration. The clinical relevance of being able to demonstrate the effect of endometrial ECM hydrogel for treatment of existing intrauterine scarring is that the rate of intrauterine adhesion occurrence is very high after adhesiolysis, which remains the current gold standard for managing Asherman's syndrome [9]. Therefore, there is a clinical need for an anti-scarring agent in the context of secondary prevention of adhesions.

Due to time constraints, it was beyond the scope of this thesis to repeat the *in vivo* experiment, with optimisation of the gel delivery process. This would be the first priority for future work. To prevent sufficient gel application, variable volumes of gel could be delivered depending on the size of the uterine horn, instead of one standardised volume. To minimise gel leakage, the ECM hydrogel could be pre-warmed prior to application as Rheology experiments have demonstrated that gelation is initiated several minutes after a constant temperature of 37 ^{o}C. Alternatively, both ends of the uterine horn can be temporarily clamped after gel delivery to aid gel retention.

One important limitation in the final *in vivo* study, which should be included in future work, is the lack of a control group that received only ECM hydrogel without uterine injury. This would help to determine whether ECM hydrogel treatment increases collagen I and CTGF in the absence of uterine

injury, or whether tissue trauma is prerequisite for this effect to occur. Another notable limitation to the final *in vivo* study is the absence of a true control treatment, such as an alternative hydrogel. Although all injured horns were washed with PBS after ethanol injury, a separate volume of PBS was not injected into the injury only horns as a control, as it was felt that the PBS would leak immediately from the incisions in the horns or from the oviduct, and would effectively serve as an additional wash step rather than a control treatment. In the original plan of work for this project, the aim was to test a different ECM hydrogel, e.g. sourced from porcine SIS, in parallel with endometrial ECM hydrogel. This would allow for evaluation of whether there are tissue-specific advantages to using an ECM hydrogel in the context of endometrial regeneration. Unfortunately, there were barriers to using SIS ECM hydrogel *in vivo* due to challenges with batch-to-batch variability in SIS ECM hydrogel production, and that at matched concentration (8 mg/mL) SIS ECM hydrogel was more than 10 times weaker in stiffness compared to endometrial ECM hydrogel. Future work could therefore include the identification of a suitable alternative ECM hydrogel to test alongside endometrial ECM hydrogel, as well as an investigating an alternative, non-ECM hydrogel treatment control. An ideal potential candidate would be a hyaluronic acid gel, which is already used in clinical settings as an anti-adhesion barrier agent [35].

In future experiments, further effort could be made to optimise staining for cell proliferation markers, such as Ki67, and to characterise angiogenesis in response to ECM-gel treatment, such as staining for blood vessels in the endometrium with CD31 [312], [313] or GSL-1 [106]. Another effect that would be interesting to evaluate would be the profile of immune cells in the injured and ECM-treated horns. This could involve immunostaining and qPCR for markers of M1 and M2 phenotype macrophages (as discussed in chapter 3), as shifts in ratio of M1 to M2 macrophages may help to characterise the influence of endometrial ECM hydrogel on endometrial regeneration. Ultimately, to determine whether endometrial ECM hydrogel leads to functional endometrial regeneration, future studies would need to assess the impact of this treatment on fertility outcome. One of the key limitations to existing anti-adhesion therapies is that there is still no proven association with improved reproductive outcome in patients [32]. Lopez-Martinez et al. (2021) demonstrated that an endometrial ECM hydrogel combined with growth factors improved the pregnancy rate from 17% in the injury only control group to 45%, in a murine model of Asherman's syndrome [106]. Of note, in the ECM hydrogel-only group, the fertility rate was actually inferior (8%) to the saline control [106]. If a future *in vivo* study were to demonstrate improved fertility outcome with the endometrial ECM hydrogel prepared using the method described in Chapter 2, this would strongly suggest the importance of decellularisation protocol design on the biofunctionality of ECM hydrogels in the reproductive context.

4.6 Summary of key findings

This chapter focused on the development and validation of a reliable mouse model of intrauterine fibrosis and evaluated the effect of endometrial ECM hydrogel on preventing ethanol-induced endometrial injury and scarring. Mechanical injury methods were unsuccessful in inducing significant and reproducible endometrial fibrosis. Whereas high percentage ethanol injected briefly into the lumen of the uterine horn caused substantial endometrial damage and aberrant, excess collagen deposition. This is in keeping with recent studies published by other groups that advocate for ethanol perfusion as a more robust mouse intrauterine fibrosis model. Longer duration of ethanol exposure, as well as ethanol leakage into the peritoneal cavity, increased adverse outcomes and reduced animal survival.

Once an ethanol-induced endometrial scarring model had been optimised, the fibrosis mitigating effect of endometrial ECM hydrogel was tested in a study involving an injury-only group and an injury group that received ECM treatment immediately after trauma. In the ECM treatment group, there appeared to be a partial treatment response; 60% of mice had histological appearances that were similar to the sham control horns whilst 40% of the mice showed severe fibrosis in the ECM-treated injured horns. Ineffective gel delivery was felt to be a plausible explanation for the 2 mice that did not show any positive response to ECM treatment. When all mice were pooled, a significant difference was found between the injured and ECM-treated injured horns in the gene expression of Col1a1, which was decreased with ECM treatment. The findings from this preliminary *in vivo* work are promising and pave the way for further studies to optimise ECM gel delivery in the mouse model, evaluate longer timepoints, explore the effect of endometrial ECM for treatment of established intrauterine scarring and ultimately to test the efficacy of endometrial ECM for restoring fertility after endometrial damage.

Chapter 5 - Conclusion and implications for future research

5.1 Summary of findings

Intrauterine scarring is an important cause of infertility and other pregnancy complications, for which current treatments are not highly effective. In recent years there has been a growing trend in studying regenerative medicine approaches to treating a damaged or scarred endometrium. The aim of this thesis was to explore a biomaterials approach to endometrial repair, by developing and characterising an endometrial ECM hydrogel which was hypothesised to have favourable material and biological properties to mitigate intrauterine fibrosis and support endometrial regeneration.

In this project, a novel method for decellularising porcine endometrial tissue was described and it was demonstrated that key ECM proteins and proteoglycans were preserved in the decellularised endometrial ECM. Matrix-bound nanovesicles, with exosome-like properties, were found within the decellularised endometrial ECM. This has not been reported before in other studies on decellularised reproductive tissues. Some biochemical differences between decellularised endometrium from sow versus pig were suggested by Raman spectroscopy analysis and future studies to compare the composition and properties of sow and pig endometrial ECM in detail would be interesting. An endometrial ECM hydrogel was demonstrated to be injectable and sprayable and, like all ECM hydrogels, gelation was initiated within minutes under physiological conditions. These properties make the ECM hydrogel versatile for *in vivo* applications.

Endometrial ECM hydrogel was shown to have good cytocompatibility and led to increased angiogenesis *in vitro*. It was also able to abrogate the effect of TGF-β1 on matrix deposition in an *in vitro* endometrial fibrosis assay. When interfaced with macrophages that were stimulated with pro-inflammatory cytokines, endometrial ECM hydrogel caused a shift away from an M1 phenotype on gene expression analysis, suggesting a potential beneficial immunomodulatory effect when it comes to wound healing.

Using an ethanol-induced model of endometrial fibrosis in the mouse, the effect of endometrial ECM hydrogel on preventing endometrial damage was evaluated *in vivo*. Here, 60% of the mice in the ECM-treatment group had endometrial morphology which closely resembled the sham controls at day 7 post-injury. These mice had preservation of endometrial glands and epithelia and minimal evidence of fibrosis on Masson's trichrome staining. However, 40% of the mice in the ECM treatment group had

fibrosed and damaged endometria, similar to the injured horns in the group that did not receive ECM. This was possibly related to ineffective gel delivery following ethanol injury, as suggested by details in the surgery notes. When all the mice were pooled for analysis, there were no significant differences in the percentage of fibrosed area, endometrial gland number of collagen I and CTGF protein expression on histological assessment of injured horns compared to ECM-treated injured horns. However, collagen I gene expression was significantly downregulated in the pooled ECM-treatment group, compared to the injury-only group, suggesting a limiting effect on persistent, excessive matrix deposition at a transcriptional level. Future experiments would first prioritise a repeated *in vivo* study with carefully optimised gel delivery, which could involve modification of the gel application technique and using variable volumes of gel to adequately fill the uterine horn, instead of a standardised volume for all mice.

5.2 Future work

To further develop the understanding of the properties and bioactivity of endometrial ECM hydrogel, future studies could involve investigating the immunomodulatory properties of endometrial MBVs and to characterise the effect of endometrial ECM on stem cells. It would also be important to understand the similarities and differences between endometrial ECM and other ECM types in the context of endometrial regeneration, to appreciate whether there is a tissue-specific advantage. This could be achieved by comparing the effect of an alternative and commonly used ECM, such as SIS, in the *in vitro* endometrial fibrosis assay and in the mouse model of intrauterine damage.

The *in vivo* work presented in this thesis focused on primary prevention of intrauterine fibrosis. Further experimental work would include determining the effect of endometrial ECM hydrogel in the treatment of existing intrauterine scarring. If future studies could demonstrate the efficacy of endometrial ECM gel, alone, for endometrial regeneration and fertility restoration, this would be a significant improvement on the one existing animal study on endometrial ECM gel which found beneficial effects only when ECM was combined with growth factor delivery [106]. This is an especially important consideration for scalability and clinical translation. Whilst ECM hydrogels have been used to deliver drugs, growth factors and cells, the addition of these extra components increases the cost and complexity of manufacture and may limit the stability or shelf-life of the treatment.

The eventual goal of this research is to progress closer towards clinical translation, with a gel that can be easily applied in a surgical setting for primary or secondary prevention of intrauterine adhesions

and promotion of functional endometrial regeneration. Endometrial function is ultimately defined by fertility and maintenance of pregnancy. Therefore, future work would benefit from the investigation of pregnancy outcome when endometrial ECM hydrogel has been used to prevent or treat a damaged endometrium.

5.3 Contextualisation of this research

The use of hydrogels to prevent or treat IUA is a growing field. Hyaluronic acid (HA) gels are already used clinically for primary or secondary prevention of IUA, as well as pelvic adhesions after abdominal surgery [314]. They have been demonstrated to reduce adhesion formation but their efficacy for improving fertility and pregnancy rates is still unproven clinically [32], [314]. In future studies, a HA hydrogel could be used as a control in the *in vitro* and *in vivo* experiments. However, to select an appropriate control, a clinically approved, commercially manufactured HA would be necessary. This thesis was inspired by the observation of the uncertain impact of existing clinical therapies on pregnancy outcomes and by appraising studies on decellularised uterine tissue which showed favourable effects on uterine regeneration and fertility restoration in animal studies [62], [63], [165]. These studies suggested that there were tissue-specific advantages to using uterine ECM for endometrial repair. A study on a hydrogel made from decellularised, proliferating rabbit endometrium demonstrated its ability to support *in vitro* embryo growth, with comparable results to standard embryo culture media, highlighting the advantage of endometrial ECM in a reproductive context [169]. The recent studies by another group on the development of an endometrial ECM hydrogel for intended treatment of Asherman's syndrome and endometrial atrophy further validated the concept of designing a novel, tissue-specific approach to endometrial regeneration that may ultimately prove to be superior to existing therapies for restoring fertility [104], [106].

The results presented in this work suggested many favourable properties of ECM hydrogels for constructive tissue healing. However, this type of biomaterial has some important considerations to be borne in mind for clinical translation. Research and development focus must be given to minimising batch-to-batch variability in ECM biomaterials [202]. Rheological experiments in chapter 2 highlighted batch-to-batch variability in ECM hydrogels despite effort to maintain consistency in the methods. Biological variation of the source tissues is the most likely explanation for this issue and could likely be improved to appropriate levels by using animals of the same age, size and breed, reared in a more rigorously controlled environment. Decellularised ECM is a highly complex material biochemically and there needs to be greater emphasis on developing ways to ensure or evaluate for uniformity,

compared to hydrogels that are made from one compound or that are chemically synthesised. The mechanical properties of an ECM hydrogel could be made more consistent by incorporating cross-linkers or mixing with another type of hydrogel with more tunable physical characteristics, such as gelatin methacrolate. Another consideration for clinical translation is that there still remains a lack of standardisation as to what degree of cell and DNA removal is safe and what biochemical components are essential to be preserved in ECM biomaterials in order for them to be effective (discussed further in chapter 2). Reducing this ambiguity would improve the quality and efficacy of ECM hydrogels, ultimately resulting in more robust clinical responses.

5.4 Implications for other areas of research

Whilst the emphasis of this thesis was on intrauterine scarring, the findings generated by this work have implications for other clinical diseases that affect female reproductive health. Adhesions in the pelvis, outside of the uterus, form commonly after abdominal and pelvic surgery or as a result of endometriosis [314]. Pelvic adhesions can cause pain, infertility and surgical complications, but a recent Cochrane review found no evidence of the effectiveness of current anti-adhesion therapies for improving pelvic pain or pregnancy outcomes [314]. It would be interesting to investigate whether endometrial ECM hydrogel could also mitigate fibrosis in pelvic adhesions. Endometrial atrophy can occur in conjunction with Asherman's syndrome or as a result of uterine surgery, radiotherapy, infection or of unknown cause [315]. A thin endometrium results in lower pregnancy and live birth rates during assisted reproduction and there are limited effective treatments [315]. Endometrial ECM hydrogel was demonstrated to improve endometrial stromal cell proliferation and angiogenesis *in vitro* in this work, as well as enhance endometrial epithelial organoid growth when supplemented into the culture media in another study [105]. Therefore, there is the potential for endometrial ECM hydrogel to be investigated as a treatment for regenerating atrophic endometrium.

Enhancing cell proliferation and angiogenesis are desirable traits for tissue regeneration and whilst these same biological processes are also implicated in cancer development and progression, this author has identified no reports regarding cancer risk associated with ECM biomaterials. In fact, a study where decellularised UBM ECM was implanted simultaneously with cancer cells in a mouse model found that the ECM exhibited an anti-tumour effect [255]. UBM created a unique immune microenvironment that acted synergistically with PD1/PD-L1 checkpoint immunotherapies to inhibit cancer growth and improve survival [255]. It would be very interesting to explore, in future, the role of ECM hydrogels as an adjunctive treatment in gynaecological cancers, either in the prevention of

scarring and cancer progression following surgical removal of disease or potentially as a combination therapy with progesterone in the management of early-stage endometrial cancer when fertility sparing treatment is desired.

5.5 Concluding remark

The work presented in this thesis involved the development, characterisation and application of an endometrial ECM hydrogel produced in a novel way. Overall, the results indicated the beneficial effect of endometrial ECM hydrogel for preventing fibrosis and supporting biological processes that are important for tissue regeneration. The *in vivo* work was promising for the ability of endometrial ECM hydrogel to limit endometrial damage after injury. These findings pave the way for more research to understand the impact of endometrial ECM hydrogel for treating established intrauterine scarring and for fertility restoration.

Appendix 1 – Supplementary data for chapter 2

Table A1: Sow and pig endometrial decellularisation experiments – protocol optimisation and biological replicates. This table summarises each endometrial decellularisation experiment carried out in the preparation of this thesis, including alterations in decellularisation method for protocol optimisation.

				DNA content (ng/mg)						
Sow/Pig	**Uterus ID**	**Date of Picogreen**	**Date of decel completion**	**Native Endometrium**	**Decellularized ECM**	**% reduction in DNA**	**Amount of DNAse**	**Agitation**	**DNAse temp**	**Protocol length**
Sow		23.10.18	21.09.18	NA	750.9235855	89.48%	8000 units (in 80ml)	Stirrer, setting 2	RT	4 day protocol
Sow		30.10.18	26.10.18	7136.393019			N/A	Stirrer, setting 2	N/A	N/A
Sow		17.11.19	15.11.19	NA	376.4	94.73%	8000 units (in 80ml)	Stirrer, setting 2	RT	4 day protocol
Sow		21.11.19	16.11.19					Stirrer, setting 2	RT	5 day protocol
Sow		15.02.19	08.02.19	26699.58976	2116.278634	92.07%	8000 units (in 80ml)	Stirrer, setting 2	RT	5 day protocol
Sow		18.03.19	11.03.19	22463.78598	352.85	98.43%	3.2mg in 100ml	Stirrer, setting 2	RT	5 day protocol
Sow		12.04.19	08.04.19	12518.09514	898.4315912	92.82%	3mg in 100ml	Stirrer, setting 2	RT	5 day protocol
Sow		31.05.19	25.05.19	23588.28302	317.2678861	98.65%	3.2mg in 100ml	Stirrer, setting 2	RT	5 day protocol
Pig	1	18.02.20	08.02.20	22243	12725		None	Stirrer, setting 2	RT	2 day protocol without DNAse
Pig	1	18.02.20	08.02.20		11553		None	Stirrer, setting 2	RT	3 day protocol without Dnase
Pig	1	18.02.20	08.02.20		16692		1.5mg in 100ml	Stirrer, setting 2	RT	4 day protocol
Pig	1	11.03.20	28.02.20	51667	9695	56.41%	3mg in 100ml	Stirrer, 300rpm	RT	5 day protocol

Pig	1	10.08.20	15.03.20	25793	935	96.37%	3mg in 100ml	Stirrer, 300rpm	RT	5 day protocol
Pig	1	10.08.20	31.07.20		537	97.92%	3.28mg in 100ml	Shaker, 300rpm	37 degrees	5 day protocol
Pig	1	19.08.20	15.08.20		39	99.85%	3mg in 100ml	Shaker, 300rpm	37 degrees	5 day protocol
Pig	2	27.08.20	23.08.20	3190	1923	39.72%	3mg in 100ml	Shaker, 300rpm	37 degrees	5 day protocol
Pig	3	06.10.20	29.08.20	11342.93045	76.63127627	99.32%	3.4mg in 100ml	Shaker, 300rpm	37 degrees	5 day protocol
Pig	4	14.10.20	11.10.20		546	76.80%	3.2mg in 100ml	Shaker, 300rpm	37 degrees	5 day protocol
Pig	3	22.10.20	18.10.20		114.1798806	98.99%	3.8mg in 100ml	Shaker, 300rpm	37 degrees	5 day protocol
Pig	3	22.10.20	18.10.20		45.19194438	99.60%	3.8mg in 100ml	Shaker, 300rpm	37 degrees	5 day protocol
Pig	4	22.10.20	N/A	2353.013871			N/A	N/A	N/A	N/A
Pig	1	22.10.20	N/A	2759.890991			N/A	N/A	N/A	N/A
Pig	1	03.11.20	24.10.20		210.559685	99.18%	3.25mg in 100ml	Shaker, 300rpm	37 degrees	5 day protocol
Pig	4	03.11.20	24.10.20		69.51759255	97.05%	3.25mg in 100ml	Shaker, 300rpm	37 degrees	5 day protocol

Appendix 2 – Supplementary data for chapter 3

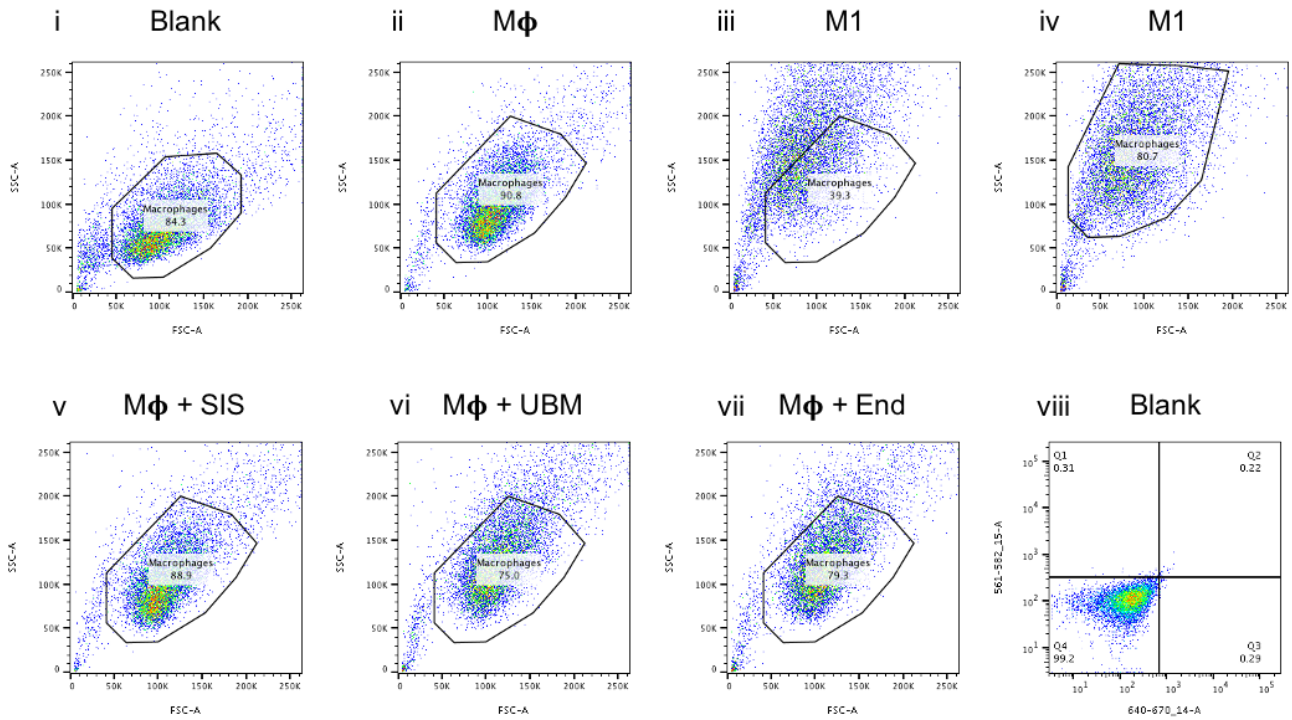


Figure A: Flow cytometry FSC/SSC plots and gating for blank (unstained) cells. Supplementary flow cytometry data referred to in section 3.3.5.4 and section 3.4.5.1. **i-vii** FSC (x-axis) versus SSC (y-axis) plots for blank, naïve (MΦ), M1-polarise, M2-polarised, SIS-treated, UBM-treated and Endometrial ECM-treated RAW 264.7 cells. **i** A gate was drawn around the relevant population in the blank (unstained) cells, to identify the macrophages. Data in the bottom left corner represents cell debris and it was important to exclude this from analysis. **ii** The gate had to be manually adjusted slightly for naïve (MΦ) macrophages as population shifted slightly upwards in SSC. **iii** The MΦ gate was then applied to all other samples and it is clearly seen that the same gate excludes the majority of M1 cells as the population shifts massively upwards in SSC, indicating increased granularity of the M1-polarised macrophages. **iv** The gate is manually adjusted for M1-polarised macrophages to include the majority of stained cells. **v** The MΦ gate applied to SIS-treated macrophages includes the majority of cells. **vi** The MΦ gate applied to UBM-treated macrophages includes the majority of cells. **vii** The MΦ gate applied to Endometrial ECM-treated macrophages includes the majority of cells. **viii** After identifying the macrophage population in the FSC/SSC plots, a gate was drawn around the blank (unstained) cells in a CD86 (x-axis) versus CD206 (y-axis) plot. The same gate was then applied to all stained samples to identify proportions of CD86+ and/or CD206+ cells.

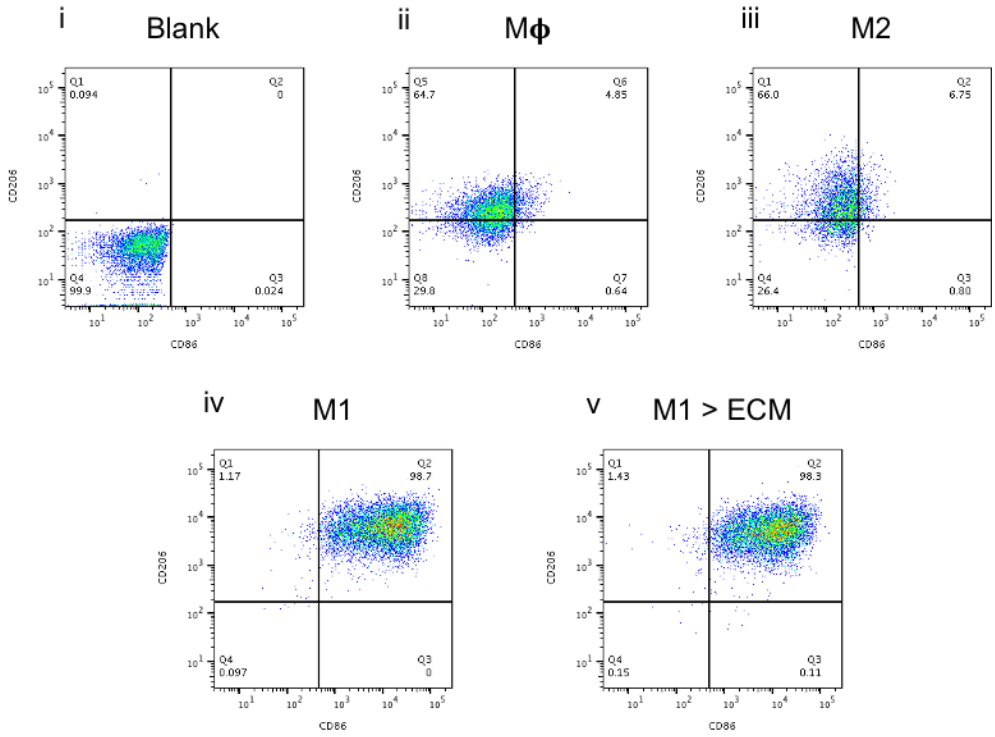


Figure B: Flow cytometry CD86/CD206 dot plots. Supplementary flow cytometry data referred to in section section 3.4.5.2. CD86 is x-axis and CD206 is y-axis. **i** Blank (unstained) macrophages. A gate is drawn around this population and the same gate is applied to all stained samples to identify proportions of CD86+ and/or CD206+ cells. **ii** MΦ macrophages – 64.7% stain positively for CD206 and few cells stain positively for CD86. **iii** M2 macrophages (after IL4 + IL13 stimulation for 24 hours) – 66% stain positively for CD206 and few cells are CD86+. **iv** M1-polarised macrophages (after LPS and IFN-γ stimulation for 2 hours, followed by a media change with normal growth medium). Almost all cells (98.7%) are CD86+ CD206+. **v** Macrophages stimulated with LPS and IFN-γ for 2 hours then treated with endometrial ECM. There is no change in CD86 or CD206+ expression compared M1-polarised macropahges in **iv**.

Appendix 3 – Supplementary data for chapter 4

Table A2: Surgery details for final *in vivo* study. Supplementary information referred to in sections 4.4.3.1 and 4.5.

Mouse	Injury	Treatment	Complication	Comment
2	90% EtOH 15 sec	Gel 50ul	Did not flush out EtOH with PBS immediately. Placed some gel first then did PBS wash, then delivered gel.	
3	90% EtOH 15 sec	Gel 50ul	None	Large uterus
4	90% EtOH 15 sec	Gel 50ul	None	?small leakage of gel
5	90% EtOH 15 sec	Gel 50ul	None	Gel leaked from uterine horn
6	90% EtOH 15 sec	None	Rupture of uterine wall during PBS flush	
7	90% EtOH 15 sec	Gel 50ul	None	
8	90% EtOH 15 sec	None	None	
9	90% EtOH 15 sec	None	None	
10	90% EtOH 15 sec	None	None	

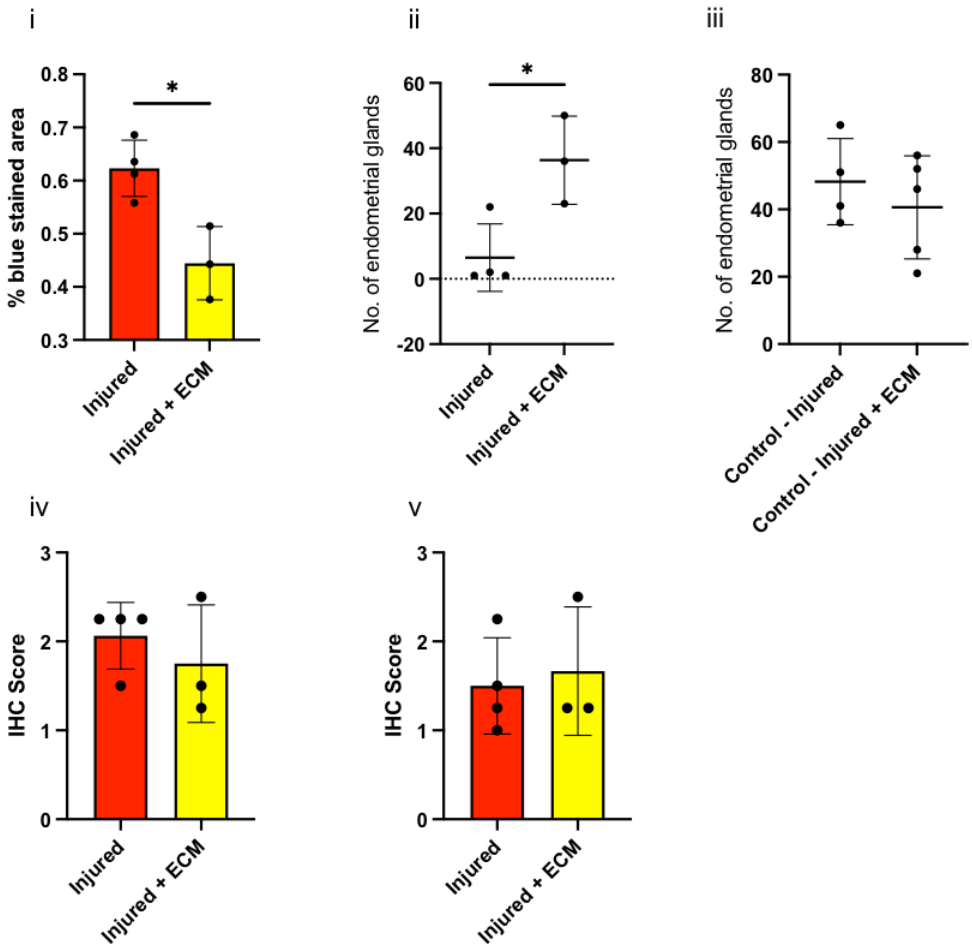


Figure C: Re-analysis of Masson's trichrome staining, endometrial gland number and immunohistochemistry for final *in vivo* study – with mouse 3 and 5 omitted. i Analysis of percentage of blue (collagen)-stained area in injury-only horns (N = 4) compared to ECM-treated injured horns (N = 4). There is a significant decrease in the area of collagen deposition in the ECM treatment group (p = 0.0114). **ii** Analysis of endometrial gland count in injury only horns (N = 4) compared to ECM-treated injured horns (N = 4). There is a significant increase in number of endometrial glands in the ECM treatment group (p = 0.0207). **iii** Comparison of the number of endometrial glands in the sham control horns of the injury only group (N = 4) and the sham control horns of the ECM-treated injured group, including mouse 3 and 5 (N = 5). No significant difference was found between the sham controls in either group. **iv** Immunohistochemistry analysis for Collagen I. No significant difference in IHC score was found between injury-only horns (N = 4) and ECM-treated injured horns (N = 3) even when mouse 3 and 5 were omitted. **v** Immunohistochemistry analysis for CTGF. No significant difference in IHC score was found between injury-only horns (N = 4) and ECM-treated injured horns (N = 3) even when mouse 3 and 5 were omitted. Statistical analyses were performed with student t tests.

Bibliography

[1] K. Diedrich, B. C. J. M. Fauser, P. Devroey, G. Griesinger, and on behalf of the E. A. R. (EVAR) W. Group, "The role of the endometrium and embryo in human implantation," *Hum. Reprod. Update*, vol. 13, no. 4, pp. 365–377, Jul. 2007.

[2] H. O. D. Critchley, J. A. Maybin, G. M. Armstrong, and A. R. W. Williams, "Physiology of the Endometrium and Regulation of Menstruation," *Physiol. Rev.*, vol. 100, no. 3, pp. 1149–1179, Jul. 2020.

[3] C. E. Gargett, K. E. Schwab, and J. A. Deane, "Endometrial stem/progenitor cells: the first 10 years," *Hum. Reprod. Update*, vol. 22, no. 2, p. dmv051, Nov. 2015.

[4] National Institute for Health and Care Excellence, "Fertility problems: assessment and treatment (Clinical Guideline 156)," 2017. [Online]. Available: https://www.nice.org.uk/guidance/cg156/chapter/Context. [Accessed: 22-Jun-2018].

[5] M. Brännström, P. Dahm Kähler, R. Greite, J. Mölne, C. Díaz-García, and S. G. Tullius, "Uterus Transplantation: A Rapidly Expanding Field.," *Transplantation*, vol. 102, no. 4, pp. 569–577, Apr. 2018.

[6] B. P. Jones *et al.*, "Uterine Transplantation in 2021: Recent Developments and the Future," *Clin. Obstet. Gynecol.*, vol. 65, no. 1, pp. 4–14, Mar. 2022.

[7] B. P. Jones *et al.*, "Endometrial autotransplantation in rabbits: Potential for fertility restoration in severe Asherman's syndrome.," *Eur. J. Obstet. Gynecol. Reprod. Biol.*, vol. 248, pp. 14–23, May 2020.

[8] R. Weiskirchen, S. Weiskirchen, and F. Tacke, "Organ and tissue fibrosis: Molecular signals, cellular mechanisms and translational implications," *Mol. Aspects Med.*, vol. 65, pp. 2–15, Feb. 2019.

[9] D. Yu, Y.-M. Wong, Y. Cheong, E. Xia, and T.-C. Li, "Asherman syndrome--one century later.," *Fertil. Steril.*, vol. 89, no. 4, pp. 759–79, Apr. 2008.

[10] J. G. Asherman, "Amenorrhoea Traumatica (Atretica)," *BJOG An Int. J. Obstet. Gynaecol.*, vol. 55, no. 1, pp. 23–30, Feb. 1948.

[11] S. Baradwan, A. Baradwan, M. Bashir, and D. Al-Jaroudi, "The birth weight in pregnant women with Asherman syndrome compared to normal intrauterine cavity," *Medicine (Baltimore).*, vol. 97, no. 32, p. e11797, Aug. 2018.

[12] E. J. Guo, J. P. W. Chung, L. C. Y. Poon, and T. C. Li, "Reproductive outcomes after surgical treatment of asherman syndrome: A systematic review.," *Best Pract. Res. Clin. Obstet. Gynaecol.*, vol. 59, pp. 98–114, Aug. 2019.

[13] J. G. Schenker and E. J. Margalioth, “Intrauterine adhesions: an updated appraisal,” 1982.

[14] X.-N. Lin *et al.*, “Randomized, controlled trial comparing the efficacy of intrauterine balloon and intrauterine contraceptive device in the prevention of adhesion reformation after hysteroscopic adhesiolysis,” *Fertil. Steril.*, vol. 104, no. 1, pp. 235–240, Jul. 2015.

[15] D. Yu, T.-C. Li, E. Xia, X. Huang, Y. Liu, and X. Peng, “Factors affecting reproductive outcome of hysteroscopic adhesiolysis for Asherman’s syndrome,” *Fertil. Steril.*, vol. 89, no. 3, pp. 715–722, Mar. 2008.

[16] L. Chen *et al.*, “Reproductive Outcomes in Patients With Intrauterine Adhesions Following Hysteroscopic Adhesiolysis: Experience From the Largest Women’s Hospital in China.,” *J. Minim. Invasive Gynecol.*, vol. 24, no. 2, pp. 299–304, Feb. 2017.

[17] A. B. Hooker, F. J. Mansvelder, R. G. Elbers, and Z. Frijmersum, “Reproductive outcomes in women with mild intrauterine adhesions; a systematic review and meta-analysis,” *J. Matern. Neonatal Med.*, pp. 1–9, May 2021.

[18] P. H. Kodaman and A. Arici, “Intra-uterine adhesions and fertility outcome: how to optimize success?,” *Curr. Opin. Obstet. Gynecol.*, vol. 19, no. 3, pp. 207–14, Jun. 2007.

[19] Y. Sonan, S. Aoki, K. Enomoto, K. Seki, and E. Miyagi, “Placenta Accreta following Hysteroscopic Lysis of Adhesions Caused by Asherman’s Syndrome: A Case Report and Literature Review,” *Case Rep. Obstet. Gynecol.*, vol. 2018, pp. 1–4, May 2018.

[20] E. Jauniaux *et al.*, “Placenta Praevia and Placenta Accreta: Diagnosis and Management,” *BJOG An Int. J. Obstet. Gynaecol.*, vol. 126, no. 1, pp. e1–e48, Jan. 2019.

[21] C. A. Salazar, K. Isaacson, and S. Morris, “A comprehensive review of Asherman’s syndrome: causes, symptoms and treatment options,” *Curr. Opin. Obstet. Gynecol.*, vol. 29, no. 4, pp. 249–256, Aug. 2017.

[22] M. M. F. Hanstede, E. van der Meij, L. Goedemans, and M. H. Emanuel, “Results of centralized Asherman surgery, 2003-2013.,” *Fertil. Steril.*, vol. 104, no. 6, pp. 1561–8.e1, Dec. 2015.

[23] A. B. Hooker *et al.*, “Systematic review and meta-analysis of intrauterine adhesions after miscarriage: prevalence, risk factors and long-term reproductive outcome,” *Hum. Reprod. Update*, vol. 20, no. 2, pp. 262–278, Mar. 2014.

[24] O. Bukulmez, H. Yarali, and T. Gurgan, “Total corporal synechiae due to tuberculosis carry a very poor prognosis following hysteroscopic synechialysis,” *Hum. Reprod.*, vol. 14, no. 8, pp. 1960–1961, Aug. 1999.

[25] M. J. Griffiths, A. L. Winship, and K. J. Hutt, “Do cancer therapies damage the uterus and compromise fertility?,” *Hum. Reprod. Update*, vol. 26, no. 2, pp. 161–173, 2020.

[26] X. Meng, D. J. Nikolic-Paterson, and H. Y. Lan, “TGF-β: the master regulator of fibrosis,” *Nat.*

Rev. Nephrol., vol. 12, no. 6, pp. 325–338, Jun. 2016.

[27] K. C. Flanders, "Smad3 as a mediator of the fibrotic response.," *Int. J. Exp. Pathol.*, vol. 85, no. 2, pp. 47–64, Apr. 2004.

[28] U. Salma *et al.*, "Role of Transforming Growth Factor- β 1 and Smads Signaling Pathway in Intrauterine Adhesion," *Mediators Inflamm.*, vol. 2016, pp. 1–13, 2016.

[29] X. Xue, Q. Chen, G. Zhao, J.-Y. Zhao, Z. Duan, and P.-S. Zheng, "The Overexpression of TGF-β and CCN2 in Intrauterine Adhesions Involves the NF-κB Signaling Pathway.," *PLoS One*, vol. 10, no. 12, p. e0146159, Dec. 2015.

[30] R. Manchanda *et al.*, "Classification systems of Asherman's syndrome. An old problem with new directions.," *Minim. Invasive Ther. Allied Technol.*, pp. 1–16, Mar. 2021.

[31] W.-L. Lee, C.-H. Liu, M. Cheng, W.-H. Chang, W.-M. Liu, and P.-H. Wang, "Focus on the Primary Prevention of Intrauterine Adhesions: Current Concept and Vision," *Int. J. Mol. Sci.*, vol. 22, no. 10, p. 5175, May 2021.

[32] J. Bosteels *et al.*, "Anti-adhesion therapy following operative hysteroscopy for treatment of female subfertility.," *Cochrane database Syst. Rev.*, vol. 11, p. CD011110, Nov. 2017.

[33] AAGL Elevating Gynecologic Surgery, "AAGL Practice Report: Practice Guidelines on Intrauterine Adhesions Developed in Collaboration With the European Society of Gynaecological Endoscopy (ESGE).," *J. Minim. Invasive Gynecol.*, vol. 24, no. 5, pp. 695–705, Jul. 2017.

[34] F. Zheng, B. Zhu, Y. Liu, R. Wang, and Y. Cui, "Meta-analysis of the use of amniotic membrane to prevent recurrence of intrauterine adhesion after hysteroscopic adhesiolysis," *Int. J. Gynecol. Obstet.*, vol. 143, no. 2, pp. 145–149, Nov. 2018.

[35] S. van Wessel *et al.*, "Anti-adhesion Gel versus No gel following Operative Hysteroscopy prior to Subsequent fertility Treatment or timed InterCourse (AGNOHSTIC), a randomised controlled trial: protocol," *Hum. Reprod. Open*, vol. 2021, no. 1, Jan. 2021.

[36] Z. Fei, Z. Bin, X. Xin, H. Fei, and C. Yuechong, "Meta-analysis on the use of hyaluronic acid gel to prevent recurrence of intrauterine adhesion after hysteroscopic adhesiolysis," *Taiwan. J. Obstet. Gynecol.*, vol. 58, no. 6, pp. 731–736, Nov. 2019.

[37] F. Zheng, X. Xin, F. He, J. Liu, and Y. Cui, "Meta-analysis on the use of hyaluronic acid gel to prevent intrauterine adhesion after intrauterine operations," *Exp. Ther. Med.*, Feb. 2020.

[38] A. B. Hooker, R. A. de Leeuw, J. W. R. Twisk, H. A. M. Brölmann, and J. A. F. Huirne, "Pregnancy and neonatal outcomes 42 months after application of hyaluronic acid gel following dilation and curettage for miscarriage in women who have experienced at least one previous curettage: follow-up of a randomized controlled trial," *Fertil. Steril.*, vol. 114, no. 3,

pp. 601–609, Sep. 2020.

[39] Y. Gao, G. Wu, Y. Xu, D. Zhao, and L. Zheng, “Stem Cell-Based Therapy for Asherman Syndrome: Promises and Challenges.,” *Cell Transplant.*, vol. 30, p. 9636897211020734, 2021.

[40] L. Ding *et al.*, “Transplantation of bone marrow mesenchymal stem cells on collagen scaffolds for the functional regeneration of injured rat uterus,” *Biomaterials*, vol. 35, no. 18, pp. 4888–4900, Jun. 2014.

[41] Y. Zhao *et al.*, “Clinical Efficacy and Safety of Stem Cell-Based Therapy in Treating Asherman Syndrome: A System Review and Meta-Analysis,” *Stem Cells Int.*, vol. 2020, 2020.

[42] C. E. Gargett and L. Ye, “Endometrial reconstruction from stem cells,” *Fertil. Steril.*, vol. 98, no. 1, pp. 11–20, Jul. 2012.

[43] A. N. Patel, E. Park, M. Kuzman, F. Benetti, F. J. Silva, and J. G. Allickson, “Multipotent Menstrual Blood Stromal Stem Cells: Isolation, Characterization, and Differentiation,” *Cell Transplant.*, vol. 17, no. 3, pp. 303–311, Mar. 2008.

[44] L. Bockeria *et al.*, “Endometrial regenerative cells for treatment of heart failure: a new stem cell enters the clinic,” *J. Transl. Med.*, vol. 11, no. 1, p. 56, Mar. 2013.

[45] S. Sharif *et al.*, “Collagen-coated nano-electrospun PCL seeded with human endometrial stem cells for skin tissue engineering applications,” *J. Biomed. Mater. Res. Part B Appl. Biomater.*, vol. 106, no. 4, pp. 1578–1586, May 2018.

[46] X. Wang, C. Wang, J. Cong, H. Bao, X. Liu, and C. Hao, “Regenerative Potential of Menstrual Blood-Derived Stem Cells and Platelet-Derived Growth Factor in Endometrial Injury.,” *Med. Sci. Monit.*, vol. 26, p. e919251, Feb. 2020.

[47] S. Zhang, P. Li, Z. Yuan, and J. Tan, “Platelet-rich plasma improves therapeutic effects of menstrual blood-derived stromal cells in rat model of intrauterine adhesion.,” *Stem Cell Res. Ther.*, vol. 10, no. 1, p. 61, 2019.

[48] H. Ma *et al.*, “Intrauterine transplantation of autologous menstrual blood stem cells increases endometrial thickness and pregnancy potential in patients with refractory intrauterine adhesion.,” *J. Obstet. Gynaecol. Res.*, Aug. 2020.

[49] Y. R. Ong *et al.*, “Bone Marrow Stem Cells Do Not Contribute to Endometrial Cell Lineages in Chimeric Mouse Models,” *Stem Cells*, vol. 36, no. 1, pp. 91–102, Jan. 2018.

[50] S. Dimmeler, S. Ding, T. A. Rando, and A. Trounson, “Translational strategies and challenges in regenerative medicine,” *Nat. Med.*, vol. 20, no. 8, pp. 814–821, Aug. 2014.

[51] B. Zhang, R. Yeo, K. Tan, and S. Lim, “Focus on Extracellular Vesicles: Therapeutic Potential of Stem Cell-Derived Extracellular Vesicles,” *Int. J. Mol. Sci.*, vol. 17, no. 2, p. 174, Feb. 2016.

[52] L. Miguel-Gómez *et al.*, “Stem cell paracrine actions in tissue regeneration and potential

therapeutic effect in human endometrium: a retrospective study," *BJOG An Int. J. Obstet. Gynaecol.*, vol. 127, no. 5, pp. 551–560, Apr. 2020.

[53] F. Liu *et al.*, "Hyaluronic Acid Hydrogel Integrated with Mesenchymal Stem Cell-Secretome to Treat Endometrial Injury in a Rat Model of Asherman's Syndrome," *Adv. Healthc. Mater.*, vol. 8, no. 14, p. 1900411, 2019.

[54] L. Xin *et al.*, "A scaffold laden with mesenchymal stem cell-derived exosomes for promoting endometrium regeneration and fertility restoration through macrophage immunomodulation.," *Acta Biomater.*, vol. 113, pp. 252–266, Sep. 2020.

[55] G. S. Saribas, C. Ozogul, M. Tiryaki, F. Alpaslan Pinarli, and S. Hamdemir Kilic, "Effects of uterus derived mesenchymal stem cells and their exosomes on asherman's syndrome.," *Acta Histochem.*, vol. 122, no. 1, p. 151465, Jan. 2020.

[56] B. Xiao, Y. Zhu, J. Huang, T. Wang, F. Wang, and S. Sun, "Exosomal transfer of bone marrow mesenchymal stem cell-derived miR-340 attenuates endometrial fibrosis.," *Biol. Open*, vol. 8, no. 5, p. bio039958, May 2019.

[57] H. Campo, I. Cervelló, and C. Simón, "Bioengineering the Uterus: An Overview of Recent Advances and Future Perspectives in Reproductive Medicine.," *Ann. Biomed. Eng.*, vol. 45, no. 7, pp. 1710–1717, Jul. 2017.

[58] R. C. Young and G. Goloman, "Allo- and Xeno-Reassembly of Human and Rat Myometrium from Cells and Scaffolds," *Tissue Eng. Part A*, vol. 19, no. 19–20, pp. 2112–2119, Oct. 2013.

[59] H. Campo, P. M. Baptista, N. López-Pérez, A. Faus, I. Cervelló, and C. Simón, "De- and recellularization of the pig uterus: a bioengineering pilot study.," *Biol. Reprod.*, vol. 96, no. 1, pp. 34–45, Dec. 2017.

[60] S. S. Daryabari *et al.*, "Development of an efficient perfusion-based protocol for whole-organ decellularization of the ovine uterus as a human-sized model and in vivo application of the bioscaffolds.," *J. Assist. Reprod. Genet.*, vol. 36, no. 6, pp. 1211–1223, Jun. 2019.

[61] T. T. Tiemann *et al.*, "Towards uterus tissue engineering: a comparative study of sheep uterus decellularisation," *Mol. Hum. Reprod.*, vol. 26, no. 3, pp. 167–178, Mar. 2020.

[62] M. Hellström *et al.*, "Bioengineered uterine tissue supports pregnancy in a rat model," *Fertil. Steril.*, vol. 106, no. 2, pp. 487-496.e1, Aug. 2016.

[63] K. Miyazaki and T. Maruyama, "Partial regeneration and reconstruction of the rat uterus through recellularization of a decellularized uterine matrix," *Biomaterials*, vol. 35, no. 31, pp. 8791–8800, Oct. 2014.

[64] T. Song *et al.*, "Regeneration of uterine horns in rats using collagen scaffolds loaded with human embryonic stem cell-derived endometrium-like cells," *Tissue Eng. Part A*, vol. 21, no.

1–2, pp. 353–61, Jan. 2015.

[65] L. Xin *et al.*, "A collagen scaffold loaded with human umbilical cord-derived mesenchymal stem cells facilitates endometrial regeneration and restores fertility," *Acta Biomater.*, vol. 92, pp. 160–171, Jul. 2019.

[66] B. Xiao *et al.*, "PGS Scaffolds Promote the In Vivo Survival and Directional Differentiation of Bone Marrow Mesenchymal Stem Cells Restoring the Morphology and Function of Wounded Rat Uterus," *Adv. Healthc. Mater.*, vol. 8, no. 5, p. 1801455, Mar. 2019.

[67] X. Han *et al.*, "Transplantation of Human Adipose Stem Cells Using Acellular Human Amniotic Membrane Improves Angiogenesis in Injured Endometrial Tissue in a Rat Intrauterine Adhesion Model.," *Cell Transplant.*, vol. 29, p. 963689720952055, 2020.

[68] Y. Liu, J. Cai, X. Luo, H. Wen, and Y. Luo, "Collagen Scaffold with Human Umbilical Cord Mesenchymal Stem Cells Remarkably Improves Intrauterine Adhesions in a Rat Model.," *Gynecol. Obstet. Invest.*, vol. 85, no. 3, pp. 267–276, 2020.

[69] W. Ji *et al.*, "3D Bioprinting a human iPSC-derived MSC-loaded scaffold for repair of the uterine endometrium.," *Acta Biomater.*, Sep. 2020.

[70] N. Lin *et al.*, "The effect of collagen-binding vascular endothelial growth factor on the remodeling of scarred rat uterus following full-thickness injury," *Biomaterials*, vol. 33, no. 6, pp. 1801–1807, Feb. 2012.

[71] X. X. Li *et al.*, "Regeneration of uterine horns in rats by collagen scaffolds loaded with collagen-binding human basic fibroblast growth factor," *Biomaterials*, vol. 32, no. 32, pp. 8172–8181, Nov. 2011.

[72] H.-L. Xu *et al.*, "Temperature-sensitive heparin-modified poloxamer hydrogel with affinity to KGF facilitate the morphologic and functional recovery of the injured rat uterus," *Drug Deliv.*, vol. 24, no. 1, pp. 867–881, Jan. 2017.

[73] H. Cai *et al.*, "Local Delivery of Silk-Cellulose Incorporated with Stromal Cell-Derived Factor-1α Functionally Improves the Uterus Repair.," *Tissue Eng. Part A*, vol. 25, no. 21–22, pp. 1514–1526, 2019.

[74] S.-S. Zhang *et al.*, "Three-dimensional structure micelles of heparin-poloxamer improve the therapeutic effect of 17β-estradiol on endometrial regeneration for intrauterine adhesions in a rat model," *Int. J. Nanomedicine*, vol. Volume 12, pp. 5643–5657, Aug. 2017.

[75] S.-S. Zhang *et al.*, "Using 17β-estradiol heparin-poloxamer thermosensitive hydrogel to enhance the endometrial regeneration and functional recovery of intrauterine adhesions in a rat model.," *FASEB J.*, vol. 34, no. 1, pp. 446–457, 2020.

[76] Q. Yao *et al.*, "Aloe/poloxamer hydrogel as an injectable β-estradiol delivery scaffold with

multi-therapeutic effects to promote endometrial regeneration for intrauterine adhesion treatment," vol. 148, p. 105316, May 2020.

[77] C. Frantz, K. M. Stewart, and V. M. Weaver, "The extracellular matrix at a glance.," *J. Cell Sci.*, vol. 123, no. Pt 24, pp. 4195–200, Dec. 2010.

[78] G. S. Hussey, T. J. Keane, and S. F. Badylak, "The extracellular matrix of the gastrointestinal tract: a regenerative medicine platform," *Nat. Rev. Gastroenterol. Hepatol.*, vol. 14, no. 9, pp. 540–552, Jul. 2017.

[79] R. Londono and S. F. Badylak, "Biologic Scaffolds for Regenerative Medicine: Mechanisms of In vivo Remodeling," *Ann. Biomed. Eng.*, vol. 43, no. 3, pp. 577–592, Mar. 2015.

[80] I. L. S. Chua, H.-W. Kim, and J. H. Lee, "Signaling of extracellular matrices for tissue regeneration and therapeutics.," *Tissue Eng. Regen. Med.*, vol. 13, no. 1, pp. 1–12, Feb. 2016.

[81] F. M. Watt and W. T. S. Huck, "Role of the extracellular matrix in regulating stem cell fate," *Nat. Rev. Mol. Cell Biol.*, vol. 14, no. 8, pp. 467–473, Aug. 2013.

[82] M. C. Cramer and S. F. Badylak, "Extracellular Matrix-Based Biomaterials and Their Influence Upon Cell Behavior," *Ann. Biomed. Eng.*, vol. 48, no. 7, pp. 2132–2153, Jul. 2020.

[83] I. T. Swinehart and S. F. Badylak, "Extracellular matrix bioscaffolds in tissue remodeling and morphogenesis.," *Dev. Dyn.*, vol. 245, no. 3, pp. 351–60, Mar. 2016.

[84] T. J. Keane, I. T. Swinehart, and S. F. Badylak, "Methods of tissue decellularization used for preparation of biologic scaffolds and in vivo relevance," *Methods*, vol. 84, pp. 25–34, Aug. 2015.

[85] T. J. Keane and S. F. Badylak, "The host response to allogeneic and xenogeneic biological scaffold materials.," *J. Tissue Eng. Regen. Med.*, vol. 9, no. 5, pp. 504–11, May 2015.

[86] W. Wang *et al.*, "Preparation and characterization of pro-angiogenic gel derived from small intestinal submucosa," *Acta Biomater.*, vol. 29, pp. 135–148, Jan. 2016.

[87] E. P. Brennan, J. Reing, D. Chew, J. M. Myers-Irvin, E. J. Young, and S. F. Badylak, "Antibacterial Activity within Degradation Products of Biological Scaffolds Composed of Extracellular Matrix," *Tissue Eng.*, vol. 12, no. 10, pp. 2949–2955, Oct. 2006.

[88] V. Agrawal *et al.*, "Epimorphic regeneration approach to tissue replacement in adult mammals," *Proc. Natl. Acad. Sci.*, vol. 107, no. 8, pp. 3351–3355, Feb. 2010.

[89] T. Zantop, T. W. Gilbert, M. C. Yoder, and S. F. Badylak, "Extracellular matrix scaffolds are repopulated by bone marrow-derived cells in a mouse model of achilles tendon reconstruction," *J. Orthop. Res.*, vol. 24, no. 6, pp. 1299–1309, Jun. 2006.

[90] M. M. Laronda, A. E. Jakus, K. A. Whelan, J. A. Wertheim, R. N. Shah, and T. K. Woodruff, "Initiation of puberty in mice following decellularized ovary transplant.," *Biomaterials*, vol.

50, pp. 20–9, May 2015.

[91] D. M. Faulk, J. D. Wildemann, and S. F. Badylak, “Decellularization and Cell Seeding of Whole Liver Biologic Scaffolds Composed of Extracellular Matrix,” *J. Clin. Exp. Hepatol.*, vol. 5, no. 1, pp. 69–80, Mar. 2015.

[92] H. Campo, X. Santamaria, I. Cervelló, and C. Simón, “Scaffolds for bioengineered uterus,” in *Handbook of Tissue Engineering Scaffolds: Volume Two*, Elsevier, 2019, pp. 283–316.

[93] S. F. Badylak, “Xenogeneic extracellular matrix as a scaffold for tissue reconstruction,” *Transpl. Immunol.*, vol. 12, no. 3–4, pp. 367–377, Apr. 2004.

[94] T. J. Keane *et al.*, “Tissue-Specific Effects of Esophageal Extracellular Matrix.,” *Tissue Eng. Part A*, vol. 21, no. 17–18, pp. 2293–300, Sep. 2015.

[95] B. Wang *et al.*, “Functional Maturation of Induced Pluripotent Stem Cell Hepatocytes in Extracellular Matrix-A Comparative Analysis of Bioartificial Liver Microenvironments.,” *Stem Cells Transl. Med.*, vol. 5, no. 9, pp. 1257–67, 2016.

[96] C. A. Batchelder, M. L. Martinez, and A. F. Tarantal, “Natural Scaffolds for Renal Differentiation of Human Embryonic Stem Cells for Kidney Tissue Engineering.,” *PLoS One*, vol. 10, no. 12, p. e0143849, 2015.

[97] T. Davidov, Y. Efraim, R. Hayam, J. Oieni, L. Baruch, and M. Machluf, “Extracellular Matrix Hydrogels Originated from Different Organs Mediate Tissue-Specific Properties and Function,” *Int. J. Mol. Sci.*, vol. 22, no. 21, p. 11624, Oct. 2021.

[98] S. B. Seif-Naraghi *et al.*, “Safety and Efficacy of an Injectable Extracellular Matrix Hydrogel for Treating Myocardial Infarction.”

[99] Y. Efraim *et al.*, “Biohybrid cardiac ECM-based hydrogels improve long term cardiac function post myocardial infarction,” *Acta Biomater.*, vol. 50, pp. 220–233, Mar. 2017.

[100] M. Okada, T. R. Payne, H. Oshima, N. Momoi, K. Tobita, and J. Huard, “Differential efficacy of gels derived from small intestinal submucosa as an injectable biomaterial for myocardial infarct repair,” *Biomaterials*, vol. 31, no. 30, pp. 7678–7683, Oct. 2010.

[101] H. D. Toeg *et al.*, “Injectable Small Intestine Submucosal Extracellular Matrix in an Acute Myocardial Infarction Model,” *Ann. Thorac. Surg.*, vol. 96, no. 5, pp. 1686–1694, Nov. 2013.

[102] M. T. Spang and K. L. Christman, “Extracellular matrix hydrogel therapies: In vivo applications and development,” *Acta Biomater.*, vol. 68, pp. 1–14, Mar. 2018.

[103] T. J. Keane *et al.*, “Restoring Mucosal Barrier Function and Modifying Macrophage Phenotype with an Extracellular Matrix Hydrogel: Potential Therapy for Ulcerative Colitis,” *J. Crohn’s Colitis*, vol. 11, no. 3, p. jjw149, Aug. 2016.

[104] S. López-Martínez *et al.*, “A Natural Xenogeneic Endometrial Extracellular Matrix Hydrogel

Toward Improving Current Human in vitro Models and Future in vivo Applications.," *Front. Bioeng. Biotechnol.*, vol. 9, p. 639688, 2021.

[105] E. Francés-Herrero *et al.*, "Improved Models of Human Endometrial Organoids Based on Hydrogels from Decellularized Endometrium," *J. Pers. Med.*, vol. 11, no. 6, p. 504, Jun. 2021.

[106] S. López-Martínez *et al.*, "Bioengineered endometrial hydrogels with growth factors promote tissue regeneration and restore fertility in murine models," *Acta Biomater.*, vol. 135, pp. 113–125, Nov. 2021.

[107] J. A. DeQuach *et al.*, "Simple and high yielding method for preparing tissue specific extracellular matrix coatings for cell culture.," *PLoS One*, vol. 5, no. 9, p. e13039, Sep. 2010.

[108] L. T. Saldin, M. C. Cramer, S. S. Velankar, L. J. White, and S. F. Badylak, "Extracellular matrix hydrogels from decellularized tissues: Structure and function," *Acta Biomater.*, vol. 49, pp. 1–15, Feb. 2017.

[109] S. Uriel *et al.*, "Extraction and Assembly of Tissue-Derived Gels for Cell Culture and Tissue Engineering," *Tissue Eng. Part C Methods*, vol. 15, no. 3, pp. 309–321, Sep. 2009.

[110] A. Shridhar, B. G. Amsden, E. R. Gillies, and L. E. Flynn, "Investigating the Effects of Tissue-Specific Extracellular Matrix on the Adipogenic and Osteogenic Differentiation of Human Adipose-Derived Stromal Cells Within Composite Hydrogel Scaffolds," *Front. Bioeng. Biotechnol.*, vol. 7, p. 402, Dec. 2019.

[111] T. L. Sellaro *et al.*, "Maintenance of human hepatocyte function in vitro by liver-derived extracellular matrix gels.," *Tissue Eng. Part A*, vol. 16, no. 3, pp. 1075–82, Mar. 2010.

[112] G. G. Giobbe *et al.*, "Extracellular matrix hydrogel derived from decellularized tissues enables endodermal organoid culture," *Nat. Commun.*, vol. 10, no. 1, p. 5658, Dec. 2019.

[113] L. Meran *et al.*, "Engineering transplantable jejunal mucosal grafts using primary patient-derived organoids from children with intestinal failure," *bioRxiv*, p. 854083, Nov. 2019.

[114] M. Saheli *et al.*, "Three-dimensional liver-derived extracellular matrix hydrogel promotes liver organoids function," *J. Cell. Biochem.*, vol. 119, no. 6, pp. 4320–4333, Jun. 2018.

[115] D. Choudhury, H. W. Tun, T. Wang, and M. W. Naing, "Organ-Derived Decellularized Extracellular Matrix: A Game Changer for Bioink Manufacturing?," *Trends Biotechnol.*, vol. 0, no. 0, Apr. 2018.

[116] M. J. Sawkins *et al.*, "Hydrogels derived from demineralized and decellularized bone extracellular matrix," *Acta Biomater.*, vol. 9, no. 8, pp. 7865–7873, Aug. 2013.

[117] S. Bartfeld and H. Clevers, "Stem cell-derived organoids and their application for medical research and patient treatment," *J. Mol. Med.*, vol. 95, no. 7, pp. 729–738, Jul. 2017.

[118] C. S. Hughes, L. M. Postovit, and G. A. Lajoie, "Matrigel: A complex protein mixture required

for optimal growth of cell culture," *Proteomics*, vol. 10, no. 9, pp. 1886–1890, Feb. 2010.

[119] J. H. Traverse *et al.*, "First-in-Man Study of a Cardiac Extracellular Matrix Hydrogel in Early and Late Myocardial Infarction Patients," *JACC Basic to Transl. Sci.*, vol. 4, no. 6, pp. 659–669, Oct. 2019.

[120] K. H. Hussein, K.-M. Park, L. Yu, H.-H. Kwak, and H.-M. Woo, "Decellularized hepatic extracellular matrix hydrogel attenuates hepatic stellate cell activation and liver fibrosis," *Mater. Sci. Eng. C. Mater. Biol. Appl.*, vol. 116, p. 111160, Nov. 2020.

[121] M. D. Diaz *et al.*, "Injectable Myocardial Matrix Hydrogel Mitigates Negative Left Ventricular Remodeling in a Chronic Myocardial Infarction Model," *JACC Basic to Transl. Sci.*, vol. 6, no. 4, pp. 350–361, Apr. 2021.

[122] J. Zhou, P. Wu, H. Sun, H. Zhou, Y. Zhang, and Z. Xiao, "Lung tissue extracellular matrix-derived hydrogels protect against radiation-induced lung injury by suppressing epithelial–mesenchymal transition," *J. Cell. Physiol.*, vol. 235, no. 3, pp. 2377–2388, Mar. 2020.

[123] S. B. Sonnenberg *et al.*, "Delivery of an engineered HGF fragment in an extracellular matrix-derived hydrogel prevents negative LV remodeling post-myocardial infarction.," *Biomaterials*, vol. 45, pp. 56–63, Mar. 2015.

[124] J.-S. Choi, S. Lee, D. Y. Kim, Y.-M. Kim, M. S. Kim, and J.-Y. Lim, "Functional remodeling after vocal fold injury by small intestinal submucosa gel containing hepatocyte growth factor," *Biomaterials*, vol. 40, pp. 98–106, Feb. 2015.

[125] J.-X. Ding, X.-J. Chen, X. -y. Zhang, Y. Zhang, and K.-Q. Hua, "Acellular porcine small intestinal submucosa graft for cervicovaginal reconstruction in eight patients with malformation of the uterine cervix," *Hum. Reprod.*, vol. 29, no. 4, pp. 677–682, Apr. 2014.

[126] J.-X. Ding, L. -m. Chen, X. -y. Zhang, Y. Zhang, and K.-Q. Hua, "Sexual and functional outcomes of vaginoplasty using acellular porcine small intestinal submucosa graft or laparoscopic peritoneal vaginoplasty: a comparative study," *Hum. Reprod.*, vol. 30, no. 3, pp. 581–589, Mar. 2015.

[127] F. Shen, X. Zhang, C. Yin, J. Ding, and K.-Q. Hua, "Comparison of small intestinal submucosa graft with split-thickness skin graft for cervicovaginal reconstruction of congenital vaginal and cervical aplasia," *Hum. Reprod.*, vol. 31, no. 11, pp. 2499–2505, Nov. 2016.

[128] J.-K. Zhang *et al.*, "A new material for tissue engineered vagina reconstruction: Acellular porcine vagina matrix," *J. Biomed. Mater. Res. Part A*, vol. 105, no. 7, pp. 1949–1959, Jul. 2017.

[129] D. Kong, L. Zhang, X. Xu, J. Zhang, Y. Li, and X. Huang, "Small Intestine Submucosa Is a Potential Material for Intrauterine Adhesions Treatment in a Rat Model.," *Gynecol. Obstet.*

Invest., no. 0, Jul. 2017.

[130] H. Zhang *et al.*, "Urinary bladder matrix scaffolds improve endometrial regeneration in a rat model of intrauterine adhesions," *Biomater. Sci.*, vol. 8, no. 3, pp. 988–996, Feb. 2020.

[131] J. Penders *et al.*, "Single Particle Automated Raman Trapping Analysis," *Nat. Commun.*, vol. 9, no. 1, p. 4256, Dec. 2018.

[132] P. M. Crapo, T. W. Gilbert, and S. F. Badylak, "An overview of tissue and whole organ decellularization processes.," *Biomaterials*, vol. 32, no. 12, pp. 3233–43, Apr. 2011.

[133] S. F. Badylak, G. C. Lantz, A. Coffey, and L. A. Geddes, "Small intestinal submucosa as a large diameter vascular graft in the dog.," *J. Surg. Res.*, vol. 47, no. 1, pp. 74–80, Jul. 1989.

[134] G. C. Lantz, S. F. Badylak, A. C. Coffey, L. A. Geddes, and W. E. Blevins, "Small intestinal submucosa as a small-diameter arterial graft in the dog.," *J. Invest. Surg.*, vol. 3, no. 3, pp. 217–27, 1990.

[135] J. L. Ungerleider *et al.*, "Extracellular Matrix Hydrogel Promotes Tissue Remodeling, Arteriogenesis, and Perfusion in a Rat Hindlimb Ischemia Model," *JACC Basic to Transl. Sci.*, vol. 1, no. 1–2, pp. 32–44, Jan. 2016.

[136] B. J. Larson, M. T. Longaker, and H. P. Lorenz, "Scarless fetal wound healing: a basic science review.," *Plast. Reconstr. Surg.*, vol. 126, no. 4, pp. 1172–80, Oct. 2010.

[137] L. H. Yagi, L. M. Watanuki, C. Isaac, R. Gemperli, Y. M. Nakamura, and P. R. S. Ladeira, "Human fetal wound healing: a review of molecular and cellular aspects," *Eur. J. Plast. Surg.*, vol. 39, no. 4, pp. 239–246, Aug. 2016.

[138] E. P. Brennan, X.-H. Tang, A. M. Stewart-Akers, L. J. Gudas, and S. F. Badylak, "Chemoattractant activity of degradation products of fetal and adult skin extracellular matrix for keratinocyte progenitor cells.," *J. Tissue Eng. Regen. Med.*, vol. 2, no. 8, pp. 491–8, Dec. 2008.

[139] D. Sood *et al.*, "Fetal brain extracellular matrix boosts neuronal network formation in 3D bioengineered model of cortical brain tissue.," *ACS Biomater. Sci. Eng.*, vol. 2, no. 1, pp. 131–140, 2016.

[140] S. Tottey *et al.*, "The effect of source animal age upon extracellular matrix scaffold properties," *Biomaterials*, vol. 32, no. 1, pp. 128–136, Jan. 2011.

[141] B. M. Sicari *et al.*, "The effect of source animal age upon the in vivo remodeling characteristics of an extracellular matrix scaffold.," *Biomaterials*, vol. 33, no. 22, pp. 5524–33, Aug. 2012.

[142] B. N. Brown, J. E. Valentin, A. M. Stewart-Akers, G. P. McCabe, and S. F. Badylak, "Macrophage phenotype and remodeling outcomes in response to biologic scaffolds with and

without a cellular component," *Biomaterials*, vol. 30, no. 8, Mar. 2009.

[143] J. Chakraborty, S. Roy, and S. Ghosh, "Biomaterials Science REVIEW Regulation of decellularized matrix mediated immune response," *Cite this Biomater. Sci*, vol. 8, p. 1194, 2020.

[144] S. D. Sackett *et al.*, "Extracellular matrix scaffold and hydrogel derived from decellularized and delipidized human pancreas," *Sci. Rep.*, vol. 8, no. 1, p. 10452, Dec. 2018.

[145] S. Funamoto *et al.*, "The use of high-hydrostatic pressure treatment to decellularize blood vessels," *Biomaterials*, vol. 31, no. 13, pp. 3590–3595, May 2010.

[146] M. Hellström *et al.*, "Towards the development of a bioengineered uterus: Comparison of different protocols for rat uterus decellularization," *Acta Biomater.*, vol. 10, no. 12, pp. 5034–5042, Dec. 2014.

[147] J. Zhou *et al.*, "Impact of heart valve decellularization on 3-D ultrastructure, immunogenicity and thrombogenicity," *Biomaterials*, vol. 31, no. 9, pp. 2549–2554, Mar. 2010.

[148] L. J. White *et al.*, "The impact of detergents on the tissue decellularization process: A ToF-SIMS study.," *Acta Biomater.*, vol. 50, pp. 207–219, 2017.

[149] J. Fernández-Pérez and M. Ahearne, "The impact of decellularization methods on extracellular matrix derived hydrogels," *Sci. Rep.*, vol. 9, no. 1, p. 14933, Dec. 2019.

[150] W. Weng *et al.*, "A simple method for decellularizing a cell-derived matrix for bone cell cultivation and differentiation," *J. Mater. Sci. Mater. Med.*, vol. 32, no. 9, p. 124, Sep. 2021.

[151] E. E. Friedrich *et al.*, "Residual sodium dodecyl sulfate in decellularized muscle matrices leads to fibroblast activation in vitro and foreign body response in vivo," *J. Tissue Eng. Regen. Med.*, vol. 12, no. 3, pp. e1704–e1715, Mar. 2018.

[152] D. M. Faulk *et al.*, "The effect of detergents on the basement membrane complex of a biologic scaffold material.," *Acta Biomater.*, vol. 10, no. 1, pp. 183–93, Jan. 2014.

[153] O. Syed, N. J. Walters, R. M. Day, H.-W. Kim, and J. C. Knowles, "Evaluation of decellularization protocols for production of tubular small intestine submucosa scaffolds for use in oesophageal tissue engineering," *Acta Biomater.*, vol. 10, no. 12, pp. 5043–5054, Dec. 2014.

[154] J. Hodde, A. Janis, D. Ernst, D. Zopf, D. Sherman, and C. Johnson, "Effects of sterilization on an extracellular matrix scaffold: Part I. Composition and matrix architecture," *J. Mater. Sci. Mater. Med.*, vol. 18, no. 4, pp. 537–543, 2007.

[155] S. R. Meyer, B. Chiu, T. A. Churchill, L. Zhu, J. R. T. Lakey, and D. B. Ross, "Comparison of aortic valve allograft decellularization techniques in the rat," *J. Biomed. Mater. Res. Part A*, vol. 79A, no. 2, pp. 254–262, Nov. 2006.

[156] M. Yang, C.-Z. Chen, X.-N. Wang, Y.-B. Zhu, and Y. J. Gu, “Favorable effects of the detergent and enzyme extraction method for preparing decellularized bovine pericardium scaffold for tissue engineered heart valves,” *J. Biomed. Mater. Res. Part B Appl. Biomater.*, vol. 91B, no. 1, pp. 354–361, Oct. 2009.

[157] EU, “REGULATION (EU) 2017/ 745 OF THE EUROPEAN PARLIAMENT AND OF THE COUNCIL - of 5 April 2017 - on medical devices, amending Directive 2001/ 83/ EC, Regulation (EC) No 178/ 2002 and Regulation (EC) No 1223/ 2009 and repealing Council Directives 90/ 385/ EEC a,” 2017.

[158] A. M. Matuska and P. S. McFetridge, “The effect of terminal sterilization on structural and biophysical properties of a decellularized collagen-based scaffold; implications for stem cell adhesion.,” *J. Biomed. Mater. Res. B. Appl. Biomater.*, vol. 103, no. 2, pp. 397–406, Feb. 2015.

[159] L. J. White *et al.*, “The impact of sterilization upon extracellular matrix hydrogel structure and function,” *J. Immunol. Regen. Med.*, vol. 2, pp. 11–20, Sep. 2018.

[160] P. Sarathchandra *et al.*, “Impact of γ-Irradiation on Extracellular Matrix of Porcine Pulmonary Valves,” *J. Surg. Res.*, vol. 176, no. 2, pp. 376–385, Aug. 2012.

[161] A. A. N. Bruyneel and C. A. Carr, “Ambiguity in the Presentation of Decellularized Tissue Composition: The Need for Standardized Approaches.,” *Artif. Organs*, vol. 41, no. 8, pp. 778–784, Aug. 2017.

[162] F. Naso, L. Iop, M. Spina, and & G. Gerosa, “Are FDA and CE sacrificing safety for a faster commercialization of xenogeneic tissue devices? Unavoidable need for legislation in decellularized tissue manufacturing,” 2014.

[163] T. J. Keane, R. Londono, N. J. Turner, and S. F. Badylak, “Consequences of ineffective decellularization of biologic scaffolds on the host response.,” *Biomaterials*, vol. 33, no. 6, pp. 1771–81, Feb. 2012.

[164] L. Huleihel *et al.*, “Matrix-bound nanovesicles within ECM bioscaffolds,” *Sci. Adv.*, vol. 2, no. 6, p. e1600502, Jun. 2016.

[165] E. G. Santoso *et al.*, “Application of detergents or high hydrostatic pressure as decellularization processes in uterine tissues and their subsequent effects on in vivo uterine regeneration in murine models,” *PLoS One*, vol. 9, no. 7, p. e103201, Jul. 2014.

[166] T. Hiraoka *et al.*, “STAT3 accelerates uterine epithelial regeneration in a mouse model of decellularized uterine matrix transplantation,” *JCI Insight*, vol. 1, no. 8, Jun. 2016.

[167] A. M. Padma, T. T. Tiemann, A. B. Alshaikh, R. Akouri, M. J. Song, and M. Hellström, *Protocols for Rat Uterus Isolation and Decellularization: Applications for Uterus Tissue Engineering and 3D Cell Culturing*, vol. 1577. 2018, pp. 161–175.

[168] X. Li *et al.*, "Reconstruction of functional uterine tissues through recellularizing the decellularized rat uterine scaffolds by MSCs in vivo and in vitro," *Biomed. Mater.*, vol. 16, no. 3, p. 035023, May 2021.

[169] H. Campo *et al.*, "Tissue-specific decellularized endometrial substratum mimicking different physiological conditions influences in vitro embryo development in a rabbit model," *Acta Biomater.*, vol. 89, pp. 126–138, Apr. 2019.

[170] E. Francés-Herrero *et al.*, "Development of Decellularized Oviductal Hydrogels as a Support for Rabbit Embryo Culture," *Reprod. Sci. 2021*, pp. 1–15, Jan. 2021.

[171] S. A. Olalekan, J. E. Burdette, S. Getsios, T. K. Woodruff, and J. J. Kim, "Development of a novel human recellularized endometrium that responds to a 28-day hormone treatment.," *Biol. Reprod.*, vol. 96, no. 5, pp. 971–981, May 2017.

[172] Z. Sargazi, S. Zavareh, M. Jafarabadi, and M. Salehnia, "An efficient protocol for decellularization of the human endometrial fragments for clinical usage.," *Prog. Biomater.*, vol. 10, no. 2, pp. 119–130, Jun. 2021.

[173] D. O. Freytes, J. Martin, S. S. Velankar, A. S. Lee, and S. F. Badylak, "Preparation and rheological characterization of a gel form of the porcine urinary bladder matrix," *Biomaterials*, vol. 29, no. 11, pp. 1630–1637, Apr. 2008.

[174] L. M. Doyle and M. Z. Wang, "Overview of Extracellular Vesicles, Their Origin, Composition, Purpose, and Methods for Exosome Isolation and Analysis.," *Cells*, vol. 8, no. 7, 2019.

[175] S. Keshtkar, N. Azarpira, and M. H. Ghahremani, "Mesenchymal stem cell-derived extracellular vesicles: novel frontiers in regenerative medicine," *Stem Cell Res. Ther.*, vol. 9, no. 1, p. 63, Dec. 2018.

[176] L. Huleihel *et al.*, "Matrix-Bound Nanovesicles Recapitulate Extracellular Matrix Effects on Macrophage Phenotype.," *Tissue Eng. Part A*, vol. 23, no. 21–22, pp. 1283–1294, 2017.

[177] L. M. Quijano *et al.*, "Matrix-Bound Nanovesicles: The Effects of Isolation Method upon Yield, Purity, and Function," *Tissue Eng. Part C Methods*, vol. 26, no. 10, pp. 528–540, Oct. 2020.

[178] G. S. Hussey *et al.*, "Lipidomics and RNA sequencing reveal a novel subpopulation of nanovesicle within extracellular matrix biomaterials," *Sci. Adv.*, vol. 6, no. 12, p. eaay4361, Mar. 2020.

[179] G. S. Hussey *et al.*, "Matrix bound nanovesicle-associated IL-33 activates a pro-remodeling macrophage phenotype via a non-canonical, ST2-independent pathway.," *J. Immunol. Regen. Med.*, vol. 3, pp. 26–35, Mar. 2019.

[180] Y. van der Merwe *et al.*, "Matrix-bound nanovesicles prevent ischemia-induced retinal ganglion cell axon degeneration and death and preserve visual function," *Sci. Rep.*, vol. 9, no.

1, p. 3482, Dec. 2019.

[181] K. Brennan *et al.*, "A comparison of methods for the isolation and separation of extracellular vesicles from protein and lipid particles in human serum," *Sci. Rep.*, vol. 10, no. 1, p. 1039, Dec. 2020.

[182] T. E. Whittaker, A. Nagelkerke, V. Nele, U. Kauscher, and M. M. Stevens, "Experimental artefacts can lead to misattribution of bioactivity from soluble mesenchymal stem cell paracrine factors to extracellular vesicles," *J. Extracell. Vesicles*, vol. 9, no. 1, p. 1807674, Sep. 2020.

[183] A. Gámez-Valero, M. Monguió-Tortajada, L. Carreras-Planella, M. Franquesa, K. Beyer, and F. E. Borràs, "Size-Exclusion Chromatography-based isolation minimally alters Extracellular Vesicles' characteristics compared to precipitating agents," *Sci. Rep.*, vol. 6, no. 1, p. 33641, Dec. 2016.

[184] R. C. Hill, E. A. Calle, M. Dzieciatkowska, L. E. Niklason, and K. C. Hansen, "Quantification of extracellular matrix proteins from a rat lung scaffold to provide a molecular readout for tissue engineering.," *Mol. Cell. Proteomics*, vol. 14, no. 4, pp. 961–73, Apr. 2015.

[185] A. S. Barrett *et al.*, "Hydroxylamine Chemical Digestion for Insoluble Extracellular Matrix Characterization," *J. Proteome Res.*, vol. 16, no. 11, pp. 4177–4184, Nov. 2017.

[186] S. Tyanova *et al.*, "The Perseus computational platform for comprehensive analysis of (prote)omics data," *Nat. Methods*, vol. 13, no. 9, pp. 731–740, Sep. 2016.

[187] D. W. Huang, B. T. Sherman, and R. A. Lempicki, "Systematic and integrative analysis of large gene lists using DAVID bioinformatics resources," *Nat. Protoc.*, vol. 4, no. 1, pp. 44–57, Jan. 2009.

[188] S. X. Ge, D. Jung, and R. Yao, "ShinyGO: a graphical gene-set enrichment tool for animals and plants," *Bioinformatics*, vol. 36, no. 8, pp. 2628–2629, Apr. 2020.

[189] M. M. Paulsson, M. E. Muller, and D. H. Edgar, "Critical Reviews in Biochemistry and Molecular Biology Basement Membrane Proteins: Structure, Assembly, and Cellular Interactions Basement Membrane Proteins: Structure, Assembly, and Cellular Interactions Mats Paulsson," *Crit. Rev. Biochem. Mol. Biol.*, vol. 27, no. 2, pp. 93–127, 1992.

[190] Z. Movasaghi, S. Rehman, and I. U. Rehman, "Raman Spectroscopy of Biological Tissues," *Appl. Spectrosc. Rev.*, vol. 42, no. 5, pp. 493–541, Sep. 2007.

[191] TA Instruments, "Understanding Rheology of Structured Fluids."

[192] G. Stojkov, Z. Niyazov, F. Picchioni, and R. K. Bose, "Relationship between Structure and Rheology of Hydrogels for Various Applications.," *Gels (Basel, Switzerland)*, vol. 7, no. 4, Dec. 2021.

[193] S. Nara, S. Chameettachal, S. Midha, S. Murab, and S. Ghosh, “Preservation of biomacromolecular composition and ultrastructure of a decellularized cornea using a perfusion bioreactor,” *RSC Adv.*, vol. 6, no. 3, pp. 2225–2240, Jan. 2016.

[194] N. Arezoo, H. Mohammad, and M. Malihezaman, “Tissue engineering of mouse uterus using menstrual blood stem cells (MenSCs) and decellularized uterine scaffold,” *Stem Cell Res. Ther.*, vol. 12, no. 1, p. 475, Dec. 2021.

[195] Q. Li *et al.*, “Proteomic analysis of naturally-sourced biological scaffolds.,” *Biomaterials*, vol. 75, pp. 37–46, Jan. 2016.

[196] N. F. Henning, R. D. LeDuc, K. A. Even, and M. M. Laronda, “Proteomic analyses of decellularized porcine ovaries identified new matrisome proteins and spatial differences across and within ovarian compartments,” *Sci. Rep.*, vol. 9, no. 1, p. 20001, Dec. 2019.

[197] C. S and B. DE, “The regulatory roles of small leucine-rich proteoglycans in extracellular matrix assembly,” *FEBS J.*, vol. 280, no. 10, 2013.

[198] A. Lucariello, E. Trabucco, O. Boccia, A. Perna, C. S. vivo, and undefined 2015, “Small leucine rich proteoglycans are differently distributed in normal and pathological endometrium,” *In Vivo (Brooklyn).*, vol. 29, no. 2, pp. 217–222, Mar. 2015.

[199] R. M. Salgado, R. R. Favaro, and T. M. T. Zorn, “Modulation of small leucine-rich proteoglycans (SLRPs) expression in the mouse uterus by estradiol and progesterone.,” *Reprod. Biol. Endocrinol.*, vol. 9, p. 22, Feb. 2011.

[200] M. C. Mccabe *et al.*, “Evaluation and Refinement of Sample Preparation Methods for Extracellular Matrix Proteome Coverage TECHNOLOGICAL INNOVATION AND RESOURCES,” *Mol Cell Proteomics*, vol. 20, p. 100079, 2021.

[201] J. Penders *et al.*, “Single Particle Automated Raman Trapping Analysis of Breast Cancer Cell-Derived Extracellular Vesicles as Cancer Biomarkers,” *ACS Nano*, vol. 15, no. 11, pp. 18192–18205, Nov. 2021.

[202] E. Jabbari, J. Leijten, Q. Xu, and A. Khademhosseini, “The matrix reloaded: the evolution of regenerative hydrogels,” *Mater. Today*, vol. 19, no. 4, pp. 190–196, May 2016.

[203] H. C. Fitzgerald, D. J. Schust, and T. E. Spencer, “In vitro models of the human endometrium: evolution and application for women’s health+,” *Biol. Reprod.*, vol. 104, no. 2, pp. 282–293, Feb. 2021.

[204] T. M. Rawlings, K. Makwana, M. Tryfonos, and E. S. Lucas, “Organoids to model the endometrium: implantation and beyond,” *Reprod. Fertil.*, vol. 2, no. 3, pp. R85–R101, Sep. 2021.

[205] M. Y. Turco *et al.*, “Long-term, hormone-responsive organoid cultures of human

endometrium in a chemically defined medium," *Nat. Cell Biol.*, vol. 19, no. 5, pp. 568–577, Apr. 2017.

[206] M. Boretto *et al.*, "Development of organoids from mouse and human endometrium showing endometrial epithelium physiology and long-term expandability," *Development*, vol. 144, no. 10, pp. 1775 LP – 1786, May 2017.

[207] J. T. Arnold, D. G. Kaufman, M. Seppälä, and B. A. Lessey, "Endometrial stromal cells regulate epithelial cell growth in vitro: a new co-culture model," *Hum. Reprod.*, vol. 16, no. 5, pp. 836–845, May 2001.

[208] J. T. Arnold, B. A. Lessey, M. Seppälä, and D. G. Kaufman, "Effect of Normal Endometrial Stroma on Growth and Differentiation in Ishikawa Endometrial Adenocarcinoma Cells 1," 2002.

[209] U. Bentin-Ley, B. Pedersen, S. Lindenberg, J. F. Larsen, L. Hamberger, and T. Horn, "Isolation and culture of human endometrial cells in a three-dimensional culture system," *Reproduction*, vol. 101, no. 2, pp. 327–332, Jul. 1994.

[210] H. Wang *et al.*, "A novel model of human implantation: 3D endometrium-like culture system to study attachment of human trophoblast (Jar) cell spheroids," *Mol. Hum. Reprod.*, vol. 18, no. 1, pp. 33–43, Jan. 2012.

[211] E. Pierro *et al.*, "Stromal-epithelial interactions modulate estrogen responsiveness in normal human endometrium.," *Biol. Reprod.*, vol. 64, no. 3, pp. 831–8, Mar. 2001.

[212] C. A. Rinehart, B. D. Lyn-Cook, and D. G. Kaufman, "Gland formation from human endometrial epithelial cells in vitro.," *In Vitro Cell. Dev. Biol.*, vol. 24, no. 10, pp. 1037–41, Oct. 1988.

[213] G. Burton, M. Turco, L. Gardner, B.-K. Koo, A. Moffett, and G. Burton, "Derivation and long-term expansion of human endometrial and decidual organoids.," *Protoc. Exch.*, Apr. 2017.

[214] H. C. Fitzgerald, P. Dhakal, S. K. Behura, D. J. Schust, and T. E. Spencer, "Self-renewing endometrial epithelial organoids of the human uterus.," *Proc. Natl. Acad. Sci. U. S. A.*, vol. 116, no. 46, pp. 23132–23142, 2019.

[215] T. M. Rawlings *et al.*, "Modelling the impact of decidual senescence on embryo implantation in human endometrial assembloids," *bioRxiv*, p. 2021.03.02.433560, Jan. 2021.

[216] M. Boretto *et al.*, "Patient-derived organoids from endometrial disease capture clinical heterogeneity and are amenable to drug screening.," *Nat. Cell Biol.*, vol. 21, no. 8, pp. 1041–1051, 2019.

[217] T. A. Wynn and T. R. Ramalingam, "Mechanisms of fibrosis: therapeutic translation for fibrotic disease," *Nat. Med.*, vol. 18, p. 1028, Jul. 2012.

[218] J. Li *et al.*, "MicroRNA-29b Inhibits Endometrial Fibrosis by Regulating the Sp1-TGF-β1/Smad-

CTGF Axis in a Rat Model," *Reprod. Sci.*, vol. 23, no. 3, pp. 386–394, Mar. 2016.

[219] S. Liu, X. Huang, Y. Liu, D. Song, and Y. Xiao, "Functional analysis of miRNAs combined with TGF-β1/Smad3 inhibitor in an intrauterine rat adhesion cell model," *Mol. Cell. Biochem.*, vol. 470, no. 1–2, pp. 15–28, Jul. 2020.

[220] M. Song *et al.*, "HMGA2-induced epithelial-mesenchymal transition is reversed by let-7d in intrauterine adhesions.," *Mol. Hum. Reprod.*, vol. 27, no. 2, 2021.

[221] N. Frangogiannis, "Transforming growth factor-β in tissue fibrosis.," *J. Exp. Med.*, vol. 217, no. 3, p. e20190103, 2020.

[222] G. Jenkins, "The role of proteases in transforming growth factor-β activation," *Int. J. Biochem. Cell Biol.*, vol. 40, no. 6–7, pp. 1068–1078, Jun. 2008.

[223] B. Hinz, "The extracellular matrix and transforming growth factor-β1: Tale of a strained relationship.," *Matrix Biol.*, vol. 47, pp. 54–65, Sep. 2015.

[224] I. B. Robertson and D. B. Rifkin, "Regulation of the Bioavailability of TGF-β and TGF-β-Related Proteins.," *Cold Spring Harb. Perspect. Biol.*, vol. 8, no. 6, 2016.

[225] J. S. Duffield, M. Lupher, V. J. Thannickal, and T. A. Wynn, "Host responses in tissue repair and fibrosis.," *Annu. Rev. Pathol.*, vol. 8, pp. 241–76, Jan. 2013.

[226] J. Di Gregorio *et al.*, "The Epithelial-to-Mesenchymal Transition as a Possible Therapeutic Target in Fibrotic Disorders," *Front. Cell Dev. Biol.*, vol. 8, p. 1591, Dec. 2020.

[227] L. A. van Meeteren and P. ten Dijke, "Regulation of endothelial cell plasticity by TGF-β.," *Cell Tissue Res.*, vol. 347, no. 1, pp. 177–86, Jan. 2012.

[228] C. Zhang *et al.*, "YY1 mediates TGF-β1-induced EMT and pro-fibrogenesis in alveolar epithelial cells," *Respir. Res.*, vol. 20, no. 1, p. 249, Dec. 2019.

[229] R. A. Evans, Y. C. Tian, R. Steadman, and A. O. Phillips, "TGF-beta1-mediated fibroblast-myofibroblast terminal differentiation-the role of Smad proteins.," *Exp. Cell Res.*, vol. 282, no. 2, pp. 90–100, Jan. 2003.

[230] C. Z. C. Chen *et al.*, "The Scar-in-a-Jar: studying potential antifibrotic compounds from the epigenetic to extracellular level in a single well.," *Br. J. Pharmacol.*, vol. 158, no. 5, pp. 1196–209, Nov. 2009.

[231] R. B. Good *et al.*, "A high content, phenotypic 'scar-in-a-jar' assay for rapid quantification of collagen fibrillogenesis using disease-derived pulmonary fibroblasts," *BMC Biomed. Eng.*, vol. 1, no. 1, p. 14, Dec. 2019.

[232] S. R. Rønnow *et al.*, "Prolonged Scar-in-a-Jar: an in vitro screening tool for anti-fibrotic therapies using biomarkers of extracellular matrix synthesis," *Respir. Res.*, vol. 21, no. 1, p. 108, Dec. 2020.

[233] Y. Yao, R. Chen, G. Wang, Y. Zhang, and F. Liu, “Exosomes derived from mesenchymal stem cells reverse EMT via TGF-β1/Smad pathway and promote repair of damaged endometrium,” *Stem Cell Res. Ther.*, vol. 10, no. 1, p. 225, Dec. 2019.

[234] L.-P. Guo, L.-M. Chen, F. Chen, N.-H. Jiang, and L. Sui, “Smad signaling coincides with epithelial-mesenchymal transition in a rat model of intrauterine adhesion.,” *Am. J. Transl. Res.*, vol. 11, no. 8, pp. 4726–4737, 2019.

[235] J. Li, B. Cen, S. Chen, and Y. He, “MicroRNA-29b inhibits TGF-β1-induced fibrosis via regulation of the TGF-β1/Smad pathway in primary human endometrial stromal cells.,” *Mol. Med. Rep.*, vol. 13, no. 5, pp. 4229–37, May 2016.

[236] Q. Yao, Y.-W. Zheng, Q.-H. Lan, L. Kou, H.-L. Xu, and Y.-Z. Zhao, “Recent development and biomedical applications of decellularized extracellular matrix biomaterials,” *Mater. Sci. Eng. C*, vol. 104, p. 109942, Nov. 2019.

[237] T. A. Wynn and L. Barron, “Macrophages: master regulators of inflammation and fibrosis.,” *Semin. Liver Dis.*, vol. 30, no. 3, pp. 245–57, Aug. 2010.

[238] K. L. Spiller and T. J. Koh, “Macrophage-based therapeutic strategies in regenerative medicine,” *Adv. Drug Deliv. Rev.*, vol. 122, pp. 74–83, Dec. 2017.

[239] T. T. Braga, J. S. H. Agudelo, and N. O. S. Camara, “Macrophages During the Fibrotic Process: M2 as Friend and Foe.,” *Front. Immunol.*, vol. 6, p. 602, 2015.

[240] P. Krzyszczyk, R. Schloss, A. Palmer, and F. Berthiaume, “The Role of Macrophages in Acute and Chronic Wound Healing and Interventions to Promote Pro-wound Healing Phenotypes.,” *Front. Physiol.*, vol. 9, p. 419, 2018.

[241] A. Sindrilaru *et al.*, “An unrestrained proinflammatory M1 macrophage population induced by iron impairs wound healing in humans and mice.,” *J. Clin. Invest.*, vol. 121, no. 3, pp. 985–97, Mar. 2011.

[242] D. T. Ploeger, N. A. Hosper, M. Schipper, J. A. Koerts, S. de Rond, and R. A. Bank, “Cell plasticity in wound healing: paracrine factors of M1/ M2 polarized macrophages influence the phenotypical state of dermal fibroblasts,” *Cell Commun. Signal.*, vol. 11, no. 1, p. 29, Apr. 2013.

[243] K. A. Jablonski *et al.*, “Novel Markers to Delineate Murine M1 and M2 Macrophages,” *PLoS One*, vol. 10, no. 12, p. e0145342, Dec. 2015.

[244] R. D. Stout, C. Jiang, B. Matta, I. Tietzel, S. K. Watkins, and J. Suttles, “Macrophages sequentially change their functional phenotype in response to changes in microenvironmental influences.,” *J. Immunol.*, vol. 175, no. 1, pp. 342–9, Jul. 2005.

[245] S. F. Badylak, J. E. Valentin, A. K. Ravindra, G. P. McCabe, and A. M. Stewart-Akers,

"Macrophage Phenotype as a Determinant of Biologic Scaffold Remodeling," *Tissue Eng. Part A*, vol. 14, no. 11, pp. 1835–1842, Nov. 2008.

[246] B. N. Brown *et al.*, "Macrophage phenotype as a predictor of constructive remodeling following the implantation of biologically derived surgical mesh materials," *Acta Biomater.*, vol. 8, no. 3, pp. 978–987, Mar. 2012.

[247] B. M. Sicari, J. L. Dziki, B. F. Siu, C. J. Medberry, C. L. Dearth, and S. F. Badylak, "The promotion of a constructive macrophage phenotype by solubilized extracellular matrix.," *Biomaterials*, vol. 35, no. 30, pp. 8605–12, Oct. 2014.

[248] D. M. Faulk *et al.*, "ECM hydrogel coating mitigates the chronic inflammatory response to polypropylene mesh," *Biomaterials*, vol. 35, no. 30, pp. 8585–8595, Oct. 2014.

[249] J. L. Dziki, D. S. Wang, C. Pineda, B. M. Sicari, T. Rausch, and S. F. Badylak, "Solubilized extracellular matrix bioscaffolds derived from diverse source tissues differentially influence macrophage phenotype," *J. Biomed. Mater. Res. Part A*, vol. 105, no. 1, pp. 138–147, Jan. 2017.

[250] A. Mantovani, A. Sica, S. Sozzani, P. Allavena, A. Vecchi, and M. Locati, "The chemokine system in diverse forms of macrophage activation and polarization," *Trends Immunol.*, vol. 25, no. 12, pp. 677–686, Dec. 2004.

[251] A. Mantovani, S. Sozzani, M. Locati, P. Allavena, and A. Sica, "Macrophage polarization: tumor-associated macrophages as a paradigm for polarized M2 mononuclear phagocytes.," *Trends Immunol.*, vol. 23, no. 11, pp. 549–55, Nov. 2002.

[252] Y. Lin, J. Xu, and H. Lan, "Tumor-associated macrophages in tumor metastasis: biological roles and clinical therapeutic applications," *J. Hematol. Oncol.*, vol. 12, no. 1, p. 76, Dec. 2019.

[253] J. P. Hodde, M. A. Suckow, W. R. Wolter, and M. C. Hiles, "Small intestinal submucosa does not promote PAIII tumor growth in Lobund-Wistar rats.," *J. Surg. Res.*, vol. 120, no. 2, pp. 189–94, Aug. 2004.

[254] S. F. Badylak, T. Hoppo, A. Nieponice, T. W. Gilbert, J. M. Davison, and B. A. Jobe, "Esophageal preservation in five male patients after endoscopic inner-layer circumferential resection in the setting of superficial cancer: a regenerative medicine approach with a biologic scaffold.," *Tissue Eng. Part A*, vol. 17, no. 11–12, pp. 1643–50, Jun. 2011.

[255] M. T. Wolf *et al.*, "A biologic scaffold-associated type 2 immune microenvironment inhibits tumor formation and synergizes with checkpoint immunotherapy.," *Sci. Transl. Med.*, vol. 11, no. 477, Jan. 2019.

[256] J.-H. Lee, P. Parthiban, G.-Z. Jin, J. C. Knowles, and H.-W. Kim, "Materials roles for promoting angiogenesis in tissue regeneration," *Prog. Mater. Sci.*, vol. 117, p. 100732, Apr. 2021.

[257] J. P. Hodde, R. D. Record, H. A. Liang, and S. F. Badylak, “Vascular Endothelial Growth Factor in Porcine-Derived Extracellular Matrix,” *Endothelium*, vol. 8, no. 1, pp. 11–24, Jan. 2001.

[258] D. M. Hoganson *et al.*, “Preserved extracellular matrix components and retained biological activity in decellularized porcine mesothelium,” *Biomaterials*, vol. 31, no. 27, pp. 6934–6940, Sep. 2010.

[259] J. A. DeQuach *et al.*, “Injectable skeletal muscle matrix hydrogel promotes neovascularization and muscle cell infiltration in a hindlimb ischemia model.,” *Eur. Cell. Mater.*, vol. 23, pp. 400–12; discussion 412, Jun. 2012.

[260] K. De Clercq, A. Hennes, and J. Vriens, “Isolation of Mouse Endometrial Epithelial and Stromal Cells for In Vitro Decidualization.,” *J. Vis. Exp.*, no. 121, Mar. 2017.

[261] R. Kaukonen, G. Jacquemet, H. Hamidi, and J. Ivaska, “Cell-derived matrices for studying cell proliferation and directional migration in a complex 3D microenvironment,” *Nat. Protoc.*, vol. 12, no. 11, pp. 2376–2390, Nov. 2017.

[262] G. Carpentier *et al.*, “Angiogenesis Analyzer for ImageJ — A comparative morphometric analysis of ‘Endothelial Tube Formation Assay’ and ‘Fibrin Bead Assay,’” *Sci. Rep.*, vol. 10, no. 1, p. 11568, Dec. 2020.

[263] T. D. Clemons *et al.*, “Coherency image analysis to quantify collagen architecture: implications in scar assessment,” *RSC Adv.*, vol. 8, no. 18, pp. 9661–9669, Mar. 2018.

[264] S. Schlie-Wolter, A. Ngezahayo, and B. N. Chichkov, “The selective role of ECM components on cell adhesion, morphology, proliferation and communication in vitro,” *Exp. Cell Res.*, vol. 319, no. 10, pp. 1553–1561, Jun. 2013.

[265] A. M. Sharkey *et al.*, “Vascular Endothelial Growth Factor Expression in Human Endometrium Is Regulated by Hypoxia [1],” *J. Clin. Endocrinol. Metab.*, vol. 85, no. 1, pp. 402–409, Jan. 2000.

[266] Y. Kawano, S. Nakamura, K. Nasu, H. Narahara, and I. Miyakawa, “The effect of epidermal growth factor on vascular endothelial growth factor secretion by endometrial stromal cells,” *Clin. Exp. Med.*, vol. 2, no. 2, pp. 69–75, Jul. 2002.

[267] F. L. Cousins, R. Pandoy, S. Jin, and C. E. Gargett, “The Elusive Endometrial Epithelial Stem/Progenitor Cells,” *Front. Cell Dev. Biol.*, vol. 9, p. 868, Apr. 2021.

[268] L. Hemeryck *et al.*, “Organoids from human tooth showing epithelial stemness phenotype and differentiation potential,” *Cell. Mol. Life Sci.*, vol. 79, no. 3, p. 153, Mar. 2022.

[269] S. Hahn *et al.*, “Organoid-based epithelial to mesenchymal transition (OEMT) model: from an intestinal fibrosis perspective.,” *Sci. Rep.*, vol. 7, no. 1, p. 2435, 2017.

[270] H. Q. Estrada, S. Patel, S. Rabizadeh, D. Casero, S. R. Targan, and R. J. Barrett, “Development of a Personalized Intestinal Fibrosis Model Using Human Intestinal Organoids Derived From

Induced Pluripotent Stem Cells," *Inflamm. Bowel Dis.*, vol. 28, no. 5, pp. 667–679, May 2022.

[271] P. P. M. van Zuijlen *et al.*, "Collagen morphology in human skin and scar tissue: no adaptations in response to mechanical loading at joints.," *Burns*, vol. 29, no. 5, pp. 423–31, Aug. 2003.

[272] K. P. Quinn *et al.*, "Optical metrics of the extracellular matrix predict compositional and mechanical changes after myocardial infarction," *Sci. Rep.*, vol. 6, no. 1, p. 35823, Dec. 2016.

[273] S. E. Brashear, R. P. Wohlgemuth, G. Gonzalez, and L. R. Smith, "Passive stiffness of fibrotic skeletal muscle in *mdx* mice relates to collagen architecture," *J. Physiol.*, vol. 599, no. 3, pp. 943–962, Feb. 2021.

[274] C. E. Witherel *et al.*, "Regulation of extracellular matrix assembly and structure by hybrid M1/M2 macrophages," *Biomaterials*, vol. 269, p. 120667, Feb. 2021.

[275] K. C. El Kasmi *et al.*, "Toll-like receptor–induced arginase 1 in macrophages thwarts effective immunity against intracellular pathogens," *Nat. Immunol.*, vol. 9, no. 12, pp. 1399–1406, Dec. 2008.

[276] L. Huleihel *et al.*, "Macrophage phenotype in response to ECM bioscaffolds.," *Semin. Immunol.*, vol. 29, pp. 2–13, Feb. 2017.

[277] M. Orecchioni, Y. Ghosheh, A. B. Pramod, and K. Ley, "Macrophage Polarization: Different Gene Signatures in M1(LPS+) vs. Classically and M2(LPS–) vs. Alternatively Activated Macrophages," *Front. Immunol.*, vol. 10, p. 1084, May 2019.

[278] K. L. Boyd, A. Muehlenbachs, M. H. Rendi, R. L. Garcia, and K. N. Gibson-Corley, "Female Reproductive System," *Comp. Anat. Histol.*, pp. 303–334, Jan. 2018.

[279] A. F. Ajayi and R. E. Akhigbe, "Staging of the estrous cycle and induction of estrus in experimental rodents: an update," *Fertil. Res. Pract.*, vol. 6, no. 1, p. 5, Dec. 2020.

[280] K. Bertolin and B. D. Murphy, "Reproductive Tract Changes During the Mouse Estrous Cycle," *Guid. to Investig. Mouse Pregnancy*, pp. 85–94, Jan. 2014.

[281] S. Zhang *et al.*, "Construction and Optimization of an Endometrial Injury Model in Mice by Transcervical Ethanol Perfusion," *Reprod. Sci.*, vol. 28, no. 3, 2020.

[282] C. Wei *et al.*, "Overactivated sonic hedgehog signaling aggravates intrauterine adhesion via inhibiting autophagy in endometrial stromal cells," *Cell Death Dis.*, vol. 11, no. 9, p. 755, Sep. 2020.

[283] Y. Zhang *et al.*, "Endometrial stem cells repair injured endometrium and induce angiogenesis via AKT and ERK pathways.," *Reproduction*, vol. 152, no. 5, pp. 389–402, 2016.

[284] S. Kilic, B. Yuksel, F. Pinarli, A. Albayrak, B. Boztok, and T. Delibasi, "Effect of stem cell application on Asherman syndrome, an experimental rat model.," *J. Assist. Reprod. Genet.*,

vol. 31, no. 8, pp. 975–82, Aug. 2014.

[285] D. Sabry *et al.*, "An experimental model: intrauterine adhesion versus subendometrial fibrosis," *Biomed. Res.*, vol. 29, no. 17, 2018.

[286] I. Cervelló *et al.*, "Human CD133+ bone marrow-derived stem cells promote endometrial proliferation in a murine model of Asherman syndrome," *Fertil. Steril.*, vol. 104, no. 6, pp. 1552-1560.e3, Dec. 2015.

[287] Jim Yeadon, "6 steps for setting up timed pregnant mice," *The Jackson Laboratory Blog post*, 2014. [Online]. Available: https://www.jax.org/news-and-insights/jax-blog/2014/september/six-steps-for-setting-up-timed-pregnant-mice. [Accessed: 28-May-2022].

[288] Y. Y. Kim *et al.*, "Synergistic regenerative effects of functionalized endometrial stromal cells with hyaluronic acid hydrogel in a murine model of uterine damage," *Acta Biomater.*, vol. 89, pp. 139–151, Apr. 2019.

[289] Q. Xu *et al.*, "MicroRNA-1291 promotes endometrial fibrosis by regulating the ArhGAP29-RhoA/ROCK1 signaling pathway in a murine model.," *Mol. Med. Rep.*, vol. 16, no. 4, pp. 4501–4510, Oct. 2017.

[290] M. Park *et al.*, "Perivascular Stem Cell-Derived Cyclophilin A Improves Uterine Environment with Asherman's Syndrome via HIF1α-Dependent Angiogenesis," *Mol. Ther.*, vol. 28, no. 8, pp. 1818–1832, Aug. 2020.

[291] J. X. Chen, X. J. Yi, P. L. Gu, and S. X. Gao, "The role of KDR in intrauterine adhesions may involve the TGF-β1/Smads signaling pathway," vol. 52, no. 10, p. e8324, 2019.

[292] F. Alawadhi, H. Du, H. Cakmak, and H. S. Taylor, "Bone Marrow-Derived Stem Cell (BMDSC) transplantation improves fertility in a murine model of Asherman's syndrome.," *PLoS One*, vol. 9, no. 5, p. e96662, May 2014.

[293] H. J *et al.*, "The expression of marker for endometrial stem cell and fibrosis was increased in intrauterine adhesious.," vol. 8, no. 2, Feb. 2015.

[294] B. Li, Q. Zhang, J. Sun, and D. Lai, "Human amniotic epithelial cells improve fertility in an intrauterine adhesion mouse model.," *Stem Cell Res. Ther.*, vol. 10, no. 1, p. 257, 2019.

[295] Y. Zhu, J. Hu, T. Yu, Y. Ren, and L. Hu, "High Molecular Weight Hyaluronic Acid Inhibits Fibrosis of Endometrium.," *Med. Sci. Monit.*, vol. 22, pp. 3438–3445, Sep. 2016.

[296] X.-L. Ma *et al.*, "The glucagon-like peptide-1 (GLP-1) analog exenatide ameliorates intrauterine adhesions in mice.," *Peptides*, vol. 137, p. 170481, Mar. 2021.

[297] Z. Jing, Y. Yi, H. Xi, L.-Q. Sun, and L. Yanping, "Therapeutic Effects of VEGF Gene-Transfected BMSCs Transplantation on Thin Endometrium in the Rat Model.," *Stem Cells Int.*, vol. 2018, p.

3069741, 2018.

[298] Y. Y. Kim, B. Bin Choi, J. W. Lim, Y. J. Kim, S. Y. Kim, and S.-Y. Ku, “Efficient Production of Murine Uterine Damage Model,” *Tissue Eng. Regen. Med.*, vol. 16, no. 2, pp. 119–129, Apr. 2019.

[299] L. de Miguel–Gómez *et al.*, “Comparison of different sources of platelet-rich plasma as treatment option for infertility-causing endometrial pathologies,” *Fertil. Steril.*, vol. 115, no. 2, pp. 490–500, 2021.

[300] J. X. Chen, X. J. Yi, P. L. Gu, and S. X. Gao, “The role of KDR in intrauterine adhesions may involve the TGF-β1/Smads signaling pathway.,” *Brazilian J. Med. Biol. Res. = Rev. Bras. Pesqui. medicas e Biol.*, vol. 52, no. 10, p. e8324, 2019.

[301] P. S. Cooke, T. E. Spencer, F. F. Bartol, and K. Hayashi, “Uterine glands: development, function and experimental model systems,” *Mol. Hum. Reprod.*, vol. 19, no. 9, pp. 547–558, Sep. 2013.

[302] X. Lin *et al.*, “Endometrial stem cell-derived granulocyte-colony stimulating factor attenuates endometrial fibrosis via sonic hedgehog transcriptional activator Gli2†,” *Biol. Reprod.*, vol. 98, no. 4, pp. 480–490, Apr. 2018.

[303] Y. Zhang, H. Yuan, Y. Sun, Y. Wang, and A. Wang, “The effects of ethanol on angiogenesis after myocardial infarction, and preservation of angiogenesis with rosuvastatin after heavy drinking,” *Alcohol*, vol. 54, pp. 27–32, Aug. 2016.

[304] Y. Zhou *et al.*, “Platelet-Rich Plasma Therapy Enhances the Beneficial Effect of Bone Marrow Stem Cell Transplant on Endometrial Regeneration.,” *Front. cell Dev. Biol.*, vol. 8, p. 52, 2020.

[305] Y. Chen *et al.*, “Sustained delivery of 17β-estradiol by human amniotic extracellular matrix (HAECM) scaffold integrated with PLGA microspheres for endometrium regeneration.,” *Drug Deliv.*, vol. 27, no. 1, pp. 1165–1175, 2020.

[306] H. Du, J. Sarno, and H. S. Taylor, “HOXA10 Inhibits Kruppel-Like Factor 9 Expression in the Human Endometrial Epithelium1,” *Biol. Reprod.*, vol. 83, no. 2, pp. 205–211, Aug. 2010.

[307] E. B. Cullinan, S. J. Abbondanzo, P. S. ANDERSONt, J. W. POLLARDt, B. A. LESSEYt, and C. L. Stewart, “Leukemia inhibitory factor (LIF) and LIF receptor expression in human endometrium suggests a potential autocrine/paracrine function in regulating embryo implantation (pregnancy/oncostatin M/ciliary neurotrophic factor/infertility/menstrual cycle),” 1996.

[308] K. E. Lipson, C. Wong, Y. Teng, and S. Spong, “CTGF is a central mediator of tissue remodeling and fibrosis and its inhibition can reverse the process of fibrosis,” *Fibrogenesis Tissue Repair*, vol. 5, no. S1, p. S24, Dec. 2012.

[309] T. A. Wynn, “Cellular and molecular mechanisms of fibrosis.,” *J. Pathol.*, vol. 214, no. 2, pp. 199–210, Jan. 2008.

[310] M. P. Alfaro *et al.*, “A physiological role for connective tissue growth factor in early wound healing.,” *Lab. Invest.*, vol. 93, no. 1, pp. 81–95, Jan. 2013.

[311] S. C. Taylor, K. Nadeau, M. Abbasi, C. Lachance, M. Nguyen, and J. Fenrich, “The Ultimate qPCR Experiment: Producing Publication Quality, Reproducible Data the First Time,” *Trends Biotechnol.*, vol. 37, no. 7, pp. 761–774, Jul. 2019.

[312] X. Zhu, F. Yu, G. Yan, Y. Hu, H. Sun, and L. Ding, “Human endometrial perivascular stem cells exhibit a limited potential to regenerate endometrium after xenotransplantation,” *Hum. Reprod.*, vol. 36, no. 1, pp. 145–159, Dec. 2020.

[313] K. W. Yi, R. Mamillapalli, C. Sahin, J. Song, R. Tal, and H. S. Taylor, “Bone marrow-derived cells or C-X-C motif chemokine 12 (CXCL12) treatment improve thin endometrium in a mouse model.,” *Biol. Reprod.*, vol. 100, no. 1, pp. 61–70, 2019.

[314] G. Ahmad *et al.*, “Barrier agents for adhesion prevention after gynaecological surgery,” *Cochrane Database Syst. Rev.*, Mar. 2020.

[315] K. E. Liu, M. Hartman, and A. Hartman, “Management of thin endometrium in assisted reproduction: a clinical practice guideline from the Canadian Fertility and Andrology Society.,” *Reprod. Biomed. Online*, vol. 39, no. 1, pp. 49–62, Jul. 2019.